A direct measurement of Higgs boson branching ratios in electron-positron collisions at 250 GeV

Jonas Kunath

INSTITUT POLYTECHNIQUE DE PARIS

NNT : 2022IPPAX099

Thèse de doctorat

ÉCOLE POLYTECHNIQUE

IP PARIS

A direct measurement of Higgs boson branching ratios in electron-positron collisions at 250 GeV

Thèse de doctorat de l'Institut Polytechnique de Paris
préparée à l'École polytechnique

École doctorale n°626 École doctorale de l'Institut Polytechnique de Paris (EDIPP)
Spécialité de doctorat : Physique des particules

Thèse présentée et soutenue à Palaiseau, le 21/10/2022, par

JONAS KUNATH

Composition du Jury :

Roberto Salerno Professeur chargé de cours, LLR (Palaiseau)	Président
Imad Laktineh Professeur des universités, IPNL (Lyon)	Rapporteur
Dirk Zerwas Directeur de recherche, IJCLab (Orsay)	Rapporteur
Lucia di Ciaccio Professeure des universités, USMB (Annecy)	Examinateur
Manqi Ruan Directeur de recherche, IHEP (Beijing)	Examinateur
Jean-Claude Brient Directeur de recherche, LLR (Palaiseau)	Directeur de thèse

Contents

Daß ich erkenne, was die Welt
Im Innersten zusammenhält

— Johann Wolfgang von Goethe *Faust*

0 Introduction

The famous polymath Dr. Faust in the tragedy that bears his name is introduced to the audience through a lamenting monologue. He is educated in philosophy, the law, medicine and even theology. Nonetheless the protagonist is complaining about the limits of his knowledge. He even surrendered his soul to magic. All that in order to achieve a single goal: To understand what holds the world together at its innermost folds.

This literary character is just one example for the everlasting human desire to understand the universe and the laws that govern it. As Physicists, we aim to describe the world through theories, mathematical models. Through reproducible experiments, scientists seek to test these models. In particle physics, we attempt to probe our models of the world on the smallest length scales. Those particles that stay apparently point-like at the highest possible resolution are called elementary particles.

The standard model (SM) of particle physics has been formalized in the 1960s [1]–[4]. It predicts and describes the elementary particles, their properties, and the interaction between them (see Fig. 1.1). On its basis, theoretical physicists have calculated more and more precise predictions of experimental observables. Over the course of over half a century, increasingly large and ambitious experiments have been realized in order to test these predictions with reduced uncertainties. While predictions and measurements have been largely compatible, there remain tensions and critical questions for which the SM provides no answers: Why is there more matter than antimatter? How can gravity, macroscopically defined by the theory of general relativity, be unified with the interaction forces described by the SM? Why are there three generations of leptons and quarks? How do neutrinos obtain their masses?

The Higgs field has a unique role among all SM particles. It has been added to the SM to account for the non-zero particle masses[1] in a way that is consistent with the SM symmetries. While other composite scalar particles are known, the SM Higgs boson is the only scalar elementary particle. Alternative forms of the Higgs mechanism, with multiple Higgs bosons or a composite Higgs boson, are also compatible with the SM symmetries. The explanation of fermion masses requires one input parameter per particle: Its coupling strength to the Higgs field.

The first subatomic particle has been discovered in 1897. Thomson identified cathode rays as "charges of negative electricity carried by particles of matter" [5]. As unique particles, their mass m and negative charge e must be independent of the gas of the cathode and its pressure. Indeed he observed that the ratio of charge over mass, m/e, is independent of the cathode's material. Thomson decided to give these

[1] The SM Higgs mechanism does not provide a mechanism to generate non-zero neutrino masses though. See Section 1.2.

"primordial atoms" the name **corpuscles**. Still today this particle, now better known as the **electron**, is believed to be an elementary particle.

In 1911 Rutherford's scattering experiment demonstrated that atoms have a substructure [6]. They are mostly empty, with the positive charge being concentrated at the center of the atom, the atomic nucleus. It has subsequently been shown that the hydrogen nucleus is present in other atomic nuclei. A chemical element is uniquely defined by the number of hydrogen nuclei in its atomic nucleus. Thus the proton, carrying the opposite charge of an electron, was discovered. After enormous advances in instrumentation a similar scattering experiment was done at the Stanford Linear Accelerator Center (SLAC) with electrons on protons [7], [8]. With the much higher energies that were available at SLAC, a substructure was resolved within the protons. The new substructure is described by the parton distribution functions. Thus, since 1969 the proton is understood to be a composite particle instead of an elementary particle. Quantum chromodynamics explains that quarks are bound together through the strong force. Gluons, the carrier particles of the strong force, together with quarks are now collectively called partons.

Weak neutral currents, already predicted by the SM, were first observed in the Gargamelle bubble chamber in 1973 [9]. While the electromagnetic interaction, associated with the massless photon, has infinite range, the weak force has a short range and is carried by particles with a high mass. A large collider had to be constructed in order to discover the bosons that carry the weak charge. In 1983, the Super Proton-Antiproton Synchrotron (Sp$\bar{\text{p}}$S), a proton-antiproton collider at CERN, allowed to confirm the existence of the $W^{\pm}$ and Z bosons [10]–[13]. Precision measurements of the electroweak sector at the electron-positron colliders Large Electron-Positron Collider (LEP) and the Stanford Linear Collider (SLC) subsequently affirmed that the $W^{\pm}$ and Z bosons behave like the particles that are predicted by the SM [14], [15]. In the mean time another proton-antiproton collider, Tevatron, brought the first observation of the top quark (1995) [16], [17]. With this discovery, all expected quarks and leptons have been confirmed. Still, there was one fundamental particle predicted by the SM that had not been observed: The Higgs boson.

In 2012, the ATLAS and CMS collaborations at the Large Hadron Collider (LHC) at CERN observed a new scalar particle, compatible with the properties of the SM Higgs boson with a mass of 125 GeV [18], [19]. Thus almost half a century after its prediction [20], [21], and over a century after the discovery of the first SM particle, the SM now seems to have been completed. But does this particle indeed hold all those properties demanded by the theory? Are all its couplings compatible with their expectations? Or are there some tensions with the predictions, that hint towards extensions of the SM?

1 The Standard Model of Particle Physics

Contents

The standard model (SM) of particle physics is a quantum field theory with gauge symmetries. It describes three of the four known fundamental forces: the strong, the electromagnetic and the weak force. Their force-carrying, spin-1 bosons are gluons, photons, $W^{\pm}$ and Z bosons. The fourth fundamental force, gravity, is not part of the SM. It is described by a classical theory: Einstein's theory of general relativity. Formulations of quantum gravity with massless spin-2 gravitons as force carriers exist. Due to gravity's imperceptible strength in comparison to the other fundamental forces, probing predictions for quantum gravity is far beyond the experimental reach.

1.1 Elementary particles

All point-like particles that have been observed so far are constituents of the SM. They can be unambiguously identified by their mass m, spin s, color c and electric charge Q. The SM particles have spin 0, 1/2 or 1. A summary is given in Fig. 1.1.

1.1.1 Fermions

Particles with half-integer spin are called fermions. All SM fermions have spin $s = 1/2$. Those fermions that couple through the strong force (color) are the quarks. The color-neutral fermions are the leptons.

Quarks Three families of quarks have been observed experimentally. Each family consists of two different quarks with electric charge difference 1. The only difference between the quark families is the mass of the particles. As both their electric charge and their color charge are non-zero, quarks interact through all three forces of the SM. Due to color confinement, quarks can never be found as free states but only confined into bound states, hadrons. Atoms, forming our everyday matter, consist of electrons, protons and neutrons. Both proton and neutron are color-neutral. The proton, with electric charge 1, is

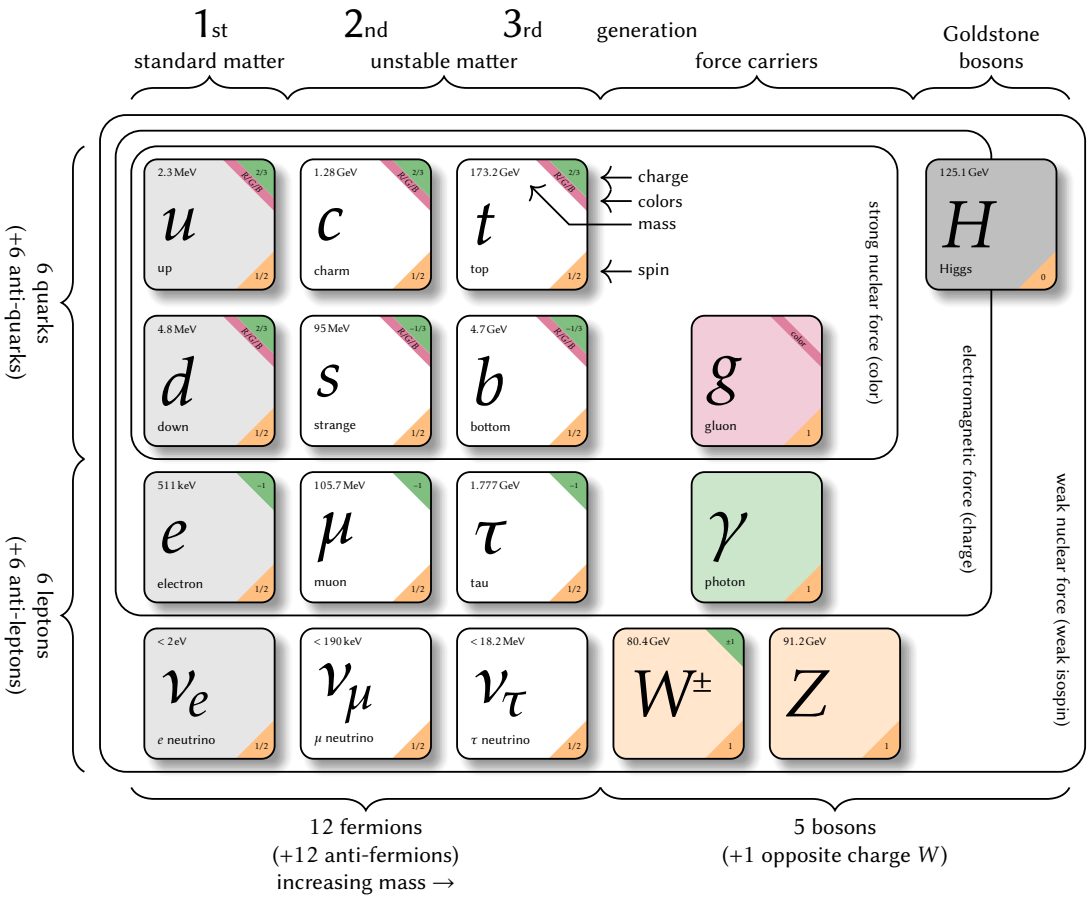

Figure 1.1: Constituents of the Standard Model of Particle Physics. Each constituent is uniquely defined by its quantum numbers: charge, colors, mass and spin. Figure adapted from [22].

composed of two up (u) and one down (d) quark (uud) while the neutron (uud) has electric charge 0. Given that the down quark has a higher mass than the up quark (and given that their mass difference is larger than the electron mass), free neutrons decay into protons (together with an electron anti-neutrino pair). The particles in the second and third generation have a higher mass and are therefore not stable. Decays of quarks to other generations (different **flavor**) are only possible through the weak interaction. The second and third generation quarks are charm (c), strange (s), top (t) and bottom (b) quark. The top quarks has the highest mass out of all elementary particles that have been observed. There are no bound states with a top quark: its mean life time is about twenty times smaller than the time scale of the strong interaction. In contrast, the five other quark types can only be experimentally found in hadrons.

Leptons The (electrically) charged leptons are electron (e), muon (μ) and tau (τ). Each of them carries electric charge -1. There is one electrically neutral lepton per family. These neutrinos (ν) only interact through the weak force. Antiparticles have the same mass but opposite color and electric charge. For Dirac fermions, particle and antiparticle are different entities. Fermions that are their own antiparticle are Majorana fermions. It is not known whether neutrinos are Dirac or Majorana fermions. As the other

fermions are massive and have non-zero color or electric charge, they must be Dirac fermions. While the electron is stable, muon and tau leptons are unstable. The muon's mean life time is large enough to consider it as a stable particle over the typical length scales of a high energy particle physics detector in a collider experiment. In contrast, tau leptons can only be detected through its decay products. Tau leptons can decay both purely to leptons and through hadronic decay modes [23].

Chirality A particle has positive (right-handed) helicity if the projection of its spin is in the same direction as its motion and negative (left-handed) helicity for a projection of the spin in the opposite direction. For massless particles, chirality is the same as helicity. If the particle is massive it is necessarily moving below the speed of light. An observer can thus change into a reference frame that moves faster than the massive particle. In this new reference frame the particle is moving backwards. Thus its helicity is flipped with respect to its helicity in the original reference frame. Chirality is a more abstract concept. It denotes the particle's transformation behavior under the Poincaré group. Therefore, chirality is a conserved quantity also for massive particles, in contrast to helicity. As will be discussed in Section 1.2, a Dirac fermion has two **chirality** eigenstates: left-handed (ψ_L) and right-handed (ψ_R). Only left-handed fermions partake in the weak interaction.

The electric charge and the color charge are independent of a particle's chirality. The third component of the weak isospin T_w^3 and the hypercharge Y differ depending on the chirality eigenstate. Therefore they were omitted from Fig. 1.1. The fermion quantum numbers are summarized in Table 1.1. The left-handed fermions form a doublet under the electroweak $SU(2)_L \times U(1)_Y$ symmetry. In contrast, the right-handed fermions transform as singlets. Only left-handed (L) neutrinos have been observed. Right-handed (R) neutrinos are not part of the SM, but are not experimentally excluded.

	generation			**quantum number**			
	1	2	3	Q	T_w^3	Y	c (color)
lepton	$\begin{pmatrix} \nu_e \\ e \end{pmatrix}_L$	$\begin{pmatrix} \nu_\mu \\ \mu \end{pmatrix}_L$	$\begin{pmatrix} \nu_\tau \\ \tau \end{pmatrix}_L$	0	$+1/2$	-1	
	e_R	μ_R	τ_R	-1	$-1/2$	-1	-
				-1	0	-2	
quark	$\begin{pmatrix} u \\ d' \end{pmatrix}_L$	$\begin{pmatrix} c \\ s' \end{pmatrix}_L$	$\begin{pmatrix} t \\ b' \end{pmatrix}_L$	$+2/3$	$+1/2$	$+1/3$	
				$-1/3$	$-1/2$	$+1/3$	r, g, b
	u_R	c_R	t_R	$+2/3$	0	$+4/3$	
	d_R	s_R	b_R	$-1/3$	0	$-2/3$	

Table 1.1: Fermion quantum numbers per chirality eigenstate.

1.1.2 Bosons

Particles with integer spins are called bosons. The SM has one scalar (spin-0) boson, the Higgs boson (H). As will be discussed in Section 1.2, it is responsible for the particle masses. There are four types of vector bosons (spin-1). These gauge bosons are the messenger particles of the three fundamental forces described by the SM. They facilitate communication between particles with a finite distance between them, in contrast to contact interactions like the Fermi theory of beta decay. The photon (γ), messenger particle of the electromagnetic interaction, is massless. The weak force has a neutral messenger particle (Z boson) as well as a variant with positive and negative electric charge ($W^\pm$). The gluon (g) is the messenger particle for the strong force and has eight independent color charge states. Both weak and strong interaction have a short range only. The short range of the weak interaction implies that $W^\pm$ and Z bosons are massive. The range of the strong force is limited by color confinement. The gluon is expected to be massless and masses above a few MeV are excluded by experimental results [24].

No elementary bosons with higher spin has been observed today. The graviton, messenger particle in quantum theories of gravity, would have to be a tensor boson (spin-2).

1.2 The Standard Model Lagrangian

The SM is described by its Lagrangian $\mathcal{L}_{\text{SM}}$. It is invariant under the local (gauge) symmetry $SU(3)_C \times SU(2)_L \times U(1)_Y$ and the global Poincaré symmetry. For a derivation of the formulas presented below, see e.g. [25].

Free fermionic field Poincaré invariance encodes special relativity: The laws of physics are invariant under translations, rotations and boosts. A fermion is described by the complex spinor $\psi(x)$ in the space-time coordinates x and the Dirac Lagrangian

$$\mathcal{L}_f = \bar{\psi}(x)(i\partial\!\!\!/ - m)\psi(x) \tag{1.1}$$

with $\partial\!\!\!/ = \gamma_\mu \partial^\mu$ where $\gamma_{0,1,2,3}$ are the Dirac matrices.

Quantum Chromodynamics (QCD) The gauge symmetry of the strong force is $SU(3)_C$. Equation (1.1) is invariant under global phase transformations $\psi(x) \to U\psi(x)$ with $U \in SU(3)$. The unitary $n \times n$ matrices with determinant 1 are a representation of $SU(N)$. This group has dimension $n^2 - 1$. The eight linear independent, hermetian, traceless Gell-Mann matrices λ^a are commonly used as the generators for the $SU(3)_C$ group. They allow to write any element in $SU(3)$ as $U = e^{ig_s\theta^a \frac{\lambda^a}{2}}$. When the symmetry is promoted to a local symmetry, $\theta^a(x)$, the Lagrangian is no longer invariant under the transformation.

In order to recover invariance, the (gluon) vector fields G^a_μ are introduced. The derivate is replaced by the covariant derivative

$$\partial_\mu \to D_\mu = \partial_\mu + ig_s \frac{\lambda^a}{2} G^a_\mu. \tag{1.2}$$

Under this gauge transformation, the new fields transforms as

$$F^a_\mu \to F^a_\mu + \partial_\mu \theta^a + ig_s \frac{\lambda^a}{2} F^a_\mu. \tag{1.3}$$

The gluon Lagrangian is

$$\mathcal{L}_g = -\frac{1}{4} F^{\mu\nu}_a F^a_{\mu\nu} \tag{1.4}$$

with the field strength tensor

$$F^{\mu\nu}_a = \partial^\mu G^\nu_a - \partial^\nu G^\mu_a + g_s f_{abc} G^\mu_b G^\nu_c \tag{1.5}$$

where f_{abc} are the structure constants of the $SU(3)$ Lie group, obeying

$$i f_{abc} \lambda^c = \left[\lambda_a, \lambda_b\right] = \lambda_a \lambda_b - \lambda_b \lambda_a. \tag{1.6}$$

The gluon Lagrangian is gauge invariant. It has a quadratic kinetic term and the three- and four-gluon interaction vertices. Substituting Eq. (1.2) into Eq. (1.1) brings out the quark-gluon interaction term $-g_s \bar{\psi}(x) \frac{\lambda^a}{2} \gamma^\mu G^a_\mu \psi(x)$. The coupling strength g_s is a free parameter of the theory and has to be determined experimentally. Combining the terms leads to the QCD Lagrangian

$$\mathcal{L}_{\text{QCD}} = \bar{\psi}(x)(i\partial\!\!\!/ - m)\psi(x) - g_s \bar{\psi}(x) \frac{\lambda^a}{2} \gamma^\mu G^a_\mu \psi(x) - \frac{1}{4} F^{\mu\nu}_a F^a_{\mu\nu}. \tag{1.7}$$

Quantum Electrodynamics (QED) When treating the electromagnetic force separately, it has a local $U(1)_{em}$ symmetry, $\psi(x) \to e^{ie\theta(x)}\psi(x)$. In contrast to the QCD symmetry group, there is only one generator for $U(1)_{em}$. This single vector boson, the photon, has no self-interaction term ($f_{abc} = 0$).

$$\begin{aligned}\mathcal{L}_{\text{QED}} =& \mathcal{L}^{\text{int}}_{\text{QED}} + \mathcal{L}^{\text{kin},f}_{\text{QED}} + \mathcal{L}^{\text{kin},\gamma}_{\text{QED}} \\ =& -e\bar{\psi}(x)\gamma^\mu A_\mu \psi(x) + \bar{\psi}(x)(i\partial\!\!\!/ - m)\psi(x) \\ & -\frac{1}{4}(\partial^\mu A^\nu - \partial^\nu A^\mu)\left(\partial_\mu A_\nu - \partial_\nu A_\mu\right)\end{aligned} \tag{1.8}$$

Electroweak interaction (EW) The electroweak interaction is jointly described by the $SU(2)_L \times U(1)_Y$ symmetry group. The concept of chirality has been introduced in Section 1.1. The chirality eigenstates can be obtained with the help of the chirality projectors:

$$\psi_{L/R} = P_{L/R}\psi = \frac{1}{2}(1 \mp \gamma^5)\psi \tag{1.9}$$

where $\gamma^5 = i\gamma^0\gamma^1\gamma^2\gamma^3$ is a product of gamma matrices. It has been experimentally shown that the weak interaction only affects left-handed particles and is thus maximally parity violating.

The $SU(2)_L$ gauge transformation

$$\psi \to e^{ig\vec{\theta}(x)\vec{T}}\psi \tag{1.10}$$

can be described using the Pauli spin matrices as generators $T_i = \sigma_i/2$. Their commutation relation is $\left[\sigma_i, \sigma_j\right] = 2i\epsilon^{ijk}\sigma_k$, where ϵ^{ijk} is the Levi-Civita tensor. Three vector bosons appear due to this gauge transformation: $W^i_\mu, i = 1, 2, 3$. The conserved quantity related to the symmetry is the weak isospin T_3.

The $U(1)_Y$ symmetry resembles the $U(1)_{em}$ symmetry that has been discussed above. Its gauge boson B_μ as well as the W^i_μ are massless. The Gell-Mann-Nishijima formula describes the electric charge in terms of hypercharge and weak isospin: $Q = T_3 + Y/2$.

The Lagrangian of the electroweak interaction is

$$\mathcal{L}_{\text{EW}} = i\bar{\Psi}_L D\!\!\!/ \Psi_L + i\bar{\psi}_R D\!\!\!/ \psi_R + \bar{\psi'}_R D\!\!\!/ \psi'_R + \mathcal{L}_{\text{gauge}} \tag{1.11}$$

with $\Psi_L = (\psi_L, \psi'_L)^T$ the left-handed fermion doublets and ψ_R, ψ'_R the right-handed singlets. The prime symbolizes the down/neutrino version of each fermion type and generation. The covariant derivate contains two symmetries and thus two interaction strengths g, g':

$$D_\mu = \partial_\mu - ig\vec{T}\vec{W}_\mu - ig'\frac{Y}{2}B_\mu. \tag{1.12}$$

The gauge boson part of the Lagrangian can be presented concisely with the help of the field strength tensors:

$$B^{\mu\nu} = \partial^\mu B^\nu - \partial^\mu B^\nu, \tag{1.13}$$

$$W^{\mu\nu}_i = \partial^\mu W^\nu_i - \partial^\mu W^\nu_i + g\epsilon_{ijk}W^\mu_j W^\nu_k, \tag{1.14}$$

$$\mathcal{L}_{\text{gauge}} = -\frac{1}{4}W^{\mu\nu}_i W^i_{\mu\nu} - \frac{1}{4}B^{\mu\nu}B_{\mu\nu}. \tag{1.15}$$

Experimentally, two massive charged boson ($W^\pm_\mu$), a massive neutral boson (Z_μ) and the massless photon (A_μ) are observed. They can be obtained through a linear combination of the fields from

Eq. (1.12):

$$W_\mu^\pm = \frac{1}{\sqrt{2}}\left(W_\mu^1 \mp i W_\mu^2\right), \tag{1.16}$$

$$\begin{pmatrix} A_\mu \\ Z_\mu \end{pmatrix} = \begin{pmatrix} \cos\theta_W & \sin\theta_W \\ -\sin\theta_W & \cos\theta_W \end{pmatrix} \begin{pmatrix} B_\mu \\ W_\mu^3 \end{pmatrix}. \tag{1.17}$$

The Weinberg angle θ_W describes the mixing between the physical fields and the (B_μ, W_μ^3) basis:

$$\tan\theta_W = g'/g,\ e = g' \sin\theta_W = g\cos\theta_W. \tag{1.18}$$

Due to its non-abelian group structure, terms of order higher than two in the gauge field are part of the Lagrangian. Two trilinear couplings (γW^+W^-, ZW^+W^-) and four quadrilinear couplings ($\gamma\gamma W^+W^-$, γZW^+W^-, ZZW^+W^-, $W^+W^-W^+W^-$) emerge when spelling out Eq. (1.15) in terms of the physical fields.

Electroweak symmetry breaking (EWSB) The electroweak Lagrangian in Eq. (1.11) includes no mass term for the gauge bosons. Adding an explicit mass term would break gauge invariance. The Brout-Englert-Higgs (BEH) mechanism [20], [21] has been proposed as a mechanism that creates the mass terms required due to experimental evidence while keeping gauge invariance.

A complex scalar field

$$\phi = \begin{pmatrix} \phi^+ \\ \phi^0 \end{pmatrix} = \frac{1}{\sqrt{2}} \begin{pmatrix} \phi^1 + i\phi^2 \\ \phi^3 + i\phi^4 \end{pmatrix} \tag{1.19}$$

with potential

$$V(\phi) = -\mu^2 \phi^\dagger\phi + \lambda\left(\phi^\dagger\phi\right)^2 \tag{1.20}$$

is introduced. The standard model Lagrangian $\mathcal{L}_{\text{SM}}$ is extended by the Higgs sector

$$\mathcal{L}_{\text{EWSB}} = \left(D_\mu\phi\right)^\dagger \left(D_\mu\phi\right) + V(\phi). \tag{1.21}$$

Using the covariant derivate D_μ, introduced in Eq. (1.12), ensures that the Lagrangian stays gauge invariant. In order to keep the potential finite, $\lambda > 0$ is necessary. For $\mu^2 \leq 0$ the potential has a single minimum, $\phi^\dagger\phi = 0$. A more interesting structure arises with $\mu^2 > 0$: A continuum of minima, $\phi^\dagger\phi = v^2 = \mu^2/\lambda$. Choosing without loss of generality the ground state

$$\phi_{\text{min}} = \frac{1}{\sqrt{2}} \begin{pmatrix} 0 \\ v \end{pmatrix} \tag{1.22}$$

breaks the symmetry as $SU(2)_L \times U(1)_Y \to U(1)_Q$. As a consequence of the Goldstone theorem [26], the broken symmetry generators resolve as three massless scalar bosons. The perturbative expansion around the minimum,

$$\phi(x) = \frac{1}{\sqrt{2}} e^{i\sigma^i\theta^i(x)} \begin{pmatrix} 0 \\ v + H(x) \end{pmatrix} \tag{1.23}$$

can be simplified by using the **unitary gauge**:

$$\phi(x) \to e^{-i\sigma^i\alpha^i(x)}\phi(x),\ \alpha^i(x) = 2\theta^i(x), \tag{1.24}$$

$$\phi(x) = \frac{1}{\sqrt{2}} \begin{pmatrix} 0 \\ v + H(x) \end{pmatrix}. \tag{1.25}$$

The single remaining physical field can be identified as the Higgs field, $H(x)$. The vacuum expectation value (VEV) v of $\phi(x)$ is non-zero.

After symmetry breaking, the Higgs sector of $\mathcal{L}_{\text{SM}}$ becomes

$$\begin{aligned}\mathcal{L}_{\text{EWSB}} =& \frac{1}{2}\partial_\mu H \partial^\mu H + \mu^2 H^2 \\ &+ \frac{\mu^2}{v} H^3 + \frac{\mu^2}{4v^2} H^4 \\ &+ \frac{g^2 v^2}{4} W_\mu^+ W^{-\mu} + \frac{1}{2}\frac{\left(g^2 + g'^2\right)v^2}{4} Z_\mu Z^\mu \\ &+ \frac{g^2 v}{2} H W_\mu^+ W^{-\mu} + \frac{g^2}{4} H^2 W_\mu^+ W^{-\mu} + \frac{g'^2 v}{2} H Z_\mu Z^\mu + \frac{g^2}{4} H^2 Z_\mu Z^\mu.\end{aligned} \tag{1.26}$$

The photon field remains massless. The remaining bosons have masses

$$m_Z = \frac{1}{2}\sqrt{g^2 + g'^2}\, v, \tag{1.27}$$

$$m_W = \frac{1}{2} g v = m_Z \cos\theta_W, \tag{1.28}$$

$$m_H = \sqrt{2\mu^2} = \sqrt{2\lambda v^2}. \tag{1.29}$$

The outstanding terms describe the Higgs couplings: trilinear and quadrilinear self-coupling, as well as interactions with the massive weak bosons (HW^+W^-, HHW^+W^-, HZZ, $HHZZ$).

Thus far, the Higgs mechanism only explains boson masses. The most general form of $\mathcal{L}_{\text{SM}}$ that is invariant under the electroweak symmetry additionally allows for Yukawa interactions:

$$\begin{aligned}\mathcal{L}_{\text{Yukawa}} =& \sum_{i,j=1,2,3} y^d_{ij} \bar{Q}_{iL} \phi d_{jR} - i y^u_{ij} \bar{Q}_{iL} \sigma_2 \phi^\star u_{jR} + \sum_{k,l=1,2,3} y^e_{kl} \bar{L}_{kL} \phi e_{lR} \\ &+ \text{hermetian conjugate } (h.c.)\end{aligned} \tag{1.30}$$

Here Ψ, ψ, ψ' were explicitly written out as Q_i, u_i, d_i for quarks and L_i, e_i, ν_i for leptons, with the subscript running over the families. Expanding around the ground state after symmetry breaking leads to

$$\mathcal{L}_{\text{Yukawa}} = -\sum_{f=u,d,e} \sum_{i,j=1,2,3} m^f_{ij} \bar{f}_{iL} f_{jR} \left(1 + \frac{H}{v}\right) + h.c. \tag{1.31}$$

where the mass matrices are related to the Yukawa coupling constants by

$$m^f_{ij} = y^f_{ij} \frac{v}{\sqrt{2}}. \tag{1.32}$$

The mass term of each fermion must be proportional to its coupling with the Higgs boson, according to Eq. (1.30). The experimental verification is shown in Fig. 1.2. There is good agreement with the SM expectation for all couplings that are currently attainable.

The Yukawa interaction includes both left- and right-handed particles. Typically, particles are described in the basis that diagonalizes the mass matrices (e.g. Fig. 1.1) with mass eigenstates d^i_L (flavor/generation). These do not necessarily coincide with the weak eigenstates. The mixing between the two bases is described by the Cabibbo-Kobayashi-Maskawa matrix:

$$d^{j\,\prime}_L = \sum_{i=1}^{3} V^{ji}_{\text{CKM}} d^i_L. \tag{1.33}$$

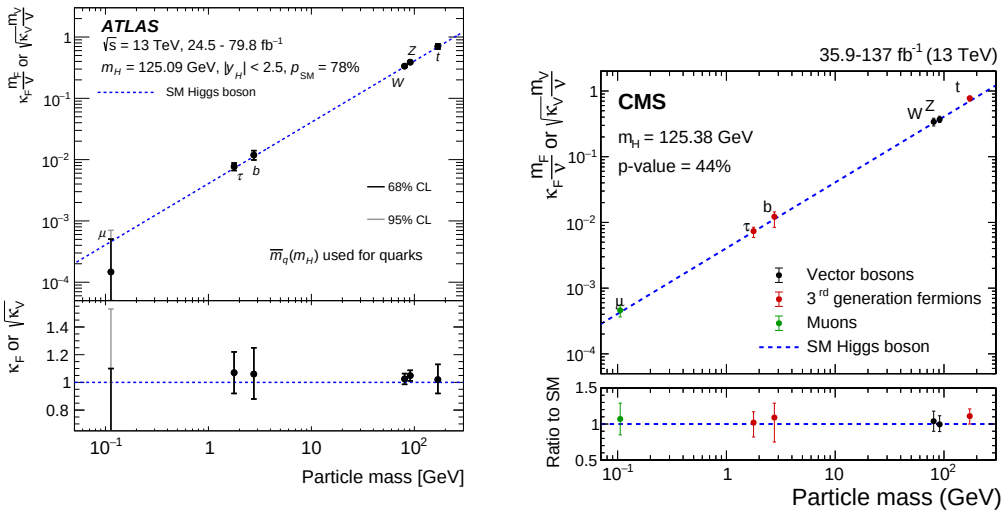

Figure 1.2: Coupling-strength modifiers κ as a function of the particles masses measured by the ATLAS [27] and CMS [28] experiments. The lower panels show the ratios between the measured coupling modifiers and their SM predictions. All measurements are found in agreement with the SM within the uncertainties.

The off-diagonal elements specify the suppression factor of flavor-changing transitions in weak interactions.

Analogously, the Pontecorvo-Maki-Nakagawa (PMNS) matrix describes the mixing between weak and mass eigenstates for the neutrinos. Right-handed neutrinos have never been observed, as they do not interact with SM particles. The observation of neutrino oscillations implies that neutrinos are not massless. Identifying the right mechanism for the generation of neutrino masses as an extension of the standard model is still an open problem.

1.3 Free parameters of the Standard Model

The SM is fixed through 19 independent numerical constants. One such set of content is described in Table 1.2. Additional parameters would have to be introduced to account for neutrino masses and neutrino oscillations. The fermion masses span almost six orders of magnitude between the electron mass ($m_e = 0.511\,\text{MeV}$) and the on-shell top mass ($m_t = 173.5\,\text{GeV}$).

#	type	variable names
9	fermion masses	$m_e, m_\mu, m_\tau, m_u, m_d, m_s, m_c, m_b, m_t$
3	CKM flavor mixing angles	$\theta_{12}, \theta_{23}, \theta_{13}$
1	CKM CP violating phase	δ
3	gauge coupling strengths	g_s, g, g' $(SU(3)_C \times SU(2)_L \times U(1)_Y)$
1	QCD vacuum angle	θ_{QCD}
1	Higgs vacuum expectation value	v
1	Higgs mass	m_H
19	sum	

Table 1.2: An independent set of input parameters for the standard model.

1.4 Effective Field Theory

An effective field theory (EFT) provides an adequate description of the physical processes at a given length scale while breaking down at shorter distances. The Fermi theory of beta decay is an EFT for the weak interaction at longer distances. In Fermi's theory, the beta decay $n \to pe^-\bar{\nu}_e$ is represented by a four fermion vertex with coupling strength G_F. The cross section for beta decay rises quadratically with the energy, $\sigma \propto G_F^2 E^2$. At small distances, probed with energies above 100 GeV, this EFT is no longer a valid description of the electroweak theory.

SMEFT It is worthwhile to apply the EFT framework to the SM. A standard model effective field theory (SMEFT) fit combines the measurements from different experiments and different data channels in order to produce a set of coefficients of SMEFT operators, called Wilson coefficients. The determination of these coefficients and their corresponding uncertainties and correlations uses the synergies between the measurements. The comparison of theoretical models with the SMEFT coefficients restricts the model parameters. In the case of deviations from the SM, any new theoretical model that is supposed to explain the deviations must be compatible with the SMEFT coefficients. A SMEFT connects the weak sector to the Higgs sector.

The Fermi theory of beta decay that was introduced above is a predecessor of the SM. In the SMEFT context, the SM itself is regarded as the predecessor of a more general theory that remains valid at higher energies, the ultraviolet (UV) theory. This more general theory can have additional particles. Its low-energy predictions must be compatible with the measurements and the new theory is expected to obey the SM symmetries.

Assuming that all new particles (NP) have masses far above the EWSB scale, $M_{\text{NP}} \gg v$, these particles can be integrated out from the UV theory. The effective Lagrangian $\mathcal{L}_{\text{eff}}$ depends only on the known, light SM particles. Additional effective operators, suppressed by inverse powers of the heavy mass scale $1/M_{\text{NP}}^n$, appear. The mass scale is set by the lightest of the new particles. Grouped by the dimension of the operator, the Lagrangian $\mathcal{L}_0$ of the UV theory is described by the effective Lagrangian:

$$\mathcal{L}_0 \to \mathcal{L}_{\text{eff}} = \mathcal{L}_4 + \sum_i \frac{b_i}{M}\mathcal{O}_i + \sum_j \frac{c_j}{M^2}\mathcal{O}_j + \cdots . \tag{1.34}$$

where $\mathcal{L}_4$ includes all operators of dimension 4 and lower, the operators $\mathcal{O}_i$ are the operators of dimension 5, the operators $\mathcal{O}_j$ are the operators of dimension 6, and higher dimension operators follow.

It is reasonable to require that the general theory still respects the symmetries of the SM. The SM is the most general renormalizable quantum field theory with the known particles that respects the $SU(3)_C \times SU(2)_L \times U(1)_Y$ gauge symmetry and the Poincaré symmetry. In the SMEFT framework it is assumed that the Higgs field in $\mathcal{L}_{\text{eff}}$ is an $SU(2)$ doublet field Φ and that Φ is the only source of EWSB, as in the SM. This means that the Higgs boson is a light field at the electroweak scale (M_W) and that any deviations from the SM are due to some heavy fields at the scale M, $M \gg M_W$. Thus no terms with dimension 4 or lower other than the SM terms can be part of the SMEFT Lagrangian, $\mathcal{L}_4 = \mathcal{L}_{\text{SM}}$. The only possible operators of dimension 5 are neutrino mass terms. These could not be measured at a collider experiment. The higher-order odd operators are fermion-number violating. It therefore suffices to consider the operators of even dimensions.

After EWSB, the operators obtain expectation values, e.g. $\mathcal{O}_j \to A\Phi^\dagger\Phi$ with A obtained from loop calculations involving the heavy fields. Then naturally the order of magnitude of the dimension 6 coefficients is $c_j \sim (v/M)^2$. Assuming that the symmetry breaking scale M of the general theory is in the TeV range, and inserting the Higgs fields vacuum expectation value $v = 246\,\text{GeV}$, dimension 6 coefficients are expected to be on the order of a few percent or less. With the precision data from a Higgs factory (see Chapter 2) the leading order SMEFT description with dimension 6 operators will have to be augmented by the dimension 8 operators ($d_k \sim (v/M)^4$).

While the SMEFT framework is a powerful tool to describe corrections to the Higgs boson couplings, triple gauge boson couplings (TGC), and to the four fermion couplings, its assumptions are not necessarily fulfilled. There might still be particles with below-TeV mass.[1] Additional sources of EWSB are not described by SMEFT. They have to be studied separately but are already restricted by today's precision in Higgs measurements.

1.5 Phenomenology of the Higgs sector

The Higgs boson interacts with all massive particles of the SM. Given that the coupling strength is proportional to the particle's mass, this interaction is especially important for the more massive particles. The branching ratio (BR) quantifies the probability of the Higgs boson to decay into the specific state:

$$BR(H \to X) = \frac{\Gamma(H \to X)}{\sum_i \Gamma(H \to X_i)} = \frac{\Gamma(H \to X)}{\Gamma_H}. \tag{1.35}$$

The partial widths Γ of an elementary particle can be calculated in quantum field theory. The total width Γ_H is the sum over all partial widths. At tree level, the partial width for a fermion final state is

$$\Gamma(H \to f\bar{f}) = N_C \frac{m_f^2 m_H}{8\pi v}\left(1 - \frac{3m_f^2}{m_H^2}\right)^{\frac{3}{2}}. \tag{1.36}$$

Since the Higgs coupling is independent of the color charge, the quark widths acquire an additional factor three in comparison to the lepton final states from the sum over the color states. Considering that the top mass is large ($m_t > m_H$), the Higgs decay to a top pair is suppressed. No such kinematic constraint exists for the $t\bar{t}H$ production mode.

The tree level partial widths for the massive gauge bosons are

$$\Gamma(H \to W^+W^-) = \frac{1}{4\pi}\frac{m_W^4}{m_H v^2}\left(1 - \frac{4m_W^2}{m_H^2}\right)^{\frac{1}{2}}\left(3 + \frac{1}{4}\frac{m_H^4}{m_W^4} - \frac{m_H^2}{m_W^2}\right), \tag{1.37}$$

$$\Gamma(H \to ZZ) = \frac{1}{8\pi}\frac{m_W^4}{m_H v^2}\left(1 - \frac{4m_W^2}{m_H^2}\right)^{\frac{1}{2}}\left(3 + \frac{1}{4}\frac{m_H^4}{m_W^4} - \frac{m_H^2}{m_W^2}\right). \tag{1.38}$$

The final states with one or more massless gauge bosons ($gg, \gamma\gamma, Z\gamma$) arise in higher order perturbation theory through virtual loops with massive particles.

The Higgs mass is a free parameter of the SM. The evolution of the Higgs branching ratios over a reasonable range of Higgs masses is presented in Fig. 1.3. Combining the Higgs mass measurements of the ATLAS and CMS experiments yields $m_H = 125.25 \pm 0.17\,\text{GeV}$ [24], [29]–[31]. In this Higgs mass region, numerous decay modes are sufficiently abundant for detection. The main branching ratios expected for a SM 125 GeV Higgs boson[2] are summarized in Table 1.3. For the direct theoretical uncertainties the effect of missing higher orders in perturbation theory for electroweak and QCD calculation must be estimated. Important parametric uncertainties stem from the uncertainty in the quark masses and in the strong coupling constant. The cited uncertainties are calculated as the sum in

[1] New particles in the $\mathcal{O}(100\,\text{GeV})$ mass range mean that neglecting the higher order terms is no longer justified. But in such a scenario it can be expected that the dimension-6 operators will also show large deviations.

Very light new particles that have not been observed yet can only have a feeble coupling to SM particles. Thus there effect on electroweak precision observables is expected to be small.

[2] The samples used in this thesis were created under the $m_H = 125\,\text{GeV}$ assumption.

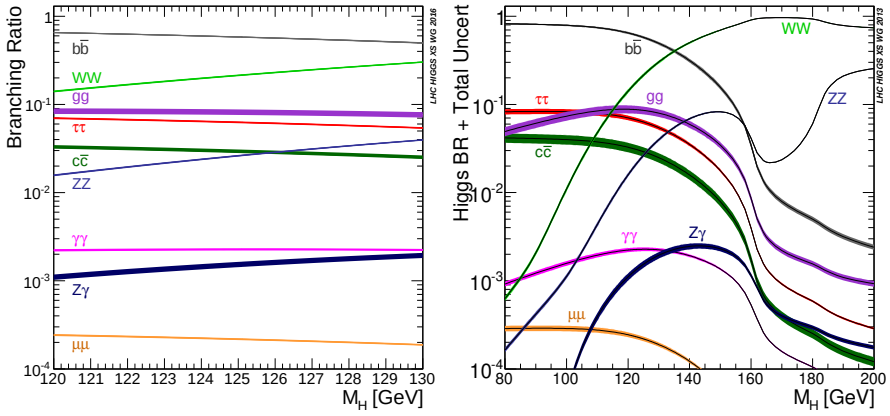

Figure 1.3: The main branching ratios of the SM Higgs boson near $m_H = 125\,\text{GeV}$ [32] and over a wider range [33]. The theoretical uncertainties are indicated as bands.

quadrature of these three contributions. While the $BR(H \to \mu^+\mu^-)$ is comparably small, the excellent reconstruction capabilities of modern particle physics detectors enable analyses with comparably high reconstruction efficiency and purity.

Decay channel	BR [%]	Absolute	Relative uncertainty
$H \to b\bar{b}$	58.24	$+0.72/-0.74$	$+1.2\%/1.3\%$
$H \to W^+W^-$	21.37	± 0.33	$\pm 1.5\%$
$H \to gg$	8.19	± 0.42	$\pm 5.1\%$
$H \to \tau^+\tau^-$	6.27	± 0.10	$\pm 1.6\%$
$H \to c\bar{c}$	2.89	$+0.16/-0.06$	$+5.5\%/2.0\%$
$H \to ZZ$	2.619	± 0.040	$\pm 1.5\%$
$H \to \gamma\gamma$	0.2270	± 0.0042	$\pm 2.1\%$
$H \to Z\gamma$	0.1533	± 0.0089	$\pm 5.8\%$
$H \to \mu^+\mu^-$	0.02176	± 0.00037	$\pm 1.7\%$

Table 1.3: SM predictions of the main branching ratios (BR) for a SM Higgs boson with $m_H = 125\,\text{GeV}$ [24], [32].

A summary of the Higgs couplings measured by the ATLAS and CMS collaborations is given in Fig. 1.2. The measured couplings are in good agreement with the SM expectation. Note that the $H \to \mu^+\mu^-$ result is the only coupling to a second generation fermion that was already measured precisely enough to be included here. Even though the $H \to c\bar{c}$ BR is more than 100 times higher, its analysis is more challenging at a hadron collider. The large QCD backgrounds, especially for the dominant Higgs production modes gluon fusion and vector boson fusion, make it difficult to reconstruct the Higgs boson from hadronic decay products.

Higgs production at an e^+e^- collider Likewise to the Higgs BRs depending on the Higgs mass, the Higgs production modes have a Higgs mass dependency. The tree level Feynman diagrams of the three most important Higgs production modes at a lepton collider are depicted in Fig. 1.4. The graphs were produced for a $m_H = 125\,\text{GeV}$ Higgs boson mass and the left polarization scenario of initial beams at the ILC. This collider will be introduced in Chapter 2.

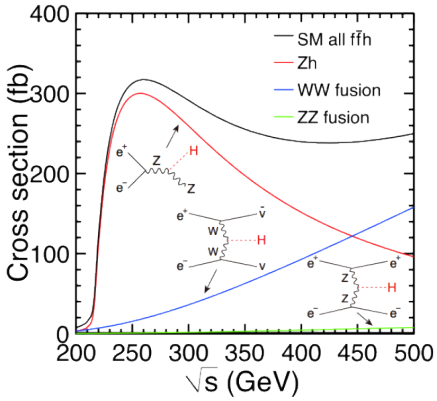

Figure 1.4: Cross sections for the three major Higgs production processes as a function of the center-of-mass energy. Figure taken from [34].

Barely any Higgs bosons are produced for center-of-mass energies below $\sqrt{s} = 210\,\text{GeV}$.[3] The exact $\sqrt{s}$ position of the peak of the **Higgsstrahlung** cross section depends on accelerator details: Bremsstrahlung reduces the effective center-of-mass energy from the colliding electron-positron pair. For a more massive Higgs boson, this peak would shift towards higher center-of-mass values. The peak region of Higgsstrahlung (ZH) around 250 GeV provides an ideal environment for Higgs decay studies. For higher center-of-mass energies the cross section of this s-channel process decreases with $\sigma_{ZH} \sim 1/s$. Above 450 GeV the production through (t-channel) vector boson fusion (VBF) dominates. Only ZZ-fusion is possible if the initial electron and positron have the same polarization.

[3] No Higgs production by Higgsstrahlung ($M_H + M_Z \approx 91\,\text{GeV} + 125\,\text{GeV} = 216\,\text{GeV}$), but still a small Higgs production from vector boson fusion. See also Fig. 2.3.

2

The International Linear Collider

Contents

The International Linear Collider (ILC) is a proposal for a future electron-positron collider at the energy frontier. The underlying accelerator technology is described in Section 2.1. Section 2.2 features a recapitulation of the planned running modes and the main physics goals that can be targeted at each of the collision energy stages. A comparison with alternative proposals for new lepton colliders is made in the subsequent Section 2.3. The complementarity of the physics program at ILC with what can be achieved at the (already scheduled) High Luminosity Large Hadron Collider (HL-LHC) is discussed in Section 2.4.

2.1 Accelerator overview

A thorough overview of the ILC project is provided in volumes 1 through 4 of the Technical Design Report (TDR) [35]–[39]. This chapter generally follows the ILC summary document prepared for Snowmass 2021 [40].

The main acceleration devices at the ILC are two arms equipped with 1.3 GHz superconducting radio-frequency (SCRF) cavities that bring the energy per beam from 5 GeV up to the collision energy. The 2013 TDR design proposed an initial stage with $\sqrt{s} = 500\,\text{GeV}$ center-of-mass energy from collisions of a polarized electron beam with a polarized positron beam with $E_{\text{beam}} = 250\,\text{GeV}$ each in a 31 km long tunnel. The relatively low mass of the Higgs boson means that a first peak in the Higgs production cross section at an e^+e^- collider already occurs at around $\sqrt{s} = 250\,\text{GeV}$, as has been shown in Fig. 1.4. There, a rich SM precision program, with Higgs physics mainly driven by production through the Higgsstrahlung process, can be conducted. Now the ILC is proposed as a 20.5 km long $\sqrt{s} = 250\,\text{GeV}$ **Higgsfactory**. This leads to a substantially cheaper initial laboratory with possible upgrades to higher energies.

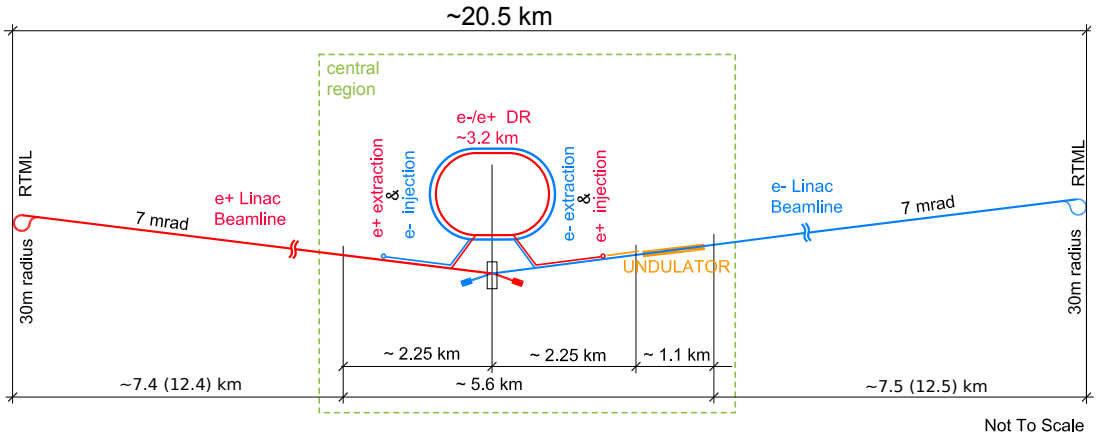

Figure 2.1: Schematic layout for the ILC250. Figure taken from [40].

The ILC accelerator infrastructure is illustrated in Fig. 2.1. A laser extracts 85% polarized electron bunches from a GaAs photocathode. A series of acceleration units increases their energy up to 5 GeV before injection into a damping ring. In order to produce the positron beam, the electron main beam is sent through a helical undulator. The resulting circularly polarized photons convert to e^+e^- pairs in a rotating target. The selected positrons maintain 30% beam polarization. The beam is likewise accelerated to 5 GeV and injected into a damping ring. Higher positron polarizations of up to 60% could be achieved by extending the undulator and adding a photon collimator. An unpolarized positron beam can be produced by an electron-driven positron source. While this alternative option under study leaves only the electron beam as a polarized beam, it is technologically simpler and can produce positrons independent of the electron beam line.

The two 3.2 km long damping rings (DR) are each made up of two half circles connected by straight segments. The energy lost by emission of beamstrahlung photons in each turn has to be restored. Through RF cavities and damping wigglers in the straight part of the ring, the beam energy is replenished and the horizontal and vertical emittance of the beam are reduced. The 5 GeV beams are transported from their damping rings at the center of the accelerator complex to the start of their respective main linac at the opposite edges of the facility through the Ring to Main Linac (RTML) system. In order to preserve the longitudinal beam polarization, the beam polarization vector is rotated into the transverse plane right after the beam production. This allows to preserve the polarization throughout its curved trajectory. Here, upon entering the main linac, the polarization is rotated back into the longitudinal orientation.

The bulk of the energy transfer to the beams is carried out by the two main linacs. The niobium SCRF cavities operated at 2 K achieve accelerating gradients of $31.5 - 35\,\mathrm{MV\,m^{-1}}$. These cavities are based on the TESLA technology which has already been industrially mass produced for multiple free electron laser facilities, most notably the European XFEL at DESY. At the end of the main linac, the beam delivery system (BDS) focuses the beam, now at 125 GeV, to a small beam spot at the interaction point (IP). After the collision the spent beams are guided to and disposed of at the main beam dumps.

accelerator parameter		initial	unit	upgrade
Repetition frequency	f_{rep}	5	Hz	
Bunches per pulse	n_b	1312		2625
Bunch population	N_e	2	10^{10}	
Time between bunches	Δt_b	554	ns	366
Beam pulse duration	t_{pulse}	727	µs	961
RMS bunch length	σ_z^*	0.3	mm	
Horizontal beam size at IP	σ_x^*	516	nm	
Vertical beam size at IP	σ_y^*	7.7	nm	
Horizontal emittance at IP	$\gamma\epsilon_x$	5	µm	
Vertical emittance at IP	$\gamma\epsilon_y$	35	nm	
Luminosity in top 1%	$\mathcal{L}_{0.01}/\mathcal{L}$	73	%	

Table 2.1: ILC accelerator parameters in the initial $\sqrt{s} = 250\,\text{GeV}$ stage. Only the values for parameters that are changed in the luminosity upgrade are shown in the last column.

2.1.1 Luminosity

A summary of accelerator parameters that describe the beam structure is given in Table 2.1. The instantaneous luminosity,

$$\mathcal{L}_{\text{inst}} = \frac{n_b N_e^2 f_{\text{rep}}}{4\pi\sigma_x\sigma_y} H_D, \tag{2.1}$$

has a linear dependence on the repetition frequency, f_{rep} and the number of bunches per pulse, n_b. The ILC is designed for operation in power-pulsing mode: Less then 1 ms of collider activity every 200 ms. This beam pulse duration t_{pulse} is slightly increased after the luminosity upgrade but stays below 1 ms. Within each pulse, the bunches are evenly distributed with temporal separation $\Delta t_b = t_{\text{pulse}}/n_b$. The typical length of each bunch, $\sigma_z^* = 0.3\,\text{mm}$, is short compared to the bunch spacing $c\Delta t_b$. The number of particles per bunch N_e enters quadratically in the luminosity calculation. But the optimum of N_b for analysis results is constrained by the rate of multiple hard interactions[1] per bunch crossing. Machine backgrounds are further discussed in Section 2.1.2.

The beam's spatial distribution is described by Gaussian distributions with standard deviations $\sigma_{x,y,z}^*$. The transverse beam shape depends on the emittances $\epsilon_{x,y}$ and the beta functions at the interaction points $\beta_{x,y}^*$; $\sigma_{x,y}^* = \sqrt{\epsilon_{x,y}\beta_{x,y}^*}$. In Table 2.1 the emittance is given as a product with the relativistic Lorentz factor $\gamma = E_{\text{beam}}/m_e$. With the instantaneous luminosity being inversely proportional to the transverse beam size it is thus essential to design an accelerator with small emittances and beta functions. The damping rings reduce each beam emittance by almost six orders of magnitude. The design of the final focusing system as part of the BDS determines the beta functions.

The expected instantaneous luminosity $\mathcal{L}_{\text{inst}} = 1.35 \times 10^{34}\,\text{cm}^{-2}\,\text{s}^{-1}$ is more than twice the value obtained from the calculation with the parameters that are mentioned above. The missing factor is parametrized through the (beam parameter dependent) beam enhancement factor H_D. This factor accounts for the pinch effect: The particles in a bunch are attracted by the the opposite-charge bunch. Therefore the bunches are compacted even further in the interaction region. This deflection, like any other momentum change for charged beam particles including the synchrotron radiation in a circular collider, is associated with the emission of photons. The average energy loss due to beamstrahlung is

[1] For this purpose a *hard* interaction is any $(e^-/\gamma)(e^+/\gamma)$ interaction where at least one final state particle is observed in the detector, with some minimal energy, e.g. $E_{\text{min}}^{\text{hard}} = 10\,\text{GeV}$.

proportional to [41]:

$$\delta E_{\text{beam}} \propto \frac{\gamma}{E_{\text{beam}}\sigma_z^*}\left(\frac{N}{\sigma_x^* + \sigma_y^*}\right)^2. \tag{2.2}$$

Maximizing the instantaneous luminosity according to Eq. (2.1) while minimizing the beamstrahlung effects described by Eq. (2.2) favors flat beams. With the currently proposed ILC250 beam parameters 73% percent of the luminosity is carried by particles that stay within 1% of the nominal beam energy. The planned doubling of $\mathcal{L}_{\text{inst}}$ after the ILC250 luminosity upgrade can be achieved through a doubling of the number of bunches per pulse while keeping the original bunch pulse frequency at 5 Hz.

2.1.2 Machine backgrounds

Beam-beam interactions as a source of real photons have been introduced in Section 2.1.1. Initial state radiation (ISR) is another source of photons. At the ILC, both contributions are of comparable size. Beamstrahlung played a negligible role at previous lepton colliders with lower center-of-mass energies. There it sufficed to account for interactions of two virtual photons with the Landau-Lifshitz process. The scattering of a pair of real photons is described by the Breit-Wheeler process [42]. Interactions between a real photon and a virtual photon are characterized by the Bethe-Heitler process [43]. The cross sections for photon pair annihilation into quarks and leptons at large angles decreases with the energy of the photon pair, $\sigma \propto 1/s(\gamma\gamma)$. Thus some low-$p_T$ hadron tracks are expected to enter the detector in each e^+e^- bunch crossing. The size of this underlying event strongly depends on machine parameters and the requested instantaneous luminosity. With the current ILC250 proposal, an average of 10 particles with an average total energy of 10 GeV can be expected to enter the main detector (within the polar angle range $|\cos\theta| \leq 0.95$) during each bunch crossing.

Photon-lepton processes at the ILC that are interesting to study on their own include the single gauge boson production processes ($e\gamma \to W\nu$, $e\gamma \to Ze$).

2.1.3 ILC staging

The ILC Higgsfactory at $\sqrt{s} = 250\,\text{GeV}$ (ILC250) has an attractive standalone physics case. All studies presented in this thesis are based on only the Higgsfactory stage. Still it is instructive to look at the ILC potential even beyond the Higgsfactory stage. Upgrade scenarios for the accelerator are presented here. The physics goals for a new e^+e^- collider operated at energies other than the Higgsstrahlung cross section maximum are summarized in Section 2.2.

A long term operation proposal for the ILC beyond the Higgsstrahlung stage is shown in Fig. 2.2. In this **ILC-H20 scenario** $2\,\text{ab}^{-1}$ of ILC250 data are collected in two runs. The beam parameters for both runs are given in Table 2.1. Doubling the instantaneous luminosity between the two runs by doubling the number of accelerated bunches per pulse only requires additional power.

The increase in energy to 500 GeV will then require a longer tunnel that houses the expanded main linacs. The same technology can be reused for the polarized positron beam if the helical undulator is replaced by a shorter undulator with a longer period and a smaller field. No technological advances are necessary but the upgrade can potentially benefit from cost and efficiency improvements that are achieved in the mean time.

After a first run of the ILC500 with $1\,\text{ab}^{-1}$ integrated luminosity, some data taking around the top threshold is proposed. A one year run around the top threshold suffices for a data set whose uncertainty matches the theoretical systematic errors. An ensuing $3\,\text{ab}^{-1}$ run of ILC500 concludes this long term ILC operation proposal.

The ILC250 accelerator could also be operated at lower energies, with a lower instantaneous luminosity. Nevertheless a 1.5 year long run at the Z boson resonance (Giga-Z) after the luminosity upgrade

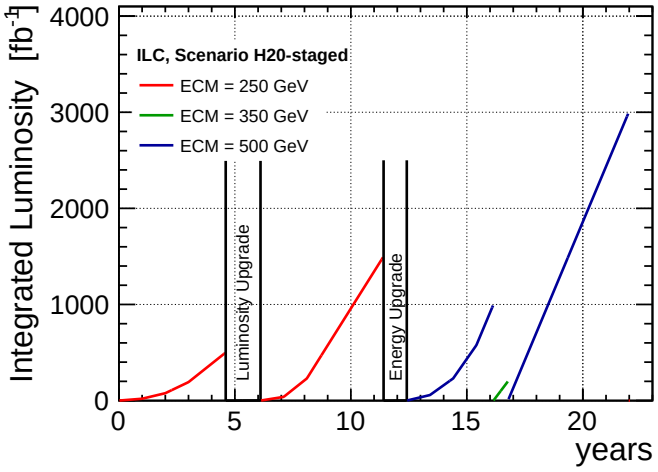

Figure 2.2: Long term operation proposal for the ILC. Figure taken from [40].

		91 GeV	**250 GeV**	**350 GeV**	**500 GeV**	**1000 GeV**
$\int \mathcal{L}$	[ab^{-1}]	0.1	2	0.2	4	8
duration	[yr]	1.5	11	0.75	9	10
$\mathcal{P}(e^-/e^+)$	[%]	80/30	80/30	80/30	80/30	80/20
(LR,RL)	[%]	(40,40)	(45,45)	(68,22)	(40,40)	(40,40)
(LL,RR)	[%]	(10,10)	(5,5)	(5,5)	(10,10)	(10,10)
δ_{ISR}	[%]	10.8	11.7	12.0	12.4	13.0
δ_{BS}	[%]	0.16	2.6	1.9	4.5	10.5

Table 2.2: Beam parameters per ILC energy stage. The rows are explained in the main text of Section 2.1.3. Table taken from [40].

would produce a sample with $5 \cdot 10^9$ Z bosons.[2] Even without a dedicated Giga-Z run, a large sample ($\mathcal{O}(10^7)$ [44]) of Z bosons almost at rest will be available from ILC250 via the $e^+e^- \to \gamma Z$ process of Z return-to-the-pole events with the photon almost collinear to the beam axis.

A summary of the most important parameters used for physics studies at each ILC energy stage is compiled in Table 2.2. The advantages of polarized beams and the reasoning for the recommended apportionment of beam time per polarization configuration will be discussed in Section 2.1.4. The last two lines give the average energy loss in the beam energy spectrum due to initial state radiation and beamstrahlung, respectively.

Upgrades of the ILC to TeV energies have also been studied. It is essential to design a collider with high power efficiency and a feasible overall power consumption. The 300 MW consumed by a 1 TeV ILC (111 MW for ILC250) correspond to 70% of todays peak power consumption at CERN [40]. Technological advances[3] or discoveries can alter the requirements for energy frontier colliders. The ILC proposal has a high degree of flexibility and can be adapted accordingly.

[2] Other low energy runs would be possible. But as of today none of them have a strong enough physics case to justify spending collision time there instead of at the Higgsstrahlung peak. Electroweak precision measurements at the W^+W^- pair production threshold have no large advantage over studies performed at the ILC250, while running at 250 GeV allows to simultaneously collect data on the Higgs sector.

[3] In the staged building scheme the new cavities added for a next stage can have a higher gradient then was previously possible. In case of large improvements, to power consumption or compactness, it might be justify the replacement of old cavities. If a new concept eventually reaches sufficient maturity, e.g. plasma wakefield acceleration, the ILC tunnel can be reused.

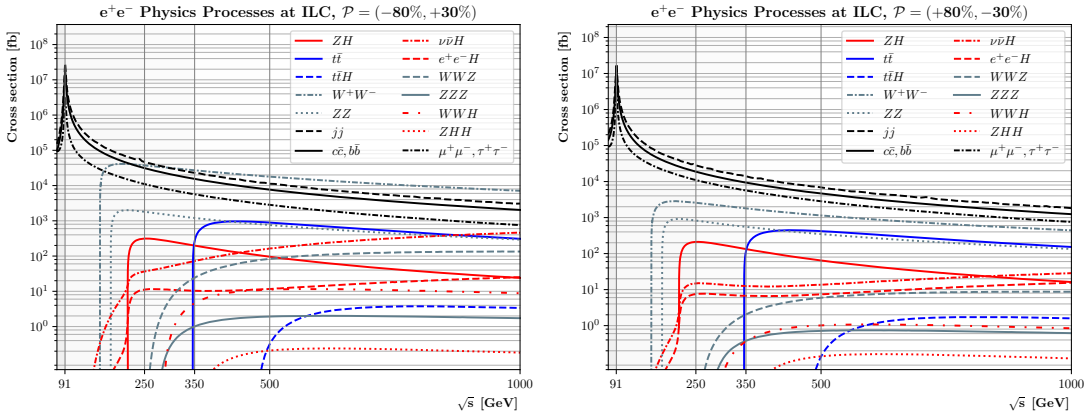

Figure 2.3: SM cross sections at the ILC over the range of proposed centre of mass energies $\sqrt{s}$ for both left (LR) and right polarization (RL) scenario. Figures taken from [40].

2.1.4 Polarization

The ILC design provides 80% beam polarization for the electron beam and 30% beam polarization for the positron beam. The polarization P of a beam with N_L left-handed and N_R right-handed particles is

$$P = \frac{N_L - N_R}{N_L + N_R}. \tag{2.3}$$

Left-handed and right-handed leptons have different $SU(2)_L \times U(1)_Y$ quantum numbers. The four configurations of polarized beams are thus effectively different scattering experiments. Their combination can be leveraged in various ways. Using partially polarized initial beams allows to favor one of the pure polarization cross sections over the others. This is especially relevant for W^+W^- fusion processes, which are only possible from the $e^-_L e^+_R$ initial state. At the left polarized ILC the W^+W^- fusion processes have the **enhanced effective luminosity**

$$\mathcal{L}_{\text{eff}}/\mathcal{L} = (1 - P_{e^-})(1 + P_{e^+}) = (1 + 0.8)(1 + 0.3) = 2.3. \tag{2.4}$$

The third and fourth row of Table 2.2 show the proposed luminosity sharing between the two opposite-polarization configurations (LR, RL) and the same-polarization configurations (LL, RR). The 350 GeV stage has the paramount goal of performing top quark measurements. At this stage it is therefore justified to favor the LR configuration. Arguments for nevertheless spending substantial time in the alternative configurations will be presented in the following paragraphs.

Choosing the right configuration can be a powerful tool for **background reduction**. Figure 2.3 compares the SM cross sections for the LR and RL configurations of the ILC. The $e^+e^- \to W^+W^-(\nu_e\bar{\nu}_e)$ process has substantial invisible energy carried by its neutrinos. Considering that the already mentioned process is strongly suppressed in the RL configuration that configuration has a cleaner environment for searches with missing energy, e.g. dark matter searches.

The photon induced $\gamma\gamma \to l^+l^-$ and single-W background process cross sections can be precisely measured in the same-polarization configurations LL and RR, where e^+e^- annihilation processes are highly suppressed.

Having data on e^+e^- annihilation for both $\sigma_{e^-_L e^+_R}$ and $\sigma_{e^-_R e^+_L}$ gives access to the **cross section as-**

symetries A:

$$\sigma_{e_L^- e_R^+ / e_R^- e_L^+} = \sigma_0(1 \pm \mathcal{A}), \tag{2.5}$$

$$A = -P_{eff}\mathcal{A},\ P_{eff} = (P_{e^-} - P_{e^+})/(1 - P_{e^-}P_{e^+}). \tag{2.6}$$

These asymmetries are an additional set of measurements that can be used as constraints in global fits.

In the ILC design, both beam polarizations can be flipped on a bunch train by bunch train level. This allows for a better **control of systematic uncertainties**. The detector acceptance and energy response can be compared between the four samples with different process compositions, but measured from an identical detector. Thus the systematic errors from temporal drifts of the detector parameters are reduced.

2.2 Physics goals

The main physics goals at each of the five energy stages that are considered for ILC operation are listed in Table 2.3. Not explicitly mentioned here are the direct searches for new physics, e.g. through missing mass signatures. Importantly there are many signatures that cannot be reconstructed at a hadron collider. Evidently the limits that can be set from these searches (in the case of non-observation) are improved when moving to a higher energy lepton collider.

$\sqrt{s}$	**Process**	**Goal**
91 GeV	$e^+e^- \to Z$	Z pole physics, calibration
250 GeV	$e^+e^- \to ZH$	Higgs couplings, spin, m_H, Γ_H
	$e^+e^- \to f\bar{f}$	Z, γ couplings
	$e^+e^- \to f\bar{f}, f\bar{f}f\bar{f}$	m_Z, Γ_Z, m_W, W branching ratios
350 GeV	$e^+e^- \to t\bar{t}$	top mass precision (threshold shape)
500 GeV	$e^+e^- \to \nu\bar{\nu}H$	Higgs couplings (VBF-fusion)
	$e^+e^- \to t\bar{t}$	top quark couplings
	$e^+e^- \to t\bar{t}H$	Higgs-top couplings
	$e^+e^- \to ZHH$	Higgs self-couplings
1 TeV	$e^+e^- \to \nu_e\bar{\nu}_e HH$	Higgs self-couplings

Table 2.3: Main physics goals at the proposed ILC center-of-mass energy ($\sqrt{s}$) stages.

While Z pole runs have already been performed at LEP, the ILC produces a larger sample taken with an improved detector. Thus the electroweak precision limits can be improved even further. Given that the electroweak limits are already strong today, data taken at the Z pole can also be used for a precise calibration of both accelerator and detector. It has already been suggested in Section 2.1.3 that return-to-the-Z-pole events at ILC250 could be sufficient.

The ILC250 functions as a Higgsfactory. More than half a million Higgs bosons will be produced during the ILC-H20 scenario, predominantly through the Higgsstrahlung process. Almost 1% of the recorded events are Higgs events. The overall number is modest compared to the LHC. But the simpler collision environment means that most Higgs events can be reconstructed and used. In more than 30.000 of these events the primary Z boson decays into an electron pair or into a muon pair. With those events an especially pure sample can be selected without bias on the Higgs decay mode. Such a sample enables a direct measurement of the total width of the Higgs boson, Γ_H. The same sample can be used for a precise Higgs mass measurement. The Higgs boson's spin can be studied in $H \to \tau^+\tau^-$ events. Higgs branching ratio measurements at ILC250 are prominently discussed in this thesis. Simultaneously to the Higgs program, the electroweak measurements that were performed at SLC

and LEP can be repeated with initial state polarization, higher luminosity, and a better detector. The increased precision further tests the SM and its proposed extensions.

The threshold scan around 350 GeV mainly serves to measure the top quark mass with a high precision in an environment with low systematic uncertainties. The top quark couplings can be measured at the ILC500. This includes couplings between the top quark and the Higgs boson. Most Higgs bosons are produced through through vector boson fusion. The Higgs coupling measurements at ILC500 will improve on the ILC250 results. The different dominating Higgs production processes at ILC250 and ILC500 can be used for cross-checks of any anomalies that have been found. The double-Higgsstrahlung process opens the door for Higgs self-coupling measurements.

With the 1 TeV ILC, Higgs self-coupling can additionally be measured in W^+W^- fusion. For both double-Higgs production processes, the full amplitude includes SM processes with two single-Higgs productions. The interference in $e^+e^- \to ZHH$ is constructive. If the self-coupling λ_{HHH} is slightly larger than its SM expectation, the cross section increases. In the case of W^+W^- fusion, the corresponding interference is destructive. When data is taken at both ILC500 and ILC1000 the Higgs self-coupling can be measured independent of its SM value. In contrast, at a hadron collider like the LHC Higgs self-coupling from gluon-fusion production dominates.

2.3 Comparison between Higgs factories

Several proposals for linear accelerators are under study. The Compact Linear Collider (CLIC) [45] is a proposal with three energy stages at 380 GeV, 1.5 TeV and 3 TeV. Considering that the CLIC concept does not plan any running near the Higgsstrahlung cross section peak, the results presented in this thesis cannot easily be applied to CLIC. Even so, a significant number of Higgsstrahlung events are created at the first CLIC stage (Fig. 2.3).

The second class of e^+e^- colliders are circular colliders, based on storage rings. The Circular Electron Positron Collider CEPC [46], [47] consists of a double-ring with 92 km circumference and at least two interaction points (IP). It is expected to produce 1 million Higgs bosons at 240 GeV, 700 billion Z bosons in a Z pole run (91.2 GeV) and 100 million signal events at the W^+W^- threshold (161 GeV). The Future Circular Collider [48] is another proposal for a 100 km circumference e^+e^- collider. It is intended to collect data at 91.2 GeV, 161 GeV, 240 GeV, 250 GeV and 365 GeV. Both circular collider concepts consider reusing their tunnels for a 100 TeV hadron collider.

The discussion on ILC upgrade plans in Section 2.1.3 showed that, up to technological improvements, the cost for a linear collider (tunnel, cavities, cooling) as well as its power consumption scales linearly with the collision energy. Power consumption at a circular e^+e^- collider is driven by energy losses due to synchrotron radiation,

$$\Delta E_{\text{synch}} \propto \frac{E^4}{m^4 R}. \tag{2.7}$$

Given that the construction costs for tunnels and magnets scale linearly with the tunnel length, the cost optimum scales with the square of the energy. On top of the cost aspect, an unnecessarily high power consumption is not justifiable from an environmental point of view. This cost scaling argument is apparent in the reuse approaches. A circular e^+e^- collider that would compete with the ILC500 or especially with the ILC1000 is not practical. Synchrotron radiation scales with the inverse fourth power of the mass of the colliding particles. Circular colliders with muons or protons are therefore not hindered by a comparable level of synchrotron radiation.

It is difficult to create substantially polarized beams in a circular collider. But the planned instantaneous luminosities of both CEPC and FCC-ee for running at the Higgsstrahlung peak are considerably higher. A higher instantaneous luminosity at a linear collider, by way of a smaller beam spot

(Section 2.1.1), leads to increased machine backgrounds (Section 2.1.2). A linear collider is naturally restricted to a single IP. Even if multiple detectors are envisaged, the beam time has to be split between them. Thus lower statistical uncertainties can be expected from circular Higgsfactory concepts. But running with multiple polarizations leads to a larger number of measurements that can be utilized in global fits. Especially in the case where deviations from the SM are found, polarized observables help to pin down the type of new physics that has lead to the deviation.

2.4 Complementarity with HL-LHC

Collisions at the LHC involve only components of the proton. Thus the kinematics of the initial state of the collision at not precisely known. Parton distributions are needed to interpret the cross sections at a hadron collider. The underlying event is complex, with numerous additional parton interactions overlaid onto each final state of interest. The situation will be further worsened by the increased pile-up in HL-LHC collisions. The elementary particle collisions at ILC are simpler. The initial state kinematics of each collision are known up to ISR and beamstrahlung. Both ISR and beamstrahlung can be precisely calculated. Then absolutely normalized cross sections can be measured at the part-per-mil level. The machine backgrounds that make up the underlying events at ILC were presented in Section 2.1.2. While larger than for previous lepton colliders, these contributions are trivial in comparison to the hadron collider environment. Without a lepton collider with center-of-mass energy above about 500 GeV the HL-LHC is needed for the measurement of the coupling of the Higgs boson to the top quark.

A general overview of physics goals was given in Section 2.2. Other analyses can be performed to better understand the hadron collider environment. The simpler collision environment compared to LHC, and the better detector compared to previous lepton colliders, allow improved measurements of QCD event shapes and jet substructures. Most jets that have been produced at LEP were quark jets, from LEP runs at the Z pole. In addition to those jets, the ILC250 produces a large sample of gluon jets from Higgs decays. Especially the Higgsstrahlung events with leptonic Z decay, $e^+e^- \to ZH \to (l^+l^-)(gg)$, create a clean sample for gluon jet studies.

3

Designing a particle flow detector

Contents

The particle flow approach, a driving force for modern detector design, is introduced in Section 3.1. This thesis is based on the ILD detector concept. Its design and how it is guided by the particle flow approach is the topic of Section 3.2. The ILD detector proposal is supported by numerous detector performance and physics reach studies. Their simulation tools are introduced in Section 3.3.

3.1 Particle Flow

The detectors at high energy particle colliders typically consist of multiple sub-detectors. Charged particles are measured in tracking systems. In the interest of also collecting information on photons and neutral hadrons, a calorimeter system is employed so that the neutral particles interact and dissolve into a shower. Typically each of these systems consists of multiple components with different characteristics. A Particle Flow algorithm (PFA) [49] identifies the contributions from different particles within a detector component. These contributions are matched and compared with the contributions from other detector components. The result is a set of particles with each particle described by a group of detector component measurements. A particle's charge and momentum are then given by the most precise sub-detector information that is available. The energy of a jet is estimated from the sum of the momenta of all particles in the jet. Such an approach for jet reconstruction has already been successfully applied at ALEPH analyses [50], outperforming the measuring of the jet energy directly from its deposits in the calorimeters. Much better jet reconstructions can be achieved for a detector that is originally designed for optimal PFA performance [51].

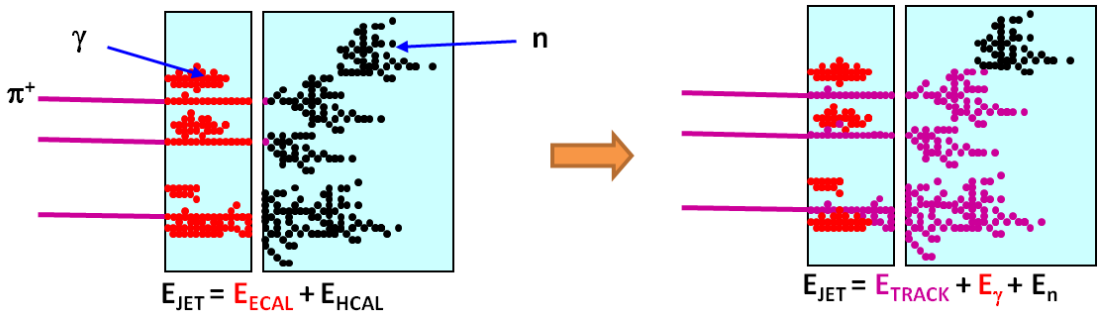

Figure 3.1: The transition from traditional calorimetry to PFA calorimetry. Figure taken from [52].

Particle type	%	ILD resolution	sub-detector
Charged particles	62	$2.0 \times 10^{-5}\,\mathrm{GeV}^{-1}$	tracker, as $\delta(1/p_T)$
Photons	27	$17\%\sqrt{E/\mathrm{GeV}}$	ECAL
Long-lived neutral hadrons	10	$50\%\sqrt{E/\mathrm{GeV}}$	ECAL & HCAL
Neutrinos	1	not detected	-

Table 3.1: Energy-weighted particle composition in typical jets, from jet fragmentation measurements at LEP [53], [54]. With the cited ILD resolutions for single particles, the energy resolution of a typical jet is roughly $30\%\sqrt{E/\mathrm{GeV}}$.

The momentum resolution in the tracking system is in general vastly superior to the energy resolution from the particle shower of a charged particle. In the traditional calorimeter approach, the jet energy is obtained as the sum of the energy deposits in all calorimeters. The transition to PFA is shown in Fig. 3.1. Charged particles are already detected in the tracker. Their energy deposits in the calorimeter are not used in the calorimeter energy summing procedure. The energy-weighted particle composition in a typical jet was measured at the LEP experiments. The jet composition and the target resolution for single particles of different particle types at ILD is given in Table 3.1. The hadronic calorimeter has by far the worst energy resolution. When using PFA, the HCAL measurement is only used for the 10% of the jet energy that are carried by long-lived neutral particles (K_L^0, n). The jet energy resolution (JER) is improved to $30\%\sqrt{E/\mathrm{GeV}}$, an improvement by factor of two with respect to previous experiments (ALEPH, CMS).

With this gain in JER, the jets from hadronic decays of W bosons and Z bosons can be separated by 3σ. Neglecting the uncertainty on the reconstruction of the angle θ_{12} between two jets, the dijet invariant mass $M_{12}^2 = 2E_1E_2(1-\cos\theta_{12})$ has the mass resolution $\sigma_M/M = 1/\sqrt{2}\sigma_E/E$. With the natural widths of $(2.7\% \approx \Gamma_W/M_W \approx \Gamma_Z/M_Z)$ and the mass separation between the electroweak gauge bosons ($\Delta M = M_Z - M_W \approx 10\,\mathrm{GeV}$) a 3σ separation requires $3-4\%$ JER. This performance goal can be achieved with particle flow calorimetry ($E_{\mathrm{jet}} \geq 50\,\mathrm{GeV}$).

A good particle flow calorimeter needs a high level of granularity in order to resolve a nearby, or overlapping, shower from a neutral particle. The particle flow performance of the ALEPH experiment at LEP [50] was hampered by the location of the coil between ECAL and HCAL, and by the insufficient segmentation of its calorimeters. Neutral hadrons could only be identified by a significant excess of the energy deposited in the calorimeter compared to the energy reconstructed from the charged particle tracks. In this thesis, the term particle flow is reserved for situations with sufficient granularity in the calorimeter system in order to resolve the calorimeter clusters of the individual particles. Additionally, it is required that the barrel HCAL is located inside the magnet, facilitating a pattern recognition approach over the full shower development.

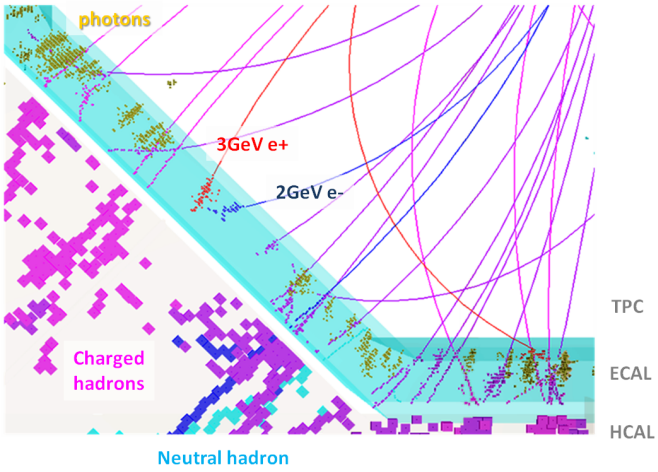

Figure 3.2: A 250 GeV jet in ILD. Given the high granularity of ILD a good particle identification can already be done by eye. Figure taken from [52].

A preliminary stage for particle flow is energy flow. If the momentum of the track associated to a cluster is significantly lower than the cluster energy, the cluster should be split into a component from the charged particle and a component due to a neutral particle. If the track momentum is significantly higher, there might be a neutral cluster that should actually be part of the shower from the charged particle. Multiple tracks leading to the same cluster similarly indicate that the cluster must actually contain the showers from multiple particles. With increasing jet energy the jets become tighter and the separation of calorimeter clusters from different particles in the jet is more challenging. Energy flow and particle flow are not separate paradigms. A reconstruction software can transition between the approaches depending on calorimeter granularity, collision energy but also on local occupancy.

3.1.1 PandoraPFA

The ILD collaboration uses PandoraPFA [53] for its particle reconstruction. A typical reconstructed 250 GeV jet is shown in Fig. 3.2. Charged particles are identified by their tracks in the TPC. The calorimeter hits are clustered into individual showers. Due to the high granularity of the calorimeters it is possible to separate showers even at small distances. From this figure it is evident why these high granularity calorimeters are also referred to as imaging calorimeters. A good object identification and track-cluster matching can already be done by eye.

With increasing jet energy the jets become narrower. The most important sources of confusion are explained in Fig. 3.3. Jet energy is lost if the algorithm fails to resolve photons or neutral hadrons. Parts of a charged particle's shower that are misidentified as a separate shower contribute twice to the jet energy calculation.

The JER with PandoraPFA for the ILD detector is empirically described by

$$\frac{\mathrm{RMS}_{90}}{E} = \frac{21}{\sqrt{E}} \oplus 0.7 \oplus 0.004E \oplus 2.1 \left(\frac{E}{100}\right)^{0.3} \% \text{ GeV}. \tag{3.1}$$

In particular due to infrequent confusion of high energy clusters the JER has larger tails than a Gaussian. The resolution is better represented by the root mean square of the smallest range containing 90% of the events, RMS_{90}. Its statistical power is here equivalent to that of a Gaussian with a standard deviation $\sigma = 1.1 \times \mathrm{RMS}_{90}$ [53]. The intrinsic calorimetric resolution scales with $1/\sqrt{E}$. The energy evolution of

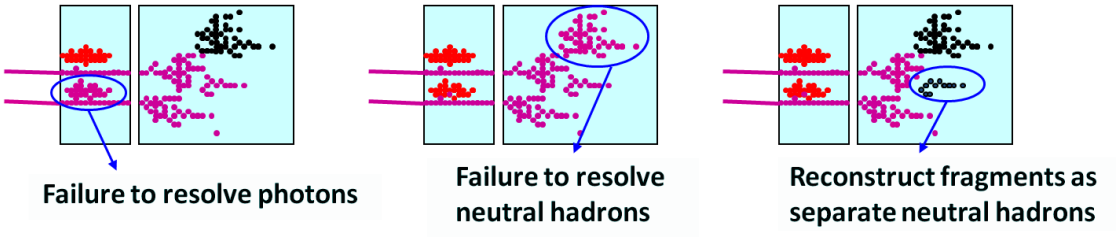

Figure 3.3: Possible sources of confusion in a particle flow reconstruction. Figure taken from [52].

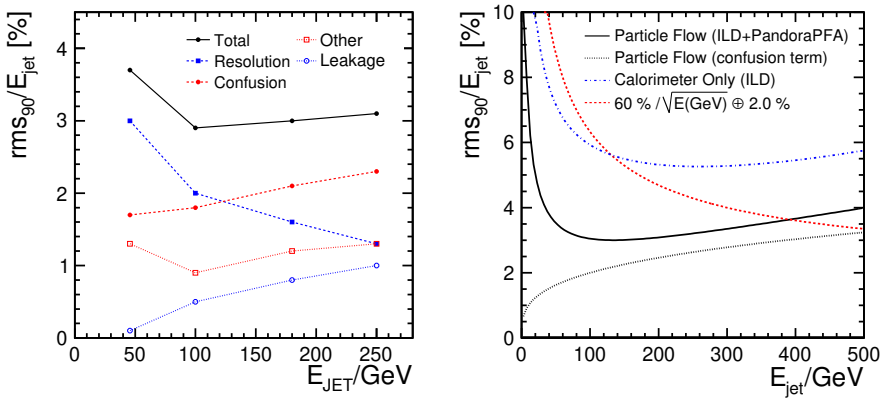

Figure 3.4: The contributions to JER obtained with PandoraPFA as a function of the jet energy. (Right) Empirical function form of the particle flow JER with the ILD detector. The dashed curve indicates the resolution that is obtained with an energy flow approach. Figures taken from [53].

the individual contributions from the intrinsic calorimetric resolution, tracking imperfections, leakage and confusion is shown in Fig. 3.4. The total uncertainty is approximately the sum in quadrature of the contributions. For jet energies above 100 GeV the JER is limited by the assignment of the energies to the different reconstructed particles. With the ILD detector, the particle flow reconstruction (solid line) performs better than a purely calorimetric jet energy estimation (dot-dashed line) for all jet energies. The energy measurement from only the energy deposits in the calorimeter suffers even stronger from shower leakage ($\propto E$). The leakage can be estimated from topological information from the imaging calorimeters. The energy flow approach (dotted line) does not try to reconstruct the individual particles. It outperforms the particle flow reconstruction for jet energies above 400 GeV. The PandoraPFA statistical reclustering algorithms ensure a smooth transition between the two regimes.

The angular dependence of the JER in ILD is shown in Fig. 3.5. The fake missing transverse momentum is limited to $1-2\%$ of the event energy.

3.1.2 Arbor

Arbor is an alternative approach for a particle flow algorithm [55]. It is used for the particle reconstruction in the CEPC simulation studies [56]. Particles are identified through tree topologies. The calorimeter hits are linked with oriented connectors. The clustering algorithm iterates until the directed graph is a tree. Then the tracks are matched with the starting nodes of a tree. Afterwards the remaining calorimeter clusters without a track are identified as photons, neutral hadrons or fragments of a charged cluster depending on the cluster properties.

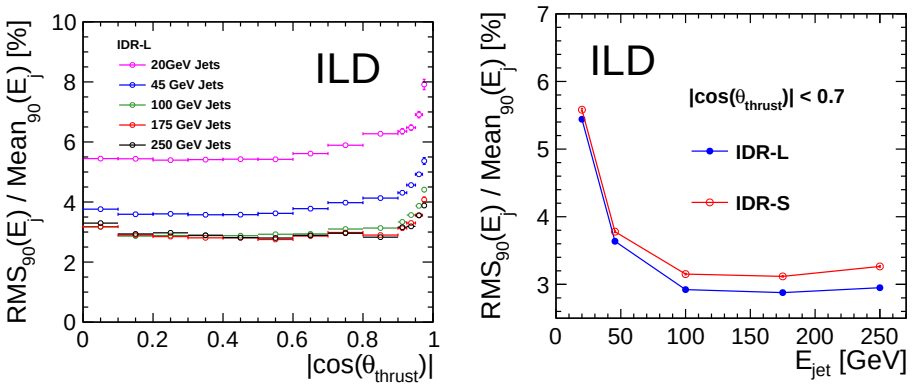

Figure 3.5: (Left) JER as function of the polar angle (thrust-axis) of the event. (Right) Comparison of the JER for the two ILD models in the barrel region. Measured in $Z \to q\bar{q}, q \in [u,d,s]$. Figure taken from [54].

3.1.3 Test beam performance

A fine granularity is needed in the calorimetric systems for a successful application of the particle flow approach. The ECAL absorber material must have a small Molière radius in order to keep the individual showers separated. A good image of the shower is obtained with a longitudinal segmentation of the order of the material's radiation length and a transverse granularity of the order of the Molière radius. To keep the ECAL compact, the radiation length must be small. A large ratio of interaction length to radiation length ensures a reliable longitudinal separation of electromagnetic and hadronic showers. These requirements are met by Tungsten ($X_0 = 0.35\,\text{cm}$, $\lambda_I = 9.95\,\text{cm}$, $R_M = 0.93\,\text{cm}$). The critical distance for photon reconstruction (e.g. $\pi^0 \to \gamma\gamma$) is two times the cell size in the ECAL.

While the development of electromagnetic showers is well understood, the simulation of hadronic showers is subject to more uncertainties. Their shower-by-shower variance is large. The single particle performance of multiple ECAL and HCAL technologies has been confirmed in test beams by the CALICE collaboration [57], including the combined data taking of ECAL and HCAL. The unprecedented granularity of these calorimeter systems allowed to validate the models for hadronic showers at an unprecedented level of accuracy.

The remaining hadronic shower modelling uncertainty for scaling the confirmed single particle performance to the full particle flow performance of a jet in a collision event can be studied by comparing the results from different hadronic shower models. The JER at jet energies relevant for ILD was found to vary by less than 5% [53].

3.1.4 Detector design considerations

Following the particle flow guidelines leads to a detector that is capable of reconstructing the individual particles that go through it. The main points to take into consideration are [53]:

1. A high precision tracking system is needed. In PFA, the tracking system's momentum resolution even enters into jet energy measurements.

2. A (high) magnetic field enables the precise momentum measurements for charged particles. As a consequence of the magnetic field, the charged particles are deflected away from the core of their jet. This should aid the identification of neutral clusters in the calorimeters.

3. Both ECAL and HCAL must be inside the solenoid.

4. Then, for both cost and technological feasibility of the solenoid, the detector must be compact.

5. A higher transverse segmentation of the calorimeters entails higher power consumption and higher cost. Eventually, the physics performance gain from higher transverse segmentation becomes negligible. Optimization studies with ILD parameters recommend $0.5 \times 0.5\,\mathrm{cm}^2$ ECAL cells and $3.0 \times 3.0\,\mathrm{cm}^2$ HCAL cells.

6. In order to prevent leakage from being a significant source of uncertainty for high energy jets ($180 - 250\,\mathrm{GeV}$), the HCAL needs to be at least $5.5 - 6.0\lambda_I$ deep.

7. The contribution of confusion to the JER (last term in Eq. (3.1)) can be parametrized as $2.1\left(\frac{R}{1825\,\mathrm{mm}}\right)^{-1.0}\left(\frac{B}{3.5\,\mathrm{T}}\right)^{-0.3}\left(\frac{E}{100\,\mathrm{GeV}}\right)^{0.3}\%$. A much higher magnetic field B is needed to compensate a smaller in radius of the ECAL for unchanged longitudinal lengths of the calorimeters.

3.2 The International Large Detector

The International Large Detector (ILD) is a PFA based detector proposal for the next energy frontier e^+e^- collider. It is a multi-purpose detector that is capable of providing measurements with the accuracy that is needed to accomplish the physics goals presented in Section 2.2.

The collision environment is gentle compared to that of the LHC experiments. The collision rates are lower and the individual bunch crossings are simpler. Apart from the forward calorimeter system, close to the beam pipe, radiation hardness is not necessary. The ILC bunch structure allows to operate the electronics with power pulsing, greatly reducing the need for cooling. At the same time unprecedented precision requirements are imposed (Fig. 3.6). Compared to LHC experiments, a 10 times better momentum resolution and and a factor 2 in jet energy resolution are desired. The granularity is increased by $2-3$ orders of magnitude. Thus dedicated R&D efforts are needed. For high granularity calorimetry, these efforts are coordinated within the CALICE collaboration.

ILD has originally been conceived for the ILC. The concept integrates subsystems that are developed by specialized R&D collaborations, e.g. CALICE or LCTPC, and combines them into a performant multi-purpose detector. Individual components as well as combinations thereof have been validated in test beams. The full detector performance is studied with the help of a realistic and detailed detector simulation. The software framework, central to the success of ILD, is introduced in Section 3.3.

The ILD concept keeps a high degree of flexibility. Several options are considered for key parts of the detector. Possible improvements from new developments, such as timing in some or all calorimeter layers, are explored. The high degree of realism that goes into the ILD analyses means that effects of individual design decisions can be studied. An update of the ILD status has been published as the Interim Design Report (IDR) [54] in 2020. There, an ILD version with a smaller tracking system (IDR-S) is introduced. In comparison to the baseline scenario (IDR-L) the TPC is shorter ($177\,\mathrm{cm} \rightarrow 143\,\mathrm{cm}$ outer radius) and the magnetic field is stronger ($3.5\,\mathrm{T} \rightarrow 4\,\mathrm{T}$). The system performance and high level reconstruction performance was studied with both detector versions, as well as the impact on a wide range of physics benchmarks.

The high level of thoroughness in the ILD concept and the similarity in the collision environments for the proposed new lepton colliders make ILD an attractive candidate also for colliders other than the ILC. Runs at multiple TeV collision energies are part of the CLIC proposal. For the higher energy jets, the containment of showers from their constituent particles becomes an important source of jet energy uncertainty. In order to keep a sufficient containment without increasing the detector size the HCAL absorber material can be switched from steel to tungsten. Circular colliders have a different beam time structure. This requires a reevaluation of the cooling and an adaption of the electronics.

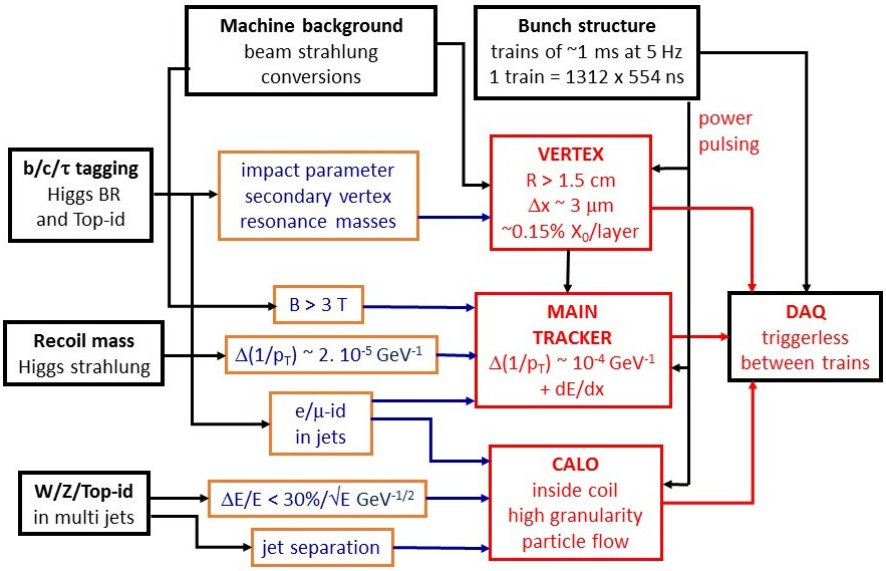

Figure 3.6: Interplay between ILC machine characteristics, physics requirements and detector specifications. Figure taken from [54].

Detector requirements for a particle flow approach to jet physics are listed in Section 3.1.4. A high level overview with additional requirements from both the physics program and the ILC accelerator characteristics is illustrated in Fig. 3.6. The machine backgrounds (Section 2.1.2) limit the inner radius of the vertex detector. A high magnetic field prevents most background particles from entering the detector. As a downside, the track reconstruction for low momentum charged particle suffers. Flavor tagging and tau reconstruction set the target for the vertex detector resolution through their dependence on the impact parameter and on the identification of secondary vertices. Further particle identification (PID) can be done through the energy loss (dE/dx) measurement in the tracker. A strict, direct target for the tracker momentum resolution is the recoil mass measurement in Higgsstrahlung events. The precision measurements for Higgs mass and for inclusive Higgsstrahlung cross section largely depend on the momentum resolution for isolated charged tracks ($ZH \rightarrow (e^+e^-, \mu^+\mu^-)H$). The ILC bunch structure with 1 ms of up time with bunch trains followed by 199 ms without collisions must be exploited by all subsystem. The heat production of the readout electronics is dramatically reduced with power pulsing. The event rates allow for a trigger-less operation and the storage of all data that is recorded.

The material budget that is used up by the ILD subsystems is shown in the first column of Fig. 3.7. The material contributions from support structures and cables are included but are not directly visible due to the averaging over the polar angle. A particle traveling through the barrel region passes on average less than 0.15 radiation lengths (X_0) before entering the electromagnetic calorimeter (ECAL). While this value rises to about $0.4X_0$ in the endcaps due to endplates and the electronic readout of the time projection chamber (TPC), the material budget is substantially smaller than in ongoing experiments like CMS. Thus the rates of multiple scattering or pair creation from photons are lower. In contrast to electromagnetic showers in the ECAL, the hadronic showers frequently start before the hadronic calorimeter (HCAL). The ECAL entails about one interaction length, λ_I. The coil is about $2\lambda_I$ deep. Thus a high resolution HCAL that is supposed to measure the shower propagation must necessarily sit within the solenoid.

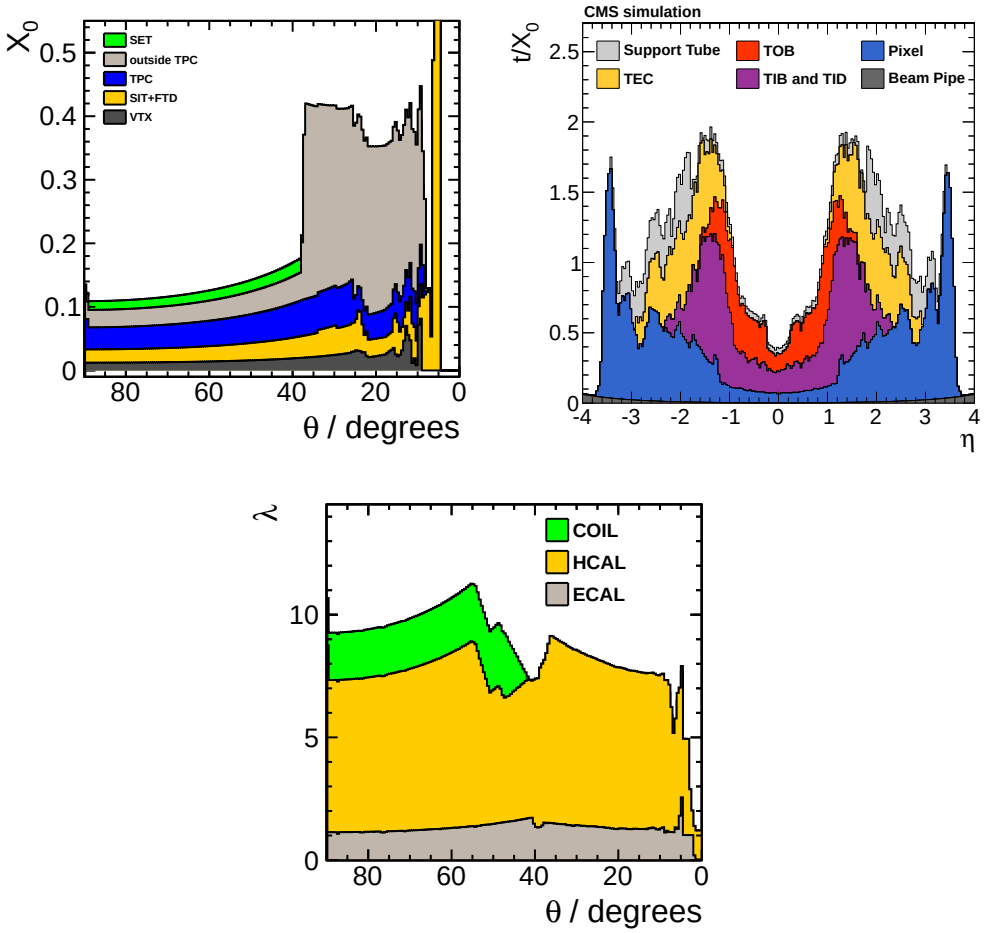

Figure 3.7: (Top row) Average total radiation length X_0 in front of the ECAL. (Bottom row) The acronyms used in the ILD plots (left column) are explained in the main text. The thickness is shown as a function of the polar angle θ. The CMS acronyms (right row) stand for tracker inner barrel (TIB), tracker inner disks (TID), tracker outer barrel (TOB), and tracker endcaps (TEC). The CMS thickness is plotted as a function of the pseudorapidity η. Figures taken from [54], [58].

The full detector with its sub-detector names is shown in Fig. 3.8. Starting from the beam pipe and going outwards the first system is a pixel detector (VTX) with three double layers. Due to the low radiation rates compared to a hadron collider its first layer can be located at a distance of only 16 mm from the beam pipe. In order to reduce the tracks from machine backgrounds the innermost layer is half as long as the following layers. The system has a low material budget. Furthermore the vertex detector provides the tracking information for low momentum particles ($\mathcal{O}(10\,\mathrm{MeV})$) that curl in the magnetic field and never reach the tracking system. The impact parameter resolution goal is $\sigma_b \leq 5 \oplus 10/p/(\sin\theta)^{4/3}$ µm for a track with momentum p and at the azimuthal angle θ. Sufficient timing resolution to distinguish between tracks from different bunch crossing seems obtainable. Amongst the possible technologies to achieve these demands, CMOS pixel sensors (c.f. ALICE Inner tracking system ITS-2) and DEPFET (Belle II) are the leading contenders.

A TPC is planned as the main tracking device. A charged particle ionizes the gas mixture while

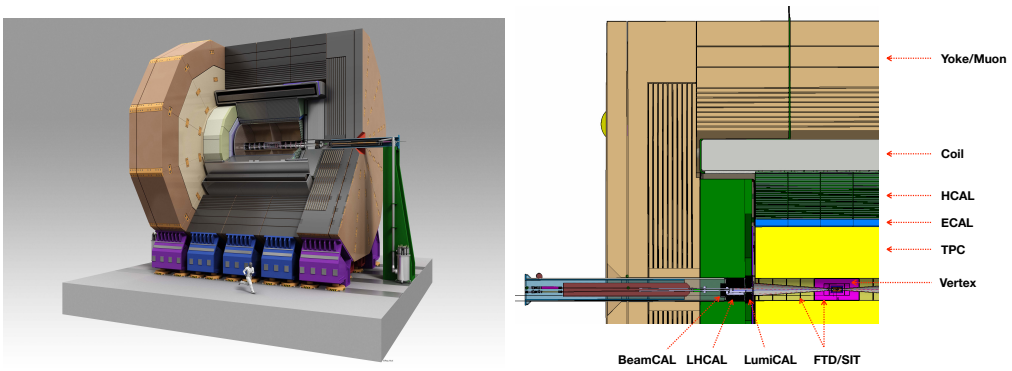

Figure 3.8: A rendering of the ILD detector and an ILD quadrant in $r-z$. Figures taken from [40], [54].

traveling through the TPC. The resulting free electrons drift to the TPC endplate, where they are detected. The drifting is caused by an electric field within the TPC's field cage. The baseline version (IDR-L) is 470 cm long and has an inner (outer) radius of 33 cm (177 cm). Up to 220 3D tracking points are reconstructed with a single-hit resolution of better than 100 µm in $r\phi$ and 1 mm in z. The identification of charged Kaons, pions and protons from measuring the energy loss dE/dx can be further aided in the difficult low-momentum regime by time of flight (TOF) information from the ECAL. The development is organized within the LCTPC collaboration.

To reach the target momentum resolution, $2.0 \times 10^{-5}\,\mathrm{GeV}^{-1}$, the TPC is complemented by a few high precision silicon layers (10 µm point resolution). In the barrel, these are the Silicon Inner Tracker (SIT) and the Silicon External Tracker (SET). This combined TPC-silicon solution is considerably lighter than a full-silicon tracking system in terms of radiation lengths. The degradation of the momentum precision for low momentum particles is reduced compared to a full-silicon solution. At higher particle momenta, the TPC is mainly responsible for the pattern recognition and track finding, while the silicon layers dominate the momentum measurement. The forward coverage is extended from the TPC inner radius up to the beam pipe by seven layers of Forward Tracking Disks (FTD).

The highly granular sampling calorimeters for the ILC are developed within the CALICE collaboration. Tungsten is used as the absorber material for the electromagnetic calorimeter (ECAL). The barrel ILD ECAL is 24 radiation lengths (X_0) deep, corresponding to one nuclear interaction length λ_I. It is segmented into 30 layers. An extended description of the SiW-ECAL technological prototype is given in Chapter 4. Silicon pin diodes with 5×5 mm pad size are used to sample the electromagnetic shower. Precise timing capabilities at the level of 100 ps is under study. This would increase the power consumption. But they have benefits, especially as a TOF measurement in the first ECAL layers for the PID identification of low energy particles. An alternative to the SiW-ECAL, the Sc-ECAL, uses thin scintillator strips (5×45 mm) as the active material. The same effective cell size as for the SiW-ECAL can potentially be obtained with an order of magnitude less readout channels through the design with perpendicular strips.

The AHCAL option is based on the analogue readout of silicon photo multipliers on 3×3 cm scintillator tiles. The SDHCAL proposal has a 2-bit (semi-digital) readout of resistive plate chambers with 1×1 cm granularity. The short interaction lengths, but especially its structural properties, make steel a good choice for the HCAL absorber material.

The endcap calorimeters will use the same technologies as their barrel counterparts. The new CMS endcap calorimeter HGCAL includes systems that are very similar to the Silicon options for the ILD ECAL and HCAL. This is a major application of and a scalability and engineering test for the underlying technologies.

The very forward region is the only part of ILD that will have to cope with high radiation doses. Calorimeters for this region are studied in the FCAL collaboration. The integrated luminosity is measured with low-angle Bhabha-scattered electrons and positrons in the LumiCal. The Luminosity Hadronic CALorimeter (LHCAL) extends the coverage of the hadronic calorimeter down to lower angles. The BeamCAL finally extends the coverage to 6 mrad from the beam pipe. Almost full 4π-hermeticity is achieved. The enormous numbers of e^+e^- bremsstrahlung pairs in the BeamCAL can be used for ab in-situ determination of beam parameters (number of particles, beam positions and beam sizes).

The compact design of ILD allows the full barrel calorimeter system to fit within the coil. The iron return yoke will be instrumented with up to 14 active layers based on a similar technology as the chosen HCAL option. The approximate layer locations are indicated as black lines in Fig. 3.8. They act as muon identification system and as tail catcher for hadronic showers.

3.2.1 SiD

An alternative detector that is proposed for the ILC is SiD [40]. If multiple detectors are constructed, they will have to share the same IP. A push-pull scheme is planned with which the detectors can be swapped within a day.

Both detector concepts feature highly granular imagine calorimeters that are well suited for the particle flow approach. Instead of using a TPC the SiD tracking is entirely based on silicon systems. The SiD design is even more compact than the small version of ILD (IDR-S). A higher magnetic field of 5 T is chosen to compensate for a smaller inner radius of the ECAL (1265 mm).

3.3 Simulation

A realistic evaluation of the detector performance and physics potential of a new experiment can only be made with the help of a detailed event and detector response simulation. The ILD concept group uses iLCSoft [59] as its software framework.

The iLCSoft framework is adopted throughout the linear collider community. The tools used for the event generation are introduced in Section 3.3.1. The subsequent simulation of the ILD detector response and the reconstruction of individual particles are described in Sections 3.3.2 and 3.3.3. Common tools for high level reconstruction that are used in this thesis are discussed in Section 3.3.4. Software tools for the SiW-ECAL technological prototype are presented in Chapter 4 and Appendix D.

The ILD concept group has recent, centrally produced, large samples for ILC collisions at 250 GeV and 500 GeV center-of-mass energy. The ILD results in this thesis are based on the 250 GeV SM samples produced since 2020. The corresponding software tools are in the iLCSoft release v02-02.

The efficiency tables for the sample selections in the Higgs branching ratios (BRs) study are reproduced in Appendix A, Tables A.1 to A.8. Each table lists the number of simulated events per process for one of the four pure initial state polarization combinations. Only processes with a significant contribution after the loose selection step are considered. The loose and tight selection steps are defined in Chapter 5. For most of the processes the produced samples are substantially larger than the expected event count even after the full H20 program. In order to allow high precision studies of the Higgs BRs about 100.000 events have produced for each of the relevant SM Higgs BRs, per Higgs production mode and per pure initial state polarization. Therefore the number of simulated Higgs events is orders of magnitude larger than the expected Higgs data set. The weight column cites the factor with which each event has to be multiplied for a data set with 1 ab^{-1} integrated luminosity in the specified pure initial state polarization.

Where not specified explicitly the 250 GeV stage of the H20 scenario of the ILC, presented in Section 2.1.3, is assumed: 2 ab^{-1} of integrated luminosity shared 40% ,40%, 10%, 10% between the four

	pure polarization sample			
ILC250 configuration	**eLpL**	**eLpR**	**eRpL**	**eRpR**
LL	58.5%	31.5%	6.5%	3.5%
LR	31.5%	58.5%	3.5%	6.5%
RL	6.5%	3.5%	58.5%	31.5%
RR	3.5%	6.5%	31.5%	58.5%
H20 combined	21.4%	28.6%	28.6%	21.4%
unpolarized beams	25.0%	25.0%	25.0%	25.0%

Table 3.2: Relative weights of the samples with pure initial state polarization for the considered beam polarization scenarios.

polarization configurations LR, RL, LL, RR. The L/R configuration refers to ±80% (30%) polarization for the electron (positron) beam. The relative weight of each pure polarization sample in a data set with ILC beam polarizations is $w_{\text{pol}} = (1 \pm 0.8)(1 \pm 0.3)/4$. The polarization weights are reproduced in Table 3.2. The expected process rates and the signal purities differ between the beam polarization configurations. Having four separate sets of measurements gives additional information that is useful for chirality dependent physics beyond the SM (BSM) and for the control on systematic uncertainties. Without beam polarization there is only one set of measurements and all pure polarization samples contribute with equal weight. The processes of interest are mainly produced from opposite initial state polarizations. The opposite-polarization configurations are favored in the H20 scenario. Thus the effective luminosity from the combination of the polarized data sets is higher than from the equivalent unpolarized data set.

For the sake of keeping the number of figures in this thesis reasonable the figures that illustrate the data sets use the H20-weighted combination instead of repeating the plot for each of the four polarization configurations. Nevertheless the four sets of measurements are used individually in order to exploit all available information and obtain the best results.

3.3.1 Event generation and machine modelling

Events are generated with tree-level matrix elements and loop corrections by WHIZARD 2.8.5 [60], [61]. They are grouped by the number of final state partons and leptons.[1] The fragmentation and hadronization of final-state quarks and gluons is performed with PYTHIA 6.422 [62], tuned to LEP data.

Initial State Radiation (ISR), Beamstrahlung and Final State Radiation (FSR) are included. The beam energy spectrum and the machine backgrounds (Section 2.1.2) are simulated for the beam parameters in Table 2.1. Beam-beam interactions at a linear collider are computed with Guinea-Pig [63]. Low-p_T hadron contributions from beamstrahlung are generated by the dedicated Barklow-generator [64] ($300\,\text{MeV} \leq \sqrt{s_{\gamma\gamma}} \leq 2\,\text{GeV}$) and by PYTHIA.

[1] The processes that are relevant here are listed in Appendix A. SM processes with 2 to 4 fermions in the final state are considered as backgrounds. No fully hadronic events are taken into consideration because they do not pass the loose selection that requires a pair of isolated leptons. The relevant backgrounds are either leptonic (2 or 4 leptons in the final state) or semileptonic (2 leptons and 2 partons in the final state). The name of each process additionally indicates the electroweak gauge bosons that facilitate the process. The Bhabha cross section (t-channel $e^+e^- \to e^+e^-$) is unmanageably high for small momentum transfers. However, only events with above a minimum momentum transfer are visible in the detector and have to considered for the $e^+e^- \to e^+e^-$ process.

The Higgs boson events are categorized by the additional fermions that are produced in them (e^+e^-, $\mu^+\mu^-$, $\tau^+\tau^-$, $\nu\bar{\nu}$, $q\bar{q}$) and by the Higgs decay mode.

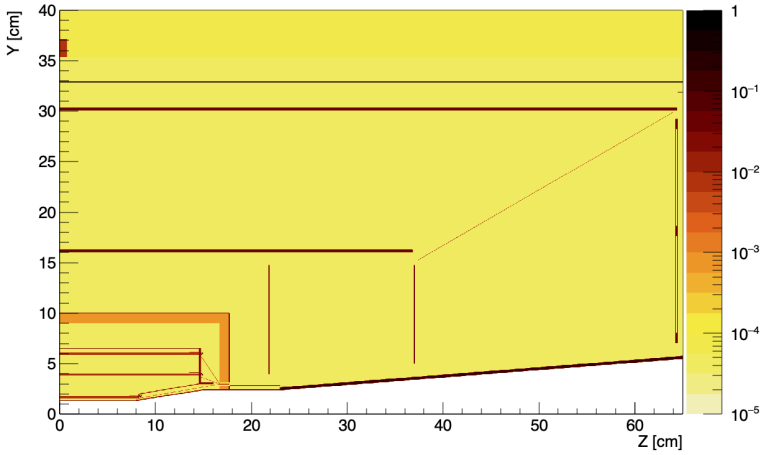

Figure 3.9: Material scan of the inner tracking region of the simulated ILD detector in units of X_0 with arbitrary absolute scaling. Figure taken from [54].

3.3.2 Detector simulation

The ILD detector (ILD_l5_v02) is implemented with great detail in the generic detector description toolkit DD4hep [65]. The average material budget used per azimuthal angle θ was shown Fig. 3.7. In a $y-z$ view of the inner tracking region the level of detail that went into the detector description becomes apparent. Not only the VTX, SID and FTD sub-detectors can be seen in the material scan in Fig. 3.9. Also the dead material from the beam pipe, the support structures, services (e.g. front end electronics for power distribution and data readout) within the detector, and cables are implemented. The DDG4 component [66] interfaces with Geant4 [67] and steers the detector response simulation. During the reconstruction and analysis steps the detector geometry information can be queried with DDRec.

LCIO [68] is the persistency framework that is used throughout the simulation and reconstruction chain and for data storage. Its event data model with four groups of classes is summarized in Fig. 3.10.

The Monte Carlo classes hold the output from event generation and detector simulation. The final state particles, before and after hadronization, and additional particles from the machine background can be stored in a **MCParticle** collection. The results of the simulated interaction with the detector material are stored as **SimTrackerHits** and **SimCalorimeterHits** respectively.

In the digitization step those simulated hits are transformed into hits that could realistically be measured in the sub-detector. For this purpose cross talk, electronic noise and signal collecting efficiencies are applied, and the hit position and time are smeared according to resolutions that have been established in test beams of the detector components.

For reconstruction and subsequent analysis the hits are combined into **Tracks**, made up of **TrackerHits**, and **Clusters** with **CalorimeterHits**. Combining those creates **Reconstructed Particles** and their **Vertices**. Where available truth information is used to link associated objects from the different groups via **LCRelations**.

The same algorithms for reconstruction and analysis can be applied to real data. Such data, e.g. from test beams of sub-detectors or in the future from the running experiment, is recorded in objects from the RawData group of LCIO classes. In order to reuse the algorithms, the RawData objects are

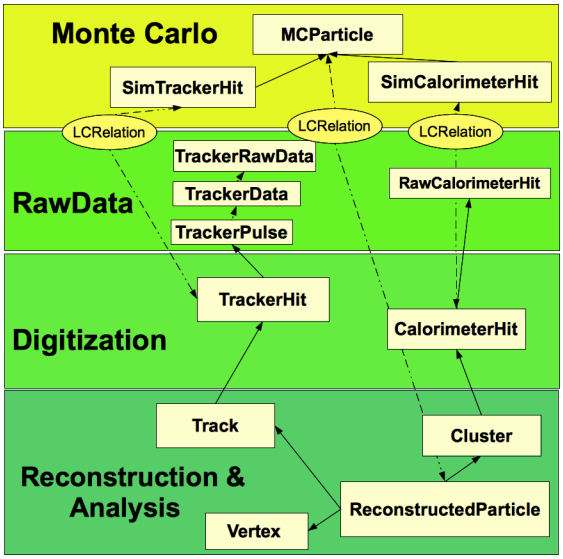

Figure 3.10: LCIO event data model. Figure taken from [40].

converted into the common **TrackerHits** and **CalorimeterHits** interface.

3.3.3 Particle Reconstruction

The simulation, reconstruction and analysis work flow is run through processors in the Marlin [69] C++ application framework. Pattern recognition algorithms that are aware of the geometry of the ILD tracking system are implemented in the MarlinTrk package [70]. The resulting tracks, together with the digitized calorimeter hits and candidates for kinks and V_0, are handed over to PandoraPFA [52], [53] for the reconstruction of the particle signatures as particle flow objects (PFOs). The particle flow algorithm and its Pandora implementation were discussed in Section 3.1.

3.3.4 High Level Reconstruction

LCFIPlus Vertex finding, jet finding, and flavor tagging can be carried out with LCFIPlus [71]. The primary vertex finding considers the uncertainty in the expected beam spot. Several jet finding algorithms are implemented. The DurhamVertex algorithm, used for the jet clustering in the Higgs branching ratios study presented below, is introduced in Section 6.2.1.

The LCFIPlus flavor tagging uses boosted decision trees (BDT) with variables from the tracks and vertices within a jet. The flavor tagging is tuned to several jet energy and multiplicity scenarios. The reference performance for b-tagging and c-tagging at $\sqrt{s} = 500\,\text{GeV}$ with 6 jets is shown in Fig. 3.11. The most appropriate tune for Higgs decays from Higgsstrahlung events at $\sqrt{s} = 250\,\text{GeV}$ is `qq91_v03_p01`.[2]

Isolated Particles Algorithms for the identification of one or multiple isolated leptons in an event are provided with additional high level reconstruction algorithms in MarlinReco/Analysis.

[2]The considered Higgsstrahlung events have an isolated lepton pair from the decay of the recoiling Z boson. From the sum of the masses of Z boson and Higgs boson being close to the collision energy it is clear the both bosons can only have a small momentum. Indeed the most common energy of the Higgs boson is approximately 140 GeV . The `qq91_v03_p01` tune is trained on hadronic Z boson decays at rest.

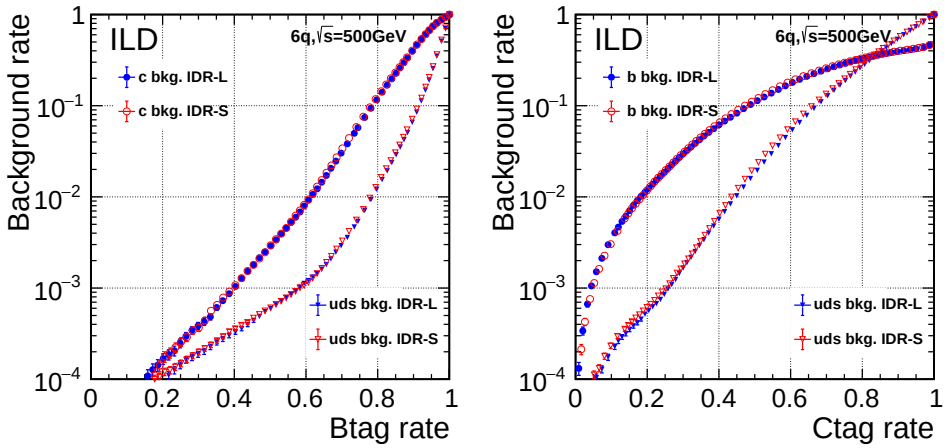

Figure 3.11: LCFIPlus flavour tagging performance. Figure taken from [54].

The **IsolatedLeptonTaggingProcessor** uses BDTs to tag one or multiple isolated electrons or muons. The particle type identification is improved over the general PandoraPFA performance. Important inputs are the ratios of the energy deposits in the different calorimetric systems and the compatibility of the particle's vertex with the interaction point. Isolation is ensured by checking the energy in a cone around the particle's momentum vector.

The cut-based **IsolatedPhotonTaggingProcessor** focuses on the isolation criterion and creates isolation cone variables similar to the IsolatedLeptonTaggingProcessor.

4 SiW-ECAL

Contents

The CALICE SiW-ECAL is proposed as the ECAL of the ILD detector at the ILC. The full ILD ECAL consists of about 100 million channels. A prototype with more than 15.000 channels has been tested at DESY in November 2021 and March 2022. This prototype is described in Section 4.1. The calibration procedure is discussed in Section 4.2. In the context of this thesis, the initial event reconstruction procedure has been revised (Section 4.3). Building on the initial event reconstruction, a semi-online monitoring procedure has been developed (Section 4.4). Finally, preliminary electron shower studies are presented in Section 4.5 for run 050282.

4.1 Technological prototype

The CALICE SiW-ECAL technological prototype [72] is the successor of the physics prototype [73]. Multiple Active Sensor Units (ASUs) are combined for performance tests. The long slab, created by the chaining of ASUs orthogonal to the expected particle direction, is discussed in Section 4.1.1. A stack of ASUs along the beam axis is used for track finding and shower studies. Fig. 4.1 shows the stack, equipped with 15 short layers, in the DESY experimental hall.

Each $18 \times 18\,\mathrm{cm}^2$ ASU consists of 4 silicon wafers that are glued onto a printed circuit board (PCB) with 16 chips (application-specific integrated circuits, ASICs). An ASIC has 64 readout channels corresponding to $0.5 \times 0.5\,\mathrm{cm}^2$ segments on the silicon sensor. A Kapton film that is glued to the other side of the silicon wafers provides the high voltage that is needed for the depletion of the sensor. The stacks that were tested at DESY are made up of heterogeneous layers, spanning multiple development

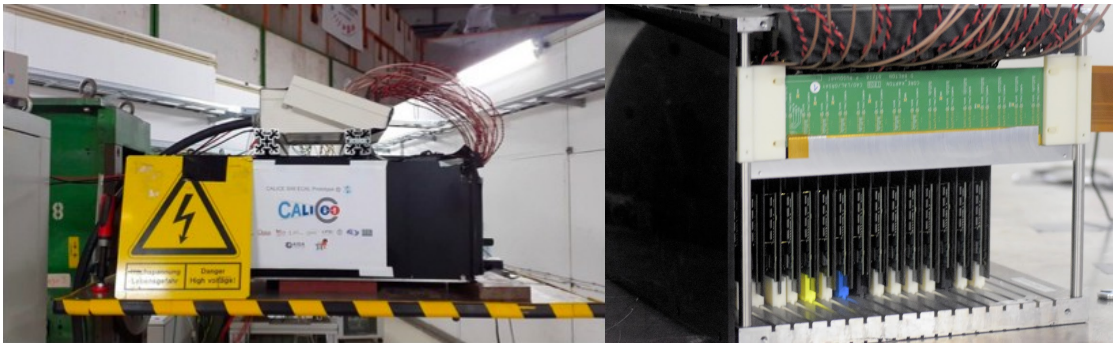

Figure 4.1: CALICE SiW-ECAL technological prototype with 15 short layers at DESY (2022).

Layer	W [mm]	Si [µm]	FEV	SKIROC	COB	Slab ID
1	2.8	650	13	2a		15
2	2.8	650	13	2a		16
3	2.8	500	11	2a	x	20
4	2.8	500	11	2a	x	22
5	2.8	320	11	2		13
6	2.8	320	11	2		11
7	2.8	320	11	2		14
8	4.2	500	12	2a		19
9	4.2	500	12	2a		17
10	4.2	500	12	2a		7
11	4.2	500	12	2a		3
12	4.2	320	11	2		4
13	4.2	320	11	2		2
14	4.2	320	10	2		6
15	4.2	320	11	2		10

Table 4.1: Layer configuration for run 050282.

iterations. SKIROC2 ASICs [74] have been used on the older boards, while the newer boards are equipped with the improved SKIROC2a chips. Four generations of PCBs (FEV10-13) are currently in use, with three different wafer thicknesses (320 µm, 500 µm and 650 µm). Table 4.1 summarizes the layer configuration for run 050282, analyzed in Section 4.5. An alternative PCB design for which the ASICs are directly wire bonded to the PCB (instead of packaged) was first exposed to particle showers during the 2021 DESY test beam. This chip on board (COB) design decreases the board thickness from 2.7 mm to 1.2 mm. The latter thickness meets the ILD requirements. A Slab ID is assigned to each board as an internal unique identifier. The mechanical structure shown in Fig. 4.1 allows to quickly replace individual ASUs or to shuffle the positioning.

For calibration runs like the ones described in Section 4.2, the prototype is operated without any absorber material. The choice of Tungsten as the ECAL absorber material has been motivated in Section 3.1.3. With the setup in Table 4.1 the prototype is 15.2 radiation lengths deep. While this is shorter than the ILD target depth, it is appropriate for the DESY electron beams with user-selectable momenta from $1 - 6\,\mathrm{GeV}/c$ [75]. Starting with thinner absorber plates offers a better precision on the shower starting point.

In contrast to the physics prototype, the technological prototype has the very front end electronics

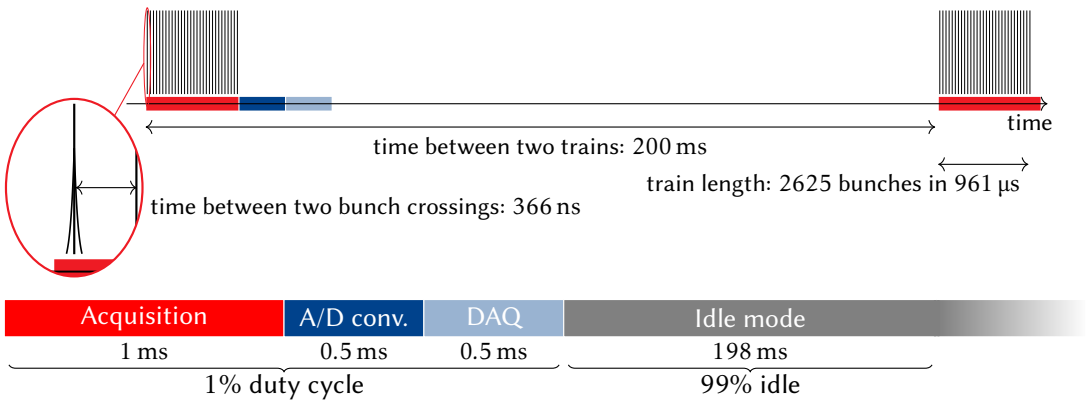

Figure 4.2: The ILC beam structure. The numbers are chosen in agreement with the ILC250 accelerator parameter after the luminosity upgrade, as presented in Table 2.1.

(VFE) embedded inside the detector. The power consumption, the size, and the fraction of active detection surface are close to the target specifications for the ILD ECAL. A large reduction in power consumption is achieved by exploiting the power pulsing operation of the ILC. The ILC beam structure is summarized in Fig. 4.2. Particle bunches are concentrated in a bunch train which passes the collision point within about 1 ms. Within each bunch train, individual bunches are regularly spaced with a few 100 ns distance. A bunch train is followed by 199 ms without any bunches. Only about 1% uptime of the SiW-ECAL electronics is necessary for data acquisition (0.5%), data conversion (0.25%) and readout (0.25%) (see Fig. 3 in [74]). The heat produced by the 25 µW of power that are needed per channel can be dissipated without active cooling for the ILD ECAL.[1]

Instead of a global trigger, each chip is triggered individually if a sufficient gain amplitude is measured in one of its 64 channels. Then a bit per channel indicating if it has been triggered, the low gain, and the high gain[2] of each channel are stored in a 15 entry deep physical switched capacitor array (SCA). Additionally, the bunch crossing ID (BCID) provides a coarse $\mathcal{O}(100\,\text{ns})$ timing measurement that can be used to combine the triggered events from different chips. After each acquisition window, the triggered data is converted and read out. Without this auto-trigger capability, the data rate from the full, highly granular ILD ECAL ($\mathcal{O}(10^8)$ channels) would be unmanageable. If the particle beam and the ECAL electronics are synchronized, the next cycle starts with an acquisition window at the time when the next bunch train is expected. During the DESY test beam, the ECAL electronics were not synchronized with the beam structure.

4.1.1 Long slab

An ILD ECAL module will consist of up to 12 ASUs that are chained together and are operated through a single front end board. This poses additional challenges with respect to the standard test beam stack with a single ASU per layer. The boards have to be connected and the stability of the high and low voltage must be ensured over the full slab length. Clock and signal should also be independent of the

[1] In the ILD ECAL design, the PCBs of a long slab are attached to a heat shied made of copper. The heat shield itself is cooled by water, outside of the active detection area. At the opposite side of the ASU, after the PCB, a heat shield made of cupper facilitates heat dissipation. Reevaluating the cooling is the main prerequisite when adapting the SiW-ECAL for a particle flow based detector at a circular electron-positron collider.

[2] The low gain is ten times smaller than the high gain. Having both gains available increases the range over which the MIP (minimum ionizing particle, see Section 4.2) response is nearly linear. At the core of a high energy electromagnetic shower, the charge can be equivalent to thousands of MIPs.

ASU position. The data bandwidth is increased due to the larger number of chips that are connected to the same readout. A long slab with 8 ASU has been successfully tested and areas of improvement have been identified [76].

4.2 Calibration

A detailed description of the calibration and commissioning procedure can be found in [77]. There are three main steps:

1. **Masking:** Removal of noisy channels. A noisy channel can quickly fill up all memory cells, rendering the area covered by its chip blind for the rest of the data acquisition window.
2. **Pedestal subtraction:** The pedestal is the voltage without signal. It varies between channels and per SCA and must be measured.
3. **MIP calibration:** The pedestal-subtracted ADC count is proportional to the energy that is deposited in the sensor. The response of the detector is calibrated in units of the most probable value of the energy deposit by MIP (minimum ionizing particle).

4.2.1 Masking

A summary of the channel masking is given in Fig. 4.3. While some of the masked channels appear to be randomly distributed, others follow a clear pattern. Channel 37 has been masked on all chips besides those on the COB boards in layers 3 and 4. This channel is known to be noisy due to routing issues that can be fixed in a new FEV version. Channels 41-49 are masked for all but the first four layers on chips 1 and 9. In the earlier FEV versions, channels 41-49 of these two chips have routing issues related to their closeness to the connection to the front end electronics (SLBoard). Due to a different connection setup on the newer COB and FEV13, it was not necessary to mask these channels in the first four layers. For other channels that are often masked, e.g. channels 5 or 9, further studies are needed to identify the underlying issue. Overall 5.5% of the channels have been masked. Additionally, 31.5% of the remaining channels were flagged as having a poor calibration quality. For the most part these are channels which, due to connectivity issues, only registered very few hits, resulting in a failed fit of the MIP spectrum.

Masking a channel should only be the last resort. First, it is preferable to increase the trigger threshold for the chip (SKIROC2) or the channel (SKIROC2a). When a cell triggers a memory write due to noise, it is usually straight forward to remove it from the analysis in a later step. Noise contributions rarely happen in coincidence with the BCID of a real event. Even if the noise BCID and the event BCID are compatible, the noise cell can be anywhere in the detector and is unlikely to be mistaken as a contribution to a track or a particle shower. A more problematic consequence of noisy cells is that they can fill a chip's memory before the end of the acquisition window. For run 050282, the fraction of the data acquisition time during which any of the 240 chips was full is below 4%. This includes the effects from noise cells as well as empty events and re-triggered events that are caused by charge deposits and cannot be removed by channel masking.

4.2.2 Pedestal subtraction

The pedestal position is calculated from the values of channels without a signal. To trigger the writing to the memory, a signal can be injected in one of the channels. A Gauss error function is fitted to the distribution of ADC counts from channels without trigger, thereby describing the noise of the electronics. The mean varies for different SCA memory cells of the same channel. The variation of

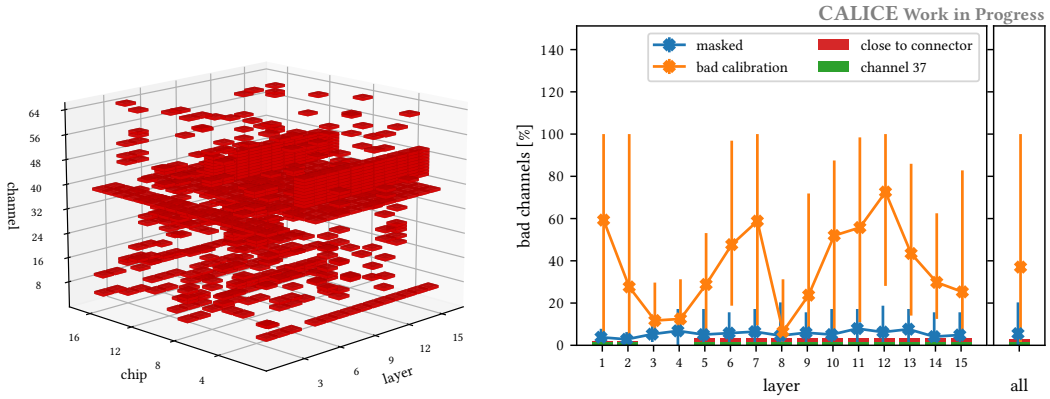

Figure 4.3: Masked channels in the SiW-ECAL technological prototype. The 3D visualization shows the masked channels per chip and layer. A few patterns of masked channels are discussed in the main text. The summary plot on the right side gives the average fraction of bad channels, and the contribution due to two known noise sources. The edges of the error bars indicate the lowest and highest fraction of bad channels for any chip in the layer.

the mean between different memory cells can be larger than the the noise itself. Thus it is necessary to measure the pedestal not only once per channel, but separately for each of the 15 memory cells. The width, together with the most probable energy deposited by a MIP in ADC units, is used for the signal-to-noise ratio.

4.2.3 MIP calibration

About 80 h^+e^- pairs per µm are created by a MIP traversing the silicon diode, equivalent to a charge of 4.1 fC for a 320 µm wafer. After subtraction of the pedestal, the ADC value is proportional to the input charge.[3] One way to collect MIP data is to wait for cosmic muons. This method is slow, especially for the edge regions of the prototype. The incidence angle of the cosmic muon should be taken into account.

Alternatively, the DESY electron beam can be regarded as a source of MIPs if the prototype is operated without tungsten plates. The combined hit map for a MIP scan with at least 450 s of beam time per position is shown in Fig. 4.4. Apart from the removal of the tungsten plates, the layer configuration is identical to Table 4.1. For this test beam, the ASUs with FEV13 PCBs had to be shifted by 60 mm in order to make space for an adapter card that was needed to communicate with the new DAQ system. White crosses in Fig. 4.4 indicate the dead space between the wafers.[4] The white squares illustrate masked channels. Two patterns of masked channels have been discussed in Section 4.2.1. Channel 37 can be identified as the four white squares that appear on all wafers, except the COB wafers with the alternative routing. From layer 5 onwards, a connected block of white squares is found at the right edges of the boards. Those are the channels that are disturbed by the noise from the SLBoards.

The scan consists of 36 positions on a grid with 3 cm spacing. At each position, a 3 GeV/c electron beam is directed perpendicular onto the detector. Due to varying beam intensities and exposure times the number of events per position is not meaningful. A linear color map has been chosen, with the

[3] The SKIROC2 chip has linearity to better than 0.5% between ADC value and MIP over the range from 2 fC up to 8 pC [74].

[4] A correct representation of the summed up hit map with all layers would not have the vertical white line. This region has obtained a few hits from the shifted FEV13 layers. To simplify the figure, the hits on the FEV13 layers between $x = -60$ mm and $x = 0$ mm have been moved by the width of the dead space between wafers, 2.1 mm, in negative x direction. The adjustment is only applied for the hit map with all layers.

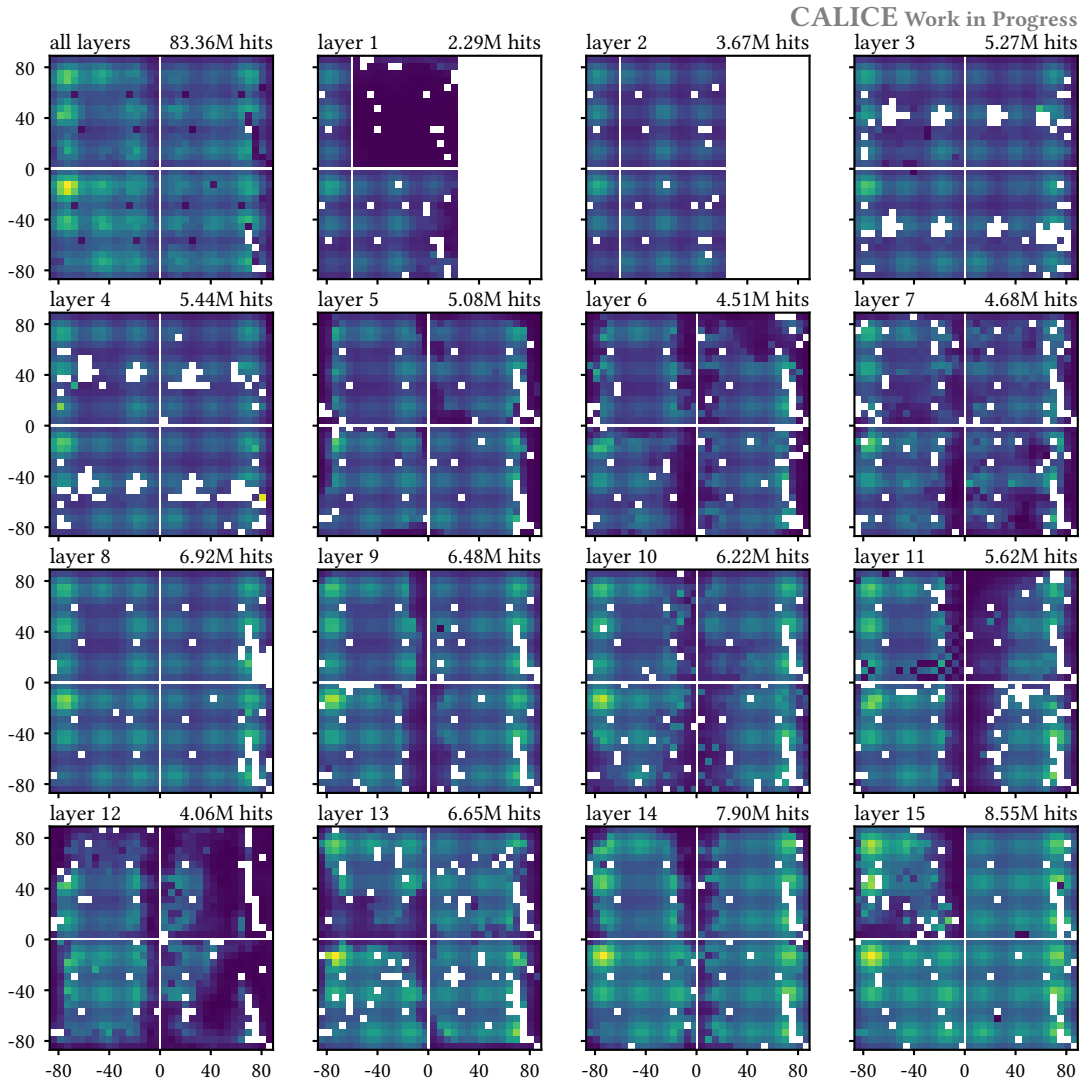

Figure 4.4: Combined hit maps of a MIP scan.

same maximum value for all single layer hit maps. Due to a shortage of available layers at the time, ASUs with known efficiency problems where nonetheless included in the stack.[5] Some channels are even disconnected from the high voltage. In run 050282, the beam has been centered on $(x, y) = (-35\,\mathrm{mm}, -35\,\mathrm{mm})$. This is a good region for all ASUs.

The combined hit energy spectrum from the MIP scan is shown in Fig. 4.5. In order to compare different channels, the ADC count has to be converted into units of MIP. For this purpose, the pedestal mean per channel and SCA is subtracted from the ADC count. Then the position of the most probable value (MPV) per channel is calculated by a fit on the pedestal-subtracted ADC count spectrum of the

[5] The bad wafer in layer 1 has been recovered after the MIP program.

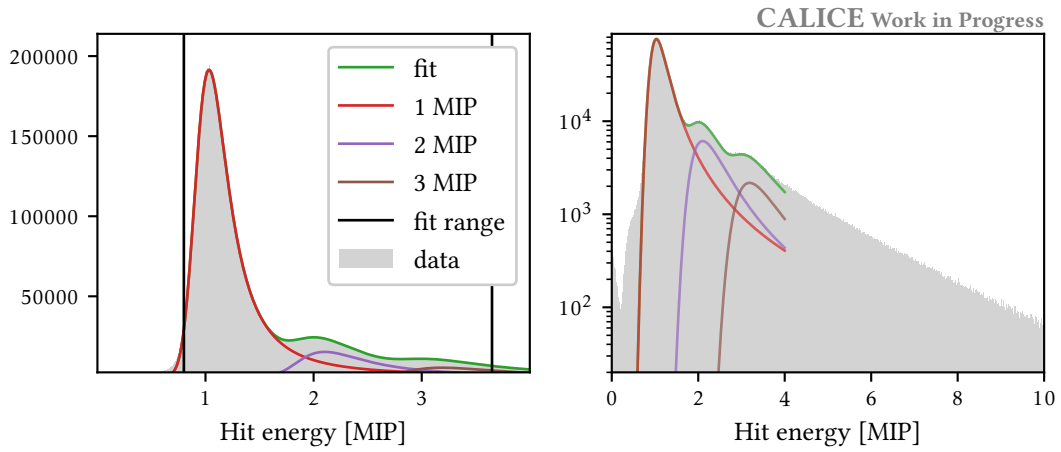

Figure 4.5: Hit energy distribution in units of MIP. All good hits from the MIP scan are used. The curves show the fit and its 1, 2, 3 MIP components. The same data is presented with linear (left) and logarithmic (right) scale on the y axis.

channel, obtained from the MIP scan. This value is the scaling factor from pedestal-subtracted ADC count to MIP. After conversion into units of MIP, the spectra from different channels, including different wafer thicknesses, can be compared on equal footing.

To reduce noise contributions, only hits that belong to a set of at least 6 hits, in coincidence and connected by a straight line, are considered. The energy deposit of a MIP traversing through matter is described by the Landau distribution

$$L(x;m,\eta) = \frac{1}{\pi\eta}\int_0^\infty e^{-t}\cos\left(\frac{2t}{\pi}\ln(\frac{t}{\eta}) + t\left(\frac{x-m}{\eta}\right)\right)\mathrm{d}t \tag{4.1}$$

with location parameter m and scale parameter η. It is convenient to replace the location parameter by the MPV, $L(x;m^{\mathrm{MPV}},\eta)$. Measurement uncertainties are taken into account through the convolution with a Gaussian,

$$\tilde{L}(x;m^{\mathrm{MPV}},\eta,\sigma) = \int_{-\infty}^{\infty} L(\tau;m^{\mathrm{MPV}},\eta)\mathcal{G}(x-\tau;0,\sigma)\,\mathrm{d}\tau. \tag{4.2}$$

This convolution accounts for the noise from the chip, typically about 1/10 MIP, and small calibration uncertainties. The rate at which multiple particles from the same bunch reach the detector depends on the accelerator settings. A good description of the core region of the observed MIP spectrum is by a superposition of a 1, 2, and 3 MIP spectrum:

$$\begin{aligned} &f(x;m_1^{\mathrm{MPV}},\eta_1,\sigma,m_2^{\mathrm{MPV}},\eta_2,f_2,m_3^{\mathrm{MPV}},\eta_3,f_3) \\ &\quad = \tilde{L}(x;m_1^{\mathrm{MPV}},\eta_1,\sigma) + f_2\tilde{L}(x;m_2^{\mathrm{MPV}},\eta_2,\sigma) + f_3\tilde{L}(x;m_3^{\mathrm{MPV}},\eta_3,\sigma). \end{aligned} \tag{4.3}$$

Table 4.2 summarizes the fit. In contrast to Eq. (4.2), the m^{MPV}values from the fit indicate the MPV position after the noise convolution. The MPV of the unfolded Landau distribution is closer to 1, $m_1^{\mathrm{MPV}} = 1.007$.

Figure 4.6 shows the spectrum broken down into the contributions per layer. The MIP position varies by 0.24% between layers. The importance of the multi-MIP contributions increases with the

	Value	Relative uncertainty
A	38300	±4.5%
f_2	0.0800	±0.14%
f_3	0.0284	±0.26%
m_1^{MPV}	1.033	±0.0096%
η_1	0.0794	±0.089%
σ_1	0.0747	±0.2%
m_2^{MPV}	2.102	±0.024%
η_2	0.191	±0.26%
m_3^{MPV}	3.186	±0.041%
η_3	0.249	±0.52%

Table 4.2: Fit results and relative uncertainty for a fit on the MIP spectrum with up to 3 MIPs.

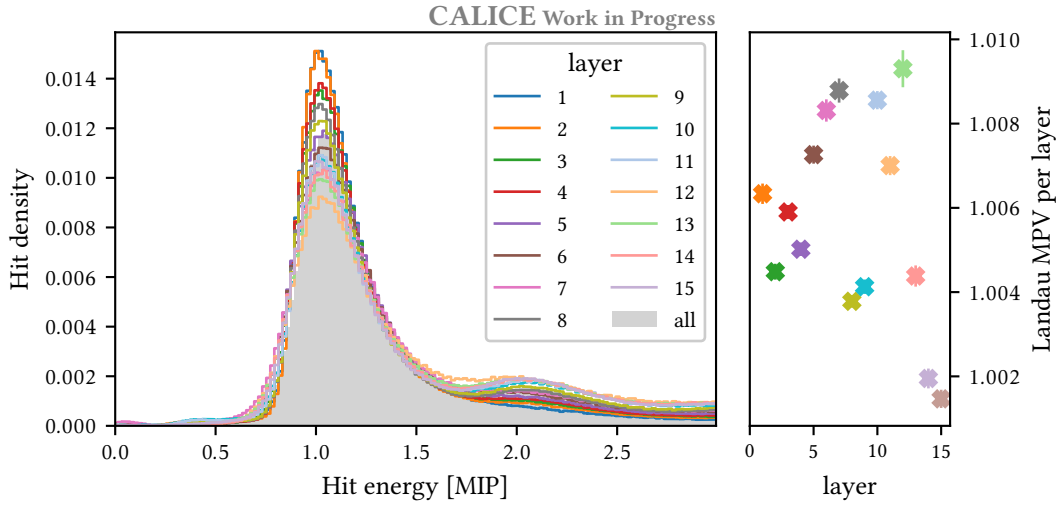

Figure 4.6: Hit energy distribution per layer in units of MIP. All good hits from the MIP scan are used. The right panel indicates the position of the MPV of the 1-MIP Landau distribution and its uncertainty, obtained from a fit on the spectrum of each layer.

layer position: Even without the absorber plates, some electrons interact with the detector material. After the creation of a bremsstrahlung photon and a subsequent pair creation, three MIPs will pass through each layer ($e^-(e^+e^-)$). Given the high granularity of the detector, a small opening angle is sufficient for them to contribute to different channels.

The expected energy deposit of a particle traversing a sensor under an angle α to the normal vector scales with $1/\cos(\alpha)$. Exploiting the high granularity of the detector, the particle's track can be reconstructed, and an angle-dependent down-scaling of the measured energy can be applied to all cells that are part of the trajectory. When the MIP calibration is performed with cosmic muons, this per-track correction is essential. Another consequence of particles that traverse the detector under non-zero incidence angles is the charge sharing between neighboring cells. As shown in Fig. 4.7, the contributions from particles at the cell edges create a plateau region below the MIP peak. In the observed spectrum,

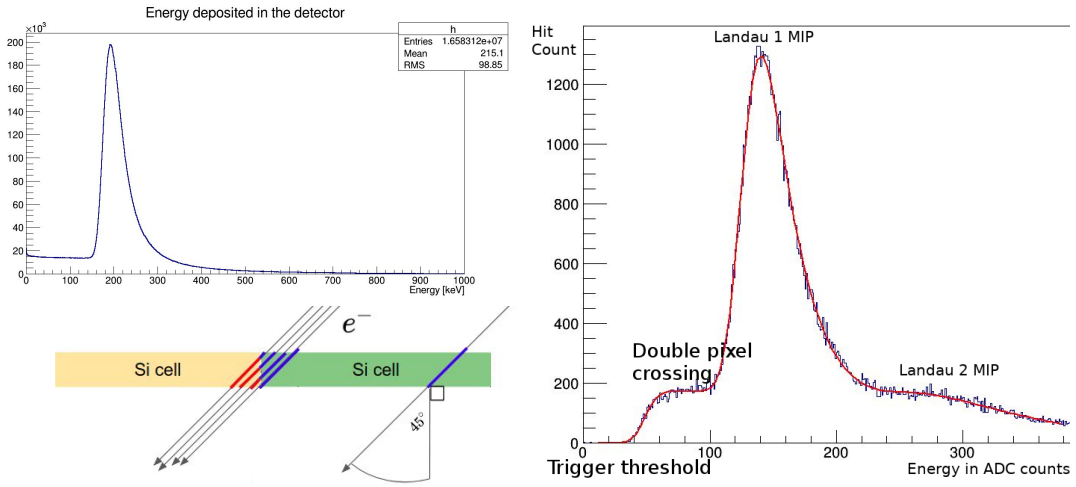

Figure 4.7: Simulated (left) and observed (right) MIP spectrum in a single pixel from a particle with 45° incidence angle. The low-energy plateau in the GEANT4 simulation is populated by particles that traverse the pixel at its edge. Figures taken from [76].

this plateau is truncated at the trigger threshold.

4.2.4 Calibration summary

Low gain and high gain have to be calibrated independently. While the range of the high gain is sufficient for the DESY beam energies, it will be saturated for channels at the core of high energy showers at the ILC. Almost half a million calibration constants are required for the description of the SiW-ECAL technological prototype.

- $(15 + 1)$ calibration constants per channel and gain: One pedestal mean per SCA memory cell and the MIP scaling factor.
- 2 gains.
- 64 channels per chip.
- 16 chips per ASU.
- 15 layers.

$\rightarrow$ 491520 calibration constants.

4.3 Initial event reconstruction

After each data acquisition window, the hit data is collected separately for each chip. A new event reconstruction script for the SiW-ECAL technological prototype has been written for this thesis. Starting from the data collected per chip during one acquisition cycle, full ECAL events with calibrated hit energies are created.

The default configuration file for event reconstruction is reproduced in Listing D.1. Based on these settings, each channel is mapped to its position in the detector. Quality checks are performed for the pedestal and for the MIP calibration. Those entries that failed the checks are referred to as

bad calibration in Fig. 4.3. Their calibration constants are replaced by suitable averages and a flag (`hit_is_commissioned == 0`) is toggled.

It is not sufficient to combine the hits from all chips that recorded data at the same BCID within an acquisition cycle. The different chip logics lead to slightly different clock distributions. Additionally, the shapers for channels with a larger charge deposit rise faster, and therefore pass the trigger threshold earlier. Instead, by default, contributions from different chips are combined into a single event if their BCIDs are within a window of 3 BCID units. New insights on the accumulation of nearby triggered BCIDs on a single chip prompted modifications in the within-chip hit selection procedure. They are presented in Sections 4.3.1 and 4.3.2.

4.3.1 Empty frames

A summary of several types of fake events is given in Fig. 4.8. All layers have recorded a similar number of frames during the MIP run that these summary statistics are based on. Over all layers, 2.2% of the recorded frames have been identified as being part of a **retrigger chain**. This term refers to the repeated writing to a chip memory during a small BCID window. Oftentimes the retrigger chains fill the chip's memory up to the last SCA, rendering the detector region covered by that chip blind for the remainder of the acquisition window.[6] It is suspected that retrigger chains are induced by distortions of the power supply baseline [77], [78]. Since the preamplifiers of the SKIROC2/2a chips are referenced to the analog power supply level, a voltage dip increases the chance for electronic noise to surpass the trigger threshold. A single power supply is shared by all slabs. Therefore these fake events can occur anywhere, not necessarily on the chip that produced the voltage drop.

The overall rate of full chip memories depends also on the trigger thresholds that have been set and on the strictness of the masking. The fraction of full chip memories that are explained by retrigger chains varies from 4% to 80% between layers.

When one of the channels of a SKIROC2 chip passes the trigger threshold, the chip's `OR64` signal is activated. A triggered channel is read a fixed time interval after the start of its trigger signal. Channels without a trigger signal are read at the end of a slow clock cycle if the `OR64` signal was active during that cycle. For triggers that occur towards the end of a slow clock cycle, the `OR64` signal can stay activate beyond the start of a new clock cycle. Then a good event is written for BCID−1, while only non-triggered channels are written in BCID. The rate of such empty events has been significantly reduced for SKIROC2a by shortening the `OR64` signal.

During the optimization of the BCID merging procedure for the initial event reconstruction, additional types of empty events where discovered. A breakdown of empty event types is given in the bottom panel of Fig. 4.8. Given that frames that are part of a retrigger chain should be discarded in general, it is uncontroversial to discard empty frames that occur during such a chain. The few empty frames for which a channel has been triggered in both BCID−1 and BCID+1 can also be considered as part of a retrigger chain, even though they do not meet the definition given here. Empty frames in BCID, followed by a readout with a triggered channel in BCID+1, have not been reported before. Their existence has since been confirmed on a test bench, but further studies are needed to identify their cause. The charges from the triggered channel and from the same channel in the adjacent BCID without any triggered channels are compared in Fig. 4.9. Both categories of triggered channels, BCID−1 and BCID+1, have the expected charge spectrum of a triggered channel on the considered ASU. The charge spectrum of the channel from the empty frame after the trigger in BCID−1 is compatible with the channel pedestals. For trigger-free channels before a trigger occurring in the consecutive BCID+1, the

[6] Here, a retrigger chain consists of at least five recorded frames within a BCID window of width 20. With this definition, 21% and 30% of the retrigger chains on the ASUs with COB chips lasted until the chip memory was full. For the other ASUs, this rate of maximum length retrigger chains increases to (70 ± 3)%.

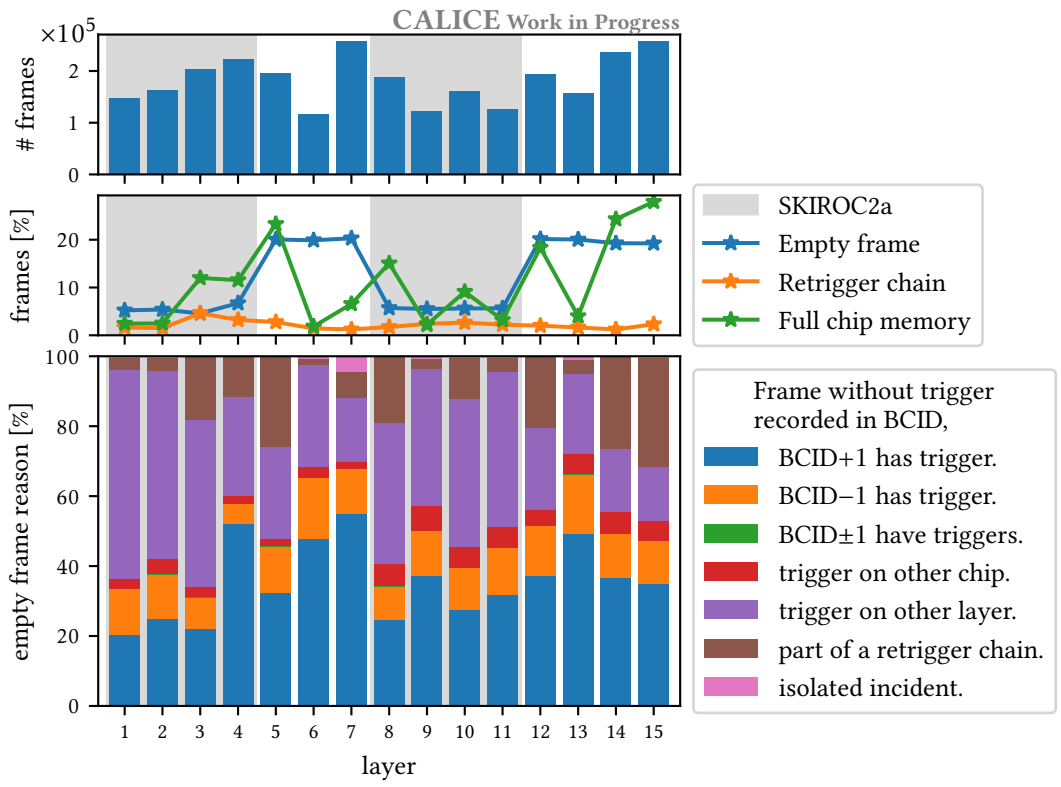

Figure 4.8: Summary of the recorded frames per layer.

charge is usually considerably above the pedestal mean but somewhat smaller than the typical charge that is deposited by a MIP. This indicates that these empty frames indeed measure the charge of a true event, but during the rise of the charge curve before its maximum. The subsequent measurement of the channel's charge in BCID+1 has a better compatibility with the expected MIP spectrum. Thus it is concluded that the ADC count should be taken from the frame that actually has the triggered channels.

Only about half of the empty frames have a triggered channel in a neighboring BCID on the same chip. Almost all empty frames occur at most two BCIDs after an event is recorded in any of the chips in the detector. The distribution of the highest charge in these empty frames looks similar to the distribution shown in Fig. 4.9 for the empty frames with a trigger in the following BCID+1. Importantly, the spectrum is centered at smaller counts than expected for the deposits from a MIP. It can therefore be excluded that these empty frames are proper event frames with only the trigger missing. For the event reconstruction, any frames without triggers can simply be dropped.

4.3.2 Merging of chip hits

To account for imperfections in the synchronization of the slow clocks, the event reconstruction usually allows the combination of frames from different chips within a BCID window. Many frame pairs of consecutive BCIDs on the same chip with different triggered channels between the two frames have been observed in the electron showers recorded at the 2022 DESY test beam. To account for this

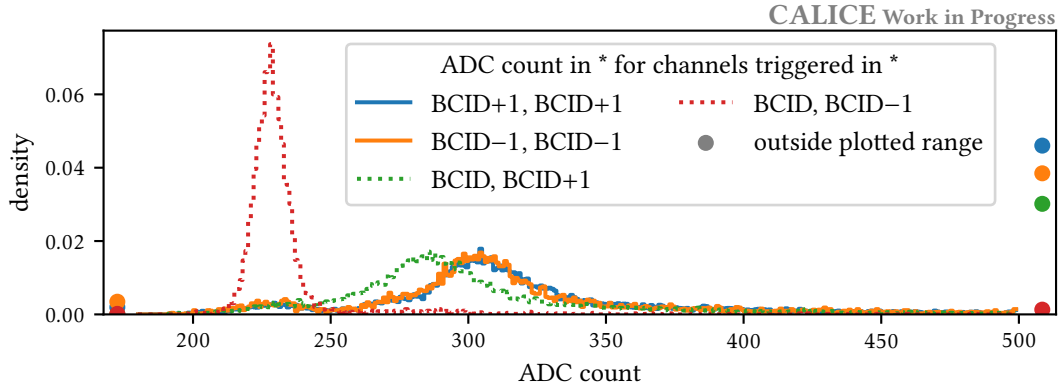

Figure 4.9: ADC count for empty frames in BCID. For this layer, a typical pedestal mean is 230 ADC units and a typical MIP response in ADC units is approximately 70.

phenomenon, the option to combine the triggered channels from consecutive BCIDs on the same chip has been added to the event reconstruction. The distribution of the number of hits that are collected in the detector for a 3 GeV electron beam is shown in Fig. 4.10. The standard approach has been to only consider the first recorded frame with triggered channels per chip, within the BCID selection window for the event reconstruction. Any subsequent frames within a small BCID window are assumed to be part of a retrigger chain and are discarded. Alternatively, the union of triggered channels can be used for the event reconstruction. The distribution of the number of hits using the merging approach has a smaller width and a mean that is closer to the expected mean from simulated events. A longer tail towards less hits per shower is expected. The simulated number of hits does not take into account mask channels or detection inefficiencies in the problematic layers. Some chips can be missed by the frame combination algorithm for the event reconstruction. If the frame combination algorithm is too lenient, channels with fake signals increase the high tail of the distribution. When the merging of triggered channels on the same chip is allowed, fake signals from a retrigger chains might be added to the initially reconstructed event.

The shower energy uncertainty with and without the merging of channels on the same chip is presented in Fig. 4.11. For this simple comparison, no cleanup based on the cell positions has been performed. The subset of good events contains events for which none of the chip memories was full at the end of the acquisition window, and for which hits have been recorded in each of the first 11 layers.[7] Two simple energy reconstruction algorithms are tested. At low shower energies, including this 3 GeV electron beam, the counting of triggered channels has a better precision than the energy sum from the triggered channels. Both energy sum and cell count have been adjusted according to the sampling fraction of each layer. The significantly smaller distribution widths in the second row of Fig. 4.11 demonstrate that it is necessary to allow multiple frames from the same chip in the event reconstruction. So far, no pattern has been found that explains which channels are triggered during the first BCID. The channel position in the shower or the energy deposited in the channel does not seem to play a role.

[7] Full chip memories at the end of the acquisition window disqualified 89% of the shower candidates. In the simulated data set, 98.5% of the events have signals above the detection threshold in all layers up to layer 11. 74% Given the known efficiency problems of the prototype

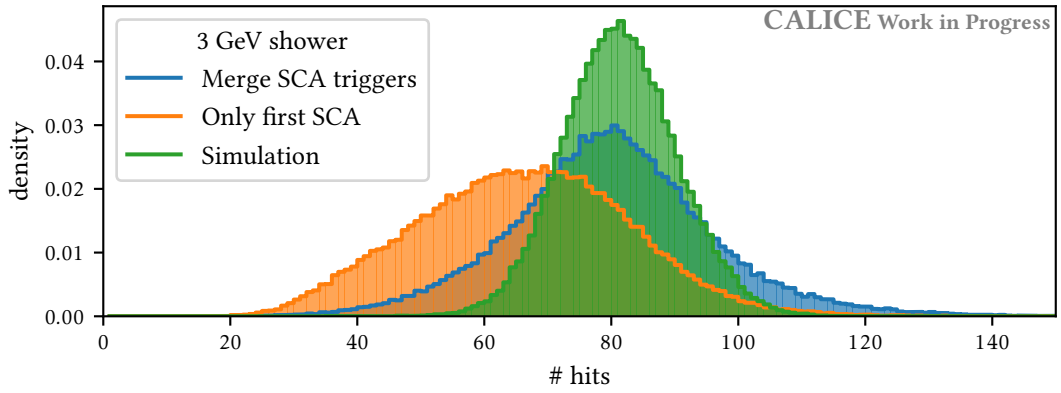

Figure 4.10: Number of triggered cells per shower event with and without the merging of channels on the same chip that were triggered in consecutive BCIDs.

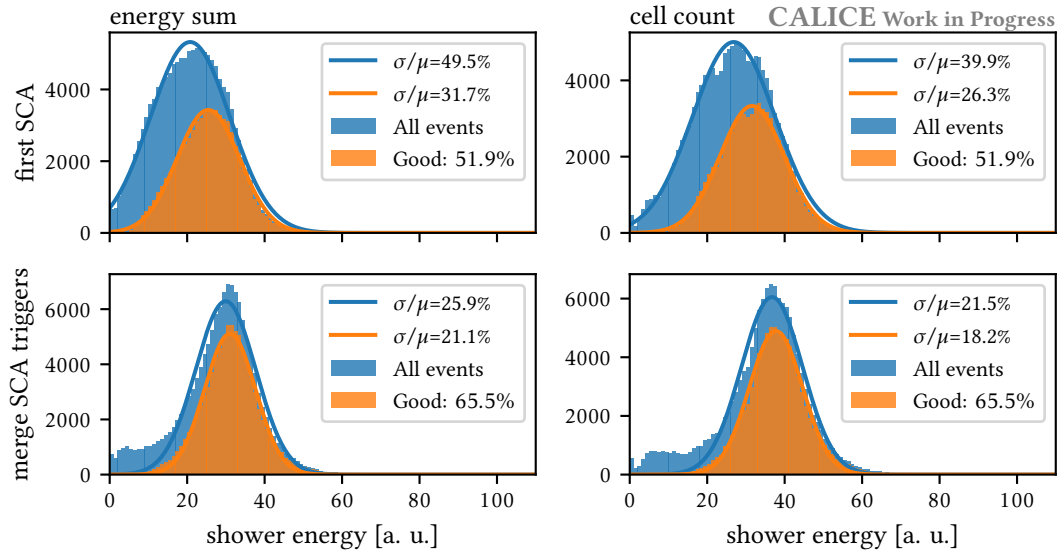

Figure 4.11: Preliminary shower energy uncertainty without (top row) and with (bottom row) the merging of channels on the same chip that were triggered in consecutive BCIDs.

4.4 Semi-online monitoring

The initial event reconstruction, introduced in Section 4.3, can be leveraged for the creation of monitoring tools. First, the DAQ output must be converted into a standard format. Then, the initial event reconstruction is performed. Dummy calibration files can be used if no (preliminary) calibration is available yet. The default configuration file for the monitoring is reproduced in Listing D.2. Since the initial event reconstruction is one of the steps in the monitoring pipeline, its configuration is a subset of the monitoring configuration.

A change of the monitoring configuration is only necessary after changing the detector setup. For the monitoring of a new run, it suffices to provide the path to which the DAQ system writes the run data. The delay between the start of a run and the first semi-online monitoring information is determined by the frequency at which the DAQ system writes to disk. A reasonable feedback can be obtained after a few minutes.

In contrast to the DAQ system's online monitoring tools that are based on the data of individual chips, the semi-online tools have access to full detector events. Thus they can provide timely feedback on the data quality. A flagship use case for the semi-online monitoring is the determination of the desired duration of a run based on the number of recorded events for which a minimum number of layers have recorded data in coincidence. While the DAQ's online hit maps contain all recorded hits, the semi-online hit maps reject most noise hits due to the missing coincidence with hits from other layers. Figure 4.12 shows an event display produced during the monitoring and the an equivalent, noise free, simulated event. A good benchmark for the noise level is the fraction of reconstructed events for which at least one of the chips was not available due to full memory.

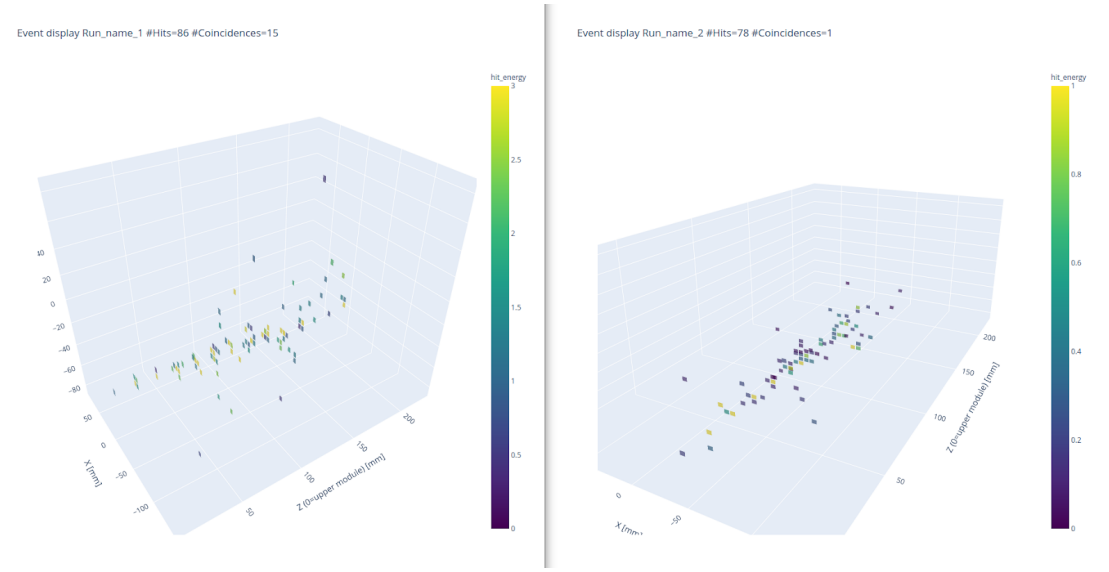

Figure 4.12: Event display of a real (left) and a simulated (right) 3 GeV electron shower event in the SiW-ECAL technological prototype.

4.5 Test beam results

This section takes a closer look at run 050282. Its layer configuration is presented in Table 4.1 and its masked channels are summarized in Fig. 4.3. A shower event display from this 3 GeV electron run is given in Fig. 4.12.

The same layer configuration has been used in a GEANT4 based simulation of electron shower events [79], [80]. After the application of digitization effects, the simulated events are converted into a format that is compatible with the output of the initial event reconstruction for real events, described in Section 4.3. At this stage, some important challenges for real events are not implemented in the simulated events. It is known that some of the layers used in the 2022 prototype have efficiency issues. They are related to the wafer gluing and mainly affect the border region of a wafer. Hits on chips with a full memory are also not recorded. This issue can be removed from the analysis by restricting the data set to events from each acquisition window to those that occur before any of the chips in the detector is full. In real events, hits will be missing if the event reconstruction fails to link their chips to the event, for example due to discrepancies in the clock synchronization. Channel masking is not applied to the simulated events, but can be added in a final step. However, the underlying issues that lead to the need for the masking of a channel are not simulated. Fake hits can be accidentally included in the reconstructed events. The merging of channels from the same chip in consecutive BCIDs makes the event building more vulnerable towards retrigger artifacts. A proper event reconstruction takes advantage of the high granularity of the detector and removes cells from the events based on their position. This goes beyond the scope of the initial, universally applicable event reconstruction introduced in Section 4.3.

Figure 4.13 shows the cumulative hit maps per layer for the run 050282. These low energetic electromagnetic showers are mostly contained in the 15.2 X_0 deep detector. The same figure with the maximum of the color scale fixed individually in each layer is provided in Fig. 4.18.

The longitudinal shower profile in terms of the number of hits per layer is shown in Fig. 4.14. Error bars indicate the mean and the standard deviation of the distribution for observed and simulated events.

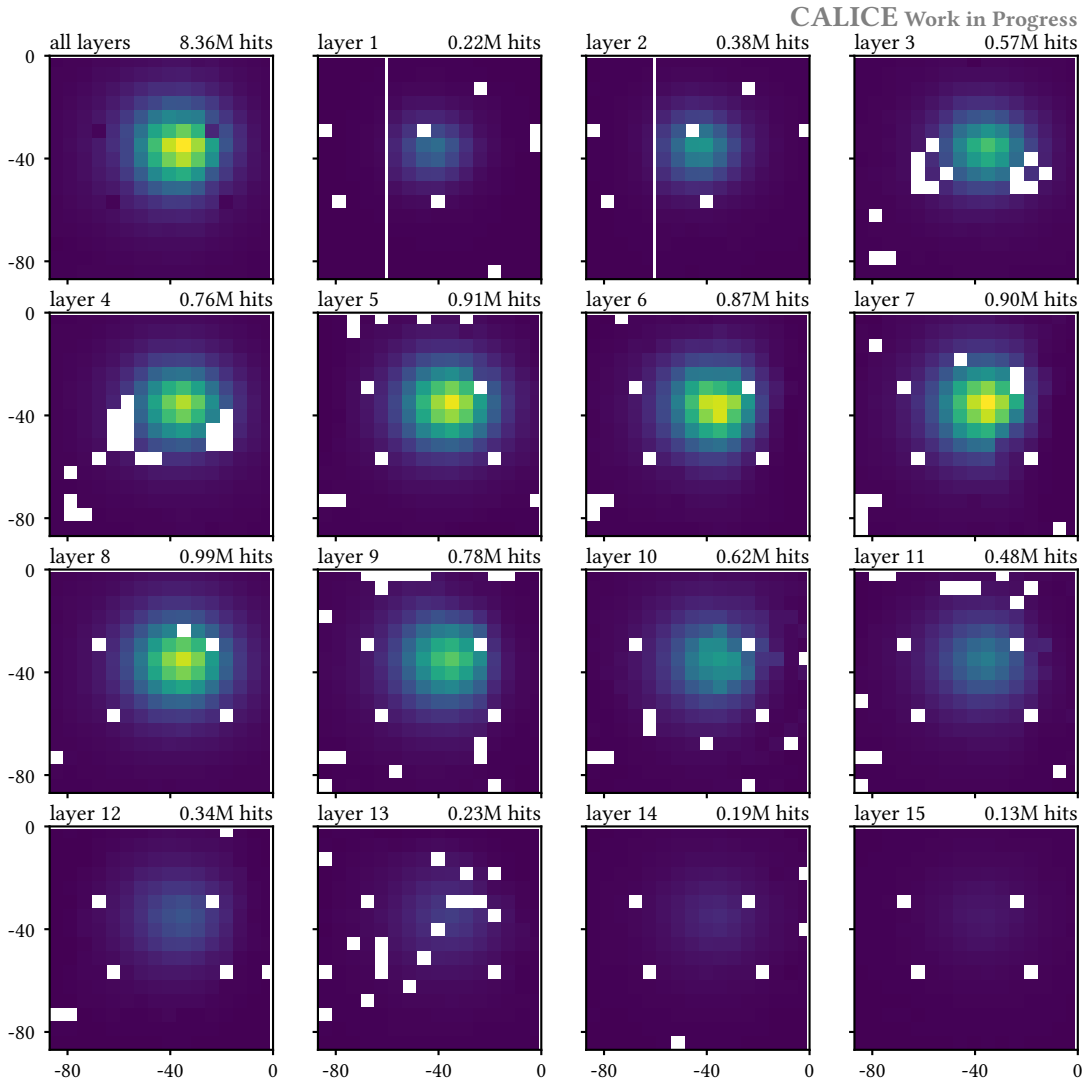

Figure 4.13: Hit maps for run 050282. Only the detector quadrant that includes the beam spot is shown.

The average number of hits in the first layers is larger than expected from the simulation. A position-dependent hit rejection could help to improve the matching between data and simulation, but goes beyond the scope of the initial event reconstruction. Overall, the observed distribution is considerably wider than the simulated distribution.

The shower energy uncertainty based on the events after initial event reconstruction has been presented in Section 4.3.2 and Fig. 4.11. In Fig. 4.15, this is compared to the shower energy uncertainty for simulated events. Without any further processing, the reconstructed uncertainty is 70% worse when using the cell energy sum and 62% worse when estimating the shower energy by counting the number of hit cells. While the simulated energy uncertainty is well described by a Gaussian, the observed uncertainty is impacted by heavier tails. Comparing only the central parts of the distributions, the shower energy uncertainty on data is 49% worse when summing up the cell energies, and 49%

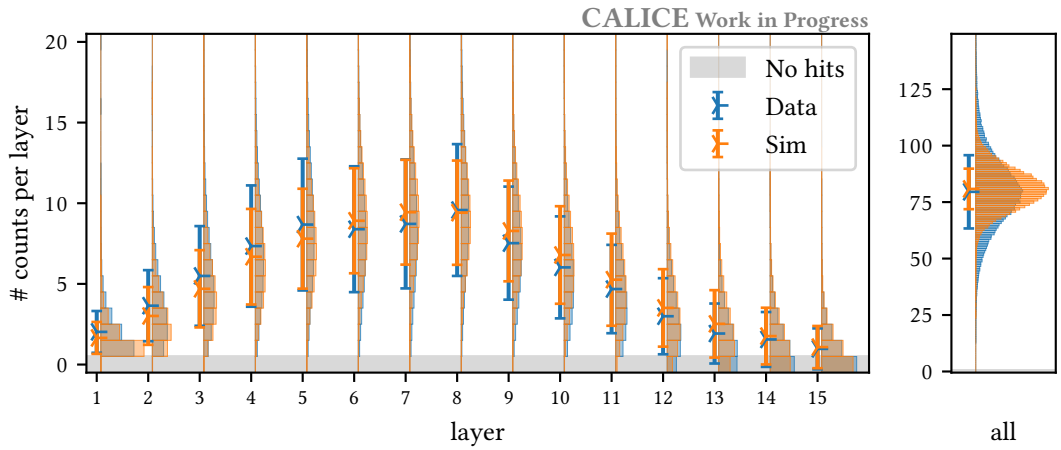

Figure 4.14: Comparison of the number of triggered cells per shower in run 050282 with simulated events for the same Tungsten configuration.

worse when counting the cells.

4.5.1 Quiet acquisition windows

As mentioned in Section 4.3.1, a single power supply has been shared by all slabs during the DESY test beams. Fake hits due to a distortion in the power supply baseline can therefore easily affect many slabs at once. Those fake hits that occur shortly after the real shower event can be misidentified as part of the shower by the initial event reconstruction. An accumulation of fake hits can be reconstructed as a fake shower if they appears after a delay larger than the BCID merging window defined for the initial event reconstruction.

Such effects are largely removed by restricting the analysis to isolated events. A **quiet cycle** in Fig. 4.16 refers to acquisition windows in which the BCID window of the good event is the only time during the acquisition window during which 6 or more layers have been triggered in coincidence. This condition holds for 41% of the good events in run 050282. It should be noted that this condition not only rejects acquisition windows during which noise on multiple layers in coincidence. Additionally, all acquisition windows with multiple real shower events are rejected. For the remaining acquisition windows, the energy uncertainty reaches 13.3%. This uncertainty is close to the shower energy uncertainty obtained from the simulation, in particular when the channel masking is added to the simulated showers. The longitudinal shower profile restricted to showers during quiet acquisition windows is shown in Fig. 4.17.

Acknowledgements The measurements leading to these results have been performed at the Test Beam Facility at DESY Hamburg (Germany) [75], a member of the Helmholtz Association (HGF).

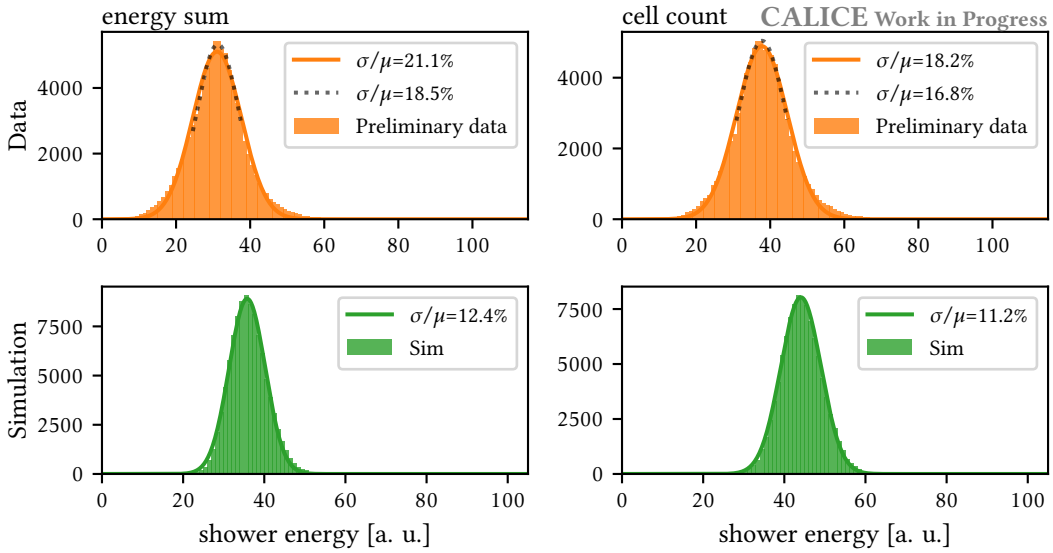

Figure 4.15: Preliminary shower energy uncertainty in data (top row) and from simulation (bottom row). The dotted lines show a Gaussian fit that focuses on the core of the data distribution ($\mu \pm 1\sigma$ region with μ, σ from the fit over the full data range).

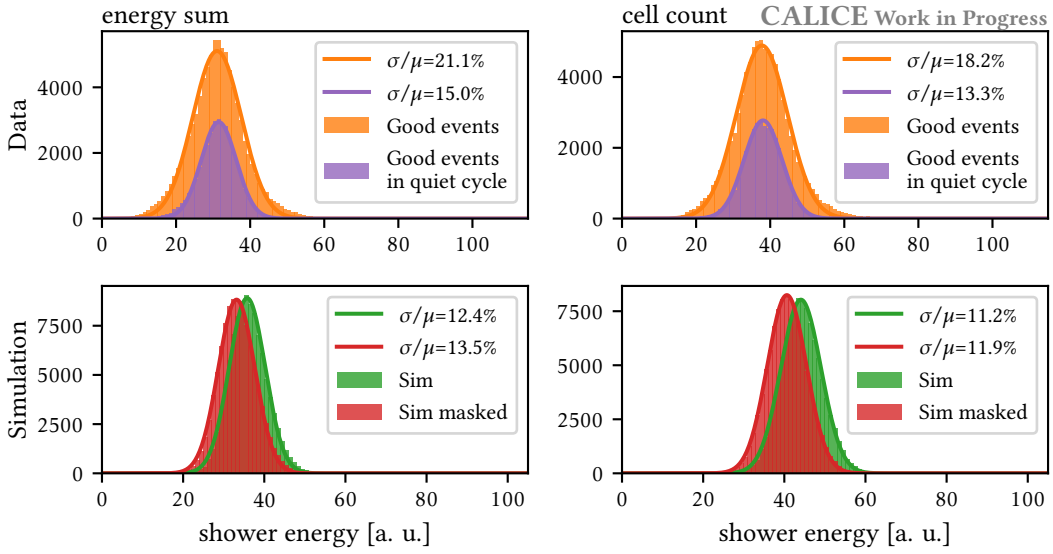

Figure 4.16: Same as Fig. 4.15, with two additions. Data events recorded during quiet acquisition windows are singled out. A masking, roughly equivalent to the masking during the data taking, is applied to the simulation.

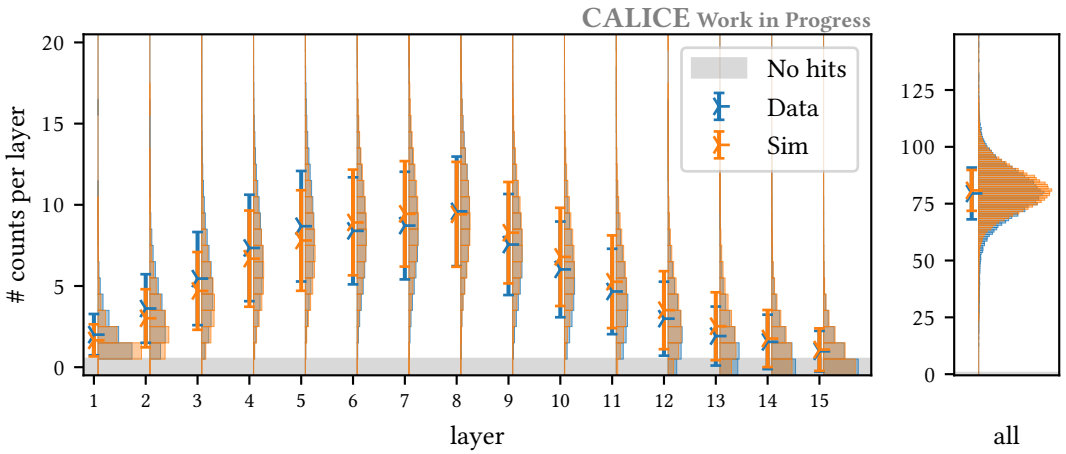

Figure 4.17: Same as Fig. 4.15 but with only those events that were recorded during a quiet acquisition window.

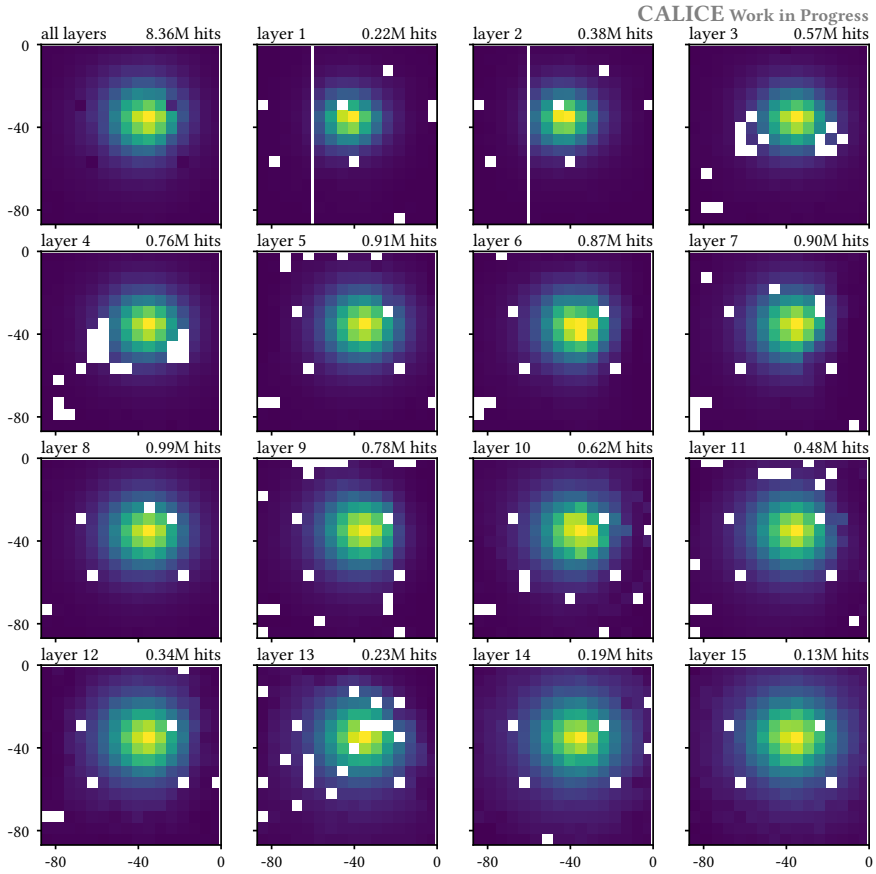

Figure 4.18: Hit maps for run 050282. Only the detector quadrant that includes the beam spot is shown. Here the maximum of the color map is calculated separately for each layer.

5

Higgsstrahlung event selection

Contents

Higgsstrahlung is the main production mode for Higgs bosons at ILC250. By exploiting the kinematics of the Higgsstrahlung process and the high reconstruction efficiency and momentum precision of isolated leptons, a high purity sample of Higgs bosons can be selected without a bias on the Higgs decay mode. The samples that are built here will be used for the inclusive Higgs branching ratio analysis in Chapter 6.

5.1 Z decay kinematics

The relevant tree-level Feynman diagrams for Higgs production at ILC250 are reproduced in Fig. 5.1. The e^+e^-H and $\nu_e\bar{\nu}_eH$ final states receive contributions from Higgsstrahlung ($Z \to e^+e^-$ and $Z \to \nu_e\bar{\nu}_e$), VBF (ZZ-fusion and WW-fusion) and the interference terms of the corresponding processes. Higgs boson production in association with $\mu^+\mu^-$, $\tau^+\tau^-$ or $q\bar{q}$ at the ILC250 needs the Higgsstrahlung process.

In the clean e^+e^- collision environment a Higgs decay independent sample can be selected by taking advantage of the kinematic signature of Higgsstrahlung events. Without ISR and beamstrahlung the incoming particles have four-momenta $(0, 0, \pm 125, 125)$ GeV. The Z boson is identified by its decay products. From the four-momentum difference between the initial state and the reconstructed Z boson the mass of the recoiling system is

$$M^2_{\text{recoil}} = P^2_{\text{recoil}} = \left(\left(\vec{0}, 250\,\text{GeV}\right) - (\vec{p}_Z, E_Z)\right)^2. \tag{5.1}$$

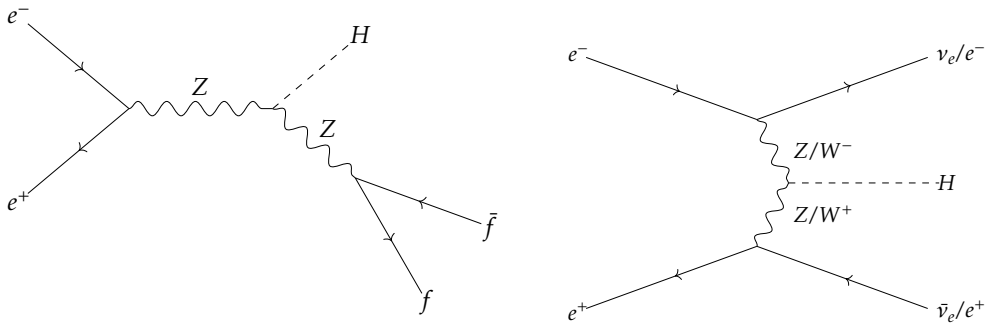

Figure 5.1: Tree-level Feynman diagrams of the Higgsstrahlung process (left) and vector boson fusion (right).

If the event is indeed a Higgsstrahlung event the recoil mass should be close to the Higgs boson mass. The recoil mass distribution has a long tail towards higher masses: ISR and beamstrahlung lead to initial states with non-zero momentum (especially along the beam axis z) and less energy. The identification efficiency and the quality of the energy and momentum reconstruction depend on the Z boson decay type:

- $Z \to \nu\bar{\nu}$: Neutrinos leave no traces in the detector. Thus the recoil mass technique cannot be applied ($BR(Z \to \nu\bar{\nu}) \approx 20.0\%$).
- $Z \to q\bar{q}$: Most ($\approx 69.9\%$) Z bosons decay to hadrons. In Higgsstrahlung events at ILC250 the momenta of both Higgs boson and Z boson are small. Therefore the jets can have large opening angles. Two types of confusion have to be considered. A jet from the Higgs boson decay can be falsely identified as one of the two Z boson jets. The second type of confusion is within-jet confusion. Additional reconstructed particles, from the Higgs decay or from machine backgrounds, can be misidentified as jet components. Conversely reconstructed particles that originate from the Z boson decay might not end up in the reconstructed Z boson jets. For both types of confusion the importance depends on the Higgs decay mode.
- $Z \to \tau^+\tau^-$: Given the large fraction of the energy that is typically carried away by neutrinos from the tau decays, the reconstructed four-momentum vector has a poor precision. The wide range of leptonic, semi-leptonic and hadronic $\tau^+\tau^-$ final states necessitates multiple event selection procedures and the consideration of various background processes. Similar to the Higgsstrahlung events with hadronic Z decays there can be significant confusion between reconstructed particles from the Higgs boson decay and from the Z boson's $\tau^+\tau^-$ pair. In combination with the small branching ratio of approximately 3.4% these obstacles make the $\tau^+\tau^-$ less attractive for model independent Higgs studies.
- $Z \to e^+e^-, \mu^+\mu^-$: The ILD detector has a high reconstruction efficiency and remarkably good momentum resolution for isolated leptons. Even in Higgs boson decays with isolated leptons it is unlikely that isolated leptons from the Higgs and Z boson decays are accidentally swapped, given the ILD momentum resolution for charged particles. The e^+e^- and $\mu^+\mu^-$ decay modes are perfect for the recoil mass technique but have a small branching ratio of only approximately 3.4% each.

Due to their larger sample size the $q\bar{q}H$ and $\nu\bar{\nu}H$ channels can dominate the measurement of some Higgs observables. The analysis that is cited in [34] for the ILC250 precision on the hadronic Higgs branching ratios $H \to b\bar{b}$, $H \to c\bar{c}$, $H \to gg$ combines the measurements from the four channels $q\bar{q}H$,

$\nu\bar{\nu}H$, e^+e^-H and $\mu^+\mu^-H$. For all three branching ratios the uncertainties from the $q\bar{q}H$ and $\nu\bar{\nu}H$ samples are $2-3$ times smaller than the uncertainties obtained from the Higgsstrahlung samples with leptonic Z boson decay [81].

In order to interpret a measurement from a hadronic Higgsstrahlung sample as (effectively) Higgs decay model independent it is necessary to study the importance of the aforementioned confusion. By shifting the Higgs BRs to the limits of their current experimental uncertainties the systematic error from model dependence is explored. Likewise the effect of new Higgs decays, e.g. additional invisible decays, must be studied. If the shift in the result is considerably smaller than the statistical uncertainty, or if this shift is included as a systematic uncertainty, the measurement is model independent (over the range of models that were studied). An example of such a measurement is the inclusive hadronic Higgsstrahlung cross section measurement in [82]. The same study points out the large background contributions in the $M_{q\bar{q}}$ vs. M_{recoil} signal region for $\sqrt{s} = 250\,\text{GeV}$ from $e^+e^- \to ZZ^*$, $e^+e^- \to W^+W^-$ and $e^+e^- \to Z\gamma^*$ close to the kinematic limit ($M_{q\bar{q}} + M_{\text{recoil}} \to \sqrt{s}$). The Higgsstrahlung process at $\sqrt{s} = 350\,\text{GeV}$ produces only 2/3 of the signal events from the same integrated luminosity. The uncertainty on the inclusive hadronic Higgsstrahlung is nonetheless only half as large as close to the Higgsstrahlung cross section peak, because the signal region if further away from the kinematic limit and the separation between signal and background is improved.

The remainder of this chapter focuses on the e^+e^-H and $\mu^+\mu^-H$ Higgsstrahlung samples at ILC250 in order to obtain Higgs samples without a bias on the Higgs decay mode (inclusive) with the highest possible purity.

5.2 Loose selection

Isolated leptons are identified with the `IsolatedLeptonTaggingProcessor` that has been introduced in Section 3.3.4. Only particles with energy above 5 GeV are considered. A candidate event needs to have a pair of opposite-charge isolated electrons (for e^+e^-H) or muons (for $\mu^+\mu^-H$). Photons that are close to an isolated lepton ($\left|\cos\theta_{l^\pm\gamma}\right| \geq 0.99$) are recognized as FSR photons and thus added to the lepton pair four-momentum. In events with multiple candidate pairs from the same family, the pair with pair mass (after FSR recovery) and recoil mass resulting in the smaller χ^2 is selected:

$$\chi^2_H = \begin{cases} \frac{(M_{\text{recoil}} - M_H)^2}{(5\,\text{GeV})^2}, & M_{\text{recoil}} \leq M_H \\ \frac{(M_{\text{recoil}} - M_H)^2}{(25\,\text{GeV})^2}, & M_{\text{recoil}} > M_H \end{cases} \tag{5.2}$$

$$\chi^2 = \frac{\left(M_{l^+l^-(\gamma)} - M_Z\right)^2}{(10\,\text{GeV})^2} + \chi^2_H. \tag{5.3}$$

The conditions for passing **loose selection** are the same for both channels:

1. A pair of opposite-sign isolated electrons/muons.
2. $(M_Z - M_{l^+l^-(\gamma)})^2 \leq (10\,\text{GeV})^2$.
3. $120\,\text{GeV} \leq M_{\text{recoil}} \leq 145\,\text{GeV}$.

The cumulative contributions from the signal process and for each background group over an assortment of variables are displayed as lines in Figs. 5.6, 5.7, 5.16 and 5.17. The selection efficiency tables per process for each pure polarization are collected in Appendix A, Tables A.1 to A.8.

5.2.1 Final state radiation recovery

Due to the energy carried by FSR photons, the reconstructed Z boson mass from only the electron pair can be far too low. The black line in Fig. 5.2 shows the distribution of the reconstructed mass of the primary Z boson in Higgsstrahlung events with the Z boson decaying to an electron pair. Gray bands starting 10 GeV below and above the Z boson mass indicate the mass range of the previously defined loose selection. FSR photons tend to be collinear to the particle that they were radiated off. Especially high energy FSR photons are produced at only a small angle with the lepton. Identifying all photons[1] within a small cone around the electron or positron as FSR and adding them to the electron pair greatly reduces the low-mass tail of the distribution. Contrariwise the high-mass tail is more pronounced due to the contamination with non-FSR photons. As a compromise, $\left|\cos\theta_{l^\pm\gamma}\right| \geq 0.99$ is chosen as the photon recovery angle. Contributions from the Higgs boson decay in this small detector volume are very unlikely and thus the model independence is kept. Before FSR recovery the recoil mass spectrum has a sharply rising edge just below the Higgs mass. Non-FSR contributions and the lower momentum energy and direction precision for photons smear out the sharp edge. Then long tail with large recoil masses is reduced in favor of the region around the Higgs mass. Beamstrahlung and initial state radiation entail that the initial state assumption in Eq. (5.1) is not always exactly satisfied. Due to the high activity in the beam pipe region a similar photon recovery procedure is not feasible there. Even with perfect FSR recovery the recoil mass spectrum for Higgsstrahlung events will therefore have a longer tail with recoil masses above the Higgs mass.

Most of the FSR photon energy is detected in a very small cone around the electron. Photon energy density maps in terms of the angle between photon and electron ($\cos\theta_{\text{full}}$) as well as when only considering the difference in the polar angle ($\cos\theta_{\text{polar}} = \cos(\theta_{e^\pm} - \theta_\gamma)$) are shown in Fig. 5.3. From geometric considerations it is evident that the expected energy density for two random independent particles is uniform in units of $\cos\theta_{\text{full}}$ but not in the chosen two dimensional space. In order to have a meaningful comparison the photon energy density is given in relation to the expected energy density for arbitrary particles.

Indeed the bulk of the FSR photon energy is found in close proximity to the electron.[2] The highest resolution versions of the energy density maps show an energy concentration at the smallest differences in polar angles ($1 - \cos\theta_{\text{polar}} \gg 1 - \cos\theta_{\text{full}}$), indicating a spread in the azimuthal angle. Such small angular distances can be distinguished due to the superb granularity in the ECAL. The magnetic field bends the trajectories of charged particles. Photons are charge-free and are therefore not affected by the magnetic field. But they also do not produce a track and can only be initially detected in the ECAL. The azimuthal angle of a track point changes with the point's distance to the interaction point. The curvature of the track depends on the particle's energy and polar angle. Usually the original azimuthal angle can be precisely determined. When an energetic photon is produced by the interaction of the electron with the detector material in the tracking system, the track curvature is larger afterwards. Whereas the track reconstruction from the two parts with slightly different curvature produces a small bias for the energy and azimuthal angle measurement the polar angle measurement is not impaired. Therefore some photons reconstructed at negligible polar angle distance but with a noticeable azimuthal angle difference to the electron are expected from bremsstrahlung photon production within the tracking system.

[1] In practice it is favorable to consider only photons above some energy threshold, e.g. $E_\gamma \geq 1$ GeV. The cautious approach to the Pandora particle flow cluster merging (Section 3.1) in the ILD reconstruction leads to some spurious photon clusters in electron showers, with low photon cluster energy. Since the electron's energy is measured from its track, the extra energy from false photon clusters gives an upwards bias to the Z boson energy reconstructed by Pandora ($\mathcal{O}(1\,\text{GeV})$ on average).

[2] An additional structure can be spotted in the left-most, full version of the map. The photon energy density rises below $\cos\theta_{\text{full}} \approx -0.35$. This is the kinematically favored region for the angle between the two leptons from the Z boson decay (see e.g. Fig. 5.4). Thus the increase in photon energy density is caused by photons from the Z decay's positron.

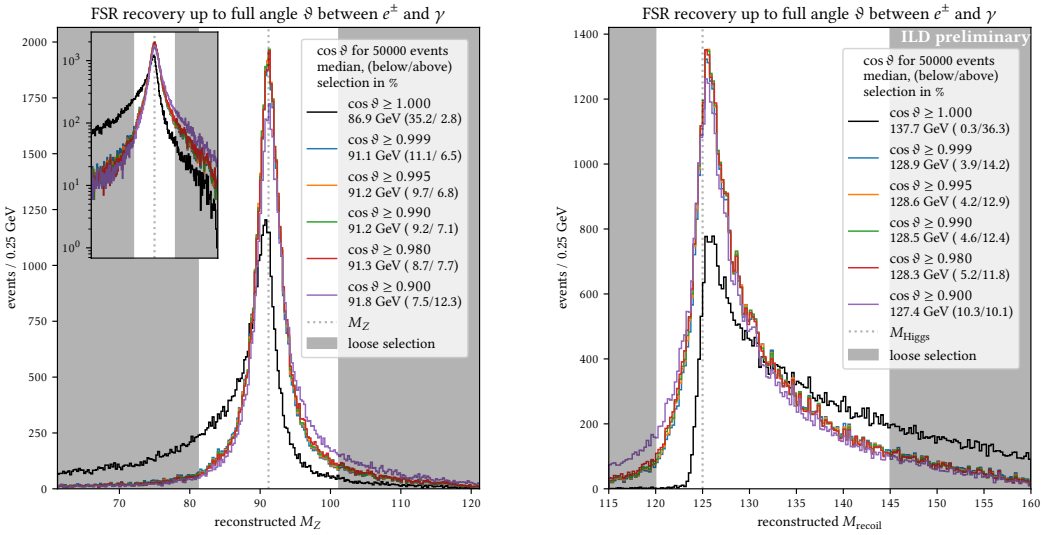

Figure 5.2: (Left) Reconstructed mass of the e^+e^- pair from the decay of the primary Z boson in a Higgsstrahlung event. A photon is identified as FSR if the full angle φ between the photon and the electron or positron is small enough. The inset log scale version emphasizes the tail structure of the distribution. Without FSR photon reconstruction, the black line is obtained.
(Right) Reconstructed recoil mass with the same choices for the maximum photon recovery angle.

Due to the almost 200 times larger muon mass, the muon pair final states are not affected by FSR at a comparable level. Even though it is not necessary for the muon sample, the same photon recovery recombination procedure is applied for both sample.

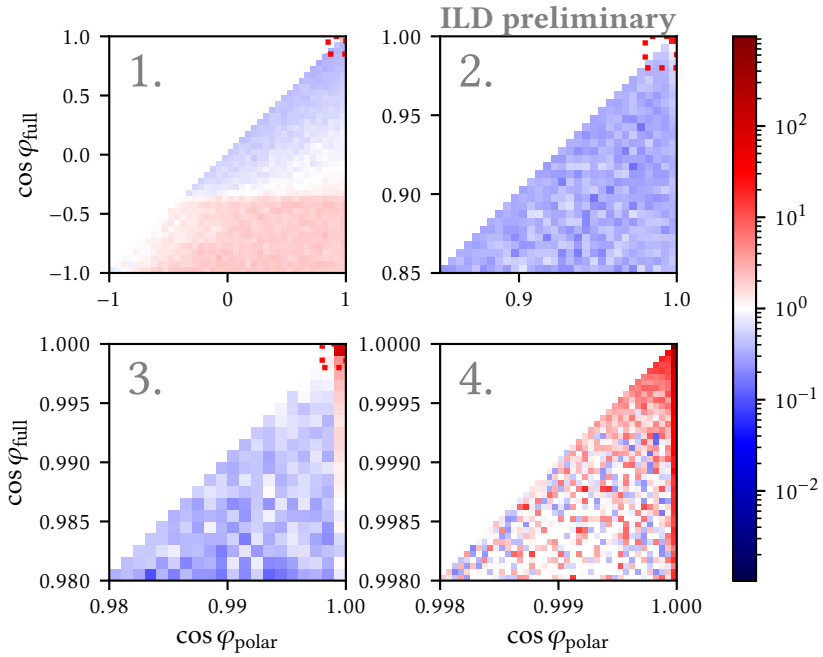

Figure 5.3: Photon energy density maps in terms of the angular distance between the electron from the Z boson decay and any reconstructed photon in Higgsstrahlung events. The energy density is normalized to the expectation for two random independent particles. The maps zoom into smaller regions of full angle (see Fig. 5.2) vs polar angle ($\varphi = \theta_{e^\pm} - \theta_\gamma$) distance between photon and electron.

5.3 Higgs decay mode independent variables

The distributions of variables that are based on only the four-momenta of the pair of isolated leptons are by construction independent of the Higgs boson's decay.[3] The tight selection uses:

- $\cos\theta_{l^+l^-}$: Angle between the lepton and anti-lepton that form the pair.
- $\cos\theta_{l^-}/\cos\theta_{l^+}$: The angle between the (electron) beam axis and the lepton/anti-lepton. These two variables are especially powerful in the e^+e^-H sample. Bhabha events ($e^+e^- \to e^+e^-$, t-channel) where either initial positron or electron have lost a large fraction of their energy to ISR/bremsstrahlung photons can pass the loose selection.
- $\cos\theta_Z$: Angle between the reconstructed Z boson momentum and the (electron) beam axis.
- M_{recoil}: Recoil mass, as defined in Eq. (5.1).
- M_Z: Pair mass from the lepton pair with potential FSR photons.
- p_T^Z: Transverse momentum of the reconstructed Z boson.

[3] There could be a difference for Higgs decays with additional isolated leptons, e.g. $H \to \mu^+\mu^-$ or $H \to ZZ^*, Z \to l^+l^-$. With the χ^2 selection from Eq. (5.3) such an effect is not visible in Fig. 5.4.

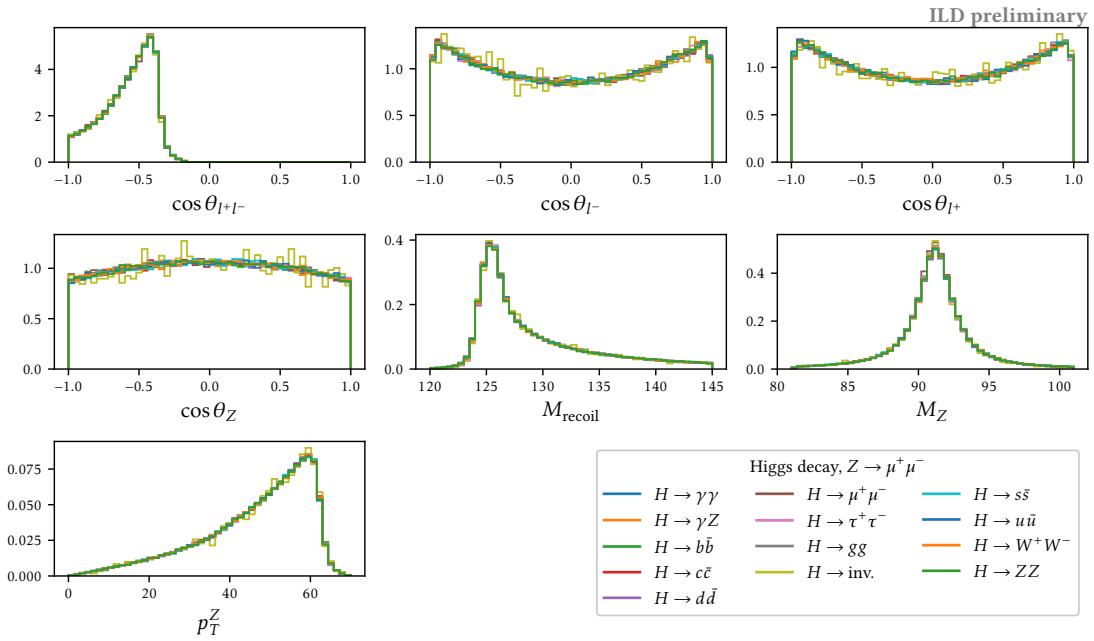

Figure 5.4: Normalized distributions per Higgs boson decay. The distributions are compatible within the statistical uncertainties. The Monte Carlo sample used for $H \to$ invisible is smaller and therefore has larger bin to bin variations.

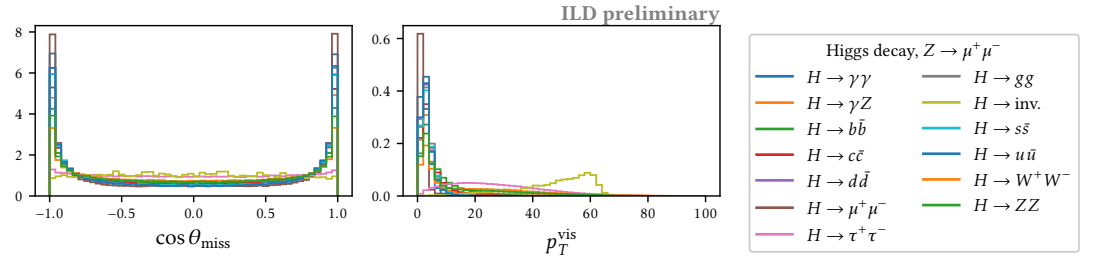

Figure 5.5: Normalized distributions per Higgs boson decay. The distributions of both the missing angle and the visible energy along the transverse direction clearly depend on the type of the Higgs decay.

Figure 5.4 demonstrates that the distributions of the variables that are introduced above are indeed independent of the type of the Higgs decay within the statistical uncertainties from the finite size of the Monte Carlo sample. The stacked distributions per background group are shown in Figs. 5.16 and 5.17 (or alternatively Figs. 5.6 and 5.7).

The background rejection, especially against $e^+e^- \to l^+l^-(\gamma)$ events, could be greatly improved by using the angle of the missing momentum with the beam axis $\cos\theta_{\text{miss}}$ or the visible transverse energy p_T^{vis}. Their normalized distributions per Higgs decay mode are shown in Fig. 5.5.

The smallest average transverse visible momentum is expected for events with both Higgs and Z boson decaying to a muon pair. The muon momenta a precisely reconstructed. Part of the energy

from the e^+e^- annihilation might escape reconstruction in the form of ISR or beamstrahlung photons at angles below the detector coverage. But such photons have necessarily only a small transverse momentum and therefore do not affect the visible transverse momentum much. The observed p_T^{vis} spectrum for $e^+e^- \to ZH \to (\mu^+\mu^-)(\mu^+\mu^-)$ is primarily determined by the expected rates of the machine backgrounds. In Higgs events with decays to taus a large fraction of the event energy is carried by neutrinos and escapes detection. In events with invisible Higgs decays the visible momentum is unbalanced. Only the lepton pair from the Z boson decay and the overlay contributions from the machine background contribute to the visible momentum. The transverse visible momentum regularly reaches $50-60\,\text{GeV}$, in line with the expectation from the distribution of the transverse momentum of the reconstructed Z boson.

In absence of machine backgrounds the angle of the missing momentum would be nearly uniform in $\cos\theta_{\text{miss}}$ and independent of the Higgs decay type. Before radiating the Higgs boson, the off-shell Z boson produced by the annihilation of the initial electron pair has only a small momentum. Therefore Z boson and Higgs boson are produced almost democratically over all angles. For most Higgs decays nearly all the energy can be measured in the detector. Then the missing momentum vector is small. Machine backgrounds are concentrated at small angles to the beam pipe. A single $\gamma\gamma$ interactions that causes hadrons with a combined energy of a few GeV to reach the detector volume can then easily become the dominant contribution to the missing momentum vector. Hence, for Higgs decays without large neutrino contributions, small angles of the missing angle with the beam pipe are favored, $|\cos\theta_{\text{miss}}| \to 1$. On the contrary events with a Higgs decaying to a tau pair, and more so events with invisible Higgs decays, have a large missing momentum that is a lot less biased by the machine backgrounds.

The inclusive Higgsstrahlung cross section measurement study presented in [83] uses amongst others a cut on the visible energy ($E_{\text{vis}} > 10\,\text{GeV}$). They argue that model independence is sustained by performing a separate analysis for the Higgsstrahlung cross section with invisible Higgs decays, and by showing that the selection efficiency depends only marginally on the SM Higgs decay mode.

The event selection procedures that are presented below use exclusively the model independent variables from Fig. 5.4. This limits the achievable sample purity. For the measurement of the Higgs branching ratios, the samples will subsequently be divided into regions with varying support for the different Higgs final states. At that point it will be possible to isolate the remaining backgrounds for whose rejection the information from the lepton pair's four momenta was not sufficient.

5.4 Baseline cuts

A simple set of cuts for each of the two sample types is proposed in Table 5.1. They provide the performance baseline over which a more complicated selection procedure must improve. The stacked distributions before and after the baseline cuts for the signal process and per background group are shown in Figs. 5.6 and 5.7. The cut on the angle of the lepton to the beam axis is only powerful for the e^+e^-H sample where it can diminish the t-channel Bhabha process. It was demonstrated above that a selection involving the angle of the missing momentum would not be Higgs decay mode independent.

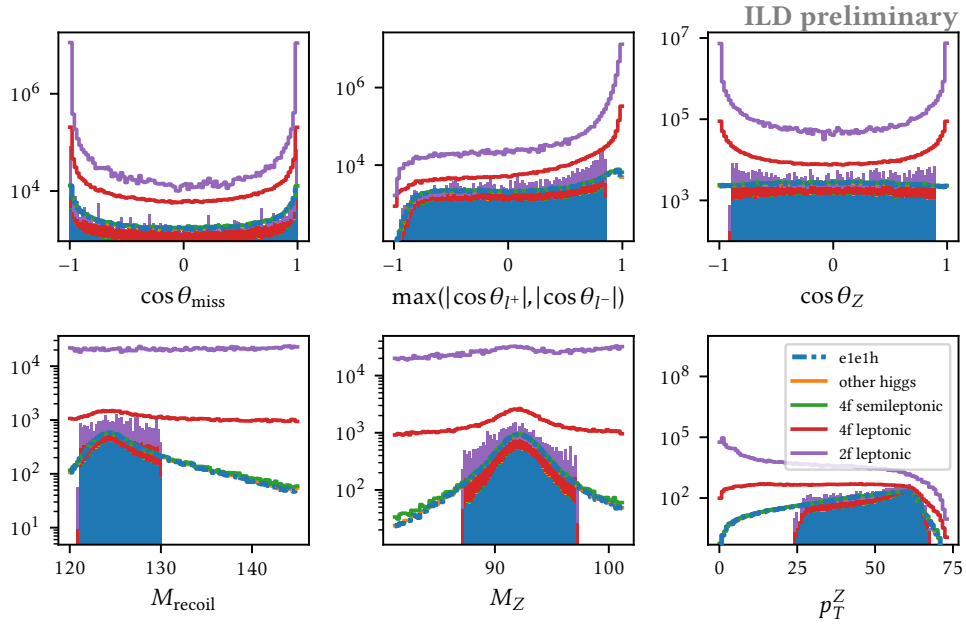

Figure 5.6: Stacked distributions for e^+e^-H signal and background groups. The lines are based on all events passing the loose selection. Only those events that pass the cuts in Table 5.1 are used for the bars.

	$\mathbf{e^+e^-H}$	$\mu^+\mu^-\mathbf{H}$
$\max(-\cos\theta_{l^+},\cos\theta_{l^-})$	≤ 0.85	-
$\lvert\cos\theta_Z\rvert$	≤ 0.9	≤ 0.9
M_{recoil}	$\in [121\,\text{GeV}, 130\,\text{GeV}]$	$\in [123\,\text{GeV}, 130\,\text{GeV}]$
M_Z	$\in [87.19\,\text{GeV}, 97.19\,\text{GeV}]$	$\in [87.19\,\text{GeV}, 95.19\,\text{GeV}]$

Table 5.1: Baseline cuts for a Higgs decay mode independent selection in the e^+e^-H and $\mu^+\mu^-H$ samples.

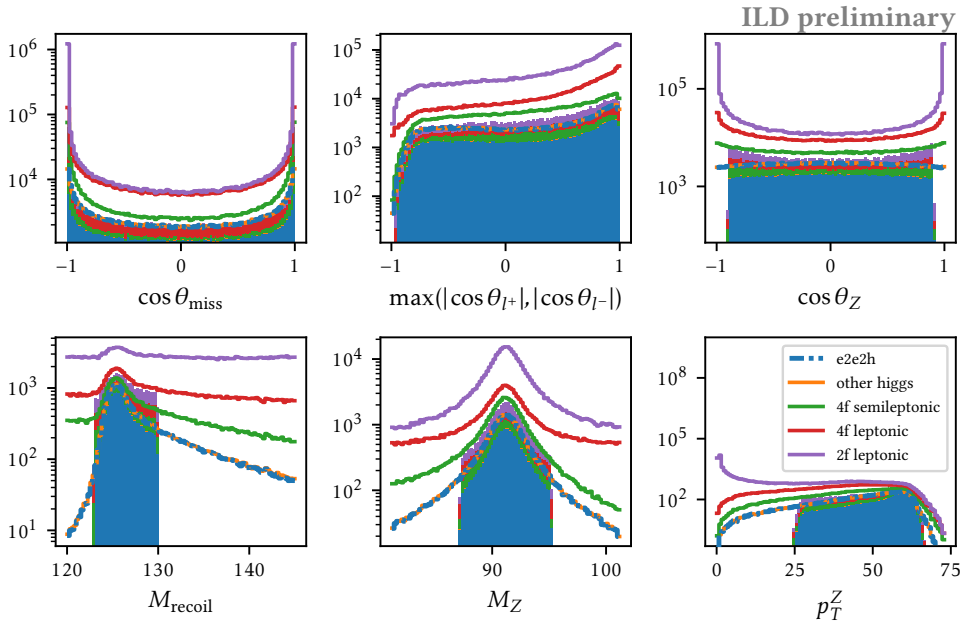

Figure 5.7: Stacked distributions for $\mu^+\mu^- H$ signal and background groups. The lines are based on all events passing the loose selection. Only those events that pass the cuts in Table 5.1 are used for the bars.

5.5 Explainable boosting machine

A set of selection cuts is an example of a **glassbox model**: A model with a transparent scoring mechanism that can be understood from the outside. For a given collection of input values it is clear how the model arrives at its prediction. It is then also possible to specify some value changes that would change the prediction.

For example an event where the Z boson is reconstructed with a small angle to the beam axis will not pass the selection because of the high background concentration in that region. The same event, rotated by a few degrees in the polar angle, might pass the selection. In general the required rotation can only be worked out by passing some artificial, rotated events to the model and tracking the change in scoring. A glassbox model can be interpreted without additional data. Given the transparent scoring, the resulting changes from arbitrary rotations are readily available.

A blackbox model on the other hand does not offer an explanation for its decision. The decision process can be arbitrarily complex and thus can potentially incorporate more information. Random forests (RF) and boosted decision tree (BDT) are standard, high-performance machine learning methods for tabular data. Random forests combine a large number of decision trees that are trained independently on different subsets of instances and features. In a boosting procedure the estimators are not independent but are being built sequentially. A new estimator is now tasked with predicting the residual, the difference between the target and the prediction of the ensemble of previous estimators.

The explainable boosting machine (EBM) algorithm creates glassbox models that are typically as performant as RFs and BDTs [84]. Results presented here are based on version `0.2.7` of the InterpretML python package.

In its main step, the EBM uses a generalized additive model (GAM),

$$g(E[y]) = \beta_0 + \sum_i f_i(x_i). \tag{5.4}$$

For a classification task Eq. (5.4) gives the log-odds, the logarithm of the odds $p/(1-p)$ where $p = E[y]$ is the probability of belonging to the class. In agreement with logistic regression the class probability is obtained from the inverse of the link function $g(z)$,

$$g^{-1}(z) = 1/(1+e^{-z}). \tag{5.5}$$

The function is drawn in Fig. 5.8 together with box plots for signal and background data for each of the samples.

The intercept β_0 and the lookup feature functions f_i of the EBMs that have been trained for the e^+e^-H and $\mu^+\mu^-H$ samples are illustrated in Figs. 5.9 and 5.10, respectively. Under the hood BDTs trained sequentially on one feature at a time are used to build the lookup functions. The training is performed in a way that promotes the fair sharing of the feature score in the case of co-linearity between features. As all information that is necessary for the model evaluation can be read out from the step-wise constant feature functions the model that was used to train the feature functions can be deleted.

The sharing of an additive constant between the features is arbitrary. All feature functions are shifted such that their weighted mean score on the training sample is zero. The resulting additive term is the intercept β_0.

For every final model 8 independent EBMs are trained on their own random 85% sub-samples of the training data. This procedure increase the model's robustness. The final model uses the average score. Gray bands depict the standard deviation of the model scores from the 8 individual models.

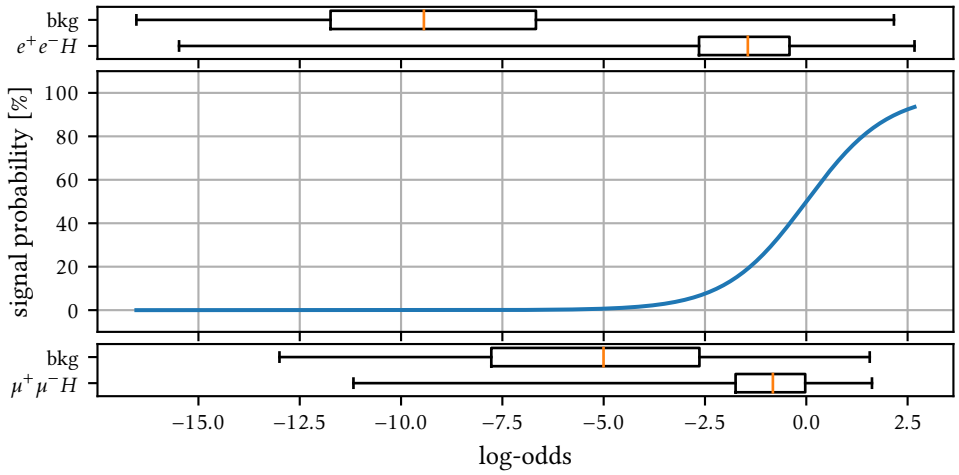

Figure 5.8: The logistic function over the log-odds range that is realized in data. The box plots indicate the minimum, first quartile, median, third quartile and maximum (0th, 25th, 50th, 75th, 100th percentiles) for signal and background separately in both Higgsstrahlung samples after the loose selection step.

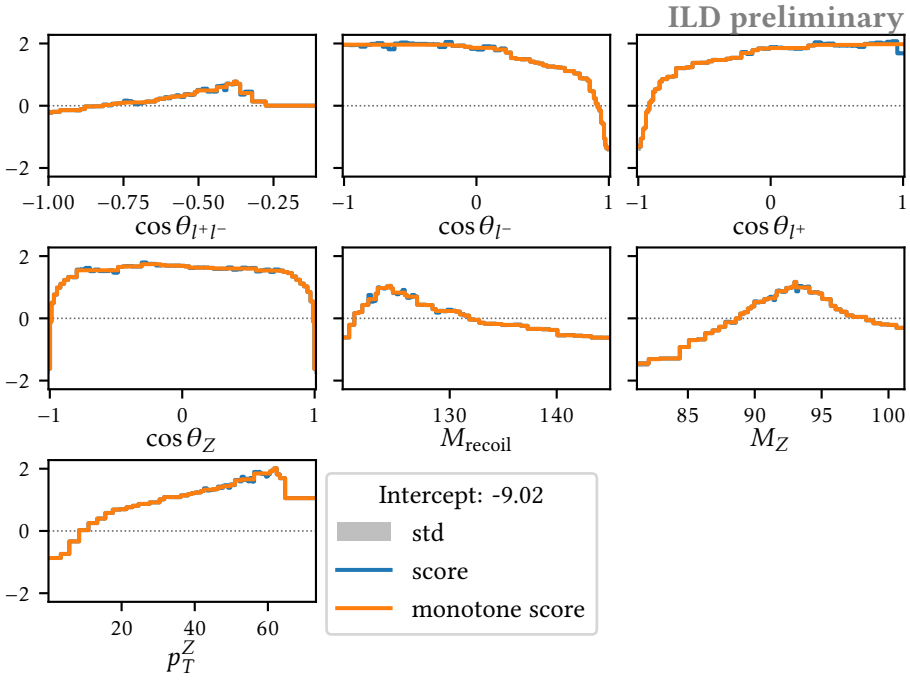

Figure 5.9: Lookup functions of the scores per feature for the e^+e^-H EBM model.

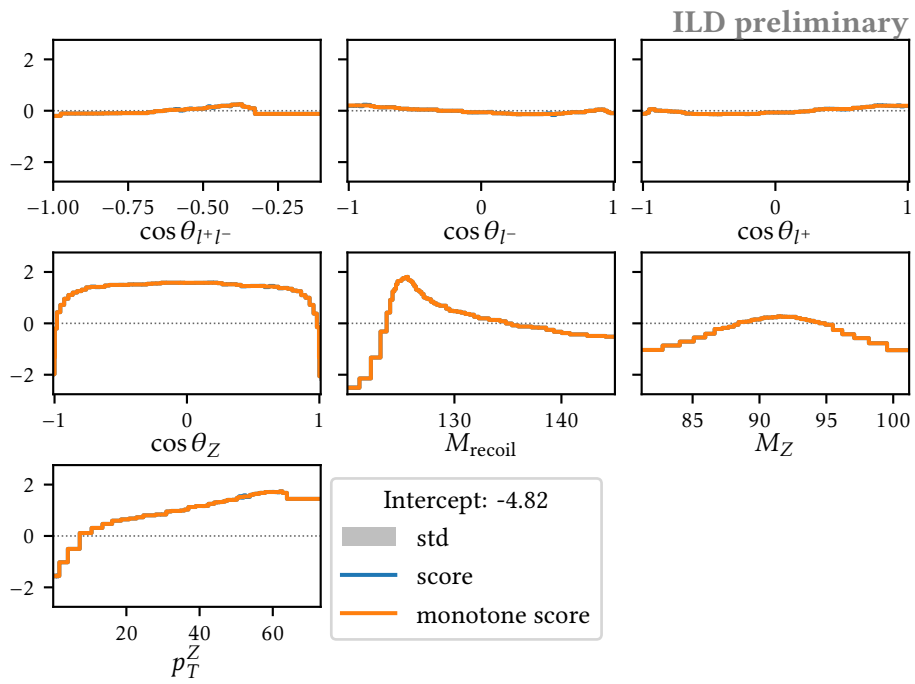

Figure 5.10: Lookup functions of the scores per feature for the $\mu^+\mu^- H$ EBM model.

Local monotonicity is enforced on the feature score functions in a post-processing step. This is an example for using domain knowledge for the sake of simplifying the model and its interpretability. Some local optima for the scoring function are expected. For instance the most probably recoil mass for a Higgsstrahlung event should be the Higgs mass while events with considerably higher or lower masses are more likely to be background events. Spikes in the feature score at other masses are not expected. If they occur it is likely that they are just the result of overtraining. It is an advantage of the chosen model class that such an effect can be spotted and fixed. A blackbox model can suffer from similar overtraining effects in a feature region without them ever being caught.

Figure 5.11 shows the interaction scores, the signal purity, the background density and the signal density for one pairwise interaction. The Higgsstrahlung signal is concentrated at pair masses close to the Z boson masses and recoil masses close to the Higgs mass. The background density has no preferred recoil mass region. The t-channel Bhabha process is the most important background in the e^+e^-H sample after the loose selection step. Its electron and positron do not actually originate from the decay of a Z boson and therefore the pair mass is not concentrated around the Z boson mass.

The general trend is described by the feature functions f_{M_Z}, $f_{M_{\text{recoil}}}$. But when treating the two features in isolation, the purity for both masses being below their most probable signal value is overestimated. From the definition of the recoil mass in equation Eq. (5.1) it is evident that the signal distribution of the two masses are not independent. If the reconstructed pair mass in a Higgsstrahlung event is too small, e.g. due to FSR photon energy that was not recovered, it is more likely that the recoil mass is high.

The most important pairwise interactions can be automatically detected and incorporated into the

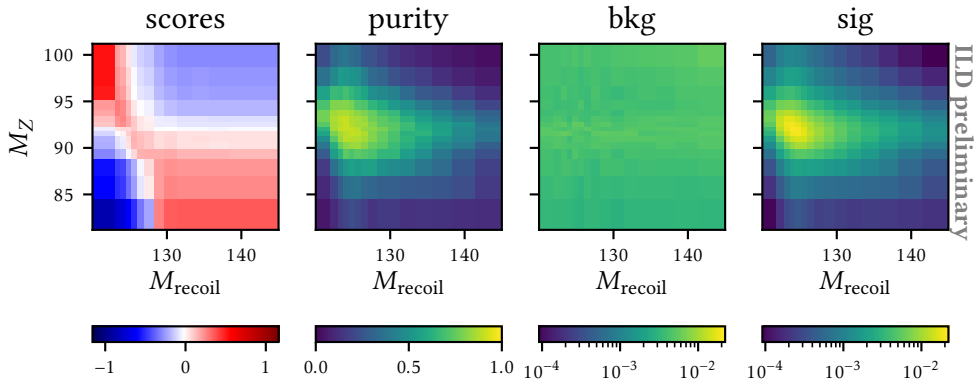

Figure 5.11: Interaction scores for pair mass M_Z and recoil mass M_{recoil}. This is one of the interactions that are considered for the e^+e^-H EBM. All interaction scores are shown in Appendix B.

model [85]:

$$g(E[y]) = \beta_0 + \sum_i f_i(x_i) + \sum_{i,j} f_{i,j}(f_i, x_j). \tag{5.6}$$

The inclusion of many interaction terms increases the model complexity. Then the model is less easily interpreted and over-fitting to the training data becomes more likely.

A model trained on simulated data should only exploit actual characteristics of background and data, in contrast to spurious features that might depend on the simulation. With the chosen class of models this can be ensured visually by checking the feature scores and the interaction scores. It should be appreciated that the model behavior is exactly defined by these scores. No higher-order correlations are learned.

5.6 Tight selection

5.6.1 Threshold choice

The number of sample events above the class probability threshold t are shown in Fig. 5.12. Only few simulated events remain above high thresholds, producing artificial variations in the purity curve in this region.

If the background rate b is well-established, from Monte Carlo simulations or side-bands of the signal region, the uncertainty on the signal rate s is smallest at the maximum of $s/\sqrt{s+b}$ (e.g. statistics review in [24]). Here s (b) is the signal (background) rate after the selection. It is equivalent to take the maximum of the product of efficiency and purity, ϵp.

But it is not the Higgsstrahlung production cross section that is to be measured after the selection step. Instead the partition within the sample will be used to infer the Higgs decay rates. Therefore it is not obvious that ϵp is the right quantity to be optimized for when choosing the selection threshold. Furthermore, the optimal thresholds for the smallest branching ratio uncertainty will depend on the individual Higgs decay mode and its dilution by the remaining background events. Finally, the best threshold value depends on the relative importance that is given to the individual branching ratio measurements.

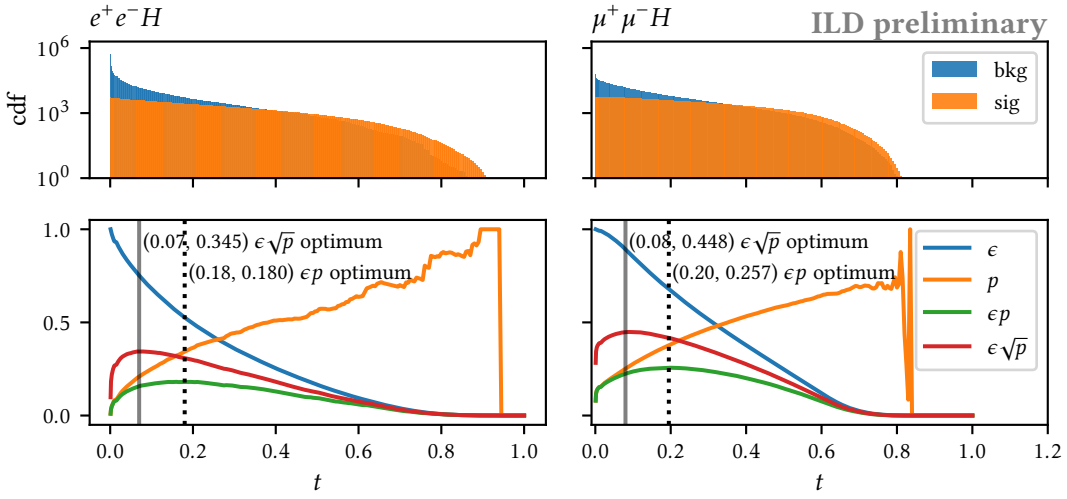

Figure 5.12: (Top) Cumulative distribution functions of the number of signal and background events above a class probability threshold for both samples.
(Bottom) Efficiency ϵ and purity p for a tight selection at threshold t. The curves and the maxima for ϵp and $\epsilon\sqrt{p}$ are also shown.

Having additional analysis steps after the tight selection motivates placing a higher weight on the efficiency than on the purity, resulting in lower thresholds. In what follows the selection threshold that optimizes $\epsilon\sqrt{p}$ is chosen. Several threshold choices are compared in Section 6.7.5.

The performance of the EBM models is compared to the baseline cuts in Fig. 5.13. Indeed both EBM models are better than their respective baseline cut. In comparison to the cuts, the EBM models at the chosen thresholds put more emphasis on reaching a high signal efficiency. The area under the curve (AUC) from background efficiency and signal efficiency at various thresholds is a performance metric that is independent of the final choice of the threshold. More background events are expected in the e^+e^-H sample. But a larger share of them is easily distinguished from the Higgsstrahlung signal. Hence for the same signal efficiency the background efficiency is typically smaller for the e^+e^-H sample while the $\mu^+\mu^-H$ sample has the higher purity. Even though the purity in each of the full Higgsstrahlung samples is only about 25%, the categories that will be built for the different Higgs decay modes within the full samples can have substantially higher purities. A comparison with the AUC curves of XGBoost [86] models trained on the same data sets is presented in Appendix C. This study confirms that the EBM models can indeed achieve a comparable performance to state-of-the-art blackbox models.

5.6.2 Model fine tuning

In machine learning, hyperparameters are those parameters that must be set to steer the learning process of the algorithm. This is in contrast to parameters. Parameters are learned during the training from the training data. For the EBM model, the edges and the values of the feature score step functions are parameters. Additionally the pairwise interactions and the corresponding scores are learned.

To demonstrate that the chosen hyperparameters are appropriate for the data set, alternative models have been trained. In each alternative model, one of the 7 hyperparameters that are relevant for the EBM algorithm has been altered. The performance is evaluated with the AUC metric. The

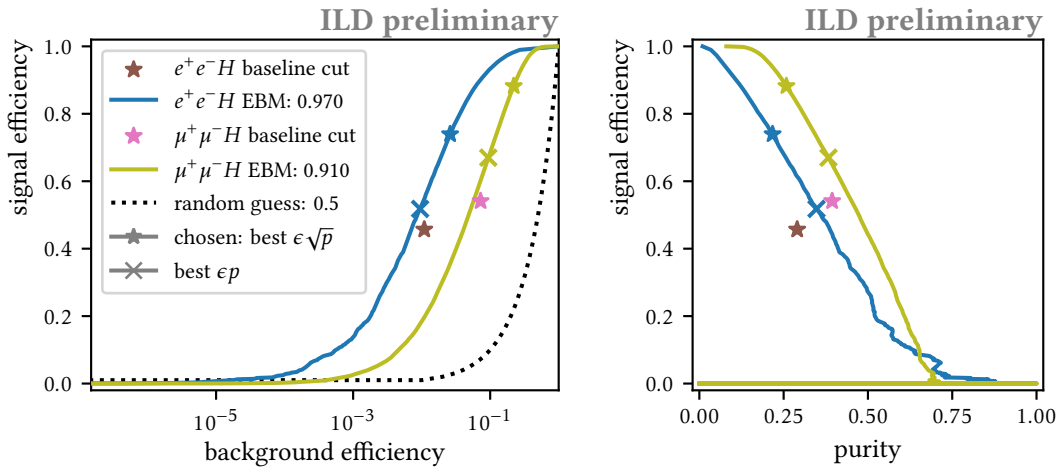

Figure 5.13: Performance curves for the tight selection step.
(Left) The receiver operating characteristic (ROC) curve displays the signal and background efficiencies at various thresholds for the EBM models. Markers indicate the maximum of the product of efficiency and purity, the chosen threshold and the performance of the baseline cut. The performance for a random guess model is added as a visual aid. The trailing number is the area under the ROC curve (AUC).
(Right) Signal efficiency and purity at various thresholds, for the same models.

hyperparameter search for the e^+e^-H sample is illustrated in Fig. 5.14. A gray cross indicates the AUC performance with the chosen set of hyperparameter values and the chosen hyperparameter value.

The extend to which an evaluation during the training is allowed to alter the model is set by the `learning_rate`. If the learning rate is too high the change in the model can go beyond the optimum. A low learning rate leads to smaller model changes per evaluation step. Consequentially the training time will be longer. It is also more likely for the algorithm to get stuck in a local optimum.

The number of EBM model parameters, and thus the model complexity, is directly related to the number of steps per feature score function (`max_bins`) and the number of and binning for the pairwise interactions (`n_interactions`, `max_interaction_bins`). Without a sufficient number of bins the model will fail to describe all important features of the data (under-fitting). Therefore the model performance is expected to improve when more bins are used. Upon increasing the number of bins, the number of training samples per bin decreases. Then it is more likely that the model learns effects that are not present in the underlying true data distribution, but only arise due to statistical fluctuations (over-fitting). A notably better performance on the training data than on a statistically independent validation data set can be a sign of over-fitting.

The AUC performance receives a substantial improvement from considering pairwise interactions. It suffices to consider the 10–12 most important pairwise interactions. The EBM algorithm automatically chooses them out of the $7 \cdot 6 = 42$ candidates. One way of defining the feature importance is to take the absolute score of a feature, or a pairwise interaction, averaged by the expected event counts per bin. This metric is shown in Fig. 5.15.

The recoil mass peak is muon pair sample is reconstructed more cleanly, resulting in this feature being more important for the muon pair sample. A decidedly larger fraction of the background muon pairs stem from a real Z boson. The angle between the lepton and the beam axis is for the most part

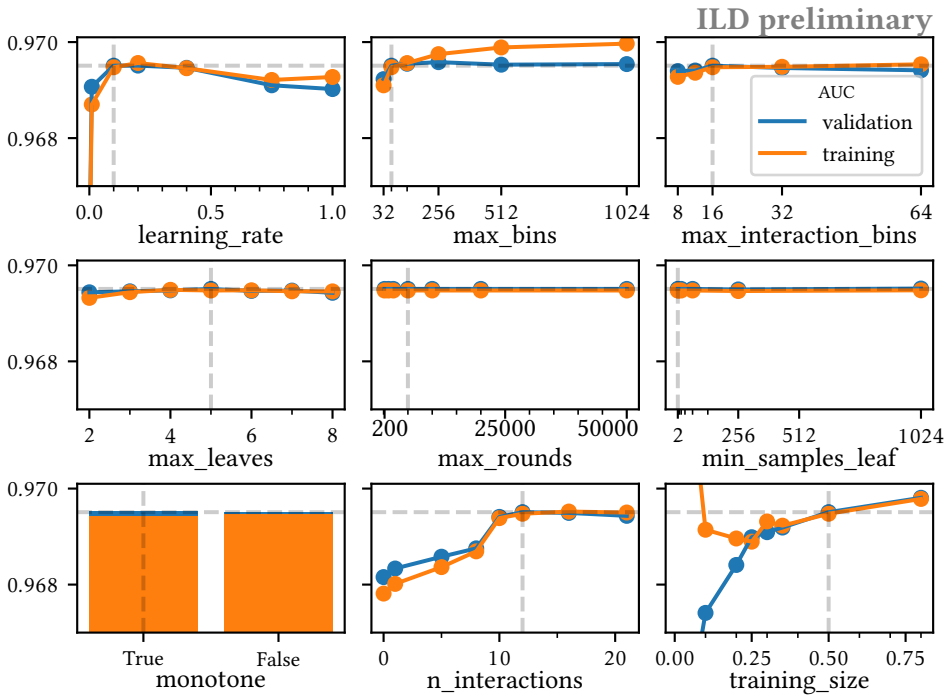

Figure 5.14: EBM model performance for different choices of the model hyperparameters. The gray lines indicate the chosen parameter value and the achieved AUC on the e^+e^-H validation data set.

used to isolate the t-channel Bhabha events. For the $\mu^+\mu^-H$ sample, where the two fermion final state can only arise from s-channel annihilation, the $\cos\theta_{l^\pm}$ features are the least important features. Consequently the four pairwise interactions that are included in the e^+e^-H EBM but not in the $\mu^+\mu^-H$ EBM involve $\cos\theta_{l^+}$ or $\cos\theta_{l^-}$.

In both samples the pairwise interaction between pair mass and recoil mass is the most important one. The e^+e^-H sample variant of this interaction has been described above in Fig. 5.15. The full set of feature interaction scores is collected in Appendix B.

Higher order interactions would be conceptually possible, but are normally not advantageous. The number of interaction groupings that would have to be considered quickly rises to an unmanageable, or at least non-interpretable, extend. For each high-order interaction the curse of dimensionality means that an enormous training sample is necessary to properly populate the whole feature space. If the training sample is not big enough, the number of bins has to be reduced. Then local interaction effects are hidden within the large bin volume.

The behavior that is learned by the Higgsstrahlung EBM models is simple enough that it does not benefit from additional evaluation rounds on the training data set (`max_rounds`). Changing the depth (`max_leaves`) or the minimum occupancy per leaf (`min_samples_leaf`) of the decision trees that are used during model training has but a mild effect on the model performance over a reasonable parameter range.

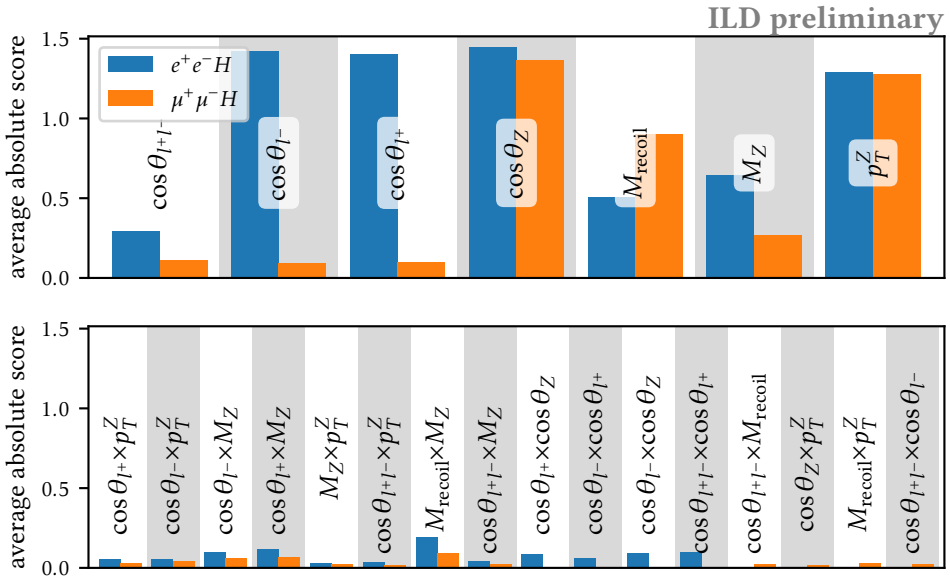

Figure 5.15: Feature importance, measured as the absolute value of the feature's score function averaged by the expected event counts. The pairwise interactions (bottom row) that are included can be different for each sample.

Enforcing the monotonicity constraints in a post-processing step, in the way that has been discussed in Section 5.5, actually improves the AUC score. This is especially true for the performance on the validation data set. It seems plausible to assume that the monotonicity simplification indeed succeeded to correct sizeable effects due to statistical fluctuations in the training sample.[4]

Another parameter that is evaluated here, even though it is not technically an EBM hyperparameter, is the fraction of the sample that is allocated for model training (`training_size`). For a much smaller training sample the chosen hyperparameters would result in noticeable over-fitting to statistical fluctuations. With a larger training set a slightly better classifier could have been built. Allocating more than half the simulated data set as the training sample is disadvantageous for the final measurement. The other half of the data, here only used for model validation, is later on used as the source of truth for the number of events per Higgs decay category. A fair sharing of the available sample between the intended purposes results in the smallest systematic uncertainties due to limited Monte Carlo statistics.

5.6.3 The Higgstrahlung samples

The Higgsstrahlung samples before and after the tight selection are presented in figures 5.16 (e^+e^-H) and 5.17 ($\mu^+\mu^-H$). In contrast to the baseline cuts defined in Section 5.4 the tight selections based on the EBM score do not necessarily exclude any value ranges of the Higgs decay mode independent variables defined in Section 5.3. Even very low feature scores from one feature, e.g. $|\cos\theta_Z| > 0.95$, can

[4] Some processes in the Monte Carlo sample have a large event weight, see Appendix A. If deemed necessary, a small Monte Carlo production focussing on the phase space region that passes the loose selection could help to obtain smoother feature functions, or would allow to increase the EBM complexity. Here the smoothening effect from the monotonicity introduction in a post-processing step is considered sufficient.

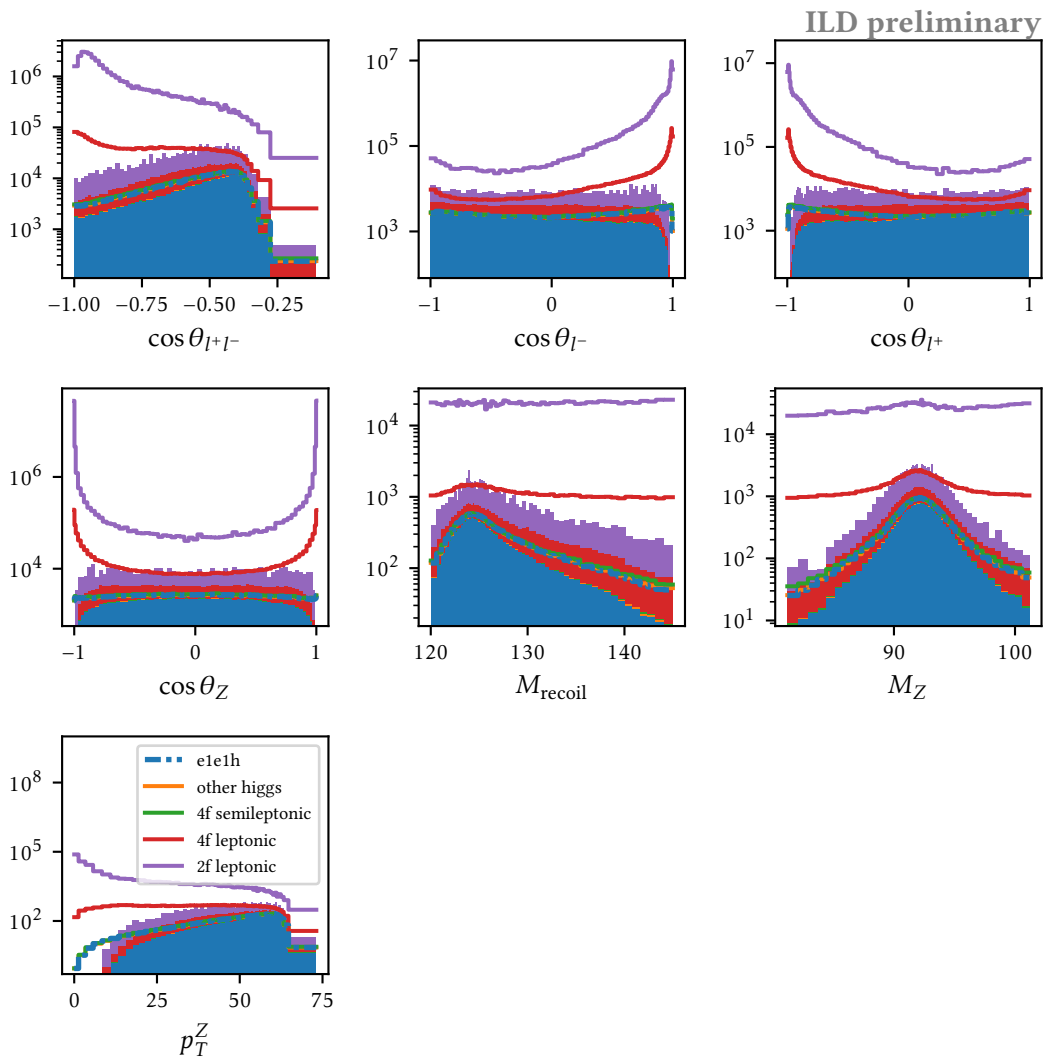

Figure 5.16: Stacked distributions for e^+e^-H signal and background groups. The lines are based on all events passing the loose selection. Only those events that pass the sample's tight selection are used for the bars. Consistent with Fig. 5.9 the binning is chosen so that a similar number of counts is expected in every bin.

be compensated by the other features.

Figure 5.18 summarizes the signal selection procedure for the Higgsstrahlung samples. The selection efficiencies in the muon pair sample are almost independent of the polarizations of the electron and positron beam. In almost 7% of the events the reconstruction of one of the isolated muons was not successful:

- The muon has not been reconstructed *or*
- The particle identification failed *or*

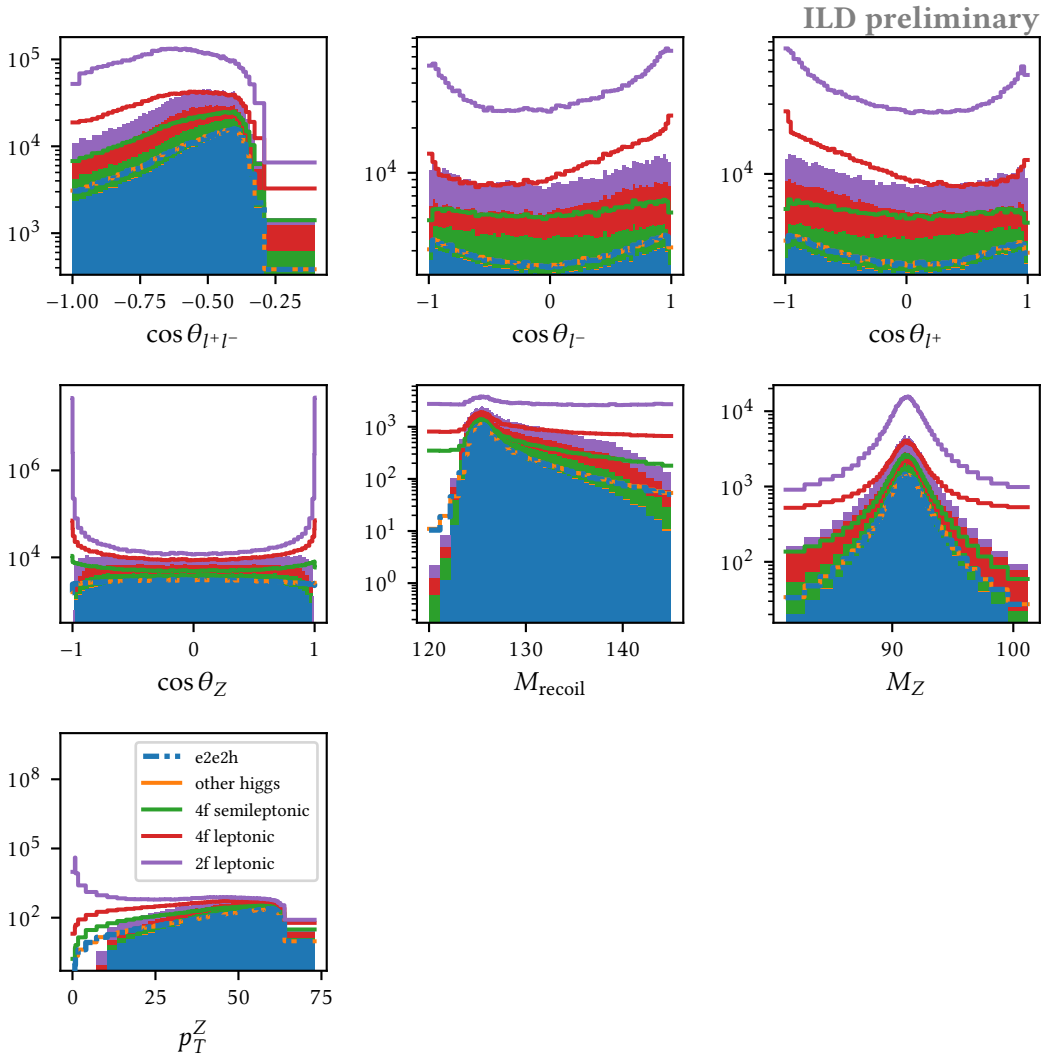

Figure 5.17: Stacked distributions for $\mu^+\mu^- H$ signal and background groups. The lines are based on all events passing the loose selection. Only those events that pass the sample's tight selection are used for the bars. Consistent with Fig. 5.10 the binning is chosen so that a similar number of counts is expected in every bin.

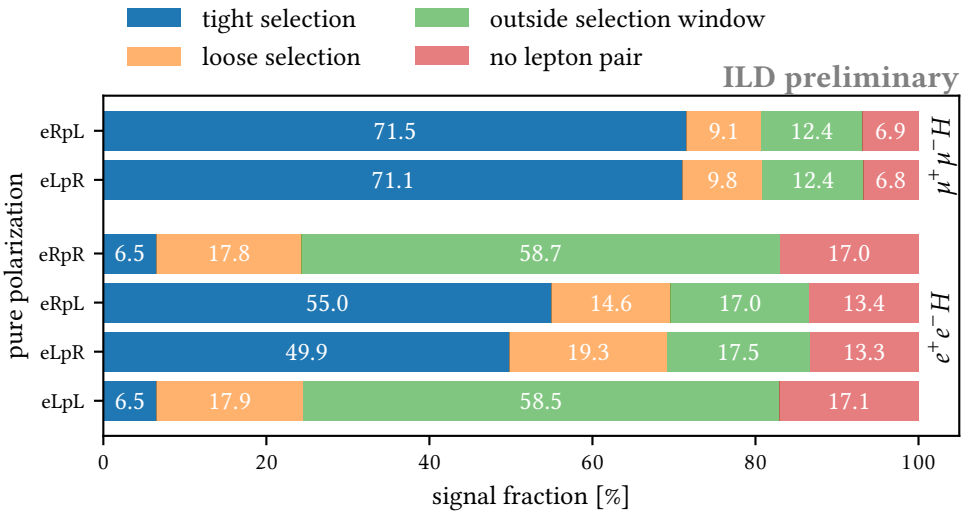

Figure 5.18: Higgsstrahlung signal selection summary.

- The isolation criterion was not satisfied *or*
- The wrong charge has been assigned to the muon.

About 80% of the signal events pass the loose cut defined in Section 5.2 that is based on the pair mass and recoil mass only. For the chosen threshold more than 71% of the signal events remain after the final selection step. Including the background events that pass the selection, Higgs events account for roughly 1/4 of the events in the muon pair Higgsstrahlung sample, assuming the Higgs production rates that are predicted by the SM.

The electron pair sample has four noteworthy impairments compared to the muon pair sample:

1. The identification of isolated electrons is harder than for isolated muons ($\sim 7\% \rightarrow 13\%$ probability for not finding the lepton pair).
2. The momentum resolution for the electrons is worse. Not all FSR photons can be recovered. Even if an FSR photon is correctly identified the photon energy resolution is much worse than the momentum resolution from the track of a charged particle.
3. In addition to Higgs production from Higgsstrahlung, Higgs production from WW-fusion is also relevant. This fusion process is the only relevant contribution for initial states with the equal polarization. Due to the chirality dependence of the weak interaction the fusion process contributes more to the eLpR cross section than to the eRpL cross section. The selection is optimized with the Higgsstrahlung kinematics in mind. Therefore it is expected that the Higgs selection efficiency is lowered by the presence of another Higgs production mode.
4. There are more relevant background contributions. An important source are the t-channel Bhabha contributions ($e^+e^- \rightarrow e^+e^-$).

6

Higgs branching ratios

Contents

A method for the direct measurement of the Higgs boson branching ratios is presented in this Chapter. The standard way to determine a BR is through the signal yield of an analysis focusing on the corresponding decay channel. In the simplest setup, the signal yield S of an analysis depends on the product of the cross section of the targeted Higgs production mode, σ_{HP}, and the branching ratio $\mathcal{B}(H \to X)$:

$$S^{HP,H\to X} = N^{HP,H\to X} - B^{HP,H\to X} = \mathcal{B}(H \to X)\epsilon\sigma_{HP}\mathcal{L}. \tag{6.1}$$

Here $N^{HP,H\to X}$ is the observed number of events in the analysis, $B^{HP,H\to X}$ is the expected background contribution, ϵ the signal efficiency and $\mathcal{L}$ the integrated luminosity. Higgsstrahlung is the dominant

Higgs production mode at the ILC250. Therefore the Higgsstrahlung cross section is a shared source of uncertainty for all such Higgs BR measurements.

Alternatively, the Higgs branching ratios can be measured from the relative importance of each Higgs decay mode in samples that have a Higgs decay independent selection efficiency. The sample selection procedure has been established in Chapter 5. A short description of the data sets is provided in Section 6.1. To determine the relative importance of different Higgs decays, the data sets must be partitioned into classes with varying support for each considered decay mode. The variables that are used for this partitioning are introduced in Section 6.2, and the class definitions are motivated in Section 6.3. All branching ratios are measured simultaneously with the fit described in Section 6.4. The fit stability is verified in Section 6.5. Then in Section 6.6 the reach of this method is compared to other measurement that will be available at the same time. Finally, the influence of deviations from the standard model and from alternative experimental setups are discussed in Section 6.7.

6.1 The data sets

The event selection procedures have been discussed in Chapter 5. Two Higgs production modes are considered: Higgsstrahlung event selection with the associated Z boson decaying to a muon pair or to an electron pair. The process cross sections depend on the polarization of the initial particles. If a collider can produce polarized beams, it is best to study each initial state polarization data set separately. Here the beam parameters from the $\sqrt{s} = 250\,\text{GeV}$ stage of the ILC-H20 proposal (Table 2.2) are assumed. The four different polarization configurations are shown individually in Fig. 6.1.

While a different selection procedure has been applied for muon and electron pair samples, the same classifier and selection threshold is used independent of the polarization configuration. Higher cross sections are expected in the LR configuration than in the RL configuration. The strength of the electroweak interaction depends on the particle's polarization. In particular the charged current interaction (W^- boson exchange) is only possible if the initial state electron is left polarized.

Beyond the shorter time that is allocated for the same-polarization running, the number of expected events is further suppressed by these configurations being unfavorable for the electroweak interaction. The pair annihilation into a Z boson, amongst other processes also needed for the Higgsstrahlung signal process, is only allowed if electron and positron have opposite polarization. Given that the beams are only partially polarized the same-polarization samples will still contain some Higgsstrahlung events.[1]

The Higgsstrahlung signal bars indicate the expected number of events per Higgs decay mode under the SM Higgs assumption. Whilst the background cross sections are assumed to be precisely known, the inclusive Higgsstrahlung cross section is a free nuisance parameter in this study. The data set purities, displayed at the right side of the graph, also assume the SM Higgsstrahlung cross section. As the sample selection procedure is carefully set up in a Higgs decay independent way, the expected relative contribution to the signal per type of Higgs decay is the same in each of the eight data sets. The final branching ratio estimation will make use of all eight statistically independent measurements of the branching ratios.

[1] In the limit of pure same-polarization beams the low cross section ZZ-fusion process is the dominant Higgs production mode.

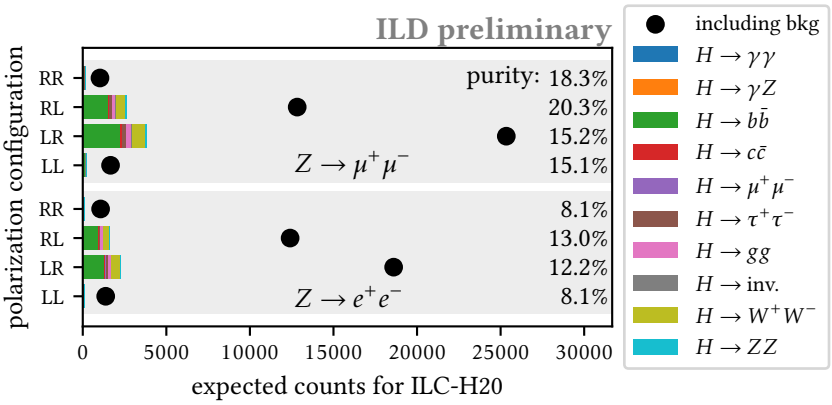

Figure 6.1: Expected number of events per Higgsstrahlung sample after the $\sqrt{s} = 250\,\text{GeV}$ runs that are planned in the ILC-H20 proposal.

6.2 Event classes preparation

By construction, counting the number of events in one of the data sets yields no information on the branching ratios. For a branching ratio measurement it is necessary to study the distribution of the events within the sample. The simplest approach is to partition the sample into various classes where each class has a distinct Higgs decay mode and background composition. Then the deviation of a branching ratio from the SM expectation leads to a characteristic, BR-dependent pattern of excesses and deficits in the class counts.

To gain a better understanding of the jet based variables the jet clustering is explained in Section 6.2.1. All 24 variables that have been used for the definition of one or more of the 46 classes are briefly described in Section 6.2.2. The event classes themselves are described in Section 6.3. In order to simplify the presentation the event classes are introduced as 7 groups that are outlined in Section 6.2.3.

6.2.1 Jet clustering

As already mentioned in Section 3.3.4, the jet clustering and subsequent flavor tagging are performed with LCFIPlus [71]. The DurhamVertex algorithm in LCFIPlus extends the traditional Durham algorithm [87]. Vertices and leptons are treated as **jet cores**. If a specific number of jets is requested, those jet cores that are closest to each other are combined until the target quantity N_J is reached. The so far unconsidered particles, identified by neutral clusters or by tracks that are not part of a vertex, are merged with a jet core if they are within a cone of radius 0.2 radian to that jet core. This cone-based step reduces the number of objects that have to be considered in the clustering step and therefore reduces the clustering time. The jet distance measure y_{ij} in the DurhamVertex algorithm is

$$y_{ij} = \frac{2\min(E_i^2, E_j^2)(1 - \cos\theta_{ij})}{Q^2} + \alpha_{ij} \tag{6.2}$$

Here E_i and E_j are the energies of the pseudo-jets i and j, θ_{ij} is the angle between the two pseudo-jet momenta and Q is the energy scale. The energy scale is the visible energy in the event after removing the isolated lepton pair used for the sample tagging. Equation (6.2) differs from the standard Durham distance measure only by the additional parameter α_{ij}. Setting this parameter to a large value if both

pseudo-jets contain a jet core ($\alpha_{ij}^{\text{both with jet core}} > 2$, $\alpha_{ij}^{\text{else}} = 0$) ensures that none of the previously found jet cores are combined.

Multiple jet finding runs are performed per event to appropriately describe the divers Higgs decay final states and background processes. The runs require the clustering of the event into four, three or two and jets respectively. Since the isolated lepton pair from the primary Z decay has already been removed from the event the jet finding uses only the particles from the Higgs decay candidate and contributions from the machine background. The masses of pairs of jets are calculated for the runs with the four-jet and three-jet hypothesis. Flavor tagging is performed on the two-jet hypothesis. Therefore every event has two $b$tag values and two $c$tag values with $b\text{tag}_i + c\text{tag}_i \leq 1$, $b\text{tag}_1 \geq b\text{tag}_2$. The distance measure between the two remaining jets after jet finding with the requirement of two final jets is y_{12}^{2j}. From the discussion of the Higgsstrahlung kinematics in Section 5.1 it is evident that the Higgs boson can only be produced with a rather low momentum (typically about 60 GeV). Large distances between the jets formed by the final state partons as well as large jet opening angles are thus expected.

6.2.2 Higgs variables

Here all variables that are employed for the definition of the event classes are briefly introduced. These variable have been chosen for their power in disentangling the various Higgs decay modes, or due to their power in discriminating between Higgs and background contributions. The section numbers in the square brackets indicate the sections that describe the event class groups in which a variable is explicitly used.

Angle of the leading charged hadron ($|\cos\theta_{h_1^\pm}|$)
Angle between the charged hadron with the highest energy and the beam axis. [6.3.2, 6.3.3, 6.3.5]

Angle of the leading neutral particle ($|\cos\theta_{h_1^0}|$)
Angle between the neutral PFO with the highest energy and the beam axis. [6.3.2]

Angle of the missing momentum ($|\cos\theta_{\text{miss}}|$)
Angle between the visible momentum and the beam axis. The visible momentum is obtained by summing up all reconstructed four-momenta in the event. This is the only variable that uses information from both the decay products of the primary Z boson and of the Higgs boson. [6.3.1–6.3.3, 6.3.5–6.3.7]

Angle of the second neutral particle ($|\cos\theta_{h_2^0}|$)
Angle between the neutral PFO with the second highest energy and the beam axis. [6.3.3]

Energy of the leading charged hadron ($E_{h_1^\pm}$)
Single particle energy of the charged hadron with the highest energy. [6.3.4]

Energy of the leading charged lepton ($E_{l_1^\pm}$)
Single particle energy of the charged lepton with the highest energy. [6.3.2, 6.3.4]

Flavor tag for bottom-likeness of the first jet ($b\text{tag}_1$)
LCFIPlus bottom flavor tag of the jet with the higher bottom-likeness when requiring two jets in the way that is described in Section 6.2.1. [6.3.5–6.3.7]

Flavor tag for bottom-likeness of the second jet ($b\text{tag}_2$)
LCFIPlus bottom flavor tag of the jet with the lower bottom-likeness when requiring two jets in the way that is described in Section 6.2.1. [6.3.5–6.3.7]

Flavor tag for charm-likeness of the first jet ($c\text{tag}_1$)
LCFIPlus charm flavor tag of the jet with the higher bottom-likeness when requiring two jets in the way that is described in Section 6.2.1. [6.3.6, 6.3.7]

Flavor tag for charm-likeness of the second jet ($c\text{tag}_2$)
LCFIPlus charm flavor tag of the jet with the lower bottom-likeness when requiring two jets in the way that is described in Section 6.2.1. [6.3.6, 6.3.7]

Higgs energy (E_H)
Visible energy in the Higgs part of the event. [6.3.1, 6.3.4, 6.3.5]

Higgs mass (M_H)
Mass from the visible four-momentum vector of the Higgs part of the event. [6.3.2]

Isolated photon angle ($|\cos\theta_{\gamma_1}|$)
Angle between the isolated photon with the highest energy and the beam axis. [6.3.3]

Isolated photon angle of the second photon ($|\cos\theta_{\gamma_2}|$)
Angle between the isolated photon with the second highest energy and the beam axis. [6.3.3]

Isolated photon energy (E_{γ_1})
Energy of the isolated photon with the highest energy. [6.3.3]

Isolated photon pair mass ($M_{\gamma\gamma}$)
Invariant mass of the pair of isolated photons in the event with the highest energy. [6.3.3]

Jet pair mass of jet 1 and jet 2 in a four jet topology ($M^{\max}_{j_{i/4},j_{j/4}}$)
Largest invariant mass from the combination of two jets when forcing the Higgs part of the event into four jets. The clustering algorithm is discussed in detail in Section 6.2.1. [6.3.2]

Jet pair mass of jet 1 and jet 2 in a three jet topology ($M_{j_{1/3},j_{2/3}}$)
Pair mass from the two most energetic jets when forcing the Higgs part of the event into three jets. The clustering algorithm is discussed in detail in Section 6.2.1. [6.3.2]

Muon pair mass ($M_{\mu^+\mu^-}$)
The highest mass that can be formed from a pair of opposite charge isolated muons. Zero if no such pair is found in the event. For the definition of isolated leptons, see number of isolated leptons. [6.3.1]

Number of charged hadrons ($N_{h^\pm}$)
The number of particles that are reconstructed by the particle flow algorithm and identified as charged hadrons. [6.3.2, 6.3.3, 6.3.5, 6.3.7]

Number of isolated leptons ($N_{\text{iso } l^\pm}$)
Isolated leptons were already used for the loose sample selection step introduced in Section 5.2. Here the same definition, including the 5 GeV minimum energy requirement, is applied. As stated previously, those particles that are identified as remnants from the decay of the primary Z boson are not considered in the definition of the Higgs variables. [6.3.1, 6.3.2]

Number of isolated photons ($N_{\text{iso } \gamma}$)
Only isolated photons with energy above 5 GeV are taken into account. [6.3.4]

Number of PFOs (N_{PFO})
The number of particles that are reconstructed by the particle flow algorithm regardless of their type. [6.3.2]

Two jet distance measure (y_{12}^{2j})
DurhamVertex distance measure between the two remaining jets after jet finding with the requirement of two final jets. The clustering algorithm is discussed in detail in Section 6.2.1. [6.3.2, 6.3.6]

6.2.3 Class groups

The grouping of the event classes is solely introduced to give structure to the event class descriptions in Section 6.3. The fit, and therefore the BR results, are based on the individual event classes without any notion of event groups.

Each event belongs to exactly one group. An event that passes a group selection criterion is not considered for the subsequent groups. Correspondingly the order of the groups, as well as later on the order of the event classes, is relevant. The following sectors are defined:

I. **e2e2** At least one isolated muon and anti-muon ($M_{\mu^+\mu^-} > 0\,\text{GeV}$).

II. **il** At least one isolated lepton ($N_{\text{iso } l^\pm} > 0$).

III. **a** At least one high-energy isolated photon ($E_{\gamma_1} > 20\,\text{GeV}$).

IV. **inv** No isolated leptons, isolated photons, or charged hadrons with high energy ($N_{\text{iso } l^\pm} = N_{\text{iso } \gamma} = 0$, $E_{h_1^\pm} < 5\,\text{GeV}$).

V. **tau** Only a few charged hadrons ($N_{h^\pm} \leq 15$).

VI. **y12** A small two jet distance measure ($y_{12}^{2j} < 0.15$).

VII. **qq** All remaining events.

The Higgs decay mode and background compositions per sector are illustrated in Fig. 6.2. Group sizes vary widely.

Only few event with a muon pair are expected and less than 5% of those events are expected to be Higgsstrahlung events. This sector was especially created to provide a clean region to search for an excess of the $H \to \mu^+\mu^-$ BR, thus motivating the group name `e2e2`. Decays of the Higgs boson to a vector boson pair, $H \to W^+W^-$ and $H \to ZZ$, can also fall into this sector if the muons are created in the vector boson decay. Their much higher Higgs BRs can more than compensate that only a small fraction of the decays will have a muon pair. A measurement of the $H \to \mu^+\mu^-$ BR, or of a good upper limit, needs a region that has a better purity. Therefore an additional partitioning step within this sector is carried out as discussed in Section 6.3.1.

The next sector, `il`, contains all remaining events with at least one isolated lepton. Without an additional partitioning step the high background level would for the most part wash out the Higgs BR information that is contained in events with isolated leptons. Most Higgsstrahlung events in the `il` group are expected to stem from $H \to W^+W^-$ decays with a smaller contribution of about 10% from $\tau^+\tau^-$ Higgs decays.

Requiring an isolated photon with large energy retains most of the Higgs decay events for which an isolated photon is expected in the final state, $H \to \gamma\gamma$ and $H \to \gamma Z$. These two BRs are each an important part to the signal in the `a` sector. But an isolated photon is also part of most of the background events. This is especially true for the $e^+e^- \to Z \to (e^+e^-)/(\mu^+\mu^-)$ annihilation process where a high energy ISR photon is necessary to get a kinematic situation that passes the selection in Chapter 5. Bhabha t-channel events additionally contribute to the $e^+e^- \to e^+e^-$ background in the $Z \to e^+e^-$ samples. Then ISR photons are not only required for a high enough recoil mass (see Eq. (5.1)),

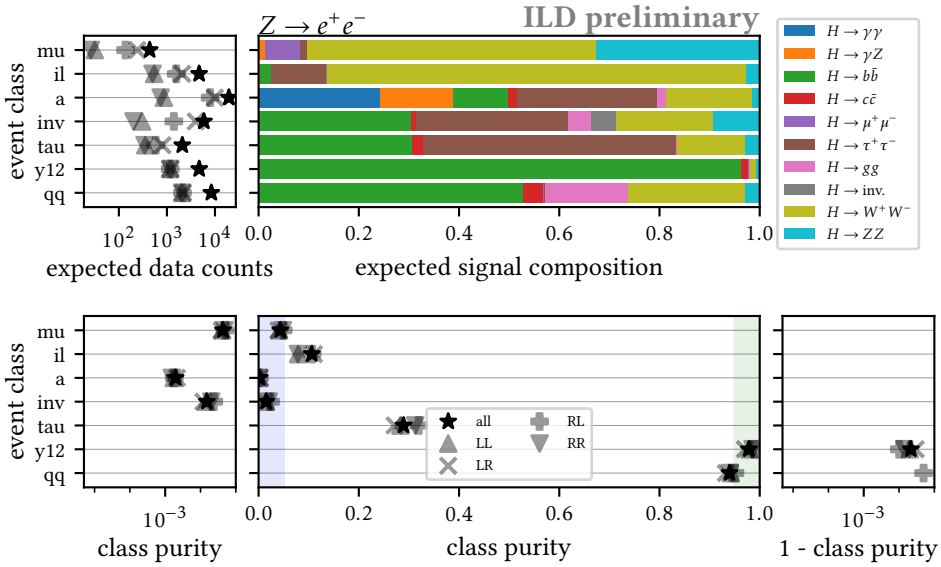

Figure 6.2: Expected event composition per group of event classes. The central bar plot in the top row shows the relative Higgs decay contributions per group for SM Higgs BRs. Given the Higgs decay independent sample selection procedure these portions are independent of the initial state polarization. The Higgsstrahlung signal cross section as well as the background cross sections are polarization dependent. In the top left plot the expected number of events per group after the full $\sqrt{s} = 250\,\text{GeV}$ program outlined in the ILC-H20 proposal is indicated by a black star. Each contribution from a fixed polarization configuration is also displayed independently. The central plot in the bottom row depicts the signal purity per group. The border regions of class purity are reproduced as logarithmic scale versions. This figure presents the situation for the Higgsstrahlung samples where the primary Z boson decays to an electron pair.

but also for the pair mass being close to the Z boson mass without a Z boson being part of the event. It is inevitable to create narrow classes within a to have a measurement of the Higgs BRs with photons which is not completely inundated by the background contributions.

The presented study fully takes into account the ILC machine backgrounds. It has been discussed in Section 2.1.2 that it usual to have about 10 GeV deposited in the event by hadrons that are uncorrelated with the event. Therefore it is not realistic to expect zero visible energy, apart from the decay products of the primary Z boson, in an event with an invisible Higgs decay. As a first approximation, the `inv` group collects all events where there is no charged hadron with more than 5 GeV and no isolated photon. Any event with an isolated lepton is already caught by the `il` group and therefore does not have to be explicitly rejected any more. For the purpose of this analysis the $ZZ \to \nu\bar{\nu}\nu'\bar{\nu}'$ events are split off from the $H \to ZZ$ BR and are treated separately. New physics that interacts with the Higgs boson can lead to large BR for invisible Higgs decays. Setting an upper limit on this effect motivates narrowing down the invisible region in the Higgsstrahlung sample as far as possible.

Most of the background events have less final state particles than the hadronic Higgs decays. Requiring less than 15 charged hadrons in the event keeps most of the remaining background events. While the other hadronic Higgs decays can occasionally have such few charged hadrons it is mostly the remaining $H \to \tau^+\tau^-$ events that make up the signal in this group. The decay of the tau pair rarely results in more than eight charged hadrons. Therefore even after taking into account the charged hadrons from the potential machine background nearly all tau pair events stay below the charged hadron threshold.

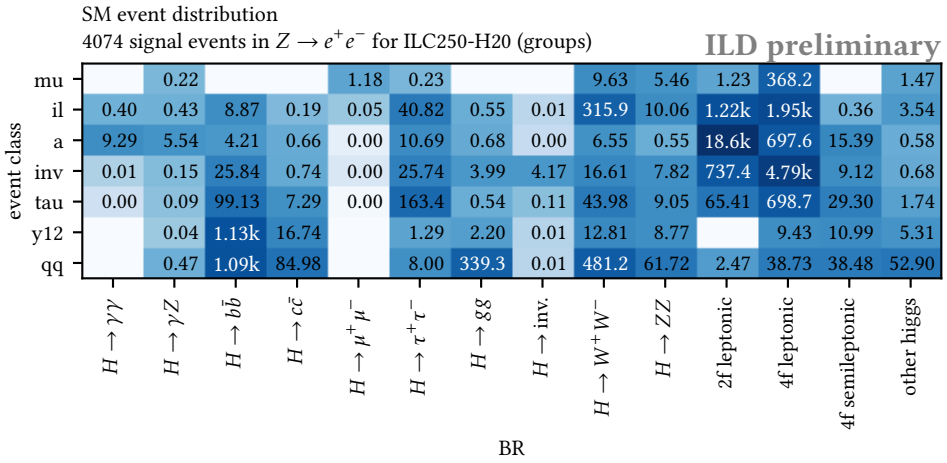

Figure 6.3: Expected number of events per group of event classes. Shown is the sum of the four polarization configurations from the $\sqrt{s} = 250\,\text{GeV}$ program outlined in the ILC-H20 proposal. White boxes indicate that no simulated event from the respective process belongs to the group of event classes.

In the remaining region the background contributions are all but vanishing. About 3/4 of the Higgsstrahlung events fall into the remaining classes. It is thus of highest importance to separate the different Higgs decays. The two jet distance measure can be small for the $b\bar{b}$ or $c\bar{c}$ quark pair decays of the Higgs boson but is seldomly small for the other hadronic Higgs decay modes.

The number of expected events per group of event classes are summarized in Fig. 6.3. This figure shows the contributions from the Higgs decays that are expected to be most important and the contributions per background group. It is coherent with the sample selection requirement of having a lepton pair that no fully hadronic backgrounds contribute to the sample. The `other higgs` contributions to the sample are mainly Higgsstrahlung events with a hadronic decay of the primary Z boson and a $H \to ZZ^*$ decay where the on-shell Z boson decays to a lepton pair, with the lepton generation appropriate for the considered sample.

While the actual analysis considers all four polarization configurations individually, only the sum of the four data sets is given in Fig. 6.3. The number of events and the signal purity per group for the individual polarization configurations can instead be read out from Fig. 6.2. Figures 6.2, 6.3 and 6.5 to 6.18 are all based on the sample with the primary Z boson decaying to an electron pair. For the sake of brevity the same figures are not repeated for the muon pair samples. All polarization configurations and both lepton pair type samples use the same event class definitions. Only Fig. 6.3 is reproduced with the muon pair data. The comparison with Fig. 6.4 shows three main differences. The muon pair sample selection has a much higher efficiency with almost 75% more events passing that selection than the electron pair selection. This higher selection efficiency comes partly from the better momentum reconstruction and partly at the cost of higher background rates. Two fermion final states in the muon pair sample require the annihilation of the initial state electron pair. The two fermion process has no t-channel contribution, resulting in a lower cross section.

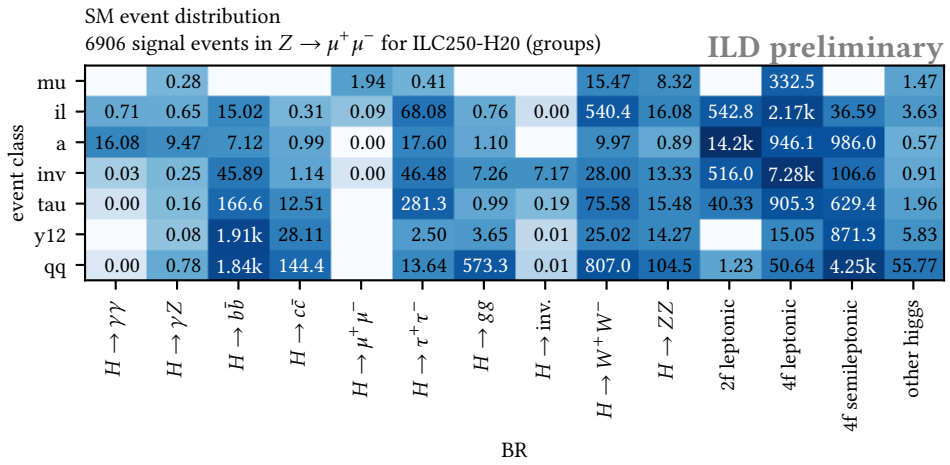

Figure 6.4: Expected number of events per group of event classes. For a detailed description see Fig. 6.3.

6.3 Event classes

6.3.1 Muon pair events

Figures 6.5 and 6.6 illustrate the classes for events with a muon pair. The following class selection criteria are applied consecutively on the remaining events:

1. `mu_tight`:
   - $124.5\,\text{GeV} < M_{\mu^+\mu^-} < 125.5\,\text{GeV}$
2. `mu_loose`:
   - $120\,\text{GeV} < M_{\mu^+\mu^-} < 127\,\text{GeV}$
3. `mu_vv`:
   - $0\,\text{GeV} < M_{\mu^+\mu^-} < 70\,\text{GeV}$
   - $|\cos\theta_{\text{miss}}| < 0.95$
   - $E_H < 125\,\text{GeV}$
4. `mu_rest`:
   - $M_{\mu^+\mu^-} > 0\,\text{GeV}$
   - $N_{\text{iso } l^\pm} \neq 4$

If the Higgs boson decays to a muon pair the four momentum of the Higgs boson is precisely measured from the sum of the four momenta of the muon pair. Requiring a muon pair mass close to the Higgs mass keeps most of the $H \to \mu^+\mu^-$ signal while reducing the background expectation to only a few events during the whole ILC-H20 program. But nevertheless this measurement is limited by the low expected BR. As the muon pair momentum can be reliably reconstructed even in more complicated environments the best measurement of the coupling of the Higgs boson to muons must use Higgs production modes with a larger cross section. Following the discussion in Section 5.1 most of the significance is expected from the $q\bar{q}H$ and $\nu\bar{\nu}H$ production modes that produce more than 90% of the Higgs bosons at ILC250. Their combination yields an expected precision of 23% [88].

Here, using the e^+e^-H and $\mu^+\mu^-H$ production modes, only about one signal event is expected in the samples from each of them. Therefore only an upper limit can be set from the inclusive branching ratio analysis presented here unless the signal yield is much higher than expected from the SM.

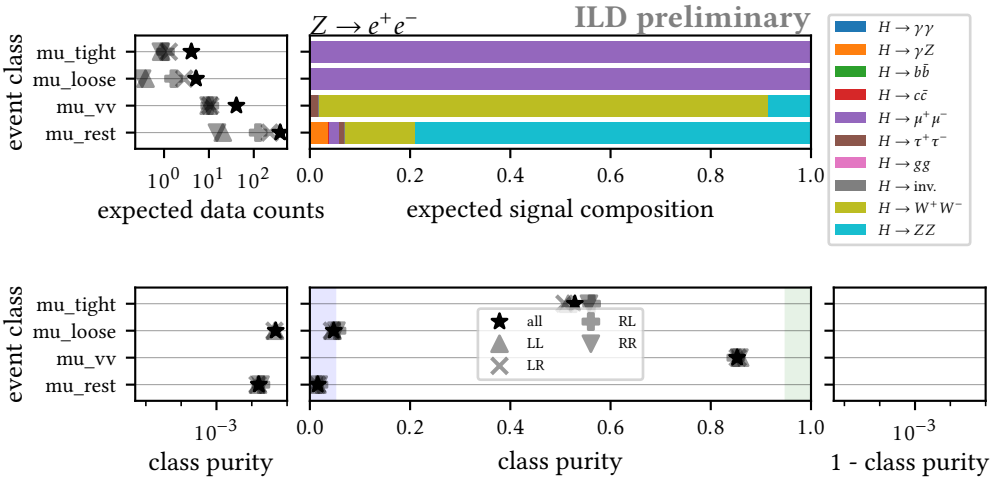

Figure 6.5: Expected event composition per class in the e2e2 sector. For a detailed description see Fig. 6.2.

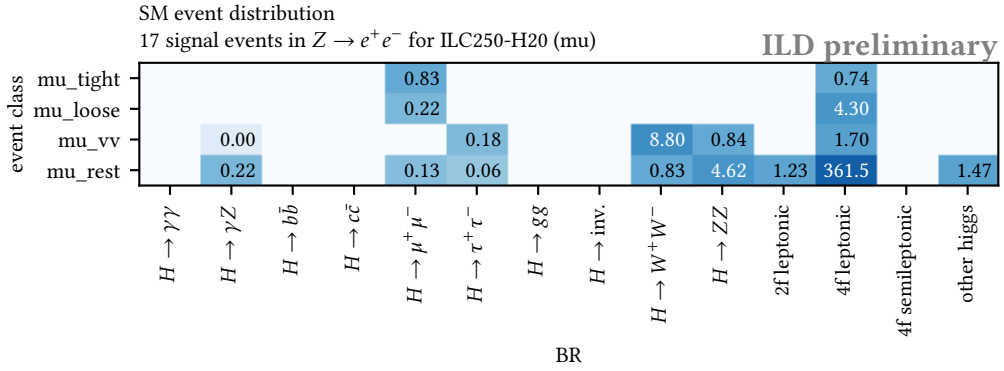

Figure 6.6: Expected number of events per class in the e2e2 sector. For a detailed description see Fig. 6.3.

Another source of an opposite-sign muon pair is the Higgs decay to a W^+W^- pair with both bosons decaying to a muon. In this case a large fraction of the Higgs boson's energy will be carried by neutrinos and therefore will not be detected. The muon pair mass will likely be lower than if the muon pair would have originated from a Z boson decay. An additional cut on the direction of the missing momentum reduces the background contributions while the signal process has no angular preference.

All remaining events with an opposite-sign muon pair are collected in the `mu_rest` class. A class similar to the `mu_vv` class that focuses on the $H \to ZZ$ decay is not of avail. Most of the background events in `mu_rest` have themselves a muon pair from a Z decay, and the momentum of that Z boson is similar to the Z boson's momentum for the $H \to ZZ$ signal.

6.3.2 Isolated lepton events

Figures 6.7 and 6.8 illustrate the classes for events with isolated leptons. The following class selection criteria are applied consecutively on the remaining events:

5. `il_4`:
   - $N_{\text{iso } l^\pm} = 4$
6. `il_2zz`:
   - $N_{\text{iso } l^\pm} = 2$
   - $N_{h^\pm} > 15$
   - $E_{l_1^\pm} < 40\,\text{GeV}$
   - $|\cos\theta_{h_1^\pm}| < 0.9$
   - $50\,\text{GeV} < M^{\text{max}}_{j_{i/4},j_{j/4}} < 110\,\text{GeV}$
7. `il_2ww`:
   - $N_{\text{iso } l^\pm} \geq 2$
   - $|\cos\theta_{\text{miss}}| < 0.95$
   - $5\,\text{GeV} < M^{\text{max}}_{j_{i/4},j_{j/4}} < 60\,\text{GeV}$
8. `il_tight`:
   - $N_{\text{iso } l^\pm} = 1$
   - $N_{\text{PFO}} > 15$
   - $|\cos\theta_{h_1^\pm}| < 0.85$
   - $|\cos\theta_{\text{miss}}| < 0.99$
   - $|\cos\theta_{h_1^0}| < 0.95$
   - $y_{12}^{2j} < 0.05$
   - $M_{j_{1/3},j_{2/3}} < 100\,\text{GeV}$
9. `il_loose`:
   - $N_{\text{iso } l^\pm} = 1$
   - $N_{\text{PFO}} > 15$
10. `il_tau`:
    - $N_{\text{iso } l^\pm} = 1$
    - $N_{\text{PFO}} \leq 15$
    - $|\cos\theta_{\text{miss}}| < 0.75$
    - $25\,\text{GeV} < M_H < 115\,\text{GeV}$
11. `il_rest`:
    - $N_{\text{iso } l^\pm} \leq 1$

An important contribution to events with two or more isolated leptons are again $H \to W^+W^-$ events where both $W^\pm$ bosons decay to leptons. When clustering the event into four jets it is expected that two of the jets are mainly made up by the isolated leptons while the remaining two jets collect the particles from the machine background. Then as before the invariant mass from the two isolated leptons should be below the mass of a Z boson. Now the jet pair mass is express as the mass from the combination of the two most energetic jets out of four jets in the event. While there is no preferred direction for the angle of the leptons in the $H \to W^+W^-$ events, the second most energetic lepton in some of the background processes comes from overlay particles whose production is forward peaked.

The $H \to W^+W^-$ decay is also an important process for events with exactly one isolated lepton. In this case one of the $W^\pm$ bosons decayed hadronically. Therefore it is reasonable to expect many particles in the event. The most energetic charged hadron and neutral particle should come from the $W^\pm$ decay. In contrast to particles from the machine backgrounds the $W^\pm$ bosons have no preferred angular direction. Additional cuts on the two jet distance measure and on the leading jet pair mass help to realize a high purity class. When there are fewer particles in the event it is also likely that it is an event with a Higgs boson decaying to a tau pair, with one tau decaying to a lepton and the other tau decaying hadronically.

6.3.3 Isolated photon events

Figures 6.9 and 6.10 illustrate the classes for events with isolated photons. The following class selection criteria are applied consecutively on the remaining events:

12. `a_a_tight`:

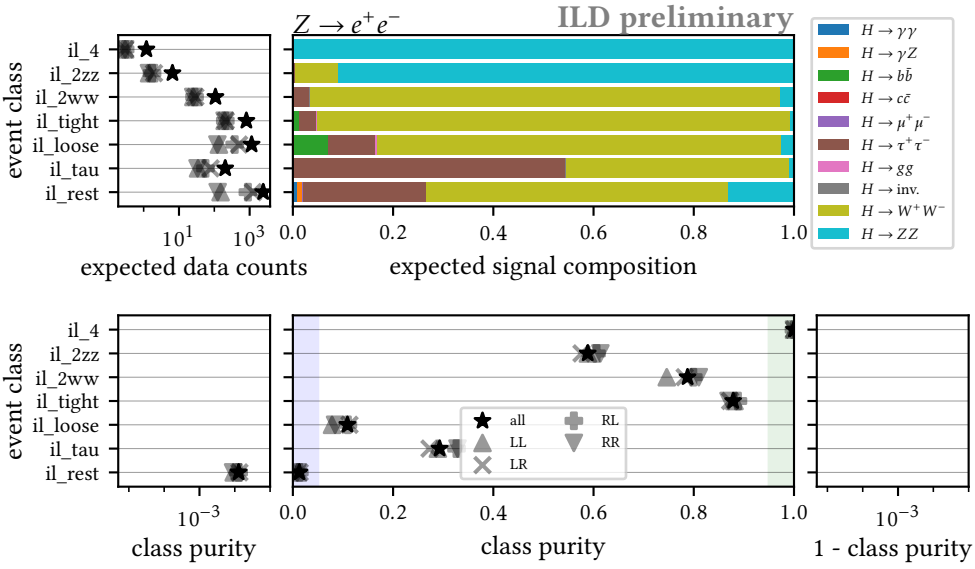

Figure 6.7: Expected event composition per class in the `il` sector. For a detailed description see Fig. 6.2.

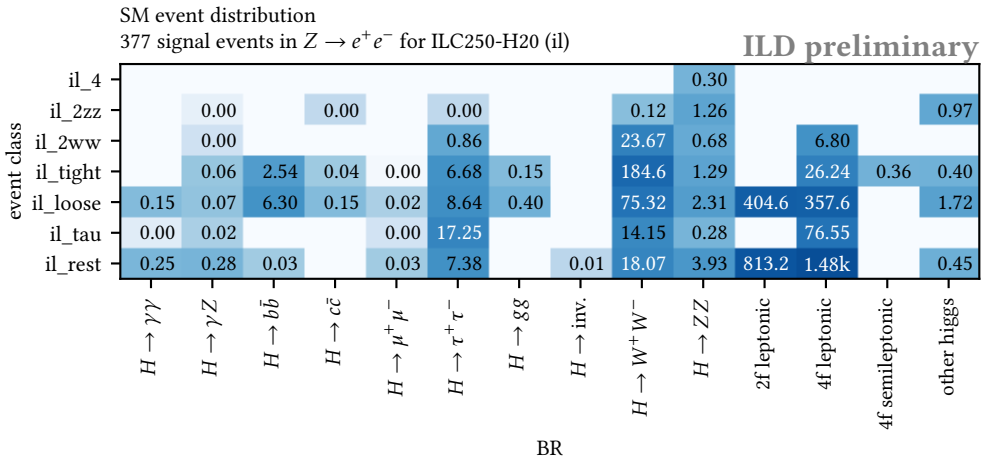

Figure 6.8: Expected number of events per class in the `il` sector. For a detailed description see Fig. 6.3.

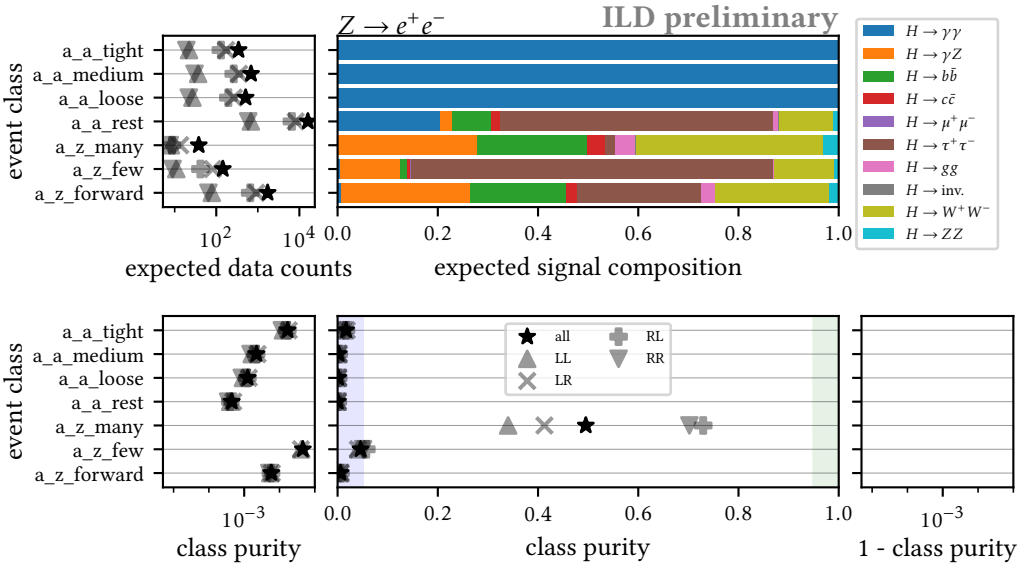

Figure 6.9: Expected event composition per class in the a sector. For a detailed description see Fig. 6.2.

- $E_{\gamma_1} > 50\,\text{GeV}$
- $|\cos\theta_{\gamma_1}| < 0.9$
- $115\,\text{GeV} < M_{\gamma\gamma} < 135\,\text{GeV}$
- $|\cos\theta_{\gamma_2}| < 0.7$

13. `a_a_medium`:
    - $E_{\gamma_1} > 50\,\text{GeV}$
    - $|\cos\theta_{\gamma_1}| < 0.9$
    - $115\,\text{GeV} < M_{\gamma\gamma} < 135\,\text{GeV}$
    - $|\cos\theta_{\gamma_2}| < 0.9$
14. `a_a_loose`:
    - $E_{\gamma_1} > 50\,\text{GeV}$
    - $|\cos\theta_{\gamma_1}| < 0.9$
    - $115\,\text{GeV} < M_{\gamma\gamma} < 135\,\text{GeV}$
    - $|\cos\theta_{\gamma_2}| < 0.98$
15. `a_a_rest`:
    - $E_{\gamma_1} > 50\,\text{GeV}$
16. `a_z_many`:
    - $20\,\text{GeV} < E_{\gamma_1} \leq 50\,\text{GeV}$
    - $|\cos\theta_{\gamma_1}| < 0.9$
    - $|\cos\theta_{\text{miss}}| < 0.95$
    - $|\cos\theta_{h_1^\pm}| < 0.9$
    - $|\cos\theta_{h_2^0}| < 0.95$
    - $N_{h^\pm} > 15$
17. `a_z_few`:
    - $20\,\text{GeV} < E_{\gamma_1} \leq 50\,\text{GeV}$
    - $|\cos\theta_{\gamma_1}| < 0.9$
    - $|\cos\theta_{\text{miss}}| < 0.95$
    - $|\cos\theta_{h_1^\pm}| < 0.9$
    - $|\cos\theta_{h_2^0}| < 0.95$
    - $N_{h^\pm} \leq 15$
18. `a_z_forward`:
    - $20\,\text{GeV} < E_{\gamma_1} \leq 50\,\text{GeV}$

Isolated photons with high energy can be the result of beamstrahlung, ISR and FSR. The simple cone-based algorithm that is used for the identification of isolated photons can also sometimes misidentify photons from within a jet or from a tau decay as isolated. Consequentially there are large background contributions that complicate the measurement of the $H \to \gamma\gamma$ and $H \to \gamma Z$ BRs. In

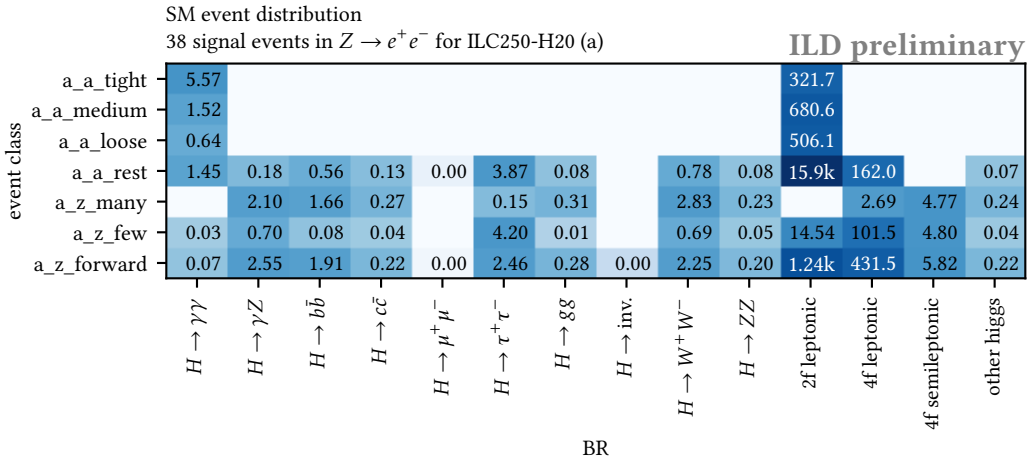

Figure 6.10: Expected number of events per class in the a sector. For a detailed description see Fig. 6.3.

the former case the mass from the two most energetic photons should be close to the Higgs boson mass. The backgrounds can be reduced by excluding photons with a small angle to the beam axis. Still the electron pair sample's photon pair classes contain many background $e^+e^- \to e^+e^-$ events with two isolated photons at large angles. The $e^+e^- \to \mu^+\mu^-$ background in the muon pair sample is much smaller.

As the decaying Higgs boson has a low energy, usually about 140 GeV, and the Z boson has a high mass, the isolated photon from a $H \to \gamma Z$ decay is expected to have less energy. Again it is sensible to apply angular cuts to remove background contributions.

6.3.4 Invisible events

Figures 6.11 and 6.12 illustrate the classes for events with low activity. The following class selection criteria are applied consecutively on the remaining events:

19. `inv_tight`:
    - $N_{\text{iso }\gamma} = 0$
    - $E_{h_1^\pm} < 5\,\text{GeV}$
    - $E_{l_1^\pm} < 5\,\text{GeV}$
    - $E_H < 20\,\text{GeV}$
20. `inv_medium`:
    - $N_{\text{iso }\gamma} = 0$
    - $E_{h_1^\pm} < 5\,\text{GeV}$
    - $E_{l_1^\pm} < 5\,\text{GeV}$
    - $E_H < 50\,\text{GeV}$
21. `inv_loose`:
    - $N_{\text{iso }\gamma} = 0$
    - $E_{h_1^\pm} < 5\,\text{GeV}$
22. `inv_w_photon`:
    - $N_{\text{iso }\gamma} > 0$
    - $E_{h_1^\pm} < 5\,\text{GeV}$

The uncorrelated contributions from machine backgrounds mean that it is not realistic to expect zero activity even in an event with a Higgs boson that decays without leaving a trace in the detector. Instead it is possible to require that there are no high energy particles in the event. No angular cut can be applied here. The particles with the highest energy for the targeted signal process itself are from the machine background and are therefore mainly produced in the forward region.

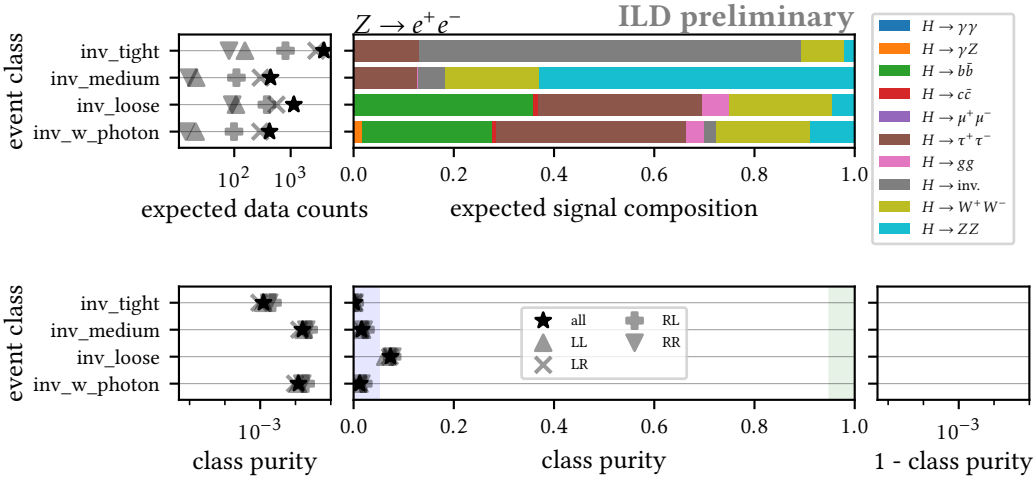

Figure 6.11: Expected event composition per class in the `inv` sector. For a detailed description see Fig. 6.2.

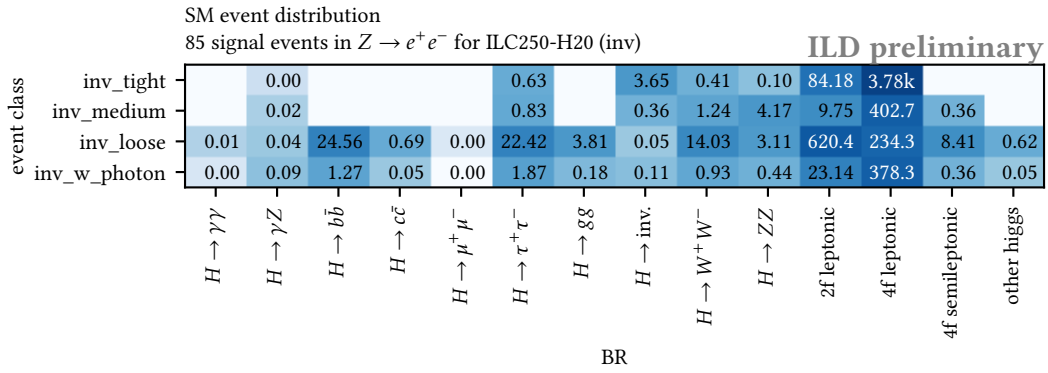

Figure 6.12: Expected number of events per class in the `inv` sector. For a detailed description see Fig. 6.3.

6.3.5 Events with few hadrons

Figures 6.13 and 6.14 illustrate the classes for events with few charged hadrons. The following class selection criteria are applied consecutively on the remaining events:

23. `tau_tight`:
    - $N_{h^\pm} \leq 15$
    - $|\cos\theta_{\text{miss}}| < 0.9$
    - $|\cos\theta_{h_1^\pm}| < 0.9$
    - $E_H > 30\,\text{GeV}$
    - $b\text{tag}_1 \leq 0.8$
    - $b\text{tag}_2 \leq 0.8$
24. `tau_medium`:

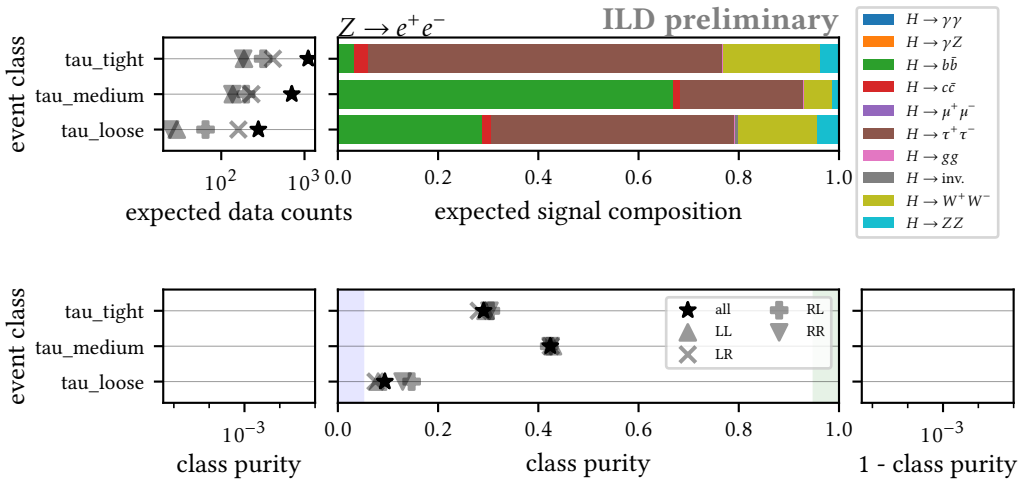

Figure 6.13: Expected event composition per class in the `tau` sector. For a detailed description see Fig. 6.2.

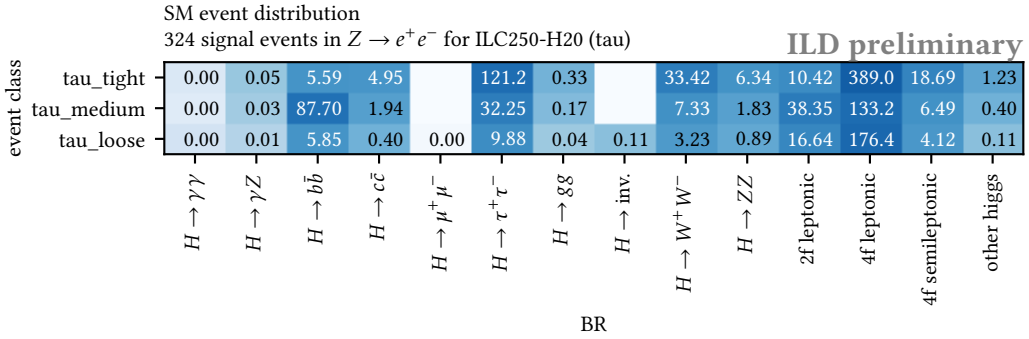

Figure 6.14: Expected number of events per class in the `tau` sector. For a detailed description see Fig. 6.3.

- $N_{h^\pm} \leq 15$
- $|\cos\theta_{h_1^\pm}| < 0.95$
- $E_H > 30\,\text{GeV}$

25. `tau_loose`:
    - $N_{h^\pm} \leq 15$

Here few hadrons means at most 15 charged hadrons. The tau decays have normally less particles. Still, due to their large BRs, there are significant contributions from the Higgs decays to a $b\bar{b}$ pair or a W^+W^- pair. Angular cuts and a minimum energy requirement improve the the purity. Furthermore the $b$tagvalues are used to separate the $b\bar{b}$ pair decays of the Higgs boson.

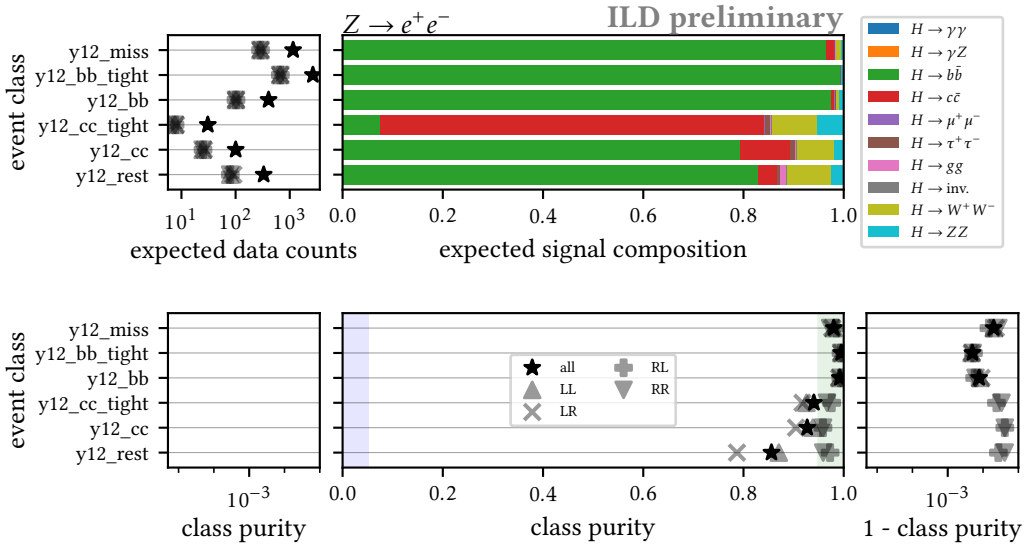

Figure 6.15: Expected event composition per class in the y12 sector. For a detailed description see Fig. 6.2.

6.3.6 y_{12}

Figures 6.15 and 6.16 illustrate the classes for events with a small two jet distance measure. The following class selection criteria are applied consecutively on the remaining events:

26. `y12_miss`:
    - $y_{12}^{2j} < 0.15$
    - $|\cos\theta_{\text{miss}}| > 0.9$
27. `y12_bb_tight`:
    - $y_{12}^{2j} < 0.15$
    - $b\text{tag}_1 > 0.8$
    - $b\text{tag}_2 > 0.8$
28. `y12_bb`:
    - $y_{12}^{2j} < 0.15$
    - $b\text{tag}_1 > 0.8$
29. `y12_cc_tight`:
    - $y_{12}^{2j} < 0.15$
    - $c\text{tag}_1 > 0.7$
    - $c\text{tag}_2 > 0.7$
30. `y12_cc`:
    - $y_{12}^{2j} < 0.15$
    - $c\text{tag}_1 > 0.7$
31. `y12_rest`:
    - $y_{12}^{2j} < 0.15$

All classes have a high Higgsstrahlung purity. The $b$tag and $c$tag flavor tag scores allow for classes with a very large fraction of $H \to b\bar{b}$ and $H \to c\bar{c}$ events respectively.

6.3.7 qq

Figures 6.17 and 6.18 illustrate the classes for the remaining events. The following class selection criteria are applied consecutively:

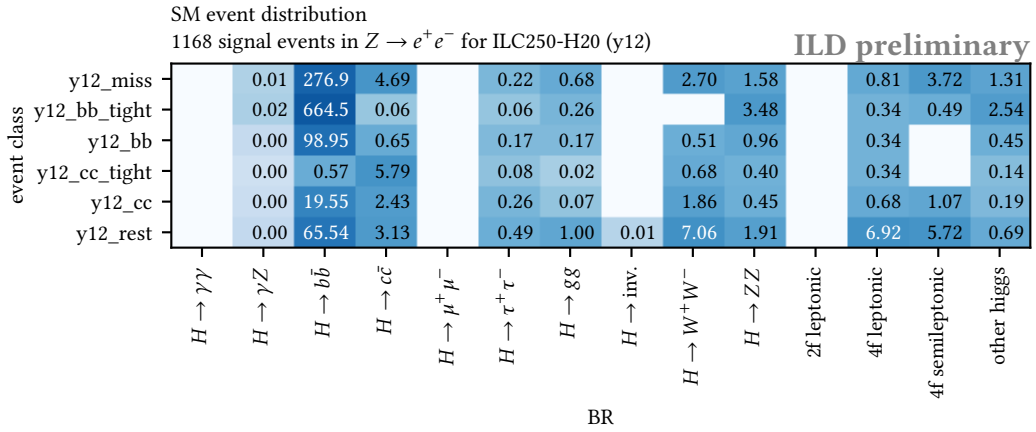

Figure 6.16: Expected number of events per class in the y12 sector. For a detailed description see Fig. 6.3.

32. `qq_miss`:
    - $|\cos\theta_{\text{miss}}| > 0.9$
33. `qq_bb_tight`:
    - $b\text{tag}_1 > 0.9$
    - $b\text{tag}_2 > 0.9$
34. `qq_bb_loose`:
    - $b\text{tag}_2 > 0.8$
35. `qq_cc_tight`:
    - $c\text{tag}_1 > 0.7$
    - $c\text{tag}_2 > 0.7$
36. `qq_cc_medium`:
    - $c\text{tag}_1 > 0.7$
37. `qq_cc_loose`:
    - $c\text{tag}_1 > 0.4$
38. `qq_lq_few`:
    - $b\text{tag}_1 + c\text{tag}_1 < 0.5$
    - $N_{h^\pm} < 20$
39. `qq_lq_many`:
    - $b\text{tag}_1 + c\text{tag}_1 < 0.5$
    - $N_{h^\pm} > 40$
40. `qq_lq`:
    - $b\text{tag}_1 + c\text{tag}_1 < 0.5$
41. `qq_few`:
    - $N_{h^\pm} < 20$
42. `qq_many_bb`:
    - $N_{h^\pm} > 40$
    - $b\text{tag}_1 > 0.7$
43. `qq_many_gg`:

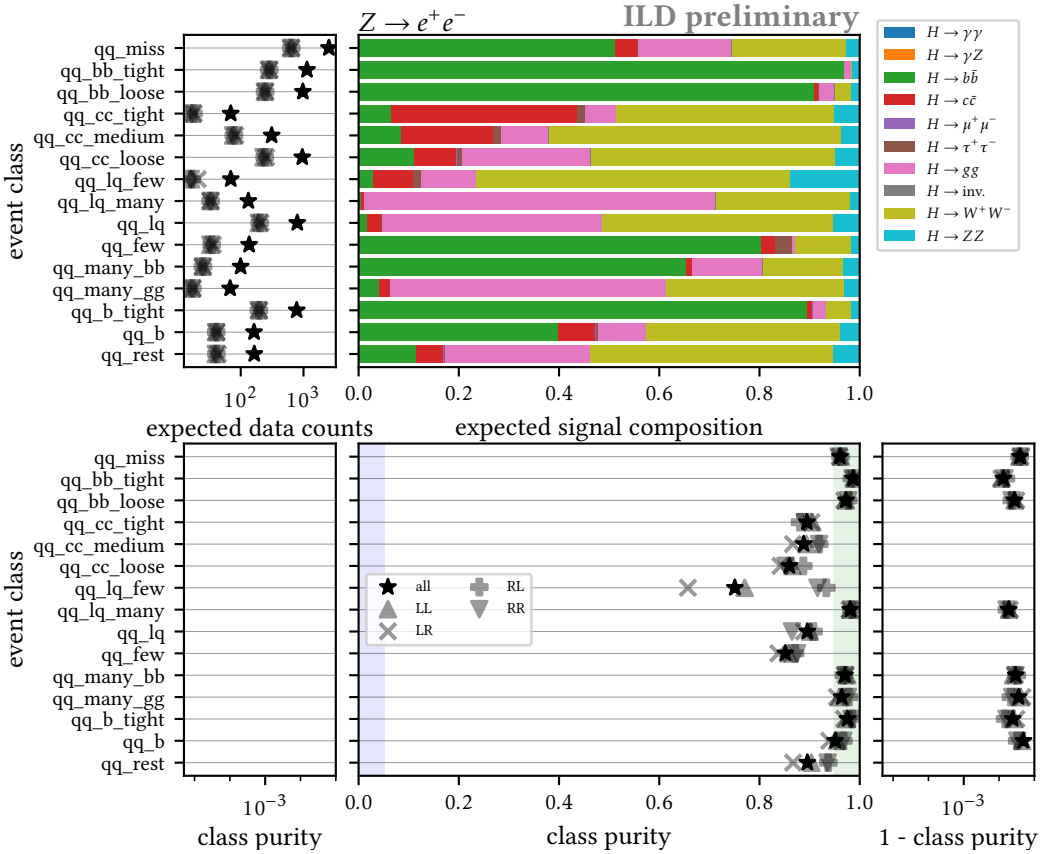

Figure 6.17: Expected event composition per class in the qq sector. For a detailed description see Fig. 6.2.

- $N_{h^\pm} > 40$
- $b\text{tag}_1 \leq 0.7$

44. `qq_b_tight`:
    - $b\text{tag}_1 > 0.8$
45. `qq_b`:
    - $b\text{tag}_1 > 0.6$
46. `qq_rest`: All remaining events.
    - $b\text{tag}_1 \leq 0.6$

Apart from the `qq_lq_few` class, all classes are expected to contain Higgsstrahlung events to more than 80%. The flavor tag scores and the number of charged hadrons are used to partition the remaining event space into regions that have different sensibility to the various hadronic decays of the Higgs boson. Especially the Higgs decay to gluons has not been caught by any classes so far. Compared to the quark jets, the gluon jets tend to have a higher multiplicity of charged hadrons.

6.3.8 Summary of the event classes

In this section the Higgsstrahlung samples have each been partitioned into 46 exclusive regions. For the sake of simplicity the same class definitions are used for all eight data sets. While the relative

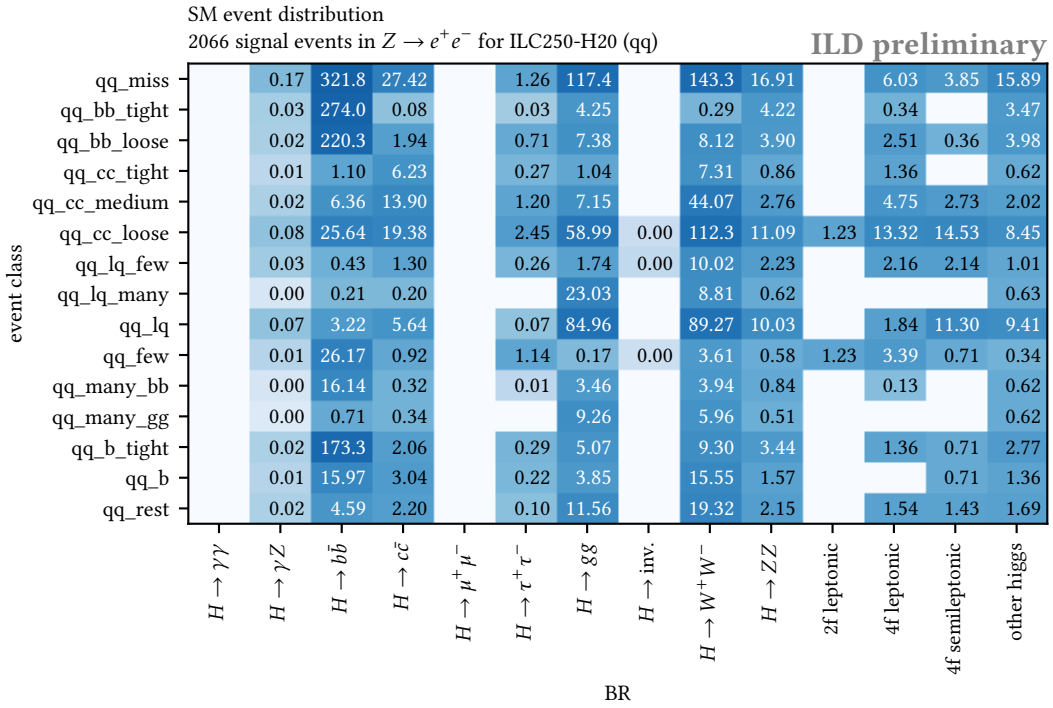

Figure 6.18: Expected number of events per class in the qq sector. For a detailed description see Fig. 6.3.

importance of each Higgs decay mode is the same in each of the samples, the number of expected Higgsstrahlung events as well as the importance per type of background varies.

A limiting factor for the number of classes is the size of the simulated data sets used in the study. This is especially true for the background processes in the low count classes, e.g. for the muon pair classes. If the number of simulated background events in region becomes too small the class selection risks to depend on statistical fluctuations of the simulated data set. The dependence on statistical fluctuations with the event classes defined above is studied in Section 6.5.1. No serious over-tuning to statistical artifacts is found.

The impact of Higgs decays outside of the standard model depends strongly on the specific Higgs decay. For any conjectured additional Higgs decay type a dedicated event sample should be simulated. Depending on the Higgs decay, it might be advisable to add new event classes to the analysis, to improve the discrimination between the new process, the SM Higgs decays, and the background events.

6.4 Likelihood optimization

While the Higgs production cross section σ_H is considered as a free parameter, all background cross sections are assumed to be known precisely. Therefore the expected number of background events per class is:

$$\vec{N}_B = \mathcal{L} \sum_{p \in B} \epsilon_p \sigma_p \vec{P}_p \tag{6.3}$$

where $\mathcal{L}$ is the sample's integrated luminosity, ϵ_p are the efficiencies and σ_p are the cross sections per background process. The probability vector $\vec{P}_p$ contains the probabilities for those events from a specific process that pass the event selection step to belong to each of the classes defined in Section 6.3.

Similarly, the number of Higgs events per class is obtained as:

$$\vec{N}_S = \mathcal{L}\epsilon_H\sigma_H M \cdot \vec{\mathcal{B}} = N_H M \cdot \vec{\mathcal{B}}. \tag{6.4}$$

By construction of the sample selection procedure, the signal efficiency is independent of the Higgs decay. The probability matrix M is shown in Fig. 6.19. With the same classes being chosen for all polarization configurations and for both the electron pair and the muon pair samples, this probability matrix is valid fo all data sets. The branching ratio vector is the target of the optimization. As a probability vector, its components are restricted:

$$\begin{aligned} \mathcal{B}_j &\in [0,1], \\ \sum_j \mathcal{B}_j &= 1. \end{aligned} \tag{6.5}$$

Combining Eqs. (6.3) and (6.4), the expected number of events in event class i is:

$$\nu_i = N_{B,i} + N_H \sum_j M_{ij}\mathcal{B}_j. \tag{6.6}$$

The number of observed events y_i per class i follows a Poisson distribution. In order to obtain the most likely set of branching ratios the negative log-likelihood (NLL) must be minimized:

$$\begin{aligned} \mathrm{NLL} &= -\ln L = -\sum_{\mathrm{pol}}\sum_{l} \mathrm{NLL}^{l,\mathrm{pol}} \\ \mathrm{NLL}^{l,\mathrm{pol}} &= \sum_i \nu_i^{l,\mathrm{pol}} - \sum_i y_i^{l,\mathrm{pol}} \ln \nu_i^{l,\mathrm{pol}} \\ &\mathrm{pol} \in \{LL, LR, RL, RR\},\ l \in \{e,\mu\} \end{aligned} \tag{6.7}$$

For the best precision all four ILC250 configurations, and the Higgsstrahlung data sets for the associated Z boson decaying to an electron pair a muon pair should be used in the same fit. Each of the eight data sets has an independent number of signal events, $N_H^{l,pol}$, as a nuisance parameter. The fit is executed through iminuit [89], a Python interface to `MINUIT` [90].

The fit results under the assumption of SM BRs are illustrated in Fig. 6.20. For this fit the NLLs of all eight data sets that are collected at the ILC250, with the integrated luminosities per polarization configuration as specified in the H20 program, are minimized simultaneously. If the data sets have exactly the expected counts in each of the classes, the observed BRs are the SM BRs. The uncertainties are a numerical approximation of the Hesse matrix of the likelihood function at the minimum of the fit. A Hesse matrix contains the second-order partial derivatives of a scalar function. This description gives symmetric uncertainty intervals. The toy studies in Section 6.5 show that the uncertainty approximation is accurate. Each toy data set is a potential observed data set for Higgs couplings identical to the SM expectation, taking into account the statistical uncertainties. One such toy data set has been added to Fig. 6.20 as green stars. Its pulls from the SM expectation give no indication of Higgs BR differences beyond the statistical reach of the data set.

The expected uncertainties per BR and the corresponding correlation matrix are shown in Table 6.1. With the chosen event classes the $H \to \gamma\gamma$, $H \to \gamma Z$, $H \to \mu^+\mu^-$ and $H \to$ inv. measurements are

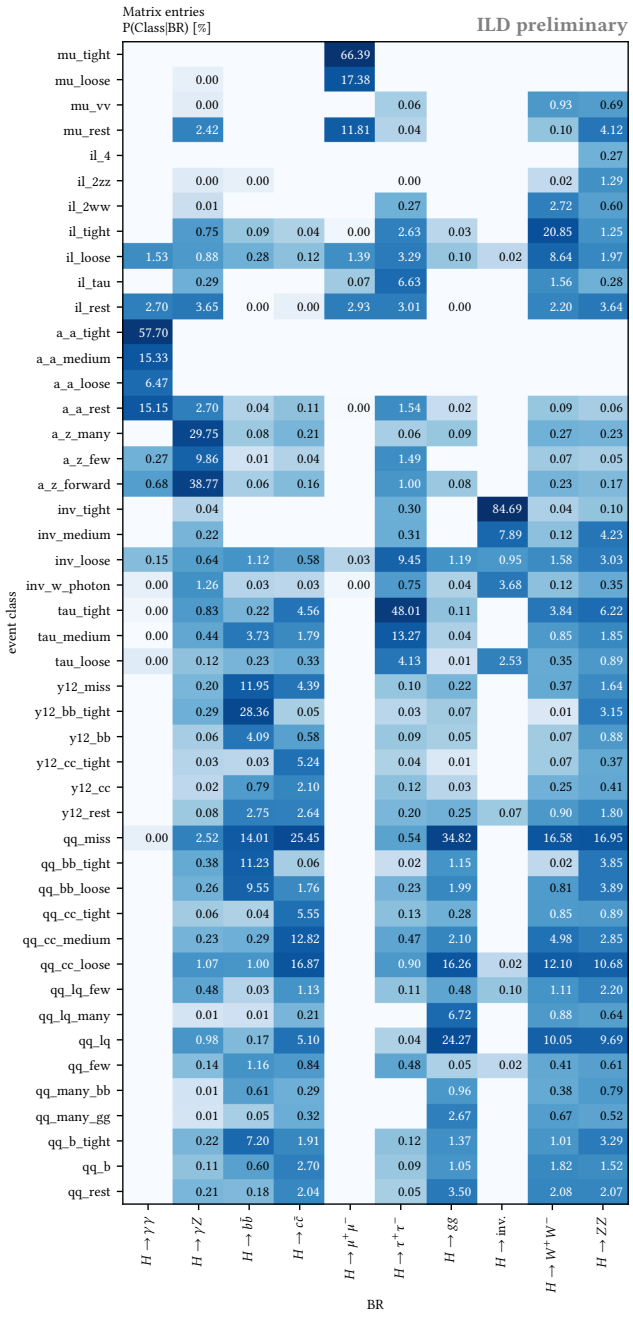

Figure 6.19: Class probability matrix for the most important Higgs decays. White boxes indicate that none of the events simulated for the respective Higgs decay belong to this event class. The probabilities refer to events that pass selection. Therefore each column sums up to 100%.

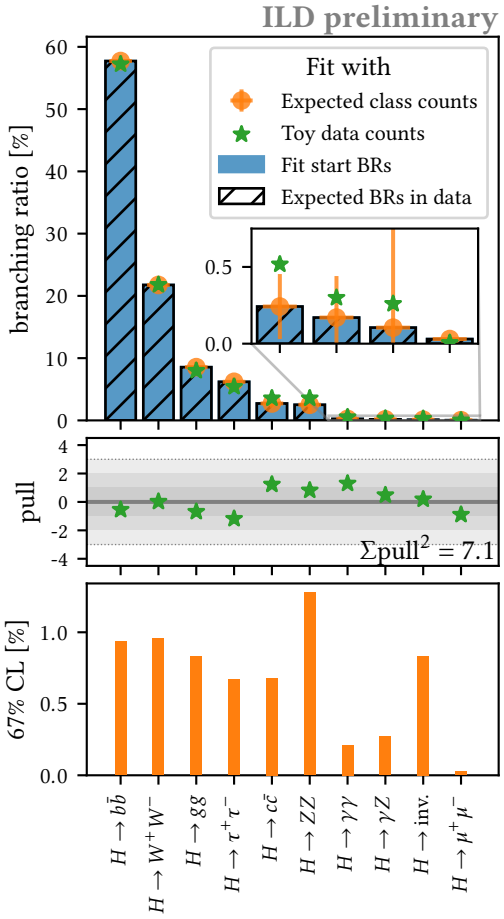

Figure 6.20: Results of the `MINUIT` fit for data sets with the SM BRs. In this fit the ten most important Higgs BRs have been considered.
(Top) The blue bars show the the starting value for the branching ratios fit, chosen to be the standard model branching ratios. The striped bars indicate the BRs that have been set for the simulated data sets. Here, these two sets of BRs are identical. But Fig. 6.21 shows fits for which Higgs couplings are different from the SM expectation. The minimum and the uncertainty from a fit on the expected class counts is displayed as orange error bars. Green stars indicate possible BRs obtained from a fit on an instance of toy data counts. This serves as a replacements for the observed data.
(Middle) Pulls of the toy data from the SM expectation. Gray bands of decreasing intensity indicate the $1\sigma, 2\sigma, 3\sigma$ range.
(Bottom) The absolute 1σ confidence levels per BR.

each almost uncorrelated with any of the studied Higgs decays. The $H \to W^+W^-$ and $H \to ZZ$ decays are followed by the decays of the weak vector bosons themselves. Those events can look similar to the quark, gluon or tau decays of the Higgs boson. It is therefore not surprising that there are discernable anti-correlations for the measurement of the Higgs branching ratios to W^+W^- and ZZ.

	$\gamma\gamma$	γZ	$b\bar{b}$	$c\bar{c}$	$\mu^+\mu^-$	$\tau^+\tau^-$	gg	inv.	W^+W^-	ZZ
$\gamma\gamma$	1.000	-.001	.000	.001	-.000	-.001	.001	.000	-.002	.000
γZ	-.001	1.000	-.001	-.002	-.000	-.014	.013	.001	-.026	-.027
$b\bar{b}$	.000	-.001	1.000	-.051	.001	.017	.025	.016	.063	-.280
$c\bar{c}$	.001	-.002	-.051	1.000	.001	.001	-.116	.016	-.189	-.252
$\mu^+\mu^-$	-.000	-.000	.001	.001	1.000	.000	.001	-.000	.000	-.003
$\tau^+\tau^-$	-.001	-.014	.017	.001	.000	1.000	.169	-.011	-.154	-.176
gg	.001	.013	.025	-.116	.001	.169	1.000	.022	-.298	-.383
inv.	.000	.001	.016	.016	-.000	-.011	.022	1.000	.013	-.060
W^+W^-	-.002	-.026	.063	-.189	.000	-.154	-.298	.013	1.000	-.218
ZZ	.000	-.027	-.280	-.252	-.003	-.176	-.383	-.060	-.218	1.000
$\mathrm{BR}_{\mathrm{SM}}$	0.242	0.170	57.720	2.718	0.030	6.198	8.550	0.105	21.756	2.511
σ_{stat}	0.212	0.271	0.934	0.680	0.028	0.669	0.831	0.835	0.956	1.278

Table 6.1: Correlation matrix for the SM fit with the most important Higgs decays.

The largest correlation is found for the $H \to \tau^+\tau^-$ and $H \to gg$ measurements. While these two Higgs decays contribute mostly to different classes, they are connected through the measurements of the weak vector boson decays. A larger-than-expected $H \to W^+W^-$ contribution, e.g. supported by many isolated lepton events (`il_tight`), does account for more events in the classes that support the Higgs decays to gluons and taus. Hence both the gluon and tau measurements are influenced in the same direction, in this case towards smaller values. Overall, none of the measurements are correlated to a degree that puts the stability of the fit at risk.

The impact of the inclusion of additional Higgs decays in the fit depends on the details of that Higgs decay. Extra event classes geared towards the added Higgs decay can be helpful. If the Higgs decay's events can be perfectly separated from the other Higgs decay events and from the background events in the sample, a branching ratio of at least 0.1% would be necessary to establish the existence of that decay at 3σ solely based on this method and the ILC250 part of the ILC-H20 program. The expected invisible branching ratio due to $H \to ZZ$ events with both Z bosons decaying to neutrinos is about 0.105%. But the event classes that support the invisible Higgs decay events have sizeable contributions from non-Higgs events. Therefore a much larger BR for invisible decays of the Higgs decay would be necessary in order to establish this decay solely based on the results of the fit. Instead, the invisible measurement is best interpreted as an upper limit. A prime candidate for inclusion in the fit is the $H \to s\bar{s}$ decay. Its SM BR is even slightly larger than the $H \to \mu^+\mu^-$ BR. However, instead of featuring a muon pair that can be easily told apart from other events in the sample, the strange decays contribute to the chosen event classes with almost identical proportioning as the gluon decays of the Higgs boson. Separate measurements of $H \to gg$ and $H \to s\bar{s}$ with the chosen event classes are highly anti-correlated. It is preferable to include the strange decays in the gluon contribution. Treating both Higgs decays as a combined entity is valid after confirming that they indeed contribute very similarly to the event classes. For a different choice of event classes, this statement might not be true. A dedicated analysis sets the 95% confidence level upper limit on the κ_s coupling modifier at $\kappa_s < 7.5$, based on the $Z \to \nu\bar{\nu}$ and $Z \to l^+l^-$ channels in the LR configuration of ILC250-H20 [91].

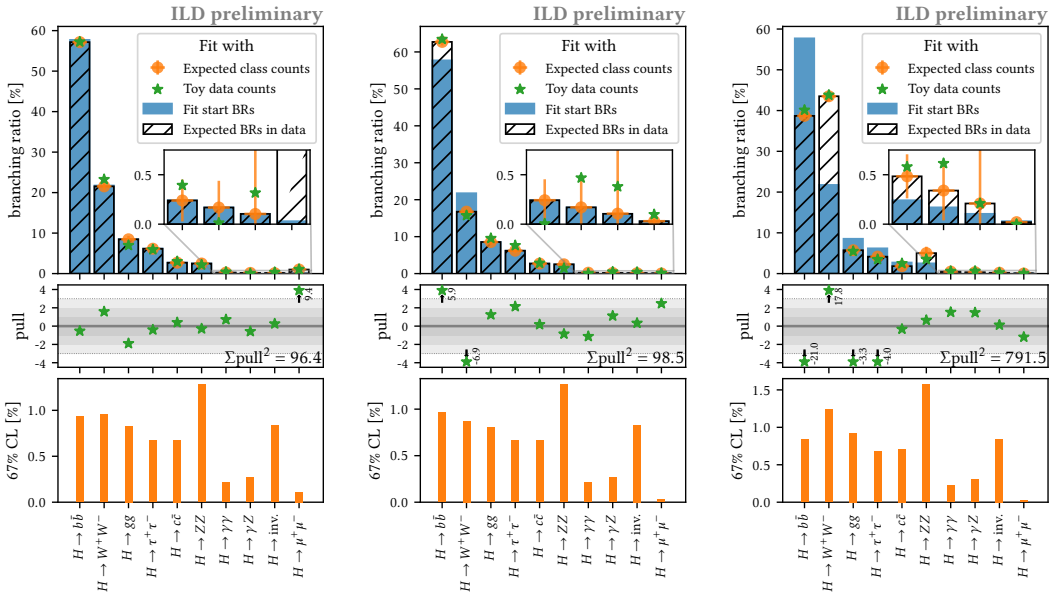

Figure 6.21: Results of the `MINUIT` fit for data sets with branching ratios different from the SM expectation. For the left panel the $H \to \mu^+\mu^-$ BR is increased to 1%, and all other BRs are shrunken proportionally to their size. For the central panel the $H \to b\bar{b}$ branching ratio is increased by 5% while the $H \to W^+W^-$ is decreased by the same amount. Finally, the right panel shows the fit results if the vector boson BRs $H \to \gamma\gamma$, $H \to W^+W^-$ and $H \to ZZ$ are doubled, while the other BRs reduced proportionally to their size. A detailed description of the features of these plots is given in Fig. 6.20.

It suggests itself to take the SM values as the starting values for the parameters of the fit. Therefore it is no surprise that the minimum from the fit with the expected class counts agrees with the SM expectation. But the columns of the probability matrix are different enough to allow the fit to adapt to scenarios far from the SM expectation. To illustrate this adaptability, alternative Higgs decay scenarios are tested in Fig. 6.21.

As a first scenario, an increase of the $H \to \mu^+\mu^-$ BR to 1% is assumed. All other Higgs BRs are reduced proportional to their size. Indeed, the minimum of the fit on the number of expected counts per class moves from the SM values that where taken as the starting values of the fit parameters to the BRs in the new scenario. Looking at the pulls from a toy data set, only the muon pair decay is clearly incompatible with the SM expectation. The relative down-scaling by about 1% for the other Higgs decay rates is too small compared to the statistical uncertainty to determine that those branching ratios are smaller than expected in the SM.

For the second tested scenario the two largest branching ratios are assumed to be different. If the $H \to b\bar{b}$ BR is 5% larger, compensated by a reduction for $H \to W^+W^-$, then both those changes lead to large pulls. Again, the fit on the expected event counts finds the right minimum corresponding to the Higgs BRs in the scenario.

Finally, a scenario in which all Higgs couplings are changed is considered. Here the electroweak vector boson BRs, $H \to W^+W^-$, $H \to ZZ$ $H \to \gamma Z$ and $H \to \gamma\gamma$, are doubled. All the other BRs reduced proportionally to their size. As before, the fit on the expected event counts finds the right minimum. The precision on $H \to \gamma\gamma$ and $H \to ZZ$ from this fit alone would not be sufficient to conclude that these Higgs decays are enhanced. But the four largest Higgs BRs are clearly different

from the SM expectation.

6.5 Toy study

The fit uncertainties are obtained from the local behavior of the likelihood function close to the found fit minimum. This requires that the correct likelihood function is being minimized and that the likelihood function is well described by a Taylor series approximation up to the second order. In order to verify these assumptions a toy study, shown in, Fig. 6.22 is conducted. For each of the toys, the observed number of events per class is drawn from a Multinomial distribution with the expected number of events in the class as its rate. Then these counts y_i are entered into the likelihood function from Eq. (6.7) and a set of observed branching ratios is deduced from the fit. This is repeated 10.000 times, and the optimal BRs per toy are collected in histograms. All toy histograms agree well with a Gaussian distribution centered at the minimum of the fit on the expected event counts, with the uncertainty of the BR parameter in that fit taken as the standard deviation of the Gaussian distribution. Negative branching ratios are not physically possible. As discussed above, all fit parameters have been limited to non-negative values. Toy data sets that due to statistical fluctuations would have been better fitted by a negative BR will most of the times settle at a minimum in which that BR is very small or zero. Therefore the additional accumulation in the lowest bin is expected. It compensates the negative BR region of the Gaussian distribution, or from an unrestricted toy study.

The precision of the measurements depends on the number of events per Higgs decay and on the quality of the class separation between the Higgs decays and from the non-Higgs events. For a second toy study, truth information is used to perfectly separate all Higgs decays from each other and from background contributions. Not all toy histograms in Fig. 6.23 are nicely characterized by a Gaussian distribution. If the expected number of events is small, the fact that the number of observed events must be an integer means that only a limited quantity of BR minima will actually be realized in the toy data set fits. Hence it is mainly the $H \to \mu^+\mu^-$, $H \to$ inv. and $H \to \gamma\gamma$ measurements that deviate from the Gaussian description. But even for these measurement, the uncertainty of the fit on the expected event counts is a decent simple characterization of the situation. Due to the background contamination in the classes that are actually used, the histograms in Fig. 6.22 are much smoother.

Comparing the uncertainties between the two toy studies show that the degree to which the precision could be improved with better event classes strongly depends on the Higgs decay. The $H \to b\bar{b}$ measurement is less than 30% worse than for perfect, process separation. In contrast, the invisible decays have to cope with large background contributions to the relevant event classes. Also the $H \to ZZ$ decay is many times more precise for the perfectly separating classes. With the event classes from Section 6.3, the $H \to ZZ$ decay mainly contributes to classes that have already large contributions from other Higgs decays, especially from $H \to W^+W^-$.

6.5.1 Bias from limited statistics

Even though this study is based on a large set of simulated events their is still a sizeable impact from the limited number of simulated background events in some of the classes. This is especially true for those classes for which only a small number of signal events are expected. A prime example are the `mu` classes that have been discussed in Section 6.3.1. Instead of simply summing up the weighted background events with a muon pair mass close to the Higgs mass the background shape is fitted over a larger range of muon pair masses. Muon pairs are expected from the $e^+e^- \to ZZ \to l^+l^-\mu^+\mu^-$. In the muon sample, the first lepton pair must also be a muon pair. One of the muon pairs must have been interpreted as the primary Z boson from a Higgs recoil. Figure 6.24 (left) shows the distribution

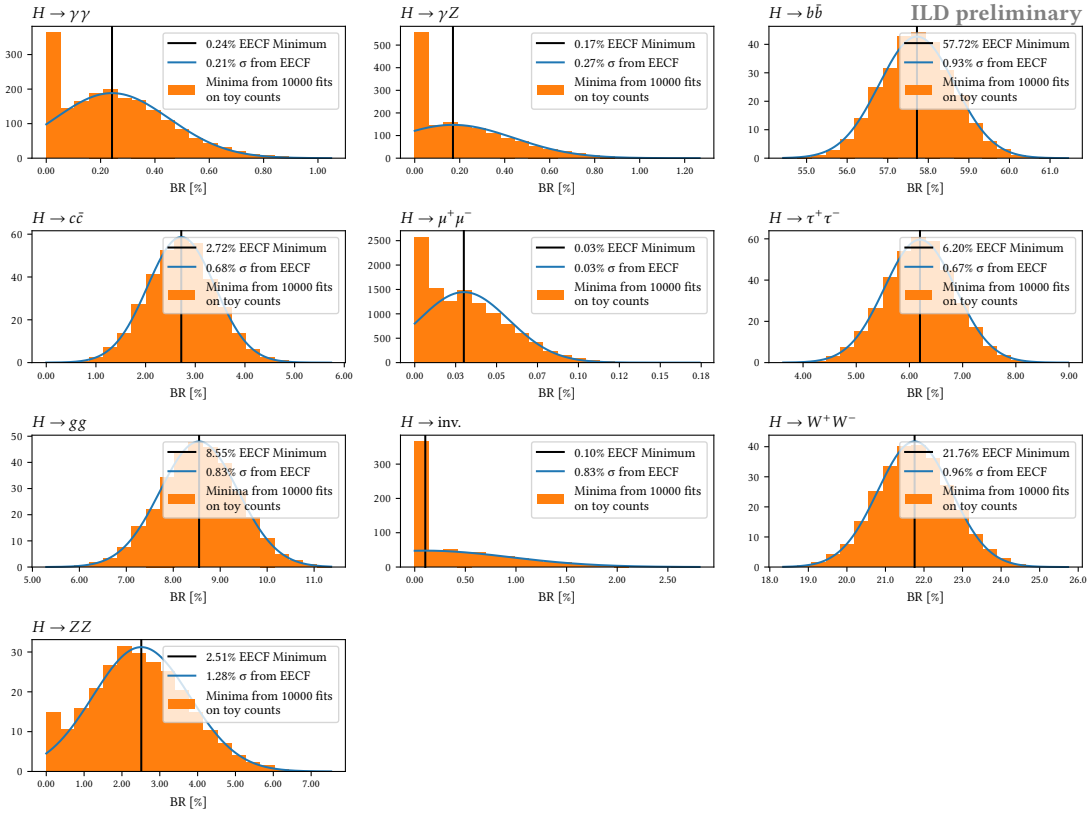

Figure 6.22: Comparison of the BR uncertainties obtained directly from the Minuit fit on the expected event counts (EECF) with the distributions from a toy study. For this figure the effects from the limited size of the simulated sample have been ignored. Both the class probability matrix and the number of expected events per class and process are based on the same sample of simulated events. Therefore the minimum of the EECF, shown as a vertical black line, is equal to the SM value of the BR. The minima from the toy fits are collected in the orange histograms. Their distributions agree well with the blue Gaussian curves that visualize the uncertainty from the EECF.

of those events that pass the sample selection step. It is described as the sum of a linear function and two Gaussians for the two mass peaks close 91 GeV and 125 GeV. Then the number of expected events per class is taken as the integral under the fitted curve over the mass range of the class.

A similar approach is taken for the background counts in the classes that focus on the $H \to \gamma\gamma$ decay. The classes `a_a_tight`, `a_a_medium` and `a_a_loose` differ only in the angle between the beam axis and the isolated photon with the second highest energy. Here the important background process has two leptons in its final state and two ISR photons at large angle with the beam axis. The lepton pair is needed in the sample selection step. As can be seen in Fig. 6.24 (right), the spectrum is well approximated by the sum of an exponential and a wide Gaussian, with a small additional constant contribution.

In a similar manner, the angle between the beam axis and the isolated photon with the highest energy is used for the $H \to \gamma Z$ classes. Here multiple types of background processes, with different shapes in $|\cos\theta_{\gamma_1}|$ contribute significantly.

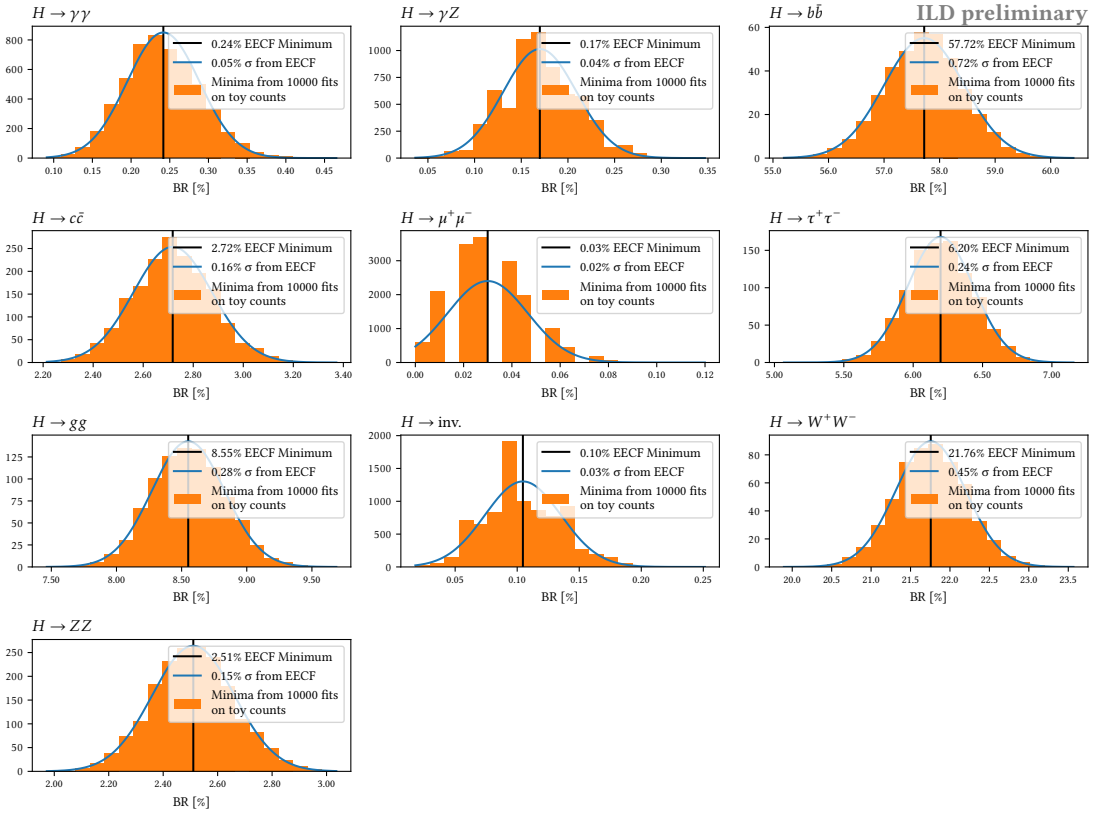

Figure 6.23: Comparison of the BR uncertainties obtained directly from the Minuit fit on the expected event counts (EECF) with the distributions from a toy study. For this figure an alternative set of classes that perfectly separates the processes is assumed. A detailed description is given for Fig. 6.22.

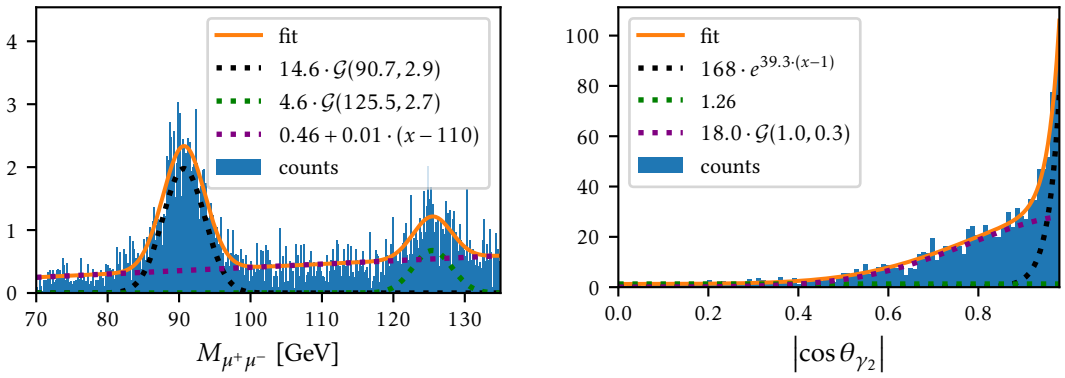

Figure 6.24: Fits of the spectra of the most important background process. Both figures are based on the $Z \to \mu^+\mu^-$ sample. The dominant background contribution to the `mu_tight` and `mu_loose` classes are final states with four leptons. Two lepton final states with two ISR photons at large angle with the beam axis are the main background in the classes created for the $H \to \gamma\gamma$ events. Each of the spectra is fitted with the sum of Gaussians, exponential functions or linear functions.

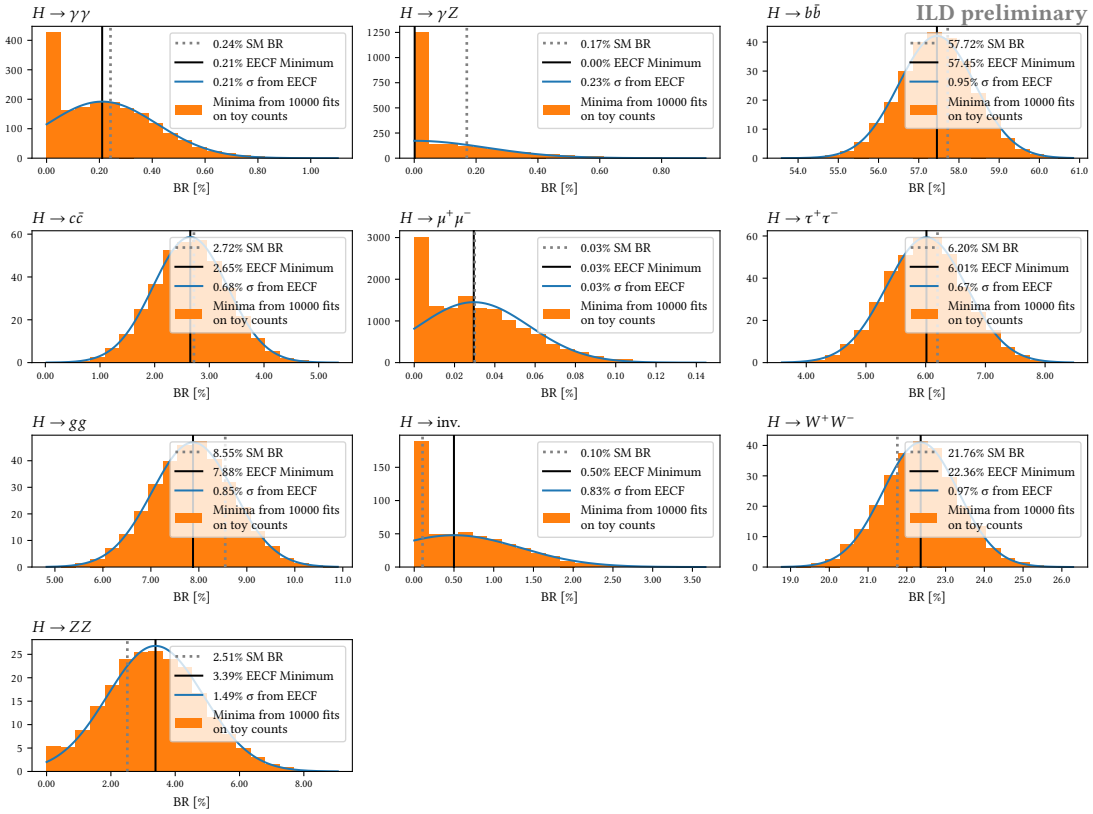

Figure 6.25: Comparison of the BR uncertainties obtained directly from the Minuit fit on the expected event counts (EECF) with the distributions from a toy study. In contrast to Fig. 6.22 separate simulated samples have been used for the class probability matrix and for the number of expected events. The gray dotted line indicates the respective SM BR.

In order to study the impact of the limited size of the simulated data sets every sample is randomly split into two statistically independent parts. With the first half of the sample the class probability matrix shown in Fig. 6.19 is built. The vector of the number of expected events per class and process is obtained from the other half of the sample. The shape fits that have been discussed above are performed independently on the two parts. Just like with Fig. 6.22 a toy study is performed and summarized in Fig. 6.25. Gray dotted lines indicate the position of the SM branching ratio. In contrast to Fig. 6.22 the minimum from the fit on the expected event counts does not coincide with the SM BR. As the distance between the two values depends on the exact split of the simulated sample into two parts, this figure should not be over-interpreted.

Repeating the random splitting multiple times allows to at least give some quantitative statements. Both $H \to b\bar{b}$ and $H \to c\bar{c}$ have only small differences between the SM BR and the minima from the fits on the expected event counts. For most branching ratios the bias from the limited size of the simulated sample stays within a 1σ uncertainty. A comparison with Fig. 6.22 shows that the while the position of the minima is biased, the uncertainty tends to be almost unaltered. While the bias for $H \to \mu^+\mu^-$ and $H \to \gamma\gamma$ can be larger than in this example, it is decent as a result of the shape fits discussed above. The $H \to \gamma Z$ branching ratio, where shape fits of multiple backgrounds are necessary, can have a larger bias from the limited size of the simulated sample. In the rather extreme example that is shown in Fig. 6.25

the $H \to \gamma Z$ backgrounds in the part of the sample that is used for the event counts have a large over-fluctuation. Therefore the minimum from the fit on the expected event counts is at the border of the allowed parameter space, at 0.0%. Here the 95% upper limit on $BR(H \to \gamma Z)$ is underestimated by more than 50% when only considering the statistical uncertainty from the fit. Similarly the invisible Higgs decays have large irreducible backgrounds. The example split of the simulated data set has a 0.5% too high expectation for the invisible BR.

For a measurement with real detector data the deviation of the fit minimum due to the limited size of the simulated data set has to be included as a systematic error source. However, at that time more resources will be available for an even larger Monte Carlo production, or for a dedicated simulation campaign in the phase space relevant here. Therefore it is expected that the associated error is negligible compared to the statistical uncertainty. An increase of the BR uncertainties from using a statistically independent simulated data set for the number of expected events per class would have indicated that the class definitions have been over-tuned to statistical artifacts in the background distributions. This could have been the case if a cut was tightened just enough to exclude some simulated background events. Given that the uncertainties are virtually unaffected if the two independent simulated data sets are used, a serious over-tuning to the simulated backgrounds is unlikely. The uncertainties obtained without the splitting the simulated data set appear to be credible.

6.6 Comparison with other projection studies

This measurement of the Higgs branching ratios will not be the only one available from the $\sqrt{s} = 250\,\text{GeV}$ program of the ILC, or of any other Higgsfactory. A comparison between the HL-LHC projections, the standard projections for the ILC, and the results from this chapter is given in Fig. 6.26.

The HL-LHC projections are based on extrapolations of current LHC analyses to an integrated luminosity of $3\,\text{ab}^{-1}$ of proton-proton collisions at 14 TeV, collected with the ATLAS and CMS experiments (Fig. 29 in [92]). Standard model cross sections for all considered Higgs production modes have been assumed in order to be able to interpret the measurements as branching ratios.

Most Higgs bosons at the ILC250 are produced by the Higgsstrahlung process. Separate measurements can be performed for each of the decay modes of the primary Z boson. A recent summary can be found in chapter 8 of the ILC report to Snowmass 2021 [40]. The Higgs decay mode results based on the decays of the primary Z boson to electrons or muons are limited by their small cross section. Usually the Higgs decay mode measurements based on the hadronic decay or the invisible decay of the primary Z boson are distinctly more precise. For some of the decay modes the results from the Z boson decay to electrons and muons have not even been included in the combined precision projection. Therefore the standard ILC Higgs BR projections can for the most part be considered as statistically independent from the results of the fit presented here. All Higgs boson decay measurements in [40] give the number of events for the product of a Higgs production cross section and a branching ratio. It is expected that the inclusive Higgsstrahlung cross section can be measured with a precision of about 1% at the ILC250 [40], [83].[2] Then the BRs can be measured without assumptions on the Higgs production cross sections. Including the uncertainty from the Higgsstrahlung cross section measurement is most important for those Higgs decay modes that can be measured with the best relative precision. The uncertainty of the $H \to b\bar{b}$ BR is dominated by the Higgsstrahlung cross section uncertainty.

[2] Scaling the $250\,\text{fb}^{-1}$ uncertainties 2.5% (LR) and 2.9% (RL) to the $900\,\text{fb}^{-1}$ that are proposed per main polarization configuration in the ILC-H20 program gives 1.3% and 1.5%, respectively. Combining both results leads to a 1.0% cross section uncertainty.

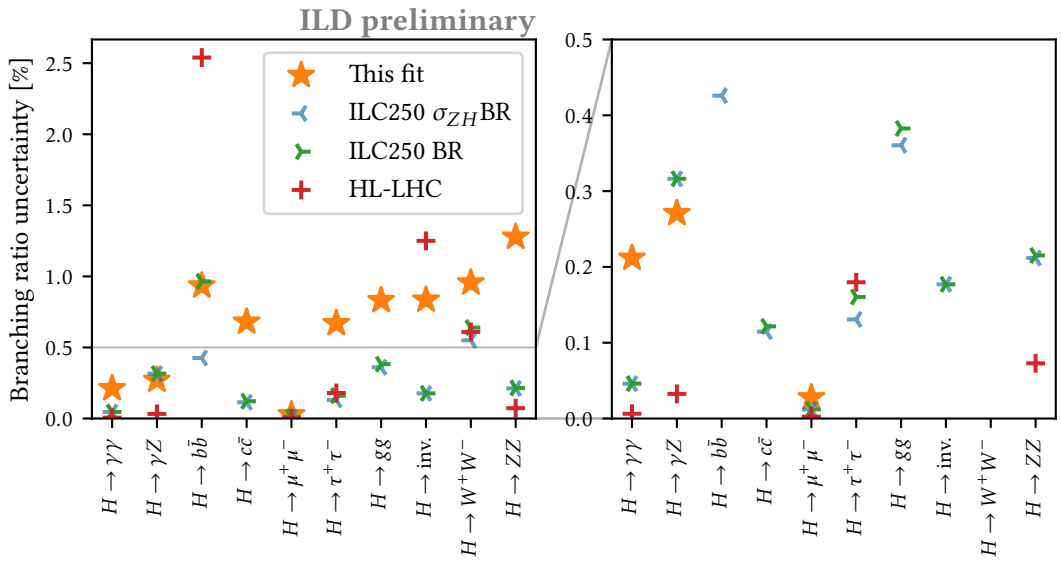

Figure 6.26: Absolute Higgs branching ratio uncertainties from the direct Higgs BR study presented in this thesis compared to the projections for the High Luminosity LHC (HL-LHC) [92] and to the standard projections for the 250 GeV program of the ILC [40]. The plot on the right hand site focuses on the small BR uncertainty region.

Figure 6.26 shows the absolute 1σ uncertainties for the measurements of the most important Higgs BRs in the SM. For those measurements for which only an upper limit can be established, the markers indicate half the 95% confidence level upper limit. Some of the Higgs BRs are measured with the best precision at the HL-LHC. However, it should be noted again that the HL-LHC results assume SM Higgs production cross sections, while the fit presented here and the standard ILC250 BR measurements are taking into account potential deviations in the Higgs production cross sections. Due to the rougher collision environment at a hadron collider, the HL-LHC measurements are most competitive for Higgs decays that can be identified by a clear signature, e.g. isolated leptons and photons with high energy. The SM BRs for $H \to \gamma\gamma$, $H \to \gamma Z$ and $H \to \mu^+\mu^-$ are small. The main benefit of a Higgsfactory measurement of these BRs is that it is not necessary to assume SM Higgs production cross sections, in contrast to the HL-LHC result. Apart from lifting this assumption, the Higgsfactory results are not expected to improve the BR precision.

A convenient way of comparing a set of experimental results with theoretical predictions is via the Wilson coefficients of a SM effective field theory, see Section 1.4. Many measurements, possibly from different colliders, are combined to derive the best set of couplings. While the $H \to ZZ$ BR uncertainty projection is smaller for the HL-LHC, the coupling between Higgs and Z bosons can additionally be measured through the Higgsstrahlung production cross section at a Higgsfactory. The latter measurement is the most important input to the coupling between Higgs and Z bosons, λ_{HZZ}, in a SMEFT fit [93]. All standard Higgs BR measurements at ILC250 directly depend on the Higgsstrahlung production cross section measurement. In contrast, the analysis presented in this chapter counts the Higgs events within each sample independently, and then assigns them to the different Higgs decay modes. Therefore no normalization by the Higgsstrahlung production cross section is necessary.

Comparable precision can be expected for the $H \to \tau^+\tau^-$ and $H \to W^+W^-$ BR measurements from HL-LHC and from a Higgsfactory. Detecting hadronic final states is much easier at a lepton collider. The hadronic Higgs decay measurements for $H \to b\bar{b}$, $H \to c\bar{c}$ and $H \to gg$ at the ILC250

are superior to the HL-LHC alternatives. Only an upper limit of 5 – 10 times the SM value is expected from HL-LHC [92]. The same source does not even include a projection for an upper limit of the gluon decay.

At a Higgsfactory, invisible Higgs decays can be detected by looking for a Z boson in a kinematic state that is compatible with the recoil against a Higgs boson. If the only particles in the event are the decay products of that Z boson (and potentially low p_T prticles from the machine background), the event is a candidate for the invisible Higgs decay. The upper limit on the invisible Higgs decays from the fit introduced in this chapter is considerably larger. The small BR of the Z boson to electrons and muons restricts the reach for measurements based on only the e^+e^-H and $\mu^+\mu^-H$ samples.

Most of the BR uncertainties derived from the fit are substantially larger than the standard ILC250 BR uncertainties. But the expected uncertainties for the $H \to b\bar{b}$ BR are similar. The uncertainty of the standard measurement is dominated by the uncertainty on the Higgsstrahlung production cross section. While the $\sigma_{ZH} \cdot \mathcal{B}(H \to b\bar{b})$ uncertainty is reduced to 0.7% when combining the samples with different decay modes of the primary Z boson, the cross section uncertainty is shared between the samples. As a result of the smaller sample sizes, the improvement from including the e^+e^-H and $\mu^+\mu^-H$ measurements is negligible [81]. Combining the standard ILC250 measurement and the new measurement from the fit in this chapter reduces the uncertainty to:[3]

$$\begin{aligned}\delta_{\mathcal{B}(H\to b\bar{b})} &= \left(\left(\delta^{\text{standard}}_{\mathcal{B}(H\to b\bar{b})}\right)^{-2} + \left(\delta^{\text{fit}}_{\mathcal{B}(H\to b\bar{b})}\right)^{-2}\right)^{-0.5} \\ &= \left((1.57\%)^{-2} + (1.62\%)^{-2}\right)^{-0.5} \\ &= 1.27\%.\end{aligned} \tag{6.8}$$

6.7 Discussion

The branching ratio fit is a simultaneous measurement of 10 observables from 8 data sets with 46 bins per data set. In this section, the impacts of some changes in the fit setup are explored.

6.7.1 Alternative Higgs decay models

A few alternative Higgs decay scenarios were already presented in Fig. 6.21. There the purpose was to verify the adaptability of the fit and the stability with respect to the starting values. Here the goal is to illustrate how the relative BR uncertainties depend on the Higgs decay model. The following scenarios are compared with the SM Higgs decays:

- `bbww`: $\mathcal{B}(H \to b\bar{b})$ increased by 5% and $\mathcal{B}(H \to W^+W^-)$ decreased by 5%.
- `e2e2`: $\mathcal{B}(H \to \mu^+\mu^-) = 1\%$ and all other BRs decreased proportional to their size.
- `inv_half`: Standard model Higgs couplings, but 50% of the Higgs bosons decay to final states with particles that are not part of the SM. These additional final states are assumed to have an invisible decay signature.
- `vb_up`: A doubling of the electroweak vector boson BRs $H \to W^+W^-$, $H \to ZZ$, $H \to \gamma Z$ and $H \to \gamma\gamma$ that is compensated by decreasing the other BRs proportional to their size.

[3] The standard uncertainty in Eq. (6.8) allows for independent deviations of the Higgsstrahlung cross section in the two main polarization configurations. If the two polarization configurations are combined, $\delta_{\sigma_{ZH}} = 1.0\%$, the standard uncertainty is reduced to $\delta^{\text{standard}}_{\mathcal{B}(H\to b\bar{b})} = 1.22\%$ and the combined uncertainty is $\delta_{\mathcal{B}(H\to b\bar{b})} = 0.97\%$.

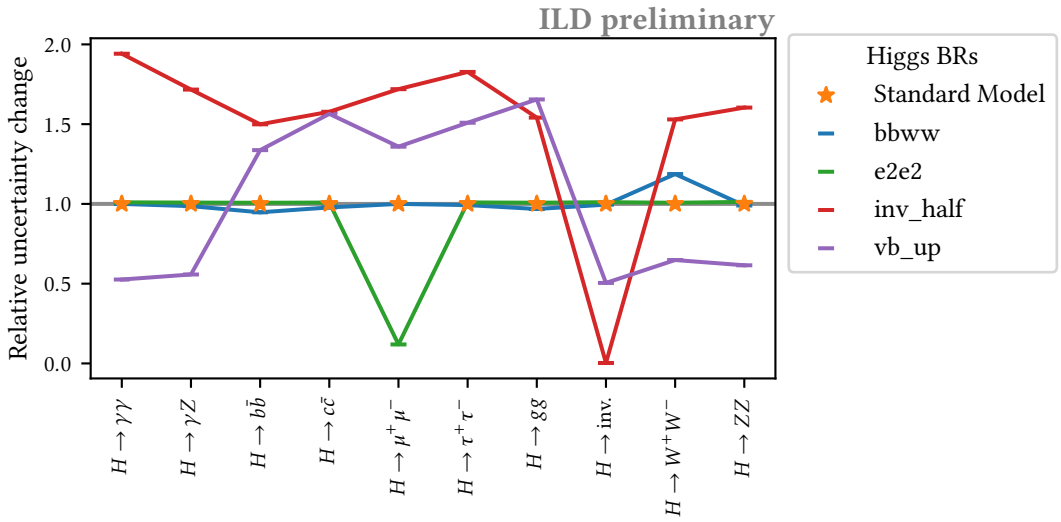

Figure 6.27: Change of the relative BR uncertainties assuming non-SM values of the main Higgs BRs. The alternative scenario are introduced in Section 6.7.1.

A larger branching ratio for a Higgs decay mode with unchanged Higgsstrahlung cross section implies more events with that Higgs decay type in the sample. Then a smaller relative uncertainty is expected. Indeed Fig. 6.27 demonstrates a smaller uncertainty for $\mathcal{B}(H \to b\bar{b})$ and a larger uncertainty for $\mathcal{B}(H \to W^+W^-)$ in the `bbww` scenario. For each of the Higgs branching ratios considered in the fit, the relative uncertainty $\sigma_\mathcal{B}/\mu_\mathcal{B}$ is compared to the relative uncertainty that would be obtained in a sample with Higgs boson decays alloted according to the SM expectation.

The $H \to b\bar{b}$ BR in the SM is considerably larger than the $H \to W^+W^-$ BR. Therefore the larger relative impact on the $H \to W^+W^-$ BR from the absolute change by 5% is expected. According to Table 6.1, the $H \to W^+W^-$ measurement has the largest anti-correlations with the $H \to c\bar{c}$, $H \to gg$ and $H \to ZZ$ measurements. Amongst the BRs that are kept at their SM expectation, the $H \to c\bar{c}$ and $H \to gg$ measurements have the largest changes in their relative uncertainty, and both uncertainties are indeed smaller in in the `bbww` scenario. The $H \to ZZ$ measurement is anti-correlated with both the $H \to b\bar{b}$ measurement and the $H \to W^+W^-$ measurement. Thus the impact from simultaneously increasing $\mathcal{B}(H \to b\bar{b})$ and decreasing $\mathcal{B}(H \to W^+W^-)$ is smaller for $H \to ZZ$ than for $H \to c\bar{c}$ or $H \to gg$.

The $H \to \mu^+\mu^-$ decay has a very unique signature that is captured with dedicated event classes. Its measurement is almost uncorrelated with all other Higgs decay measurements that are considered. Consequently the $H \to \mu^+\mu^-$ is virtually unchanged in the `bbww` scenario. With the 1% BR for $H \to \mu^+\mu^-$ that is simulated in the `e2e2` scenario, the relative uncertainty on $\mathcal{B}(H \to \mu^+\mu^-)$ obtained from the fit is almost ten times smaller. All other BRs are rescaled to roughly 99% of their SM value. In agreement with the expectation, all of their relative uncertainties increase by almost the same factor, roughly 1.01.

Increasing the invisible BR to 50% while keeping the SM Higgs production cross sections reduces the relative uncertainty only for the invisible Higgs decays. The invisible Higgs decay measurement has no large correlations with the main Higgs decay measurements. Given that the number of visible Higgs events is halved in the `inv_half` scenario, the drastic increase in relative uncertainty for the visible Higgs decay measurements is anticipated.

Doubling the electroweak vector boson BRs leads to the expected decrease in their BR measurements. Assuming that only the SM particles interact with the Higgs boson, the invisible Higgs decay rate is proportional to the $H \to ZZ$ BR. To compensate the larger electroweak vector boson BRs, the other BRs are decreased in the vb_up scenario. This is reflected in their larger relative uncertainty.

All changes of the values of the studied Higgs BRs were correctly reproduced by the minimum of the fit. Different uncertainties are expected, as the yields of the Higgs decay modes were modified. The increased relative uncertainty when a BR is smaller than in the SM expectation is not a unique feature of this analysis, but will be a shared trend for the measurements of this BR irregardless of the method. Determining the impacts from large contributions by exotic Higgs decays is difficult, as it depends on the details of that decay.

6.7.2 Individual fits per channel

Two types of Higgs samples are considered for the Higgs BR fit, identified by the decay of the primary Z boson. The log-likelihoods for the e^+e^-H and $\mu^+\mu^-H$ data sets are added for the simultaneous optimization of the Higgs BRs from both Higgsstrahlung production channels. Alternatively, the BR fit can be performed separately per channel, as shown in Fig. 6.28. The background processes and rates are different for the two channels. For example, the $e^+e^- \to e^+e^-$ background is much more important than the $e^+e^- \to \mu^+\mu^-$ background, due to the additional contributions from the t-channel Bhabha scattering Feynman diagram. Even with the lower signal efficiencies that are accepted for the e^+e^-H samples, its sample purities are smaller than the $\mu^+\mu^-H$ sample purities. The additional non-Higgs events in the samples populate predominantly the event classes that are important for the $H \to$ inv. and $H \to \gamma\gamma$ measurements. In general the measurement from the $\mu^+\mu^-H$ sample are better due to the higher Higgsstrahlung efficiency and the smaller overall background rate. A notable exception is the $H \to \gamma Z$ measurement. The relevant event classes in the $\mu^+\mu^-H$ samples have larger background expectations. With the stricter selection procedure for the e^+e^-H samples, made necessary by the additional background contributions, the backgrounds that are relevant for the $H \to \gamma Z$ measurement have been further suppressed.[4]

6.7.3 Polarization dependence

The impact of beam polarization is studied in Fig. 6.29. The luminosity sharing between the polarization configurations in the ILC-H20 proposal is summarized in Table 2.2. Here only the statistical reach is considered. Collecting data in multiple polarization configuration also gives a better control on systematic uncertainties. Measurements from different polarizations provide additional information for a global SMEFT coupling fit.

For the alternative scenarios, the total integrated luminosity of $2\,\text{ab}^{-1}$ is attributed to a single polarization configuration. Both the Higgsstrahlung cross section and some background process cross sections are larger in the LR configuration. Most statistical uncertainties would be improved by about 5% over the ILC-H20 configuration sharing results. Conversely, most uncertainties from a total RL run are expected to be about 5% worse than in the ILC-H20 scenario. The exception are the $H \to \gamma Z$ and invisible Higgs decay BR measurements.

Apart from those two measurements, the statistical uncertainties in the unpolarized configuration are comparable to the ILC-H20 results if 30% more integrated luminosity is collected with the unpolarized beams.[5]

[4] A better $H \to \gamma Z$ measurement could be obtained from the $\mu^+\mu^-H$ samples by choosing a stricter selection procedure. But then other BR measurements are worsened by the lower Higgsstrahlung efficiency. This tradeoff between the uncertainties of the different BR measurements is further discussed in Section 6.7.5.

[5] For a thorough comparison of the reach of the BR fit method for different Higgsfactory concepts, the study must be redone with samples that include the appropriate machine backgrounds.

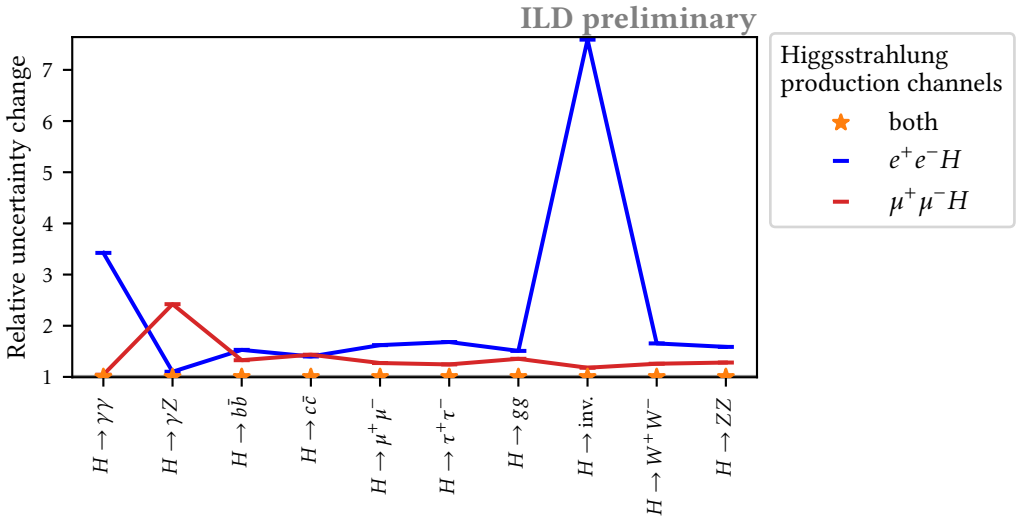

Figure 6.28: Comparison of the expected Higgs BR uncertainties from each of the Higgs production channels individually, and from the combination of both channels.

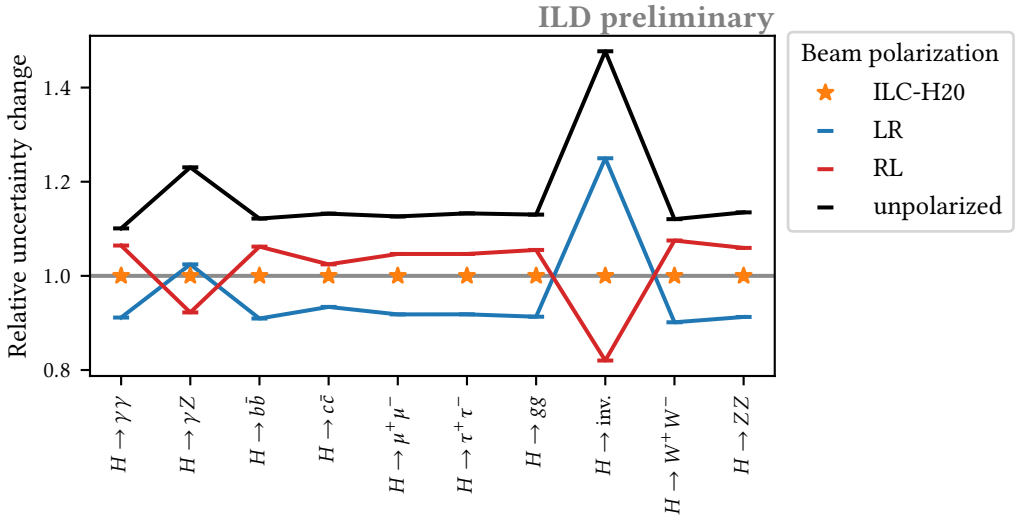

Figure 6.29: Comparison of the expected Higgs BR uncertainties from data sets with various beam polarization configurations.

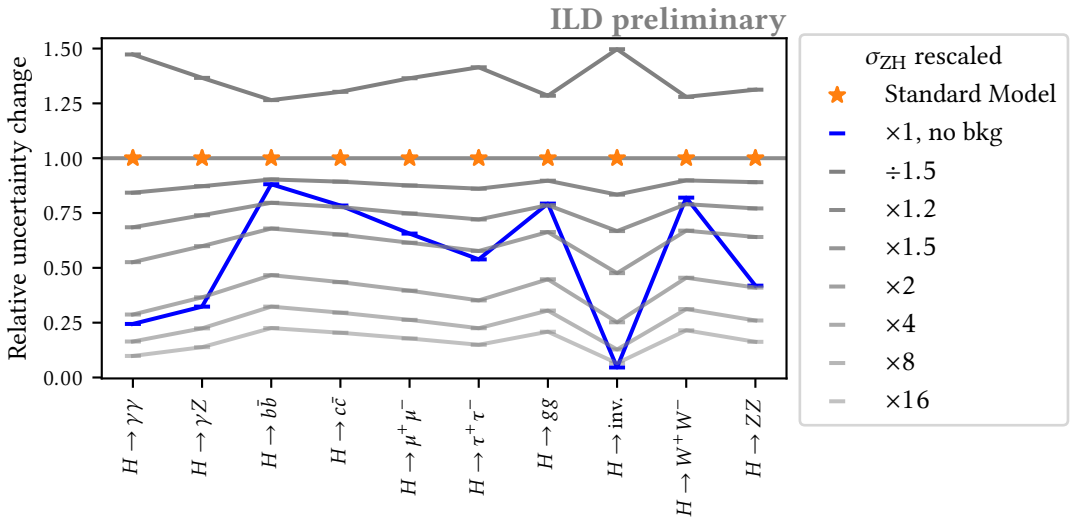

Figure 6.30: Comparison of the expected Higgs BR uncertainties for various Higgsstrahlung cross sections. Additionally, the blue graph indicates the BR uncertainties that could be achieved with perfect background separation.

6.7.4 Higgsstrahlung cross section

Fits on data sets with varying Higgsstrahlung cross section are compared in Fig. 6.30. Here the same scaling is applied to the Higgsstrahlung cross sections in all polarizations and Z decay channels. Also shown is the change of the uncertainties when assuming the SM Higgsstrahlung cross section, but with perfect background rejection. The measurements of the large, (mostly) hadronic Higgs BRs $H \to b\bar{b}$, $H \to c\bar{c}$, $H \to gg$ and $H \to W^+W^-$ are least affected by the background contamination. For the $H \to b\bar{b}$ measurement, the gain from perfect background rejection is comparable to the gain from a 20% larger Higgsstrahlung cross section.

6.7.5 Sample selection thresholds

Sample selection classifiers have been trained separately for the e^+e^-H and $\mu^+\mu^-H$ channels in Chapter 5. Their cumulative distribution functions are presented in Fig. 5.12. The maximum of the $\epsilon\sqrt{p}(t)$ curve was chosen as the event selection threshold t. This is one possible tradeoff between efficiency ϵ and purity p. The optimal threshold depends on the Higgs decay. Since only one threshold can be chosen per data set for all ten BR measurements, the best threshold depends on the relative importance that is attributed to each Higgs BR measurement. The BR uncertainties for five different threshold pair choices, listed in Table 6.2, are compared in Fig. 6.31. Here the same threshold is applied to all four polarization configuration data sets of the same channel.

Only the $H \to \gamma\gamma$ uncertainty and the invisible Higgs decay uncertainty benefit from the highest threshold pair, while all other uncertainties are substantially increased. As those two Higgs decays are poorly measured with this direct Higgs BR method, it is definitely not worth focusing on their improvement at the expense of other measurements. While the changes for the ϵp maximum pair are smaller, the same argument applies. The low threshold pair is expected to achieve slightly smaller uncertainties for the $H \to gg$ and $H \to W^+W^-$ measurements, and larger uncertainties for all other measurements. Overall, the threshold pair consisting of the respective $\epsilon\sqrt{p}$ maxima seems to be a good

	e^+e^-H	$\mu^+\mu^-H$
lowest	0.01	0.01
low	0.05	0.05
$\epsilon\sqrt{p}$	0.07	0.08
ϵp	0.18	0.20
highest	0.50	0.40

Table 6.2: Threshold pairs tested in Fig. 6.31.

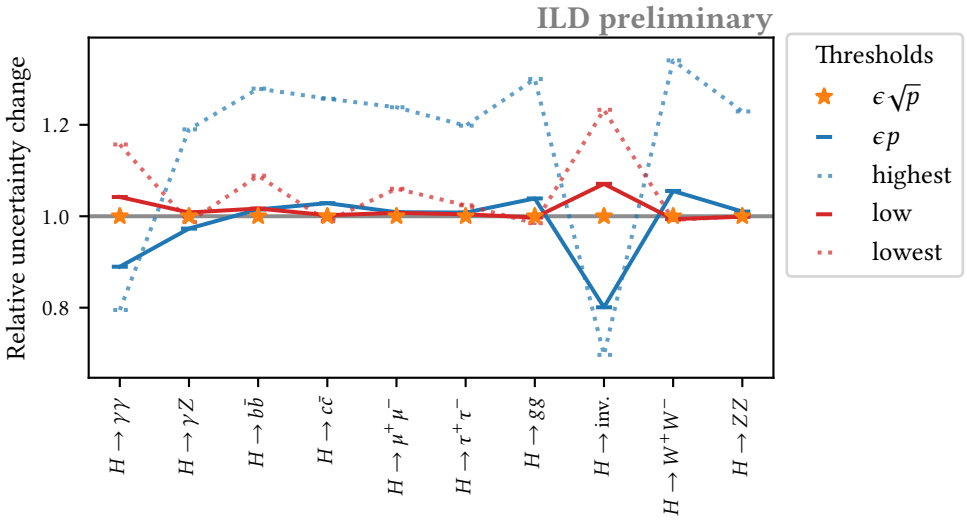

Figure 6.31: Comparison of the expected Higgs BR uncertainties from various choices for the pair of sample selection thresholds. The threshold values are listed in Table 6.2.

compromise between signal efficiency and purity.

6.8 Summary

The Higgs boson branching ratios can be measured directly from inclusive Higgs boson samples. In electron-positron collisions at $\sqrt{s} = 250\,\text{GeV}$ center-of-mass energy, most Higgs bosons are produced in association with a Z boson. Especially for Z bosons decaying to electrons or muons, the four-momentum of the Z boson can be reconstructed and used for a sample selection procedure that is independent of the Higgs boson's decay.

By partitioning a sample into several event classes and comparing the number of events per class with the expected number of events for various sets of Higgs branching ratios, the best set of BRs is identified. Because of the small BRs of the Z boson to electrons and muons, most uncertainties from this Higgs BR study are substantially larger than the expected reach for ILC250. But in contrast to the standard ILC250 BR measurements, the new results can be directly interpreted as BRs. It is not necessary to normalize them by the inclusive Higgsstrahlung cross section- The latter is usually obtained from a shape fit to the recoil mass spectrum in the e^+e^-H and $\mu^+\mu^-H$ channels.

The uncertainty on the $H \to b\bar{b}$ BR from the direct Higgs BR method is comparable in size to the standard ILC250 result. But since the two measurements are based on independent samples, they can be combined. Therefore the expected uncertainty after the $\sqrt{s} = 250\,\text{GeV}$ stage of the ILC-H20 program is $\delta^{\text{comb}}_{\mathcal{B}(H\to b\bar{b})} = 1.27\%$ (Eq. (6.8)).

7 Conclusion

A scalar particle compatible with the standard model Higgs boson has been discovered at the LHC in 2012. In the decade since, stronger bounds for extensions beyond the standard model have been set by increasingly precise measurements. The existence of additional heavy particles affects the couplings of standard model particles to the Higgs boson. Furthermore, the pattern of deviations can then be used to pin down the model type. Deviations of the order of 10% or less are expected for the major Higgs couplings in popular models of physics beyond the standard model. The projected precision after the LHC program and its subsequent HL-LHC upgrade is not sufficient to conclusively confirm or rule out those models. Further improvements are impeded by the systematic errors in proton-proton collisions.

The lowest center-of-mass energy range with a significant production rate for the $M_H = 125\,\mathrm{GeV}$ Higgs boson from electron-positron collisions is around $\sqrt{s} = 250\,\mathrm{GeV}$. This is the peak region for the Higgsstrahlung cross section. In the Higgsstrahlung process, the initial state electron-positron pair annihilates. Then the resulting intermediate off-shell Z boson is brought on-shell by its radiation of a Higgs boson. The mass of the system against which the Z boson has recoiled can be deduced from the reconstructed momentum of the Z boson. Based solely on information from the Z boson's decay products, a Higgs boson sample is selected without a bias on the decay of the Higgs bosons. The systematic errors in Higgs coupling measurements performed at a lepton collider are considerably smaller than for a hadron collider. Especially the couplings of the Higgs boson to hadrons benefit from the cleaner collision environment. With the International Linear Collider (ILC), the major Higgs couplings are expected to be measured at the percent level or below.

The International Large Detector (ILD) is a general-purpose detector proposed for the next electron-positron collider at the energy frontier. In order to obtain the desired dijet mass resolution, the entire detector is designed for optimal exploitation by particle flow algorithms. For the calorimetric system, this implies a compact design with high longitudinal and transverse granularity.

The first part of this thesis studies the performance of the CALICE SiW-ECAL technological prototype. Its $0.5 \times 0.5\,\mathrm{cm}^2$ cell size matches the specification for the ILD electromagnetic calorimeter. A stack with 15 layers and a combined depth of 15.2 X_0 has been exposed to the DESY electron beam in the $1 - 6\,\mathrm{GeV}/c$ momentum range. Over 15.000 channels were read out and combined into events. In contrast to the detector operation at the ILC, the DESY beam does not produce particles according to the timing structure that is expected by the SiW-ECAL electronics. Most importantly, events do not necessarily occur at the start of a slow clock cycle. Then hits belonging to the same event can be found in more than one slow clock cycle. The initial event reconstruction aims to combine the shower hits recorded by the 240 readout chips of the prototype into event candidates, while suppressing noise

hits. Random noise hits occur isolated and without time or location correlation with real events and are therefore easily removed. Fake hits can also be produced around the same time as a real event, if the charge deposited by the event disturbs the electronics. These effects will be greatly reduced in the next version of the front end boards. A crucial finding of this thesis is that the spreading of channel trigger times over more than one slow clock cycle occurs frequently not only for channels from different chips, but also within the same chip. By allowing the combination of consecutive readouts on the same chip for the event reconstruction, the energy uncertainty for the good events of a 3 GeV electron shower run is reduced from 26.3% to 18.2%. The energy uncertainty reaches 13.3% when only shower events recorded during quiet acquisition windows[1] are considered. 11.2% energy uncertainty has been obtained in simulated events for a detector without masked channels and without layer inefficiencies due to aging.

In the second part of this thesis, a new analysis strategy for the simultaneous determination of all major Higgs branching ratios (BR) is introduced. The study is performed based on data sets expected to be collected at the ILD during the ten year long $\sqrt{s} = 250\,\text{GeV}$ stage of the ILC (ILC-H20). Over all polarization configurations, $2000\,\text{fb}^{-1}$ are accumulated.

Higgs boson samples without a bias on the Higgs boson decay are selected from Higgsstrahlung events with the primary Z boson decaying to an electron pair (e^+e^-H) or to a muon pair ($\mu^+\mu^-H$). Averaged over the different polarization configurations, the $\mu^+\mu^-H$ samples keep $\epsilon = 71\%$ of the Higgs boson events recorded in this channel while reaching $p = 17\%$ sample purity (e^+e^-H: $\epsilon = 52\%$, $p = 12\%$). To study the apportionment of Higgs decays, each sample is partitioned into 46 categories. These categories are designed for a good discrimination between Higgs decays. Every change of Higgs BRs has a unique pattern of increases and decreases for the number of expected events per category. Given the number of observed events per category, a fit is performed to determine the contribution of each considered Higgs decay.

The fit on the number of events per category in the Higgs decay independent samples provides a simultaneous measurement of the Higgs BRs. Less than 7% of the Higgs bosons are produced in association with a Z boson decaying to an electron pair or to a muon pair. Dedicated ILD analyses that focus on a specific Higgs decay and take into account the more frequent Higgsstrahlung channels where the Z boson decays to quarks or neutrinos can usually obtain a much higher precision for the Higgs decay that they are studying. However, the $H \to b\bar{b}$ BR uncertainty obtained from the simultaneous Higgs BR fit introduced here is of comparable size to the standard ILD result. The uncertainty of this standard $\sigma_{ZH} \cdot \mathcal{B}(H \to b\bar{b})$ measurement is dominated by the uncertainty on the total Higgsstrahlung cross section. Instead of relying on the total cross section measurement, the method introduced in this thesis directly estimates the BRs by looking at the apportionment of events in a decay independent sample. The expected relative uncertainty is $\delta^{\text{direct}}_{\mathcal{B}(H\to b\bar{b})} = 1.62\%$. Removing the electron pair and muon pair channels from the channel combination in the standard method has only a minor impact on the precision. Then the new direct BR analysis and the standard analysis are uncorrelated. The resulting combined uncertainty with $2\,\text{ab}^{-1}$ of electron-positron collisions at the ILC with $\sqrt{s} = 250\,\text{GeV}$ center-of-mass energy is $\delta^{\text{comb}}_{\mathcal{B}(H\to b\bar{b})} = 1.27\%$.

[1] No other events with at least 6 layers trigger in coincidence found by the initial event reconstruction. In this run, 41% of the good shower events fall into this category.

A

Z selection efficiency tables

The presented Higgs branching ratio study uses two samples, tagged by the lepton pair (muon or electron) from the decay of the primary Z boson under the Higgsstrahlung event assumption. A separate efficiency table is produced for each of the four pure beam polarization states in both samples.

Table A.1: Efficiency table for the pure eLpL polarization of the $Z \to e^+e^-$ dataset.

			eLpL			
		σ [fb]	weight	all	loose	tight
group	process					
2f leptonic	P2f_z_eehiq	199218.270	2.97	16768566	40716	434
4f leptonic	P4f_sw_l	63.521	2.27e-1	70000	36	5
	P4f_sze_l	5619.001	2.35e-1	5989992	11680	796
	P4f_szeorsw_l	47.911	2.40e-1	50000	540	57
4f semileptonic	P4f_sw_sl	190.531	1.59e-1	298754	10	1
e1e1h	Pe1e1h_aa	0.001	3.55e-6	99750	23626	6390
	Pe1e1h_az	0.001	2.39e-6	99750	24736	6959
	Pe1e1h_bb	0.363	9.12e-4	99500	24244	6478
	Pe1e1h_cc	0.018	4.53e-5	99500	24154	6266
	Pe1e1h_dd	0.000	8.15e-8	99500	24122	6344
	Pe1e1h_e2e2	0.000	3.40e-7	99832	24472	6532
	Pe1e1h_e3e3	0.039	9.60e-5	101829	24388	6585
	Pe1e1h_gg	0.051	1.28e-4	99500	24035	6403
	Pe1e1h_inv	0.001	3.70e-5	4415	1048	290
	Pe1e1h_ss	0.000	3.85e-7	99500	24150	6346
	Pe1e1h_uu	0.000	1.88e-8	99500	24199	6417
	Pe1e1h_ww	0.133	3.28e-4	101743	25512	6759
	Pe1e1h_zz	0.016	4.02e-5	97592	24636	6854

Table A.2: Efficiency table for the pure eLpR polarization of the $Z \to e^+e^-$ dataset.

				eLpR		
		σ [fb]	weight	all	loose	tight
group	process					
2f leptonic	P2f_z_eehiq	193112.240	2.99	16168366	44254	1329
	P2f_z_l	21214.001	2.65e-1	19980000	833	143
4f leptonic	P4f_sw_l	3421.969	4.90e-2	17470376	32309	4683
	P4f_sze_l	5774.739	7.23e-2	19966638	65680	13664
	P4f_szeorsw_l	984.312	4.93e-2	4991660	128629	35693
	P4f_sznu_l	195.126	4.88e-2	999000	4	0
	P4f_ww_l	1563.418	4.89e-2	7991999	14	0
	P4f_zz_l	88.957	4.45e-2	499499	22	7
	P4f_zzorww_l	1637.057	4.88e-2	8391600	786	64
4f semileptonic	P4f_sw_sl	10264.016	1.29e-1	19900400	1406	281
	P4f_zz_sl	838.079	4.88e-2	4289250	41	7
e1e1h	Pe1e1h_aa	0.040	1.01e-4	99750	66862	48364
	Pe1e1h_az	0.027	6.79e-5	99500	68319	49208
	Pe1e1h_bb	10.285	2.58e-2	99500	68971	49821
	Pe1e1h_cc	0.511	1.28e-3	99500	69128	49840
	Pe1e1h_dd	0.001	2.31e-6	99310	68563	49479
	Pe1e1h_e2e2	0.004	9.65e-6	99833	69359	49910
	Pe1e1h_e3e3	1.108	2.72e-3	101830	69044	49991
	Pe1e1h_gg	1.447	3.64e-3	99310	68603	49362
	Pe1e1h_inv	0.019	1.03e-3	4508	3104	2286
	Pe1e1h_ss	0.004	1.09e-5	99500	68889	49685
	Pe1e1h_uu	0.000	5.33e-7	99500	68893	49748
	Pe1e1h_ww	3.782	9.29e-3	101743	70385	50422
	Pe1e1h_zz	0.444	1.14e-3	97539	67704	49131
other higgs	Pqqh_zz	8.987	4.42e-3	507907	6362	3936

Table A.3: Efficiency table for the pure eRpL polarization of the $Z \to e^+e^-$ dataset.

				eRpL		
		σ [fb]	weight	all	loose	tight
group	process					
2f leptonic	P2f_z_eehiq	190517.370	2.94	16173000	41853	1027
	P2f_z_l	16363.043	2.05e-1	19980000	641	116
4f leptonic	P4f_sw_l	29.488	4.92e-2	149833	257	164
	P4f_sze_l	5675.390	7.11e-2	19966637	54664	8214
	P4f_szeorsw_l	29.219	4.88e-2	149833	4635	2725
	P4f_sznu_l	40.683	3.39e-2	299700	8	4
	P4f_zz_l	61.417	3.84e-2	399600	13	4
	P4f_zzorww_l	55.422	4.62e-2	299700	5	1
4f semileptonic	P4f_sw_sl	86.696	3.63e-2	597260	59	33
	P4f_zz_sl	466.816	4.68e-2	2493750	14	7
e1e1h	Pe1e1h_aa	0.025	6.34e-5	99750	67550	53503
	Pe1e1h_az	0.017	4.27e-5	99750	69094	54461
	Pe1e1h_bb	6.483	1.63e-2	99500	69340	54848
	Pe1e1h_cc	0.322	8.09e-4	99500	69491	54721
	Pe1e1h_dd	0.001	1.46e-6	99310	69525	54622
	Pe1e1h_e2e2	0.002	6.08e-6	99833	69591	54900
	Pe1e1h_e3e3	0.698	1.71e-3	101830	69661	55042
	Pe1e1h_gg	0.912	2.29e-3	99500	69335	54694
	Pe1e1h_inv	0.012	7.14e-4	4086	2818	2211
	Pe1e1h_ss	0.003	6.88e-6	99500	69515	54587
	Pe1e1h_uu	0.000	3.36e-7	99500	69679	54794
	Pe1e1h_ww	2.384	5.87e-3	101490	70803	55755
	Pe1e1h_zz	0.280	7.32e-4	95677	66794	52472
other higgs	Pqqh_zz	5.751	2.83e-3	507910	6056	3735

Table A.4: Efficiency table for the pure eRpR polarization of the $Z \to e^+e^-$ dataset.

			eRpR			
		σ [fb]	weight	all	loose	tight
group	process					
2f leptonic	P2f_z_eehiq	199218.270	1.19e+1	4189566	10091	88
4f leptonic	P4f_sw_l	63.483	2.27e-1	70000	43	4
	P4f_sze_l	5629.240	2.35e-1	5989992	11721	807
	P4f_szeorsw_l	47.908	2.40e-1	50000	598	55
4f semileptonic	P4f_sw_sl	190.637	1.60e-1	298754	2	0
e1e1h	Pe1e1h_aa	0.001	3.55e-6	99750	23400	6271
	Pe1e1h_az	0.001	2.39e-6	99750	24597	7001
	Pe1e1h_bb	0.363	9.12e-4	99500	23960	6478
	Pe1e1h_cc	0.018	4.53e-5	99500	24336	6444
	Pe1e1h_dd	0.000	8.15e-8	99500	24296	6378
	Pe1e1h_e2e2	0.000	3.40e-7	99832	24329	6410
	Pe1e1h_e3e3	0.039	9.60e-5	101829	24314	6516
	Pe1e1h_gg	0.051	1.28e-4	99500	24130	6366
	Pe1e1h_inv	0.001	3.56e-5	4583	1087	304
	Pe1e1h_ss	0.000	3.85e-7	99500	24247	6423
	Pe1e1h_uu	0.000	1.88e-8	99500	24201	6413
	Pe1e1h_ww	0.133	3.29e-4	101488	25467	6657
	Pe1e1h_zz	0.016	4.02e-5	97515	24396	6811

Table A.5: Efficiency table for the pure eLpL polarization of the $Z \to \mu^+\mu^-$ dataset.

			eLpL			
		σ [fb]	weight	all	loose	tight
group	process					
4f leptonic	P4f_sze_l	5619.001	2.35e-1	5989992	2320	674

Table A.6: Efficiency table for the pure eLpR polarization of the $Z \to \mu^+\mu^-$ dataset.

				eLpR		
		σ [fb]	weight	all	loose	tight
group	process					
2f leptonic	P2f_z_l	21214.001	2.65e-1	19980000	108594	14710
4f leptonic	P4f_sze_l	5774.740	7.23e-2	19966638	14266	4714
	P4f_sznu_l	195.126	4.88e-2	999000	19500	11128
	P4f_ww_l	1563.418	4.89e-2	7992000	23542	9157
	P4f_zz_l	88.957	4.45e-2	499500	18040	10563
	P4f_zzorww_l	1637.057	4.88e-2	8391600	104612	40233
4f semileptonic	P4f_zz_sl	838.079	4.88e-2	4289250	79260	44039
e2e2h	Pe2e2h_aa	0.039	9.65e-5	99833	81348	71868
	Pe2e2h_az	0.026	6.50e-5	99833	80087	70295
	Pe2e2h_bb	9.877	2.48e-2	99750	80677	70965
	Pe2e2h_cc	0.490	1.23e-3	99750	80355	70654
	Pe2e2h_dd	0.001	2.22e-6	99500	80460	70827
	Pe2e2h_e2e2	0.004	9.26e-6	99900	77775	68393
	Pe2e2h_e3e3	1.064	2.61e-3	101898	82978	73079
	Pe2e2h_gg	1.390	3.49e-3	99500	79918	70014
	Pe2e2h_inv	0.018	9.97e-4	4459	3725	3269
	Pe2e2h_ss	0.004	1.05e-5	99750	80656	70809
	Pe2e2h_uu	0.000	5.10e-7	99750	80705	70917
	Pe2e2h_ww	3.632	8.92e-3	101744	82280	72251
	Pe2e2h_zz	0.427	1.09e-3	97629	78865	69037
other higgs	Pqqh_zz	8.987	4.42e-3	507907	6384	4005

Table A.7: Efficiency table for the pure eRpL polarization of the $Z \to \mu^+\mu^-$ dataset.

			eRpL			
		σ [fb]	weight	all	loose	tight
group	process					
2f leptonic	P2f_z_l	16363.043	2.05e-1	19980000	90798	12573
4f leptonic	P4f_sze_l	5675.390	7.11e-2	19966637	11576	3203
	P4f_sznu_l	40.683	3.39e-2	299700	3992	2277
	P4f_ww_l	14.754	4.61e-2	80000	224	120
	P4f_zz_l	61.417	3.84e-2	399600	11897	7007
	P4f_zzorww_l	55.422	4.62e-2	299700	5357	3023
4f semileptonic	P4f_zz_sl	466.816	4.68e-2	2493750	31000	17086
e2e2h	Pe2e2h_aa	0.025	6.18e-5	99833	81396	72476
	Pe2e2h_az	0.017	4.17e-5	99750	80262	71007
	Pe2e2h_bb	6.326	1.59e-2	99750	80427	71362
	Pe2e2h_cc	0.314	7.87e-4	99750	80638	71501
	Pe2e2h_dd	0.001	1.42e-6	99750	80626	71507
	Pe2e2h_e2e2	0.002	5.93e-6	99900	77869	69104
	Pe2e2h_e3e3	0.681	1.67e-3	101897	82548	73435
	Pe2e2h_gg	0.890	2.24e-3	99500	79840	70594
	Pe2e2h_inv	0.011	6.35e-4	4488	3746	3350
	Pe2e2h_ss	0.003	6.70e-6	99750	80684	71448
	Pe2e2h_uu	0.000	3.27e-7	99750	80448	71359
	Pe2e2h_ww	2.326	5.72e-3	101745	82305	72959
	Pe2e2h_zz	0.273	7.00e-4	97582	78598	69476
other higgs	Pqqh_zz	5.751	2.83e-3	507910	6525	4204

Table A.8: Efficiency table for the pure eRpR polarization of the $Z \to \mu^+\mu^-$ dataset.

			eRpR			
		σ [fb]	weight	all	loose	tight
group	process					
4f leptonic	P4f_sze_l	5629.240	2.35e-1	5989992	2390	679

B

Z selection interaction score

All feature interaction scores that are considered by the EBM models used in the tight selection procedure presented in Chapter 5.

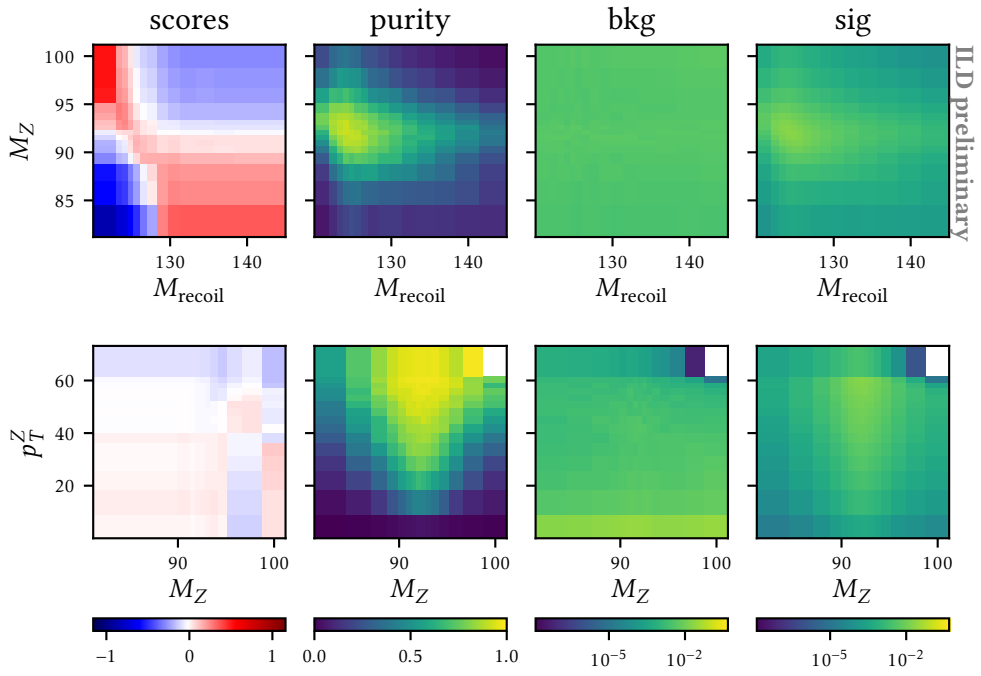

Figure B.1: Interaction scores for the $Z \to e^+e^-$ EBM. Part 1/3.

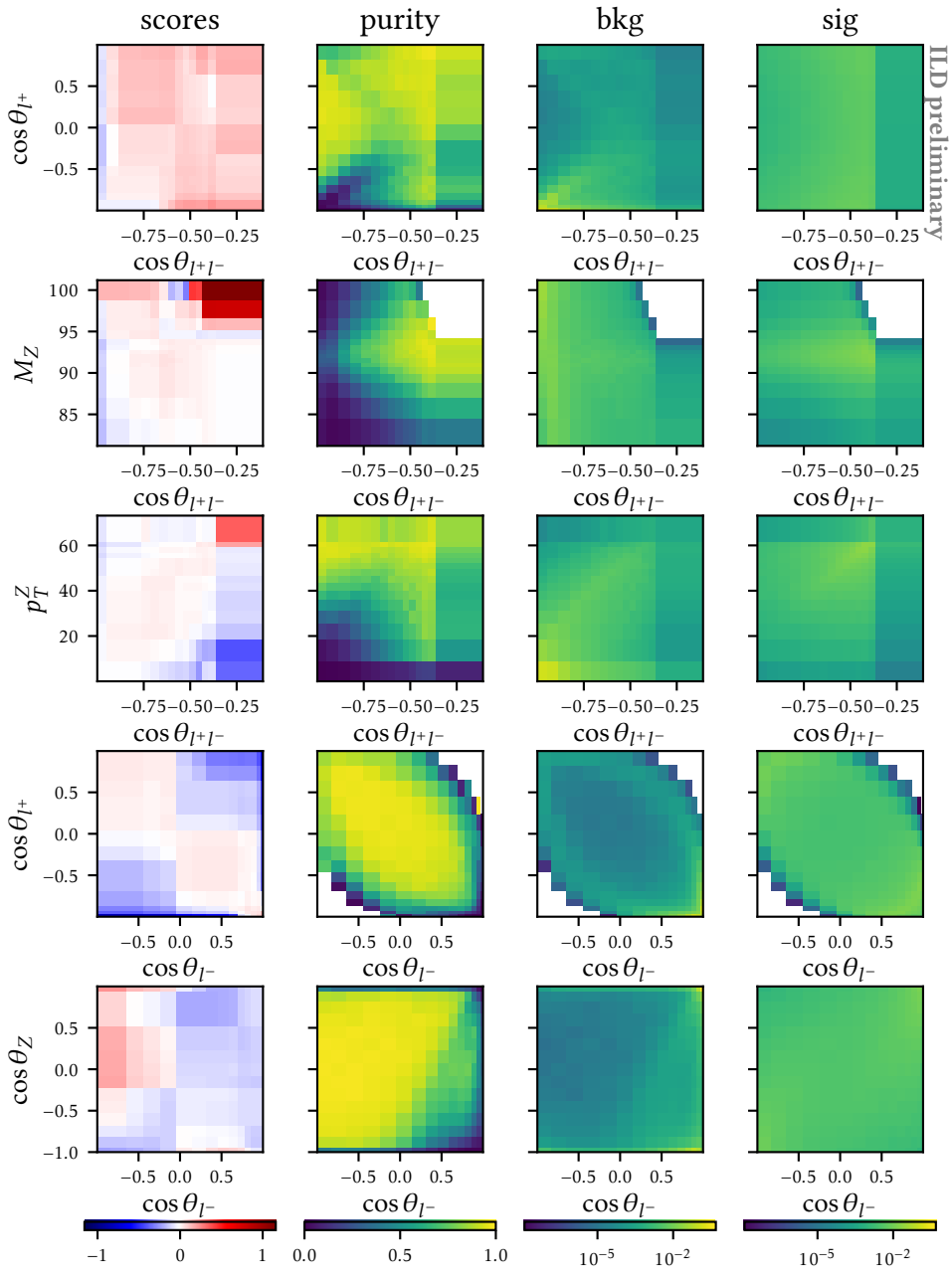

Figure B.2: Interaction scores for the $Z \to e^+e^-$ EBM. Part 2/3.

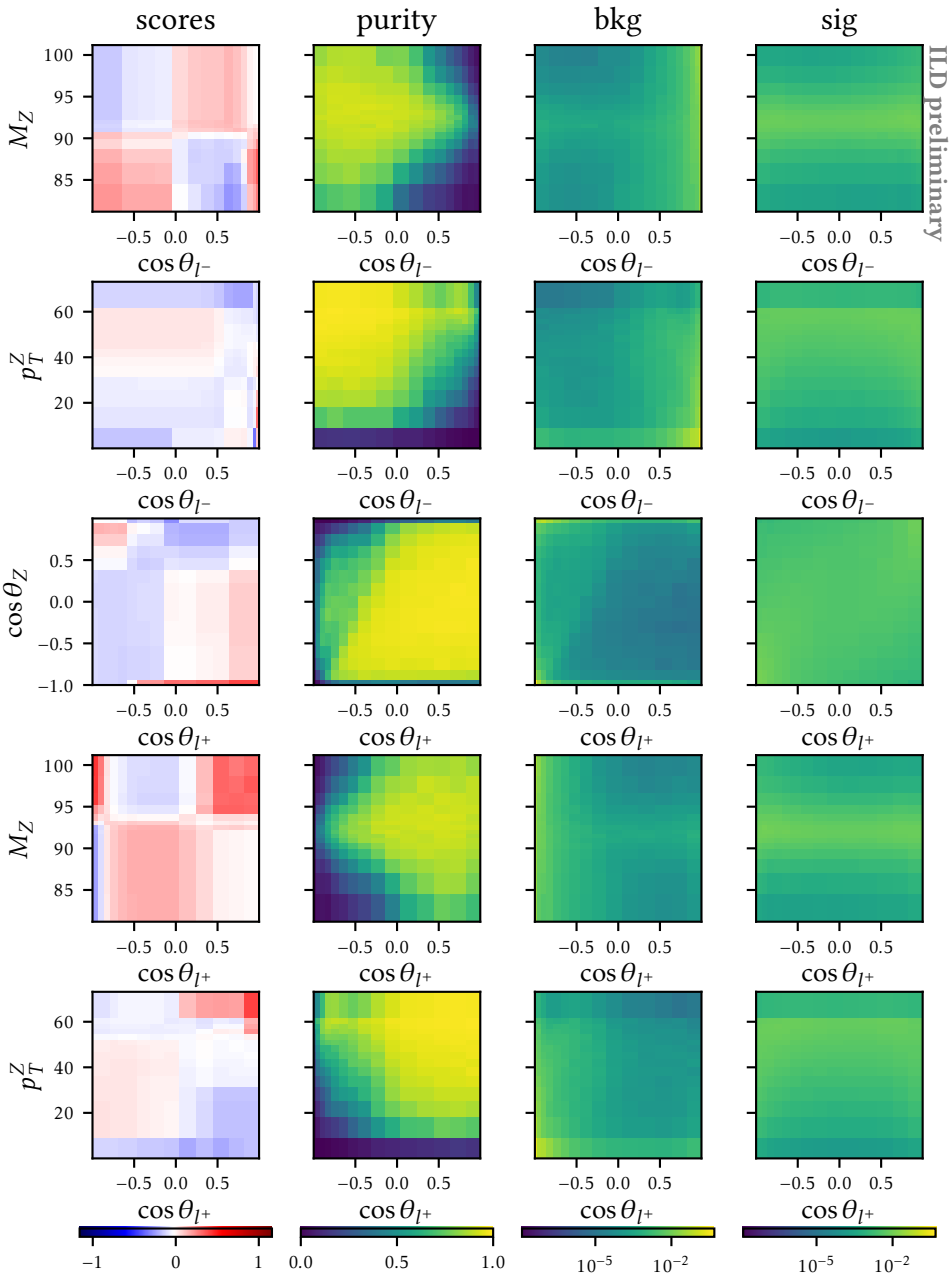

Figure B.3: Interaction scores for the $Z \to e^+e^-$ EBM. Part 3/3.

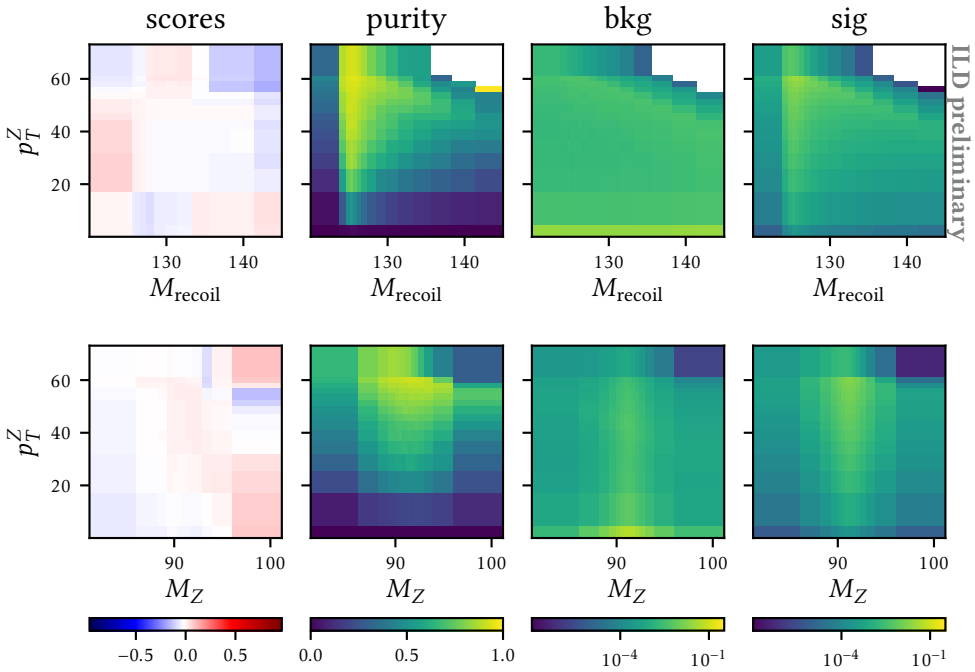

Figure B.4: Interaction scores for the $Z \to \mu^+\mu^-$ EBM. Part 1/3.

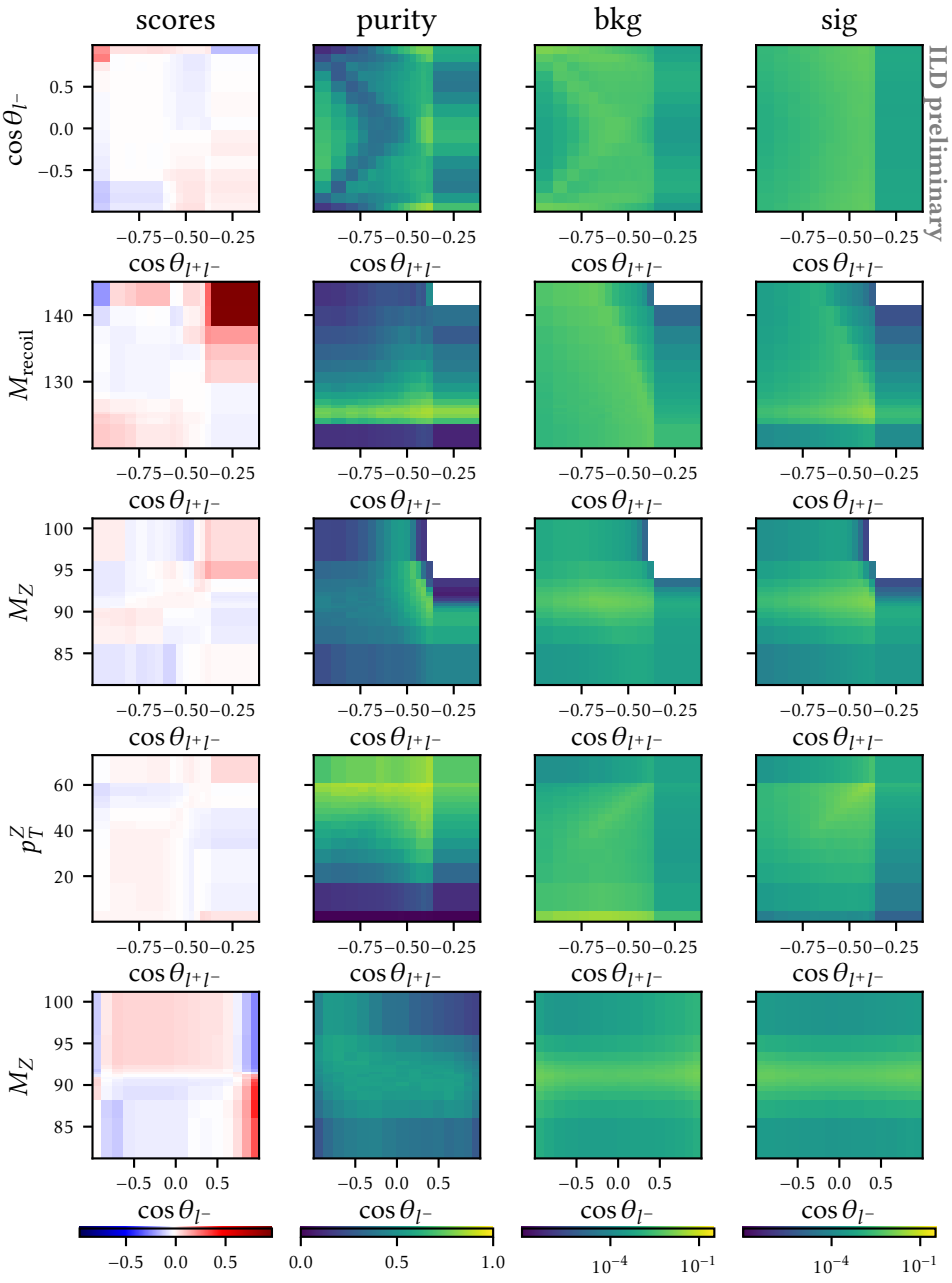

Figure B.5: Interaction scores for the $Z \to \mu^+\mu^-$ EBM. Part 2/3.

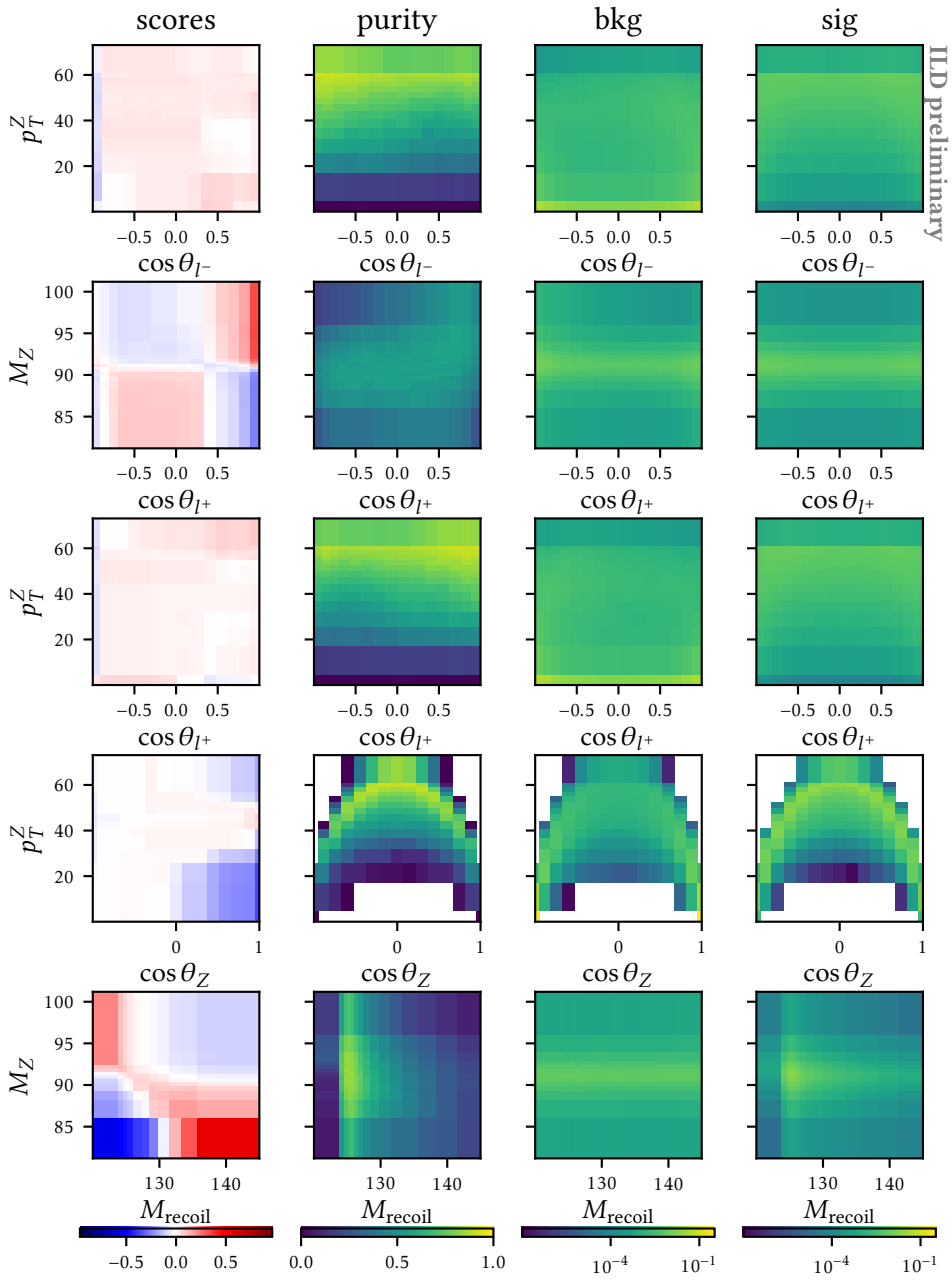

Figure B.6: Interaction scores for the $Z \to \mu^+\mu^-$ EBM. Part 3/3.

C

Z selection performance comparison

Explainable Boosting Machine (EBM) models [84] are introduced in Section 5.5. They are expected to achieve comparable performance to a blackbox model while keeping the decision process interpretable. XGBoost models [86] are a popular choice for the sample selection step in high energy physics analyses and beyond. A hyperparameter grid search found the best performance when choosing 200 estimators with a maximum depth per tree of 5 and 0.1 learning rate. Figure C.1 is a replication of Fig. 5.13 that additionally shows the performance curves of the XGBoost models trained with these optimal hyperparameters. Over the relevant range of signal efficiencies, the background efficiencies (and the purities) of the EBM model and the XGBoost model that are trained on the same data sets are indistinguishable. A noticeable difference in purity is only found at small signal efficiencies, far below the reasonable selection thresholds for this analysis. Overall, the similar AUC scores for the two types of models trained on the same data set confirm that no performance was sacrificed by choosing the interpretable EBM models for the tight sample selections step.

[86]

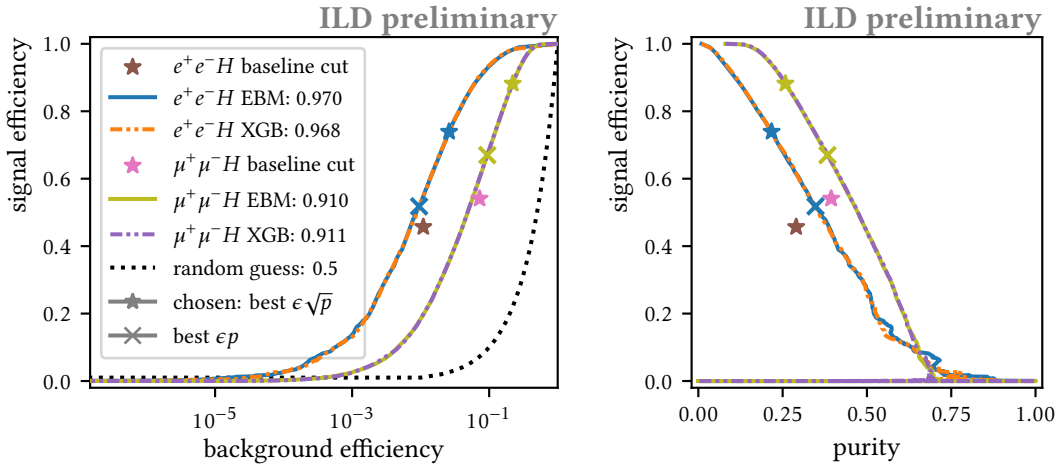

Figure C.1: Performance comparison between the chosen EBM models and XGBoost models. A version of this figure without the XGBoost model performance curves is provided as Fig. 5.13, with a full description of the figure's features. The XGBoost models used in the comparison are described in the main text of the current appendix.

D

SiW-ECAL software

The software for the operation of the SiW-ECAL technological prototype is developed within the SiWECAL-TestBeam organization on GitHub. The initial event reconstruction, introduced in Section 4.3, is closely connected to the detector commissioning. Changes to the output format of the pedestal and MIP calibration need to be reflected in the event reconstruction. Similarly, any changes to the layout of the ROOT files that contain the individual chip readout frames (`converted.root`) must be immediately propagated to the event reconstruction. Therefore it is reasonable to develop the initial event reconstruction, here termed **event building**, in synchronization with the prior steps of the analysis workflow [94]. To reduce the need for code manipulations in the future as far as possible, all numbers that are needed are provided by a default configuration file. This file is reproduced in Listing D.1. Keeping the configuration file that was used for the event building is helpful for the comparison of data files and for debugging at a later date.

```
[eventbuilding]
# The input file (must exist)
converted_path = converted.root
# The output file. If it already exists, it will be overwritten
build_path = build.root
min_slabs_hit = 4
max_entries = -1
# Integer ID of the run within the testbeam campaign
id_run = -1
# Integer ID for piece-by-piece eventbuilding within a run
id_dat = -1
# Ignore low gain
no_lg = False
# Store all channels on hit chip
zero_suppress = True
# Should not be necessary, but seems to be: We found that shower events can have
# their hit channels split over multiple BCIDs, even on the same chip.
# Without merging, the energy spread suffers a lot.
# Note: This option is incompatible with 'zero-supress = False'.
# Retriggering is handled implicitely when merging within the chip,
# so 'drop_retrigger_delta' in the [bcid] section becomes inactive.
merge_within_chip = True
# Do not (re)-build the events but only change the configuration options.
# Then 'converted_path' should be a build.root file already
redo_config = False
# Less verbose output, especially for batch processing
no_progress_info = False
# Drop events with too many hits. With -1, no events are dropped.
max_hits_per_event = -1

# For each layer, one of 10,11,12,13,COB. Comma seperated list
asu_versions = 13,13,COB,COB,11,11,11,12,12,12,12,11,11,10,11
```

```
# Tungsten thickness in mm. A single number is interpreted as per layer (e.g. 0)
w_config = 2.8,2.8,2.8,2.8,2.8,2.8,2.8,4.2,4.2,4.2,4.2,4.2,4.2,4.2,4.2,4.2

calibration_dir = ../../calibration
calibration_tag = method2_Pedestal_W_run_050263_merged
masked_file =              %(calibration_dir)s/masked/masked_%(calibration_tag)s.txt
mapping_file =             %(calibration_dir)s/mapping/fev10_chip_channel_x_y_mapping.txt
mapping_file_cob =         %(calibration_dir)s/mapping/fev11_cob_chip_channel_x_y_mapping.txt
pedestals_file =           %(calibration_dir)s/pedestals/Pedestal_%(calibration_tag)s_highgain.txt
pedestals_lg_file =        %(calibration_dir)s/pedestals/Pedestal_%(calibration_tag)s_lowgain.txt
mip_calibration_file =     %(calibration_dir)s/mip_calib/MIP_%(calibration_tag)s_highgain.txt
mip_calibration_lg_file = %(calibration_dir)s/mip_calib/MIP_%(calibration_tag)s_lowgain.txt

[bcid]
skip_noisy_acquisition_start = 50
bad_value = -999
drop_values = 0,901
drop_retrigger_delta = 2
merge_delta = 3
overflow = 4096

[geometry]
n_chips = 16
n_scas = 15
n_channels = 64
delta_x_fev13 = 60

[commissioning]
pedestal_min_average = 200
pedestal_min_scas = 3
pedestal_min_value = 10
mip_cutoff = 0.5
mip_malfunctioning_chip = 1000
```

Listing D.1: `default_eventbuilding.cfg`

New monitoring tools [95], [96], based on the event building results, are discussed in Section 4.4. Since the event building is one of the steps in the monitoring workflow, its configuration options are a subset of the monitoring configuration. An example configuration file for the monitoring is reproduced in Listing D.2. By far the most time consuming step in the monitoring loop is the conversion from the DAQ output to `converted.root` files. When allocating multiple CPU cores for the monitoring loop, was faster than the data taking at DESY.

```
[monitoring]
max_workers = 10
output_parent = data
skip_dirty_dat = False
# Only used if the raw data is in raw.bin_XXXX format. -1 for no split.
See README.md.
binary_split_M = 50
# Needs some extra python packages, and adds some extra time.
# For batch processing of finished runs, you might want to set this
# to 'quality_info'= False'.
quality_info = True

[snapshot]
after = 1, 10
every = 50
# Setting this to True can save some disk space for long runs.
delete_previous = False

# Any field in 'default_eventbuilding.cfg' can be overwritten here.
# That is also where you can find explanations of their meaning.
# (local) ./continuous_event_building/SiWECAL-TB-analysis/eventbuilding/default_eventbuilding.cfg
# (online) https://github.com/SiWECAL-TestBeam/SiWECAL-TB-analysis/tree/eventbuilding/default_eventbuilding.cfg
[eventbuilding]
min_slabs_hit = 6
# Tungsten thickness in mm. A single number is interpreted as per layer (e.g. 0)
# w_config = 2.8,2.8,2.8,2.8,2.8,2.8,2.8,4.2,4.2,4.2,4.2,4.2,4.2,4.2,4.2,4.2
w_config = 0
asu_versions = 13,13,COB,COB,11,11,11,12,12,12,12,11,11,10,11
```

```
max_entries = -1
no_lg = False
zero_suppress = True
merge_within_chip = True
pedestals_file =          /eos/project/s/siw-ecal/TB2022-03/calibration/pedestals/20220430/original_layer_sorting/Pedestal_method2_fromMIPScan_LowEnergyElectrons_highgain.txt
pedestals_lg_file =       /eos/project/s/siw-ecal/TB2022-03/calibration/pedestals/20220430/original_layer_sorting/Pedestal_method2_fromMIPScan_LowEnergyElectrons_lowgain.txt
mip_calibration_file =    /eos/project/s/siw-ecal/TB2022-03/calibration/mip_calib/20220512/original_layer_sorting/MIP_pedestalsubmode2_fromMIPScan_LowEnergyElectrons_highgain.txt
mip_calibration_lg_file = /eos/project/s/siw-ecal/TB2022-03/calibration/mip_calib/20220512/original_layer_sorting/MIP_pedestalsubmode2_fromMIPScan_LowEnergyElectrons_lowgain.txt
mapping_file =            continuous_event_building/SiWECAL-TB-analysis/mapping/fev10_chip_channel_x_y_mapping.txt
mapping_file_cob =        continuous_event_building/SiWECAL-TB-analysis/mapping/fev11_cob_rotate_chip_channel_x_y_mapping.txt
```

Listing D.2: `monitoring.cfg`

E
Résumé

Une particule scalaire compatible avec le boson de Higgs du modèle standard été découverte au LHC en 2012. Au cours de la décennie qui a suivi, des limites plus fortes pour les extensions au-delà du modèle standard ont été établies par des mesures de plus en plus précises. L'existence de particules lourdes supplémentaires affecterait les couplages entre les particules du modèle standard et le boson de Higgs. De plus, la structure des déviations peut être utilisée pour déterminer le type de modèle. On s'attend à des écarts de 10% ou moins pour les principaux couplages au Higgs dans les modèles populaires de la physique au-delà du modèle standard. La précision finale prévue après le programme LHC et son successeur HL-LHC ne sera sans doute pas suffisante pour confirmer ou infirmer de manière concluante ces modèles, et sera limitée par les erreurs systématiques dans les collisions proton-proton.

Dans les collisions électron-positron, la gammme d'énergie dans le centre de la masse la plus favorable avec un taux de production significatif pour le boson de Higgs de masse $M_H = 125\,\text{GeV}$ est autour de $\sqrt{s} = 250\,\text{GeV}$. Il s'agit de la région du pic de la section efficace du Higgsstrahlung. Dans ce processus de Higgsstrahlung, la paire électron-positron de l'état initial s'annihile en un boson Z, hors couche de masse. Ensuite, ce boson Z intermédiaire retourne sur sa couche de masse par l'émission d'un boson de Higgs. La masse de recul du boson Z peut être déduite de son impulsion reconstituée. En se basant uniquement sur les informations provenant des produits de désintégration du boson Z, un échantillon de bosons de Higgs peut être sélectionné avec un biais minimal sur leur mode de désintégration. Les erreurs systématiques sur les mesures du couplage de Higgs effectuées dans un collisionneur de leptons sont donc considérablement plus faibles que dans le cas d'un collisionneur de hadrons. En particulier, les couplages du boson de Higgs aux hadrons bénéficient d'un environnement de collision plus favorable. Avec l'International Linear Collider (ILC, collisionneur linéaire international), les principeux couplages de boson de Higgs peuvent être mesurés au niveau du pourcent ou moins. L'International Large Detector (ILD, grand détecteur international) est un détecteur polyvalent proposé pour le prochain collisionneur électron-positron à la frontière de l'énergie. Afin d'obtenir la résolution de masse de dijet souhaitée, l'ensemble du détecteur est conçu pour une exploitation optimale par des algorithmes de reconstruction du flux de particules (particle flow). Pour le système calorimétrique, cela implique un design compact avec une haute granularité longitudinale et transversale.

La première partie de cette thèse étudie les performances d'un tel calorimètre ultragranulaire, le prototype technologique CALICE SiW-ECAL. Sa taille de cellule de $0.5 \times 0.5\,\text{cm}^2$ correspond aux spécifications pour le calorimètre électromagnétique d'ILD. Un empilement de 15 couches et d'une profondeur combinée de $15.2\ X_0$ a été exposé au faisceau d'électrons du DESY dans la gamme d'impulsion $1 - 6\,\text{GeV}/c$. Plus de 15 000 de canaux ont été lus et combinés pour former des événements. Contrai-

rement au fonctionnement du détecteur à l'ILC, où un événement est attendu par cycle d'horloge, le faisceau au DESY ne fournit pas de particules selon la structure temporelle attendue par l'électronique du SiW-ECAL. En particulier, les événements ne se produisent pas nécessairement au début d'un cycle d'horloge, et les dépots d'énergie appartenant à un même événement peuvent alors être partagés entre plusieurs cycles. La reconstruction initiale de l'événement vise à combiner les dépots de gerbe enregistrés par les 240 puces de lecture du prototype en candidats d'événements, tout en supprimant les contributions du bruit. Les bruits aléatoires se produisent de manière isolée et sans corrélation temporelle ou géographique avec des événements réels. De fausses contributions peuvent également être produites en même temps qu'un événement réel, si la charge déposée par l'événement perturbe l'électronique. Ces effets seront considérablement réduits dans la prochaine version des cartes frontales. Une découverte cruciale de cette thèse est que l'étalement des temps de déclenchement des canaux sur plus d'un cycle d'horloge se produit fréquemment, non seulement pour des canaux de différentes puces de lecture, mais aussi au sein d'une même puce. En permettant la combinaison de lectures consécutives sur la même puce pour la reconstruction des événements, l'incertitude sur la mesure de l'énergie pour les bons événements d'une gerbe d'électrons 3 GeV est réduite de 26.3% à 18.2%. Elle atteint 13.3% lorsque seuls les événements de gerbe enregistrés pendant les fenêtres d'acquisition silencieuses sont pris en compte. Une incertitude de 11.2% sur l'énergie mesurée a été obtenue dans des événements simulés pour une version du détecteur sans canaux masqués et sans inefficacité des couches dues au vieillissement, ce qui représente un accord tout à fait raisonnable.

Dans la deuxième partie de cette thèse, une nouvelle stratégie d'analyse pour la détermination directe et simultanée de tous les principaux rapports de branchement de Higgs est présentée. L'étude est réalisée sur la base des échantillons de données qui devraient être collectées à l'ILD pendant l'étape $\sqrt{s} = 250\,\text{GeV}$ de l'ILC, d'une durée de dix ans (scénario ILC-H20). En sommant toutes les configurations de polarisation, une luminosité intégrée de $2\,\text{ab}^{-1}$ serait accumulée. Des échantillons de bosons de Higgs avec un biais minimal sur la désintégration du boson de Higgs sont sélectionnés à partir des événements de Higgsstrahlung où le boson primaire Z se désintègre en une paire d'électrons (e^+e^-H) ou en une paire de muons ($\mu^+\mu^-H$). Moyennés sur les différentes configurations de polarisation, les échantillons de $\mu^+\mu^-H$ conservent $\epsilon = 71\%$ des événements enregistrés dans ce canal, pour une pureté de $p = 17\%$ ($e^+e^-H : \epsilon = 52\%$, $p = 12\%$). Pour étudier la répartition des modes de désintégrations du boson de Higgs, chaque échantillon est divisé en 46 catégories, conçues pour une bonne discrimination entre les différents modes. Chaque changement des rapports de branchement présente un modèle unique d'augmentation et de diminution du nombre d'événements attendus par catégorie. Compte tenu du nombre d'événements observés par catégorie, un ajustement statistique est réalisé pour déterminer la contribution de chaque mode considéré.

L'ajustement sur le nombre d'événements par catégorie dans les échantillons indépendants du mode de désintégration permet une mesure simultanée des rapports de branchement. Moins de 7% des bosons de Higgs sont produits en association avec un boson Z qui se désintègre en une paire d'électrons ou une paire de muons. Les analyses standard à l'ILD se concentrent sur un mode de désintégration du boson de Higgs spécifique en intégrant les canaux de Higgsstrahlung les plus fréquents, où le boson Z se désintègre en quarks ou en neutrinos. Elles obtiennent généralement une précision bien plus élevée pour leur mode. Cependant, l'incertitude sur le rapport de branchement $H \to b\bar{b}$ obtenue à partir de l'ajustement simultané des rapports de branchement, introduit ici, est de taille comparable aux résultats avec la méthode standard à l'ILD. L'analyse standard extrait $\mathcal{B}(H \to b\bar{b})$ de la mesure de $\sigma_{ZH} \cdot \mathcal{B}(H \to b\bar{b})$, et est dominée par l'incertitude sur la section efficace totale du Higgsstrahlung. La méthode de détermination directe des rapports de branchements s'en affranchit. L'incertitude relative attendue est $\delta^{\text{direct}}_{\mathcal{B}(H\to b\bar{b})} = 1.62\%$.

La suppression des canaux de désintégration du Z en paires d'électrons et de muons pour la méthode standard n'a qu'un impact mineur sur la précision. Ainsi, la nouvelle analyse directe du rapports

de branchement et l'analyse standard réduite ne sont pas corrélées. Leur combinaison sur une luminosité intégrée de $2\,\mathrm{ab}^{-1}$ pour l'ensemble des collisions électron-positron à l'ILC avec une énergie au centre de masse de $\sqrt{s} = 250\,\mathrm{GeV}$ réduit l'incertitude à $\delta^{\mathrm{comb}}_{\mathcal{B}(H\to b\bar{b})} = 1.27\%$.

F

Acknowledgements

My first thanks goes to the members of the jury. Without the critical questions and demands for additional explanations from Imad Lakineh this manuscript would have been much less instructional. Thank you Dirk Zerwas for improving my understanding of the Standard Model and particle physics, first as a lecturer during my masters and still now through insightful comments on the thesis manuscript. I also want to thank Roberto Salerno, who acted as the president, and Lucia di Ciaccio and Manqi Ruan.

I am grateful to Jean-Claude for having given me a lot of freedom to explore, oftentimes fail, and thereby grow as a researcher while still making sure that I stay on track to finish this thesis. Thank you Fabricio for listening to my complaints about software struggles, and for many shared debugging sessions. Thank you Henri for many discussion on my analysis, but also on French wines, the history of France, Ampère's chair and École Polytechnique in general. Thank you Vincent especially for your guidance in the SiW-ECAL part of my thesis work.

I am grateful to all my ILD colleagues, past and present, for the great tools that they have created. A special thanks belongs to Daniel Jeans and the other members of the ILC group at KEK for hosting me during the first weeks of my PhD studies and for teaching me how to navigate the world of ILCSoft.

The days during the beam tests at DESY were long and intense, but extremely instructive and satisfying. I have learnt a lot from all members of the SiW-ECAL team but want to especially thank Stéphane and Jerôme for teaching my electronics, Yuichi for supporting my quest for modern collaborative tools and Adrián for knowing everything about the software stack.

A few years have passed since elementary school enrollment. David and Maxi, you have been my close friends ever since, and I hope this will never change. Thank you for teaching me about wine making and tractors, and for sometimes pretending that you find particle physics interesting. Muriel and Bene, it hasn't quite been since elementary school, but long enough to assume that you will stay stuck with me.

From my time in Zurich I would like to single out Andreas, Philip and Jules. Thank you for helping me to find the motivation to spend summers and winters at the ETH MathBib, but also for all the time that we spend together not studying. And of course Felix, my faithful seatmate and source of wisdom in almost every lecture. Giulia, I would have never guessed that the girl sitting next to me at the introductory meeting of the exchange semester in Hong Kong would end up studying with me over the next five years in both Zurich and Paris. What a nice surprise, let's see how many more cities we can add to that list in the future. Lucienne, thank you for showing me every field path that can be reached with the Navigo pass. Alberto, you were stuck with me both as a flatmate and as a student in the same lab. So - sorry for the dirty dishes and thank you for all the commutes, discussions and help.

Finally, I need to thank my family: my parents for providing a loving and supporting home to grow up in and come back to, and my three no-longer-small siblings Marlene, Johannes and Amelie for filling that home with life and warmth.

Bibliography

[1] S. L. Glashow, "Partial Symmetries of Weak Interactions", *Nucl. Phys.*, vol. 22, pp. 579–588, 1961. DOI: 10.1016/0029-5582(61)90469-2 (cit. on p. 1).

[2] S. Weinberg, "A Model of Leptons", *Phys. Rev. Lett.*, vol. 19, pp. 1264–1266, 1967. DOI: 10.1103/PhysRevLett.19.1264 (cit. on p. 1).

[3] A. Salam, "Weak and Electromagnetic Interactions", *Conf. Proc. C*, vol. 680519, pp. 367–377, 1968. DOI: 10.1142/9789812795915_0034 (cit. on p. 1).

[4] S. L. Glashow, J. Iliopoulos, and L. Maiani, "Weak Interactions with Lepton-Hadron Symmetry", *Phys. Rev. D*, vol. 2, pp. 1285–1292, 1970. DOI: 10.1103/PhysRevD.2.1285 (cit. on p. 1).

[5] J. J. Thomson, "Cathode rays", *Phil. Mag. Ser. 5*, vol. 44, pp. 293–316, 1897. DOI: 10.1080/14786449708621070 (cit. on p. 1).

[6] E. Rutherford, "The scattering of alpha and beta particles by matter and the structure of the atom", *Phil. Mag. Ser. 6*, vol. 21, pp. 669–688, 1911. DOI: 10.1080/14786440508637080 (cit. on p. 2).

[7] E. D. Bloom *et al.*, "High-Energy Inelastic e p Scattering at 6-Degrees and 10-Degrees", *Phys. Rev. Lett.*, vol. 23, pp. 930–934, 1969. DOI: 10.1103/PhysRevLett.23.930 (cit. on p. 2).

[8] M. Breidenbach, J. I. Friedman, H. W. Kendall, *et al.*, "Observed behavior of highly inelastic electron-proton scattering", *Phys. Rev. Lett.*, vol. 23, pp. 935–939, 1969. DOI: 10.1103/PhysRevLett.23.935 (cit. on p. 2).

[9] F. J. Hasert *et al.*, "Observation of Neutrino Like Interactions Without Muon Or Electron in the Gargamelle Neutrino Experiment", *Phys. Lett. B*, vol. 46, pp. 138–140, 1973. DOI: 10.1016/0370-2693(73)90499-1 (cit. on p. 2).

[10] G. Arnison *et al.*, "Experimental Observation of Isolated Large Transverse Energy Electrons with Associated Missing Energy at $\sqrt{s} = 540$ GeV", *Phys. Lett. B*, vol. 122, pp. 103–116, 1983. DOI: 10.1016/0370-2693(83)91177-2 (cit. on p. 2).

[11] M. Banner *et al.*, "Observation of Single Isolated Electrons of High Transverse Momentum in Events with Missing Transverse Energy at the CERN anti-p p Collider", *Phys. Lett. B*, vol. 122, pp. 476–485, 1983. DOI: 10.1016/0370-2693(83)91605-2 (cit. on p. 2).

[12] G. Arnison *et al.*, "Experimental Observation of Lepton Pairs of Invariant Mass Around 95-GeV/c**2 at the CERN SPS Collider", *Phys. Lett. B*, vol. 126, pp. 398–410, 1983. DOI: 10.1016/0370-2693(83)90188-0 (cit. on p. 2).

[13] P. Bagnaia *et al.*, "Evidence for $Z^0 \to e^+e^-$ at the CERN $\bar{p}p$ Collider", *Phys. Lett. B*, vol. 129, pp. 130–140, 1983. DOI: 10.1016/0370-2693(83)90744-X (cit. on p. 2).

[14] S. Schael *et al.*, "Precision electroweak measurements on the Z resonance", *Phys. Rept.*, vol. 427, pp. 257–454, 2006. DOI: 10.1016/j.physrep.2005.12.006. arXiv: hep-ex/0509008 (cit. on p. 2).

[15] S. Schael *et al.*, "Electroweak Measurements in Electron-Positron Collisions at W-Boson-Pair Energies at LEP", *Phys. Rept.*, vol. 532, pp. 119–244, 2013. DOI: 10.1016/j.physrep.2013.07.004. arXiv: 1302.3415 [hep-ex] (cit. on p. 2).

[16] F. Abe *et al.*, "Observation of top quark production in $\bar{p}p$ collisions", *Phys. Rev. Lett.*, vol. 74, pp. 2626–2631, 1995. DOI: 10.1103/PhysRevLett.74.2626. arXiv: hep-ex/9503002 (cit. on p. 2).

[17] S. Abachi *et al.*, "Observation of the top quark", *Phys. Rev. Lett.*, vol. 74, pp. 2632–2637, 1995. DOI: 10.1103/PhysRevLett.74.2632. arXiv: hep-ex/9503003 (cit. on p. 2).

[18] G. Aad *et al.*, "Observation of a new particle in the search for the Standard Model Higgs boson with the ATLAS detector at the LHC", *Phys. Lett. B*, vol. 716, pp. 1–29, 2012. DOI: 10.1016/j.physletb.2012.08.020. arXiv: 1207.7214 [hep-ex] (cit. on p. 2).

[19] S. Chatrchyan *et al.*, "Observation of a New Boson at a Mass of 125 GeV with the CMS Experiment at the LHC", *Phys. Lett. B*, vol. 716, pp. 30–61, 2012. DOI: 10.1016/j.physletb.2012.08.021. arXiv: 1207.7235 [hep-ex] (cit. on p. 2).

[20] F. Englert and R. Brout, "Broken Symmetry and the Mass of Gauge Vector Mesons", *Phys. Rev. Lett.*, vol. 13, J. C. Taylor, Ed., pp. 321–323, 1964. DOI: 10.1103/PhysRevLett.13.321 (cit. on pp. 2, 8).

[21] P. W. Higgs, "Broken Symmetries and the Masses of Gauge Bosons", *Phys. Rev. Lett.*, vol. 13, J. C. Taylor, Ed., pp. 508–509, 1964. DOI: 10.1103/PhysRevLett.13.508 (cit. on pp. 2, 8).

[22] C. Burgard. "Example: Standard model of physics". (2016), [Online]. Available: https://texample.net/tikz/examples/model-physics/ (visited on 05/30/2022) (cit. on p. 4).

[23] S. Schael *et al.*, "Branching ratios and spectral functions of tau decays: Final ALEPH measurements and physics implications", *Phys. Rept.*, vol. 421, pp. 191–284, 2005. DOI: 10.1016/j.physrep.2005.06.007. arXiv: hep-ex/0506072 (cit. on p. 5).

[24] P. A. Zyla *et al.*, "Review of Particle Physics", *PTEP*, vol. 2020, no. 8, p. 083C01, 2020. DOI: 10.1093/ptep/ptaa104 (cit. on pp. 5, 12, 13, 72).

[25] M. E. Peskin and D. V. Schroeder, *An Introduction to quantum field theory*. Reading, USA: Addison-Wesley, 1995, ISBN: 978-0-201-50397-5 (cit. on p. 6).

[26] J. Goldstone, "Field Theories with Superconductor Solutions", *Nuovo Cim.*, vol. 19, pp. 154–164, 1961. DOI: 10.1007/BF02812722 (cit. on p. 8).

[27] G. Aad *et al.*, "Combined measurements of Higgs boson production and decay using up to 80 fb^{-1} of proton-proton collision data at $\sqrt{s} = 13$ TeV collected with the ATLAS experiment", *Phys. Rev. D*, vol. 101, no. 1, p. 012 002, 2020. DOI: 10.1103/PhysRevD.101.012002. arXiv: 1909.02845 [hep-ex] (cit. on p. 10).

[28] A. M. Sirunyan *et al.*, "Evidence for Higgs boson decay to a pair of muons", *JHEP*, vol. 01, p. 148, 2021. DOI: 10.1007/JHEP01(2021)148. arXiv: 2009.04363 [hep-ex] (cit. on p. 10).

[29] G. Aad *et al.*, "Combined Measurement of the Higgs Boson Mass in pp Collisions at $\sqrt{s} = 7$ and 8 TeV with the ATLAS and CMS Experiments", *Phys. Rev. Lett.*, vol. 114, p. 191 803, 2015. DOI: 10.1103/PhysRevLett.114.191803. arXiv: 1503.07589 [hep-ex] (cit. on p. 12).

[30] M. Aaboud *et al.*, "Measurement of the Higgs boson mass in the $H \to ZZ^* \to 4\ell$ and $H \to \gamma\gamma$ channels with $\sqrt{s} = 13$ TeV pp collisions using the ATLAS detector", *Phys. Lett. B*, vol. 784, pp. 345–366, 2018. DOI: 10.1016/j.physletb.2018.07.050. arXiv: 1806.00242 [hep-ex] (cit. on p. 12).

[31] A. M. Sirunyan *et al.*, "A measurement of the Higgs boson mass in the diphoton decay channel", *Phys. Lett. B*, vol. 805, p. 135 425, 2020. DOI: 10.1016/j.physletb.2020.135425. arXiv: 2002.06398 [hep-ex] (cit. on p. 12).

[32] D. de Florian *et al.*, "Handbook of LHC Higgs Cross Sections: 4. Deciphering the Nature of the Higgs Sector", vol. 2/2017, Oct. 2016. DOI: 10.23731/CYRM-2017-002. arXiv: 1610.07922 [hep-ph] (cit. on p. 13).

[33] J. R. Andersen *et al.*, "Handbook of LHC Higgs Cross Sections: 3. Higgs Properties", S. Heinemeyer, C. Mariotti, G. Passarino, and R. Tanaka, Eds., Jul. 2013. DOI: 10.5170/CERN-2013-004. arXiv: 1307.1347 [hep-ph] (cit. on p. 13).

[34] P. Bambade *et al.*, "The International Linear Collider: A Global Project", Mar. 2019. arXiv: 1903.01629 [hep-ex] (cit. on pp. 14, 60).

[35] "The International Linear Collider Technical Design Report - Volume 1: Executive Summary", T. Behnke, J. E. Brau, B. Foster, *et al.*, Eds., Jun. 2013. arXiv: 1306.6327 [physics.acc-ph] (cit. on p. 15).

[36] "The International Linear Collider Technical Design Report - Volume 2: Physics", H. Baer *et al.*, Eds., Jun. 2013. arXiv: 1306.6352 [hep-ph] (cit. on p. 15).

[37] "The International Linear Collider Technical Design Report - Volume 3.I: Accelerator \& in the Technical Design Phase", C. Adolphsen *et al.*, Eds., Jun. 2013. arXiv: 1306.6353 [physics.acc-ph] (cit. on p. 15).

[38] "The International Linear Collider Technical Design Report - Volume 3.II: Accelerator Baseline Design", C. Adolphsen *et al.*, Eds., Jun. 2013. arXiv: 1306.6328 [physics.acc-ph] (cit. on p. 15).

[39] H. Abramowicz *et al.*, "The International Linear Collider Technical Design Report - Volume 4: Detectors", T. Behnke, J. E. Brau, P. N. Burrows, *et al.*, Eds., Jun. 2013. arXiv: 1306.6329 [physics.ins-det] (cit. on p. 15).

[40] A. Aryshev *et al.*, "The International Linear Collider: Report to Snowmass 2021", Mar. 2022. arXiv: 2203.07622 [physics.acc-ph] (cit. on pp. 15, 16, 19, 20, 33, 34, 37, 110, 111).

[41] A. Vogel, "Beam-induced backgrounds in detectors at the ILC", Other thesis, Aug. 2008. DOI: 10.3204/DESY-THESIS-2008-036 (cit. on p. 18).

[42] G. Breit and J. A. Wheeler, "Collision of two light quanta", *Phys. Rev.*, vol. 46, no. 12, pp. 1087–1091, 1934. DOI: 10.1103/PhysRev.46.1087 (cit. on p. 18).

[43] H. Bethe and W. Heitler, "On the Stopping of fast particles and on the creation of positive electrons", *Proc. Roy. Soc. Lond. A*, vol. 146, pp. 83–112, 1934. DOI: 10.1098/rspa.1934.0140 (cit. on p. 18).

[44] K. Fujii *et al.*, "Tests of the Standard Model at the International Linear Collider", Aug. 2019. arXiv: 1908.11299 [hep-ex] (cit. on p. 19).

[45] M. J. Boland *et al.*, "Updated baseline for a staged Compact Linear Collider", P. Lebrun, L. Linssen, D. Schulte, *et al.*, Eds., Aug. 2016. DOI: 10.5170/CERN-2016-004. arXiv: 1608.07537 [physics.acc-ph] (cit. on p. 22).

[46] "CEPC Conceptual Design Report: Volume 1 - Accelerator", Sep. 2018. arXiv: 1809.00285 [physics.acc-ph] (cit. on p. 22).

[47] M. Dong *et al.*, "CEPC Conceptual Design Report: Volume 2 - Physics & Detector", J. B. Guimarães da Costa *et al.*, Eds., Nov. 2018. arXiv: 1811.10545 [hep-ex] (cit. on p. 22).

[48] A. Abada *et al.*, "FCC-ee: The Lepton Collider: Future Circular Collider Conceptual Design Report Volume 2", *Eur. Phys. J. ST*, vol. 228, no. 2, pp. 261–623, 2019. DOI: 10.1140/epjst/e2019-900045-4 (cit. on p. 22).

[49] J.-C. Brient and H. Videau, "The Calorimetry at the future e+ e- linear collider", *eConf*, vol. C010630, N. Graf, Ed., E3047, 2001. arXiv: hep-ex/0202004 (cit. on p. 25).

[50] D. Buskulic *et al.*, "Performance of the ALEPH detector at LEP", *Nucl. Instrum. Meth. A*, vol. 360, pp. 481–506, 1995. DOI: 10.1016/0168-9002(95)00138-7 (cit. on pp. 25, 26).

[51] J. C. Brient, "Improving the jet reconstruction with the particle flow method: An introduction", in *11th International Conference on Calorimetry in High-Energy Physics (Calor 2004)*, Mar. 2004, pp. 445–451. arXiv: physics/0412149 (cit. on p. 25).

[52] J. S. Marshall and M. A. Thomson, "The Pandora software development kit for particle flow calorimetry", *J. Phys. Conf. Ser.*, vol. 396, M. Ernst, D. Düllmann, O. Rind, and T. Wong, Eds., p. 022 034, 2012. DOI: 10.1088/1742-6596/396/2/022034 (cit. on pp. 26–28, 37).

[53] M. A. Thomson, "Particle Flow Calorimetry and the PandoraPFA Algorithm", *Nucl. Instrum. Meth. A*, vol. 611, pp. 25–40, 2009. DOI: 10.1016/j.nima.2009.09.009. arXiv: 0907.3577 [physics.ins-det] (cit. on pp. 26–29, 37).

[54] H. Abramowicz *et al.*, "International Large Detector: Interim Design Report", Mar. 2020. arXiv: 2003.01116 [physics.ins-det] (cit. on pp. 26, 29–33, 36, 38).

[55] M. Ruan and H. Videau, "Arbor, a new approach of the Particle Flow Algorithm", in *International Conference on Calorimetry for the High Energy Frontier*, 2013, pp. 316–324. arXiv: 1403.4784 [physics.ins-det] (cit. on p. 28).

[56] M. Ruan *et al.*, "Reconstruction of physics objects at the Circular Electron Positron Collider with Arbor", *Eur. Phys. J. C*, vol. 78, no. 5, p. 426, 2018. DOI: 10.1140/epjc/s10052-018-5876-z. arXiv: 1806.04879 [hep-ex] (cit. on p. 28).

[57] C. Adloff, J. Blaha, J. .-. Blaising, *et al.*, "Tests of a particle flow algorithm with CALICE test beam data", *JINST*, vol. 6, P07005, 2011. DOI: 10.1088/1748-0221/6/07/P07005. arXiv: 1105.3417 [physics.ins-det] (cit. on p. 29).

[58] A. M. Sirunyan *et al.*, "Particle-flow reconstruction and global event description with the CMS detector", *JINST*, vol. 12, no. 10, P10003, 2017. DOI: 10.1088/1748-0221/12/10/P10003. arXiv: 1706.04965 [physics.ins-det] (cit. on p. 32).

[59] "The ILCSoft project". [Online]. Available: https://github.com/iLCSoft (visited on 06/16/2022) (cit. on p. 34).

[60] W. Kilian, T. Ohl, and J. Reuter, "WHIZARD: Simulating Multi-Particle Processes at LHC and ILC", *Eur. Phys. J. C*, vol. 71, p. 1742, 2011. DOI: 10.1140/epjc/s10052-011-1742-y. arXiv: 0708.4233 [hep-ph] (cit. on p. 35).

[61] M. Moretti, T. Ohl, and J. Reuter, "O'Mega: An Optimizing matrix element generator", T. Behnke, S. Bertolucci, R. D. Heuer, *et al.*, Eds., pp. 1981–2009, Feb. 2001. arXiv: hep-ph/0102195 (cit. on p. 35).

[62] T. Sjostrand, S. Mrenna, and P. Z. Skands, "PYTHIA 6.4 Physics and Manual", *JHEP*, vol. 05, p. 026, 2006. DOI: 10.1088/1126-6708/2006/05/026. arXiv: hep-ph/0603175 (cit. on p. 35).

[63] D. Schulte, "Beam-beam simulations with Guinea-Pig", *eConf*, vol. C980914, K. Ko and R. D. Ryne, Eds., pp. 127–131, 1998 (cit. on p. 35).

[64] P. Chen, T. L. Barklow, and M. E. Peskin, "Hadron production in gamma gamma collisions as a background for e+ e- linear colliders", *Phys. Rev. D*, vol. 49, pp. 3209–3227, 1994. DOI: 10.1103/PhysRevD.49.3209. arXiv: hep-ph/9305247 (cit. on p. 35).

[65] M. Frank, F. Gaede, C. Grefe, and P. Mato, "DD4hep: A Detector Description Toolkit for High Energy Physics Experiments", *J. Phys. Conf. Ser.*, vol. 513, D. L. Groep and D. Bonacorsi, Eds., p. 022 010, 2014. DOI: 10.1088/1742-6596/513/2/022010 (cit. on p. 36).

[66] M. Frank, F. Gaede, N. Nikiforou, M. Petric, and A. Sailer, "DDG4 A Simulation Framework based on the DD4hep Detector Description Toolkit", *J. Phys. Conf. Ser.*, vol. 664, no. 7, p. 072 017, 2015. DOI: 10.1088/1742-6596/664/7/072017 (cit. on p. 36).

[67] S. Agostinelli *et al.*, "GEANT4–a simulation toolkit", *Nucl. Instrum. Meth. A*, vol. 506, pp. 250–303, 2003. DOI: 10.1016/S0168-9002(03)01368-8 (cit. on p. 36).

[68] F. Gaede, T. Behnke, N. Graf, and T. Johnson, "LCIO: A Persistency framework for linear collider simulation studies", *eConf*, vol. C0303241, TUKT001, 2003. arXiv: physics/0306114 (cit. on p. 36).

[69] F. Gaede, "Marlin and LCCD: Software tools for the ILC", *Nucl. Instrum. Meth. A*, vol. 559, J. Blumlein, W. Friebel, T. Naumann, T. Riemann, P. Wegner, and D. Perret-Gallix, Eds., pp. 177–180, 2006. DOI: 10.1016/j.nima.2005.11.138 (cit. on p. 37).

[70] F. Gaede, S. Aplin, R. Glattauer, C. Rosemann, and G. Voutsinas, "Track reconstruction at the ILC: the ILD tracking software", *J. Phys. Conf. Ser.*, vol. 513, D. L. Groep and D. Bonacorsi, Eds., p. 022 011, 2014. DOI: 10.1088/1742-6596/513/2/022011 (cit. on p. 37).

[71] T. Suehara and T. Tanabe, "LCFIPlus: A Framework for Jet Analysis in Linear Collider Studies", *Nucl. Instrum. Meth. A*, vol. 808, pp. 109–116, 2016. DOI: 10.1016/j.nima.2015.11.054. arXiv: 1506.08371 [physics.ins-det] (cit. on pp. 37, 83).

[72] K. Kawagoe *et al.*, "Beam test performance of the highly granular SiW-ECAL technological prototype for the ILC", *Nucl. Instrum. Meth. A*, vol. 950, p. 162969, 2020. DOI: 10.1016/j.nima.2019.162969. arXiv: 1902.00110 [physics.ins-det] (cit. on p. 39).

[73] J. Repond *et al.*, "Design and Electronics Commissioning of the Physics Prototype of a Si-W Electromagnetic Calorimeter for the International Linear Collider", *JINST*, vol. 3, P08001, 2008. DOI: 10.1088/1748-0221/3/08/P08001. arXiv: 0805.4833 [physics.ins-det] (cit. on p. 39).

[74] S. Callier, F. Dulucq, C. de La Taille, G. Martin-Chassard, and N. Seguin-Moreau, "SKIROC2, front end chip designed to readout the Electromagnetic CALorimeter at the ILC", *JINST*, vol. 6, p. C12040, 2011. DOI: 10.1088/1748-0221/6/12/C12040 (cit. on pp. 40, 41, 43).

[75] R. Diener *et al.*, "The DESY II Test Beam Facility", *Nucl. Instrum. Meth. A*, vol. 922, pp. 265–286, 2019. DOI: 10.1016/j.nima.2018.11.133. arXiv: 1807.09328 [physics.ins-det] (cit. on pp. 40, 55).

[76] F. Magniette, J. Nanni, R. Guillaumat, *et al.*, "ILD silicon tungsten electromagnetic calorimeter first full scale electronic prototype", *Nucl. Instrum. Meth. A*, vol. 958, M. Krammer, T. Bergauer, M. Dragicevic, *et al.*, Eds., p. 162732, 2020. DOI: 10.1016/j.nima.2019.162732. arXiv: 1909.04329 [physics.ins-det] (cit. on pp. 42, 47).

[77] S. Bilokin *et al.*, "Commissioning of the highly granular SiW-ECAL technological prototype", Oct. 2018. arXiv: 1810.05133 [physics.ins-det] (cit. on pp. 42, 48).

[78] M. S. Amjad *et al.*, "Beam test performance of the SKIROC2 ASIC", *Nucl. Instrum. Meth. A*, vol. 778, pp. 78–84, 2015. DOI: 10.1016/j.nima.2014.12.011 (cit. on p. 48).

[79] F. Jimenez, "Implementation of the SiW ECAL into the simulation", CALICE collaboration meeting, Valencia, 2022. [Online]. Available: https://agenda.linearcollider.org/event/9571/contributions/50575/ (cit. on p. 53).

[80] SiWECAL-TestBeam, "SiWECAL-Sim", GitHub. [Online]. Available: https://github.com/SiWECAL-TestBeam/SiWECAL-Sim (visited on 08/20/2022) (cit. on p. 53).

[81] H. Ono and A. Miyamoto, "A study of measurement precision of the Higgs boson branching ratios at the International Linear Collider", *Eur. Phys. J. C*, vol. 73, no. 3, p. 2343, 2013. DOI: 10.1140/epjc/s10052-013-2343-8. arXiv: 1207.0300 [hep-ex] (cit. on pp. 61, 112).

[82] M. Thomson, "Model-independent measurement of the $e^+e^- \to$HZ cross section at a future e^+e^- linear collider using hadronic Z decays", *Eur. Phys. J. C*, vol. 76, no. 2, p. 72, 2016. DOI: 10.1140/epjc/s10052-016-3911-5. arXiv: 1509.02853 [hep-ex] (cit. on p. 61).

[83] J. Yan, K. Fujii, and J. Tian, "Model independence of the measurement of the $e^+e^- \to$ZH cross section using Z$\to \mu^+\mu^-$ and Z$\to e^+e^-$ at the ILC", Jan. 2016. arXiv: 1601.06481 [hep-ph] (cit. on pp. 66, 110).

[84] H. Nori, S. Jenkins, P. Koch, and R. Caruana, "Interpretml: A unified framework for machine learning interpretability", Sep. 2019. arXiv: 1909.09223 [cs.LG] (cit. on pp. 69, 133).

[85] Y. Lou, R. Caruana, J. Gehrke, and G. Hooker, "Accurate intelligible models with pairwise interactions", in *Proceedings of the 19th ACM SIGKDD International Conference on Knowledge Discovery and Data Mining*, ser. KDD '13, Chicago, Illinois, USA: Association for Computing Machinery, 2013, pp. 623–631, ISBN: 9781450321747. DOI: 10.1145/2487575.2487579. [Online]. Available: https://doi.org/10.1145/2487575.2487579 (cit. on p. 72).

[86] T. Chen and C. Guestrin, "XGBoost: A Scalable Tree Boosting System", Mar. 2016. DOI: 10.1145/2939672.2939785. arXiv: 1603.02754 [cs.LG] (cit. on pp. 73, 133).

[87] S. Catani, Y. L. Dokshitzer, M. Olsson, G. Turnock, and B. R. Webber, "New clustering algorithm for multi - jet cross-sections in e+ e- annihilation", *Phys. Lett. B*, vol. 269, pp. 432–438, 1991. DOI: 10.1016/0370-2693(91)90196-W (cit. on p. 83).

[88] S.-i. Kawada, J. List, and M. Berggren, "Prospects of measuring the branching fraction of the Higgs boson decaying into muon pairs at the International Linear Collider", *Eur. Phys. J. C*, vol. 80, no. 12, p. 1186, 2020. DOI: 10.1140/epjc/s10052-020-08729-7. arXiv: 2009.04340 [hep-ex] (cit. on p. 89).

[89] H. Dembinski, P. Ongmongkolkul, *et al.*, "Scikit-hep/iminuit: V2.0.0", version v2.0.0, Dec. 2020. DOI: 10.5281/zenodo.4310361. [Online]. Available: https://doi.org/10.5281/zenodo.4310361 (cit. on p. 101).

[90] F. James and M. Roos, "Minuit: A System for Function Minimization and Analysis of the Parameter Errors and Correlations", *Comput. Phys. Commun.*, vol. 10, pp. 343–367, 1975. DOI: 10.1016/0010-4655(75)90039-9 (cit. on p. 101).

[91] A. Albert *et al.*, "Strange quark as a probe for new physics in the Higgs sector", in *2022 Snowmass Summer Study*, Mar. 2022. arXiv: 2203.07535 [hep-ex] (cit. on p. 104).

[92] M. Cepeda *et al.*, "Report from Working Group 2: Higgs Physics at the HL-LHC and HE-LHC", *CERN Yellow Rep. Monogr.*, vol. 7, A. Dainese, M. Mangano, A. B. Meyer, A. Nisati, G. Salam, and M. A. Vesterinen, Eds., pp. 221–584, 2019. DOI: 10.23731/CYRM-2019-007.221. arXiv: 1902.00134 [hep-ph] (cit. on pp. 110–112).

[93] M. Klute, R. Lafaye, T. Plehn, M. Rauch, and D. Zerwas, "Measuring Higgs Couplings at a Linear Collider", *EPL*, vol. 101, no. 5, p. 51001, 2013. DOI: 10.1209/0295-5075/101/51001. arXiv: 1301.1322 [hep-ph] (cit. on p. 111).

[94] SiWECAL-TestBeam, "SiWECAL-TB-analysis", GitHub. [Online]. Available: https://github.com/SiWECAL-TestBeam/SiWECAL-TB-analysis (visited on 08/20/2022) (cit. on p. 135).

[95] J. Kunath, "SiW-ECAL: Better event building", CALICE collaboration meeting, Valencia, 2022. [Online]. Available: https://agenda.linearcollider.org/event/9571/contributions/50573/ (cit. on p. 136).

[96] SiWECAL-TestBeam, "SiWECAL-TB-monitoring", GitHub. [Online]. Available: https://github.com/SiWECAL-TestBeam/SiWECAL-TB-monitoring (visited on 08/20/2022) (cit. on p. 136).

ECOLE
DOCTORALE

Titre : Mesure directe des rapports d'embranchement des bosons de Higgs dans les collisions électron-positon à 250 GeV

Mots clés : Usine à Higgs, Collisionneur leptonique, Expérience ILD, ECAL, Boson de Higgs

Résumé : Les couplages des particules du modèle standard (SM) au boson de Higgs peuvent être modifiés si des particules lourdes supplémentaires existent. De nombreux modèles de physique au-delà du SM donnent lieu à des déviations de l'ordre de 10% ou moins. Cela est au-delà de la précision attendue au HL-LHC qui est limitée par les erreurs systématiques. Dans un collisionneur électron-positron avec une énergie au centre de la masse de 250 GeV, appelé une usine à Higgs, la plupart des principaux couplages de Higgs peuvent être mesurés au niveau du pourcent ou moins.
Le canal principal de production de Higgs s'accompagne d'un boson Z. Si l'impulsion du boson Z reculant contre le boson de Higgs est correctement reconstruit, l'événement peut être sélectionné indépendamment de la désintégration du boson de Higgs. Cette reconstruction fonctionne mieux pour les bosons Z qui se désintègrent en electrons ou muons. Au cours du programme 250 GeV proposé pour le ILC, plus de 10.000 bosons de Higgs devraient être collectés dans des échantillons de haute pureté et indépendants du modèle de désintégration. Chaque échantillon est divisé en régions mutuellement exclusives avec des compositions distinctes par désintégration de Higgs et par bruit de fond. Ensuite, l'écart du rapport de branchement (BR) du boson de Higgs par rapport à l'attente du SM conduit à une structure caractéristique d'excès ou de déficit dans le nombre d'événements par région. Contrairement aux mesures standards des désintégrations du boson de Higgs, il n'est pas nécessaire de normaliser ces valeurs par la section efficace. Un grand ensemble de données de simulation complète préparé pour le concept de détecteur ILD est utilisé pour la validation de cette approche.
Le calorimètre électromagnétique d'un détecteur flux de particules comme l'ILD doit pouvoir résoudre les différentes trajectoires et gerbes dans un jet. Une granularité longitudinale et transversale élevée est donc essentielle. Le calorimètre SiW-ECAL est un calorimètre d'imagerie par échantillonnage. Un prototype technologique de plus de 15.000 canaux en 15 couches avec des cellules carrées de 5 mm a été testé en faisceau au DESY. Cette thèse présente les améliorations apportées à la reconstruction à la volée des événements à partir des cellules individuelles.

Title : A direct measurement of Higgs boson branching ratios in electron-positron collisions at 250 GeV

Keywords : Higgs factory, Lepton collider, ILD experiment, ECAL, Higgs boson

Abstract : The couplings of standard model (SM) particles to the Higgs boson can be shifted if additional heavy particles exist. Many models of physics beyond the SM result in deviations of the order of 10% or less. This goes beyond the expected precision at HL-LHC that is limited by the systematic errors in proton-proton collisions. At an electron-positron collider with a center-of-mass energy of 250 GeV, referred to as a Higgs factory, most major Higgs couplings can be measured at the percent level or below.
The main Higgs production channel is the associated production with a Z boson. If the momentum of the Z boson recoiling against the Higgs boson is properly reconstructed, the event can be selected independently of the Higgs decay. This reconstruction works best for Z bosons decaying to electrons or muons. During the proposed 250 GeV program of the ILC, more than 10.000 Higgs bosons are expected to be collected in high-purity model-independent samples. Each sample is partitioned into mutually exclusive regions with distinct Higgs decay and background compositions. Then the deviation of a Higgs branching ratio (BR) from the SM expectation leads to a characteristic pattern of excesses or deficits in the number of events per region. A simultaneous measurement of the Higgs BRs is obtained from a fit to the number of events per region. In contrast to the standard measurements of Higgs decays, it is not necessary to normalize these values by a production cross section. A large full simulation data set prepared for the ILD detector concept is used to validate this approach.
The electromagnetic calorimeter in a particle flow detector like ILD must be able to resolve the individual tracks and showers within a jet. Therefore a high longitudinal and transversal granularity is essential. The SiW-ECAL is a sampling imaging calorimeter. A technological prototype featuring over 15.000 channels in 15 layers with 5 mm square cells was tested at DESY. This thesis presents improvements to the initial event reconstruction from individual hits.

Institut Polytechnique de Paris
91120 Palaiseau, France